Neuroimaging at ultra-high spatiotemporal resolutions: line-scanning fMRI

Luisa Raimondo

Neuroimaging at ultra-high spatiotemporal resolutions: line-scanning fMRI
PhD Thesis, Vrije Universiteit Amsterdam, The Netherlands

© 2023, Luisa Raimondo

VRIJE UNIVERSITEIT

Neuroimaging at ultra-high spatiotemporal resolutions: line-scanning fMRI

ACADEMISCH PROEFSCHRIFT

ter verkrijging van de graad Doctor of Philosophy aan
de Vrije Universiteit Amsterdam,
op gezag van de rector magnificus
prof.dr. J.J.G. Geurts,
in het openbaar te verdedigen
ten overstaan van de promotiecommissie
van de Faculteit der Gedrags- en Bewegingswetenschappen
op dinsdag 9 januari 2024 om 11.45 uur
in een bijeenkomst van de universiteit,
De Boelelaan 1105
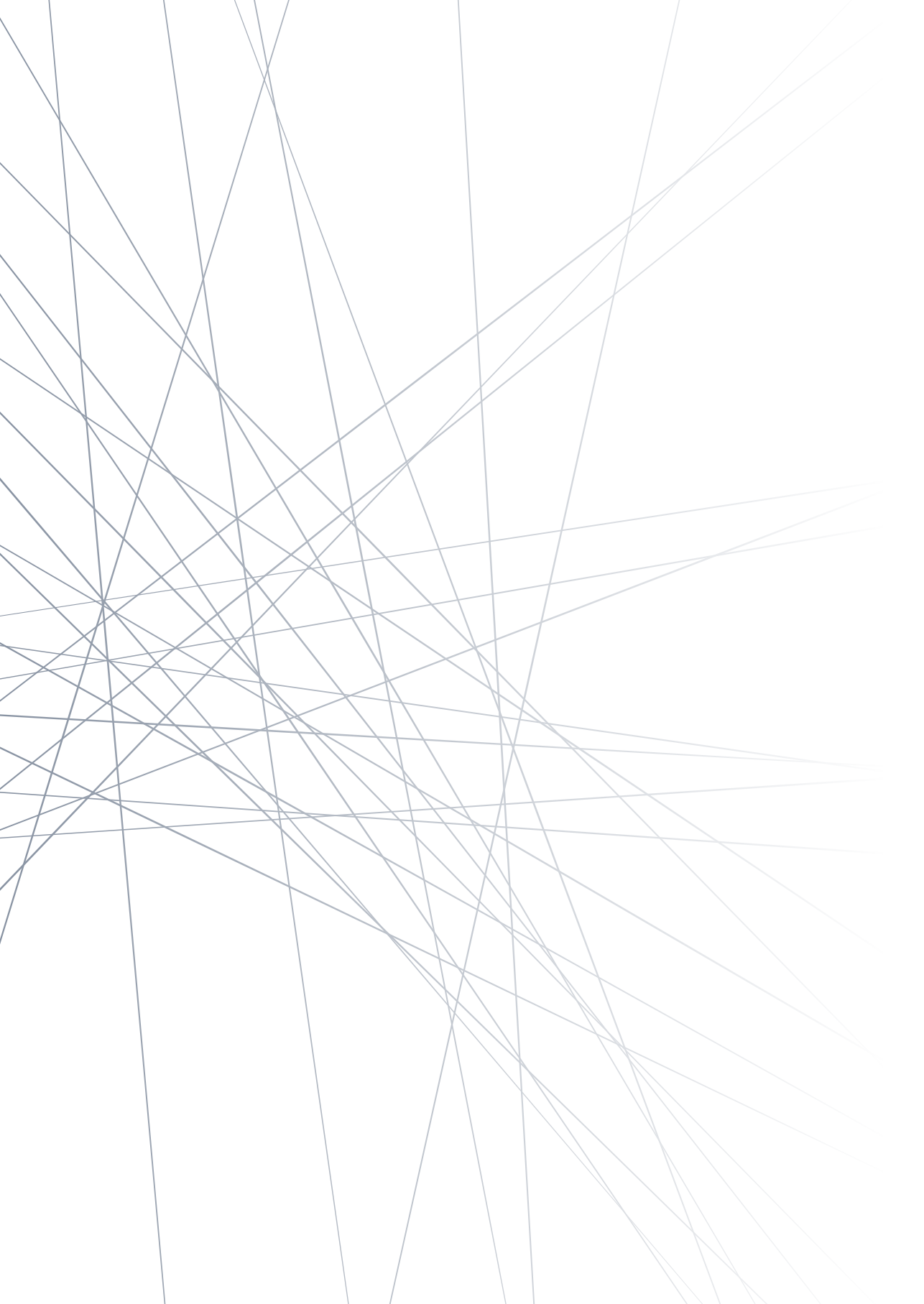
door

Luisa Raimondo

geboren te Biella, Italië

Contents

1

GENERAL INTRODUCTION

1

The interest of humans in their brain has been proved to exist since the VII century B.C., when a reference to the word "brain" was registered for the very first time in an ancient Egyptian medical text: the Edwin Smith Papyrus [1].

Either from a scientific perspective or from a philosophical point of view, the brain raises questions that we are still not able to answer, despite the effort over centuries. As the most important organ of the human nervous system, it allows us to feel sensations, perceptions and emotions, elaborate thoughts, process information, make movements and remember experiences. In simple words, it allows us to live and become the person we want to be.

In order to get more insights about how the brain functions, it is necessary to combine structural static information to repetitive measurements detecting brain dynamics. Statically, the brain can be studied at different scales, schematically represented in Figure 1.1:

- On a microscopic level the human neuronal fibers have a diameter ranging from 0.16 to 9 μm [2]

- On a mesoscopic scale neurons are organized in columnar and laminar structures in the human cortex. The thickness of the human cortex varies from 1 to 4.5 mm, with an average of 2.5 mm [3], and within this thickness layers and columns can be identified [4–6]

- On a macroscopic level, the brain can be separated into areas either having different functional specialization or different topographic organization [5]
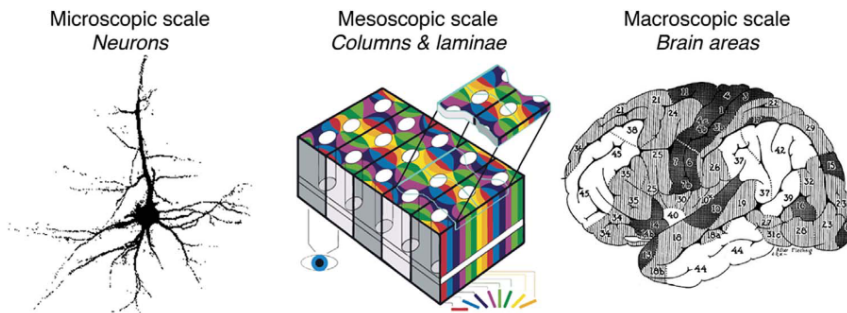
Figure 1.1: Different organization scales of the human brain, ranging from microscopic (single neurons) to mesoscopic (columnar and laminar structures) to macroscopic (brain areas, as defined by myeloarchitecture. From [5].

Functionally, the brain can be inspected if the variable "time" is introduced in the study. Again, this inspection can be performed at different scales. The classic hemodynamic response due to the changes in the vascular system that are triggered by the neuronal activity show a peak at around 3-5 s after a short stimulation (even for stimulus durations of less than 1 s) [7]. At the mesoscopic scale layers

show differences in the response time of less than 1 s [8, 9], while synaptic transmission occurs at a millisecond level [10].

Neuroscience is the discipline which has the difficult role of understanding the mechanisms that rule the functions of the nervous system, including the brain. This can be achieved through different means and at different levels. The means employed in this thesis are magnetic resonance imaging (MRI) and functional MRI.

1.1 MRI and functional MRI (fMRI)

MRI is one of the most common ways to non-invasively inspect the properties of the brain. It is a highly elegant imaging method, which relies on quantum mechanical concepts. In the macroscopic limit for quantum, quantum mechanics typically converges to classic mechanics, hence a classical description can be adequate for MRI [11]. From a classical perspective, the MR signal is a small electrical voltage induced in a receiver coil due to the precession of the net transversal magnetization during resonance and after excitation. This is the result of Faraday's Law of Induction, according to which a changing magnetic field induces a voltage in a nearby conductor [12].

Since its very early stages, MRI showed its potentials in clinical practice because of the capacity to characterize normal anatomy and show abnormal conditions in many organs and anatomic regions of the body [13]. In the context of neuroimaging, it is currently commonly used as diagnostic tool for different brain disorders, due to its versatility and vast applicability [14–18]. On the other hand, fundamental neuroscience is also taking advantage of MRI for many research applications [19].

Functional MRI (fMRI) is a very popular method to investigate brain metabolic changes [20]. There are two different ways that allows to detect an increased neural activity through MRI, via the associated hyperemia response (neurovascular coupling): an increase in local cerebral blood flow (CBF) and the accompanying changes in oxygenation concentration (Blood Oxygen Level Dependent, or BOLD, contrast). The change in CBF can be observed using arterial spin labeling (ASL) [21]. The second mechanism is the one we focused on in this work, and it is the one primarily used for fMRI experiments. The BOLD contrast was first described in 1990 by Seiji Ogawa [22], when he observed that the MR signal changed in specific brain regions according to the oxy- and deoxyhaemoglobin levels. In fact, the BOLD contrast arises from the change in magnetic field surrounding the red blood cells, which depends on the oxygen state of the haemoglobin. When a region of the brain becomes neuronally active, CBF and cerebral blood volume (CBV) increase in that region and oxygenated blood displaces deoxygenated blood. The paramagnetic properties of deoxygenated haemoglobin cause an increase in the MR signal when the deoxygenated amount of blood decreases, hence the BOLD signal is a consequence of brain activity (see Figure 1.2).

fMRI based on BOLD contrast is currently the mainstay of human neuroimaging,

1

thanks to its non-invasive nature, increasing availability, and its capacity to detect different brain areas engaged when subjects undertake particular tasks [23, 24].
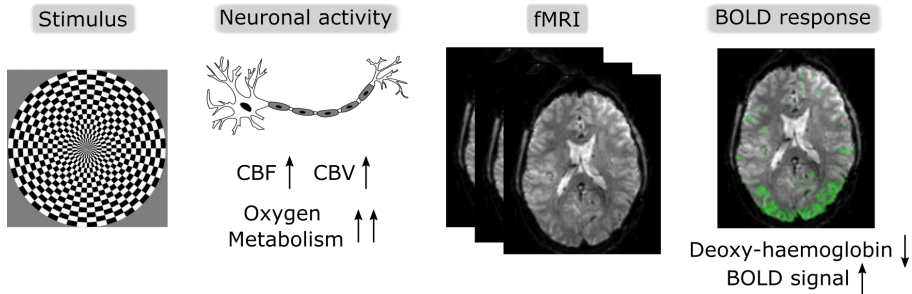

Figure 1.2: Illustration of the BOLD mechanism. The BOLD signal represents the changes in the deoxyhaemoglobin caused by local changes in the brain blood flow, volume and oxygenation. When a stimulus is presented, it induces an increase in the neuronal activity, which causes vasodilation and, as a consequence, an increase in CBV and CBF. These processes bring more oxygenated blood, hence the deoxyhaemoglobin is washed out, which results in a more homogeneous magnetic field, in which the decay of transverse magnetisation occurs more slowly and the BOLD signal increases.

Particularly, high field MRI can leverage higher signal-to-noise ratio (SNR) to increase spatial specificity through higher spatial resolution. Being able to image smaller voxels leads to a decrease in partial volume effects [25] but also a loss in SNR and functional contrast-to-noise ratio (fCNR). In this regard, ultra-high-field (UHF) MRI furnishes a solution, because of the linear dependency of the SNR with the magnetic field [26, 27] and the supralinear gains in BOLD fCNR [25, 28]. Moreover, at UHF strengths, the increased sensitivity to susceptibility effects (i.e. changes) makes the T_2^* of grey matter shorter and the BOLD contrast is enhanced [29].

Common sequences used for fMRI acquisitions at UHF aim at increasing the spatial and temporal resolutions, as well as improving the spatial specificity of the BOLD signal to better localize activation [30]. Gradient-echo echo-planar-imaging (GRE-EPI) acquisition is a typical method (T_2^*w) for fMRI studies because of its high sensitivity to deoxyhaemoglobin variations (hence BOLD signal). On the other hand, T_2w methods such as spin-echo EPI (SE-EPI) provide higher microvascular specificity, which provides better spatial localisation of the underlying neuronal activity (i.e. higher spatial specificity to neuronal activity). Again UHF allows, here as well, higher BOLD sensitivity compared to lower fields [31]. However, the higher spatial specificity of SE-EPI methods compared to GE-EPI still comes at the cost of reduced BOLD sensitivity [32].

1.2   fMRI challenges

As already mentioned, fMRI acquisition strategies have the final goal of increasing spatial and temporal resolutions, while keeping an adequate BOLD contrast. EPI is an efficient sampling method, with up to sub-millimeter spatial resolution and a temporal resolution usually in the order of seconds. However, to depict the

spatiotemporal characteristics of the hemodynamic response function (HRF) at a mesoscopic scale, sub-millimeter spatial resolution and sub-second sampling rate are highly desirable.

When available, using high field strengths is the best approach to increase spatial resolution, since it allows reduced voxels sizes as a consequence of higher SNR. In the present thesis, we used a main magnetic field of 7 tesla. Higher spatial resolution always come at the cost of longer scan time. For this reason, multiple methods have been developed to improve the temporal resolution, including undersampling techniques such as partial Fourier [33], parallel imaging [34–36] and compressed sensing [37]. Acceleration techniques can be applied to EPI sequences, but when they are used for fMRI purposes there is a time limitation due to the fact that the echo-time (TE) has to be similar to the T_2^* of grey matter to get an optimal BOLD contrast. Further acceleration can be obtained when moving from 2D to 3D or simultaneous multislice (SMS) acquisitions, where the acceleration can be performed in two directions [38–40]. Overall, these techniques allow relatively high spatial and temporal resolutions at high fields (~1-1.5 mm isotropic and TR of 1-2 s), for whole brain coverage studies. However, these resolutions are not sufficient for layer fMRI studies, for instance aiming to detect differences in the HRF across cortical depth. Laminar or layer fMRI, for example, aims to investigate the architecture of the isocortex at a sufficiently high spatiotemporal resolution, so that the functional and structural characteristics of the individual layers of the cortex can be identified separately. In this way, it is possible to gain more insights on the fundamental processes and cortical structure than what is possible when grouping the signal over the entire cortical thickness [8, 41].

Reducing the field-of-view (FOV) is an easy implementation to reach higher spatial and temporal resolution together: a multi-slice acquisition not covering the whole brain can be performed with high in-plane resolution and relatively fast TR [42]. A further reduction of the FOV allows to investigate specific regions of the brain, with high in-plane spatial resolution and fast sampling rate, due to the fact that a smaller region was imaged. For example [43] focused on ocular dominance columns in visual cortex, with an in-plane spatial resolution of 0.47 mm isotropic, while [44] focused on laminar activity of primary motor cortex with resolution of 0.75x0.75x1.5 mm^3. Alternatively, strongly anisotropic voxels can be used: Kashyap et al. mapped the BOLD signal along the cortical depth with a temporal resolution of 1.76 s and voxel sizes of 0.1x1.4x2 mm^3 [45].

A different approach to reduce the FOV is through outer volume suppression (OVS). OVS allows to push the resolutions even further such as with zoomed imaging [46], which was used to furnish BOLD responses detected at 0.5x0.5x3 mm^3 spatial and 250 ms temporal resolution. Clearly, to improve, at the same time, both the spatial and the temporal resolution, other strategies need to be adopted. An extreme version of fMRI acquisition implies scanning one dimensional data, through the removal of the phase encoding gradients. This technique is dubbed line-scanning

and will be described in the next paragraph, as it is the predominant approach that was developed and employed in this thesis.

1.3 Line-scanning

A line-scanning method was first proposed in 1976 by Mansfield and Maudsley [47], where it was used as imaging method to represent the static distribution of the free water contained in a biological sample. The very first implementation of line-scanning was then improved to produce simultaneous line images [48, 49].

In the fMRI field, the line-scanning technique was first employed in animal studies by Xin Yu et al. for ultra-high spatiotemporal resolutions (50 ms and 50 µm) [50]. They used an 11.7 T MRI scanner to detect laminar responses in the somatosensory and motor cortices of rats and showed that the laminar position of the fMRI onset coincides with distinct neural inputs along the cortex (Figure 1.3b).
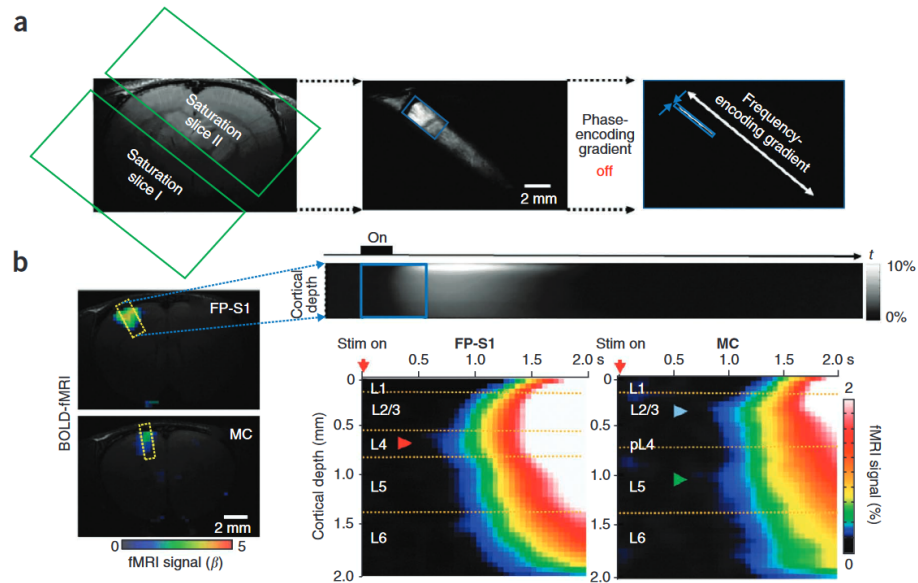
Figure 1.3: Characterization of the line-scanning fMRI method in rat somatosensory and motor cortex. (a) The procedure to set up the line-scanning method. (b) BOLD functional maps of forepaw somatosensory cortex (FP-S1) and motor cortex (MC) shown in the echo-planar imaging results (left). The fMRI line profiles were acquired from the activated FP-S1 and MC (dotted rectangles). The stimulation (Stim) paradigm was 1 s off, 1 s on, 13 s off. An fMRI percentage change map is shown corresponding to the first events during and after the stimulus. Arrowheads point to the earliest fMRI onsets in FP-S1 (red) and in MC (blue and green). The red arrows represent the start of the stimulus. Pseudo L4 (pL4) indicates the region in MC comparable to L4 in FP-S1. From [50].

The line-scanning sequence uses as template a two-dimensional gradient-echo sequence, but where the gradients in the phase-encoding direction were turned off. This means that a single line in k-space was repeatedly acquired, and all the signal coming from the slice was projected into that line. To focus only on the signal coming from a specific FOV, the addition of saturation pulses is required (outer volume

suppression). In fact, two saturation slabs were added on the top and on the bottom of the slice to ensure that the signal was coming only from the region were the line was positioned (Figure 1.3a).

Line-scanning promised to bridge the invasive neurophysiology animal experiments, where extremely high spatiotemporal resolution measurements are performed in a specific part of the cortex, with fMRI measurements where macroscopic brain areas are investigated. In fact, it combines the non-invasive nature of fMRI, with unique spatiotemporal resolution typical of electrophysiology.

1.4 Aim of the thesis

The aim of the current thesis is to implement the line-scanning method in humans, to achieve ultra-high spatiotemporal resolution.

Before diving into the line-scanning method, I first reviewed some fMRI acquisition techniques for functional connectomics (Chapter 2). This literature review can be seen as a reference to contextualize the task-based line-scanning method with respect to advanced resting-state fMRI methods.

I then focused on the line scanning method, for which I tested different implementation modalities (Chapter 3 and 5), proposed several ways for improvement (Chapter 4) and introduced a line-scanning application study (Chapter 6). More specifically, in Chapter 3, I started from the gradient-echo technique proposed by Yu et al. [50] and tested its feasibility in humans on a 7T MRI scanner. I modified my first implementation of line-scanning in Chapter 4, where I proposed three routes for improvements: a multi-echo readout, a thermal noise removal strategy and prospective motion correction. Chapter 5 focused on a different approach for the implementation of line-scanning: spin-echo lines. As this approach proved not to be suitable for fMRI experiments, in Chapter 6 I applied the gradient-echo line-scanning method in an application study, to extract a deconvolved HRF from an event related visual task. I also compared line-scanning data with standard whole brain echo-planar imaging (EPI) data to evaluate the role of line-scanning in fMRI experiments.

1.5 Thesis Outline

To be able to investigate the information processing across cortical depth non-invasively, fMRI techniques need to be improved to allow, at the same time, high spatial and temporal resolutions. In this thesis, line-scanning fMRI has been extensively studied as an extreme fMRI approach for ultra-high spatiotemporal resolution. Its one-dimensional nature requires new acquisition strategies as well as customized approaches for data reconstruction and analysis. The reader will be guided through different steps involved in development of line-scanning fMRI technique and its applications, after a short introduction on current fMRI acquisition methods for functional connectomics.

1

Chapter 2 contains a literature review on the current acquisition techniques for resting state fMRI, from the most common approaches for resting state acquisition strategies, to more recent investigations with dedicated hardware and ultra-high fields. This chapter offers an opposite point of view compared to the other chapters, going from an extended, whole brain FOV acquisitions suitable for connectivity analysis to the extremely reduced FOV of the lines, analysed with a strong focus on task-based experiments.

In Chapter 3, the first implementation of gradient-echo line-scanning is presented: I analysed the quality of line-scanning data acquisition and optimized the reconstruction strategy. I applied the line-scanning method in the occipital lobe during a visual stimulation task, showing BOLD responses along cortical depth, every 250 μm with a 200 ms repetition time. As proof-of-concept, I compared t-statistical values from line-scanning with a single slice (2D) gradient-echo echo planar imaging BOLD fMRI data with the same temporal resolution and voxel volume, and showed a good correspondence between the two.

In Chapter 4, a comprehensive update to human line-scanning fMRI is introduced. First, I investigated multi-echo line-scanning with different protocols varying the number of echoes and readout bandwidth while keeping the TR constant. I also implemented an adaptation of NOise reduction with DIstribution Corrected principal component analysis (NORDIC) thermal noise removal for line-scanning fMRI data. Finally, I tested image-based navigators for prospective motion correction and examined different ways of performing fMRI analysis on the timecourses, which were influenced by the insertion of the navigators themselves. Together those changes improve the robustness of the line-scanning method.

In Chapter 5, an alternative contrast for line-scanning is proposed. Spin-echo is a natural candidate for line-scanning, due to its innate properties of sharp line selection and the microvascular selective functional contrast. However, I could not detect any activation in the visual cortex after a very strong visual task, hence I concluded that further improvements in terms of sensitivity need to be introduced in the spin-echo line-scanning acquisition before it can be applied for neuroscientific purposes.

In Chapter 6, an example of line-scanning application is presented: I explored HRF changes in visual cortex across cortical depth in two age groups. I also bridge ageing HRF changes obtained through line-scanning with more conventional fMRI acquisitions at high-field.

The thesis concludes with a summary and general discussion in Chapter 7.
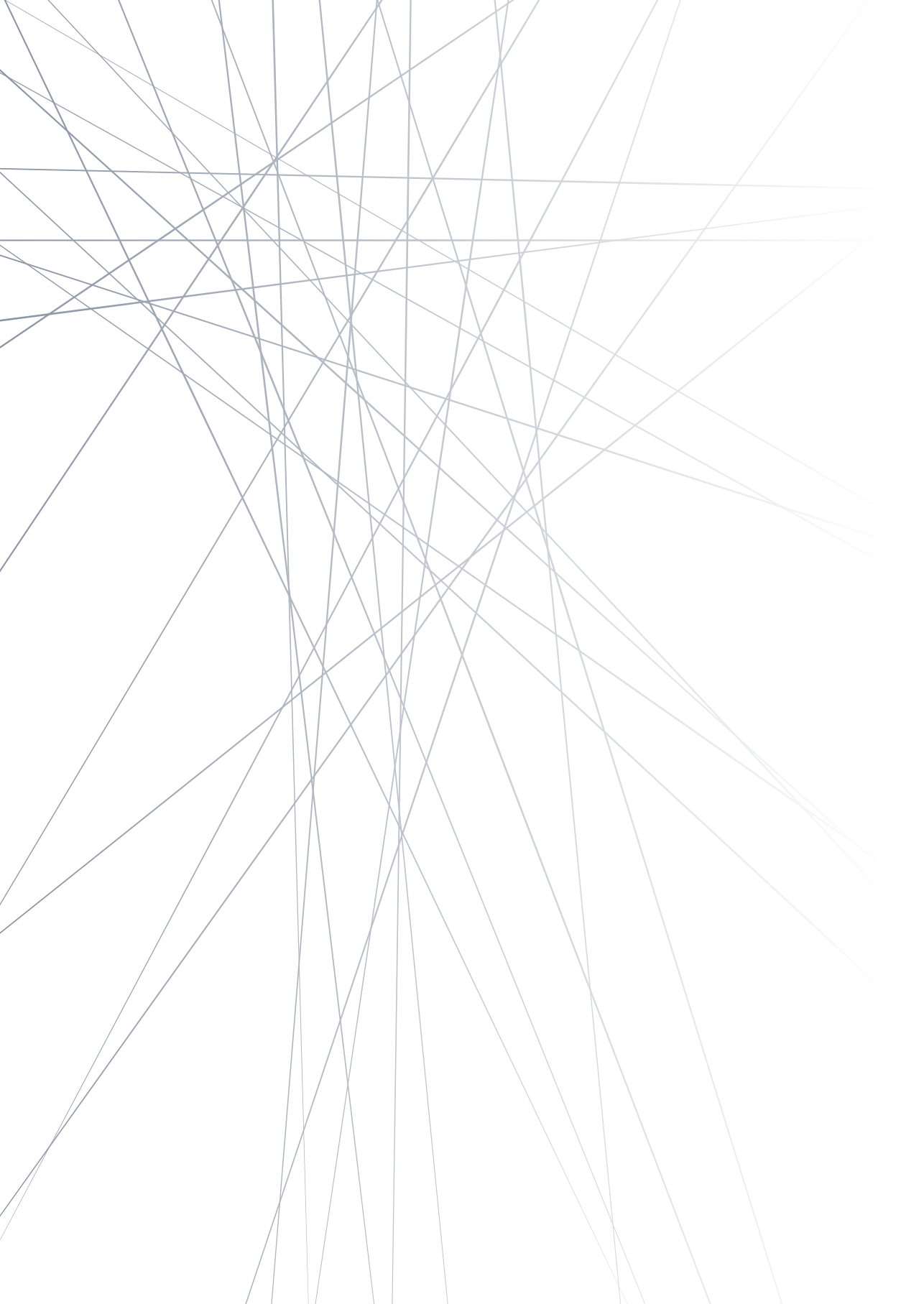
2

ADVANCES IN RESTING STATE FMRI ACQUISITIONS FOR FUNCTIONAL CONNECTOMICS

Luisa Raimondo, Icaro A.F. de Oliveira , Jurjen Heij, Nikos Priovoulos, Prantik Kundu, Renata F. Leoni, and Wietske van der Zwaag

2

Abstract

Resting state functional magnetic resonance imaging (rs-fMRI) is based on spontaneous fluctuations in the blood oxygen level dependent (BOLD) signal, which occur simultaneously in different brain regions, without the subject performing an explicit task. The low-frequency oscillations of the rs-fMRI signal demonstrate an intrinsic spatiotemporal organization in the brain (brain networks) that may relate to the underlying neural activity.

In this review article, we briefly describe the current acquisition techniques for rs-fMRI data, from the most common approaches for resting state acquisition strategies, to more recent investigations with dedicated hardware and ultra-high fields. Specific sequences that allow very fast acquisitions, or multiple echoes, are discussed next. We then consider how acquisition methods weighted towards specific parts of the BOLD signal, like the Cerebral Blood Flow (CBF) or Volume (CBV), can provide more spatially specific network information. These approaches are being developed alongside the commonly used BOLD-weighted acquisitions. Finally, specific applications of rs-fMRI to challenging regions such as the laminae in the neocortex, and the networks within the large areas of subcortical white matter regions are discussed. We finish the review with recommendations for acquisition strategies for a range of typical applications of resting state fMRI.

2.1 Introduction

Resting state functional magnetic resonance imaging (rs-fMRI) studies spontaneous fluctuations in the BOLD signal, which are synchronous between spatially distinct brain regions in the absence of a specific task, to infer functional connectivity [51–53]. Biswal et al. [54] first showed these coherent spontaneous fluctuations in the somatosensory areas, and this work was quickly followed by other brain systems (visual, auditory, cognitive (for a review, see [55])). Functional connectivity has since then been shown to provide reproducible resting state brain networks both at individual and group levels [56]. The most relevant are the default mode (DMN), motor, visual, auditory, language, and attentional networks [57]. Resting State Networks can only be obtained if sufficient quality data is acquired, covering all the brain areas of interest, either with the standard BOLD contrast, or a suitable alternative. The requirement to image specific brain areas of interest, or practical limitations in scan time or scanner availability may limit the available choices for acquisition. Practical considerations must be taken into account for the robust application of rs-fMRI.

In this review, we first discuss general recommendations or common strategies for rs-fMRI in section 2.2, before discussing the possibilities offered by ultra-high field in section 2.3, and possibilities that open up with other hardware improvements such as improved rf-coils and gradients in section 2.4. New or promising sequences used for rs-fMRI for connectomics are discussed in sections 2.5 to 2.7, detailing fast acquisitions, multi-echo echo planar imaging (EPI) and alternative contrasts, respectively. Finally, we discuss two 'new' brain areas targeted by rs-fMRI in sections 2.8 and 2.9: cortical laminae and white matter. We finish the review with recommendations for acquisition strategies for a range of typical applications of resting state fMRI, summarized in Table 2.1.

2.2 General Acquisition

Currently, 3 tesla (3T) is the most convenient field strength for acquiring reliable data from large cohorts on clinical scanners, often using gradient-echo echo-planar imaging (GE-EPI) sequences [53]. These acquisitions are fast, covering an entire brain in a few seconds, and naturally T_2^* weighted, and therefore highly efficient. The T_2^* weighting makes them sensitive to the Blood Oxygen level Dependent (BOLD) signal of interest. BOLD signal is based on oxygen concentration changes in the blood that lead to changes in T_2 and T_2^*; however, T_2^* is more affected. Therefore, GE sequences are commonly used despite the more significant effects of large vessels compared to T_2-weighted spin-echo sequences [58].

Whole-brain coverage, including the entire cerebellum, is required, with in-plane resolution as high as possible (typically about 2 to 3 mm) and a TR of 2 to 3 seconds [59]. Such parameters are feasible on commercial scanners used in standard clinical routine. However, higher temporal resolution provides a better sampling of physiological artifacts that can then be filtered out [60], as discussed in sections 2.4

and 2.5. Multi-band imaging techniques, which will be discussed in section 2.5, enable the acquisition of images with sub-second temporal resolutions [53, 56], like the ones for the Human Connectome Projects (HCP) in Development and Aging (72 slices with 2-mm isotropic voxels, TR = 800 ms) [61].

Another factor to consider when designing rs-fMRI studies is the duration of the run. Acquisition times of about 6 minutes have provided adequate sampling to obtain robust functional connectivity since estimates of correlation strengths stabilize before this time [59]. However, longer scan times are required when low spatial smoothing is used (∼ 2 mm), and small seed regions are employed [62]. Unreliable connections between two specific regions can be better measured with multiple scans per subject [63]. This approach also allows a margin of error for exclusion of data due to scanner transients and head motion. Therefore, when possible, longer acquisitions (about 12 minutes), split into short (6 minutes) runs are recommended [64]. For children, who typically do not tolerate staying in the same position for long times, multiple (4 to 6), even shorter runs (about 3.5 minutes) can be acquired [61].

During resting state experiments, participants are usually instructed to keep their eyes closed (EC), eyes open (EO), or eyes fixated on a crosshair (EO-F). Although EO and EO-F produce similar functional connectivity results [59], several studies have shown significant differences between eyes open and closed, reporting BOLD signal with decreased amplitude and lower variance in the former condition [65–67]. Dynamic changes in connectivity patterns are also dependent on eye conditions [68]. Recently, functional connectivity within the visual networks was shown to present pronounced differences between EC and EO-F in a large dataset, while only EO-F functional connectivity showed significant correlations with age, gender, and social status score [69]. Greater reliability of within-network connections was reported when participants were lying still with their eyes fixated on a cross [70, 71]. Eye-movements are better controlled, and the brain seems less active with visual fixation [72]. Therefore, EO-F is a more controlled condition that reduces experimental variability and appears to be a better choice for collecting rs-fMRI data and correlating functional connectivity with demographic and behavioral variables [69].

Although these are the most common methodologies for rs-fMRI, advances in hardware, field strength, pulse sequences, image processing and analysis have allowed other approaches that enable new applications, such as laminar connectivity.

2.3   High field MRI
As mentioned, currently most resting state fMRI data are acquired at 3T. Nevertheless, the increasing availability of 7T and even higher field scanners may provide advantages for rs-fMRI [73]. Figure 2.1 clearly shows that, regardless of the spatial smoothing, 7T networks show higher correlation coefficients. Obtaining reliable connectivity patterns with less smoothing means that the spatial characteristics of

the networks can be measured with greater spatial specificity than at lower field. This can be further increased by exchanging signal for increased spatial resolution of the acquired data.
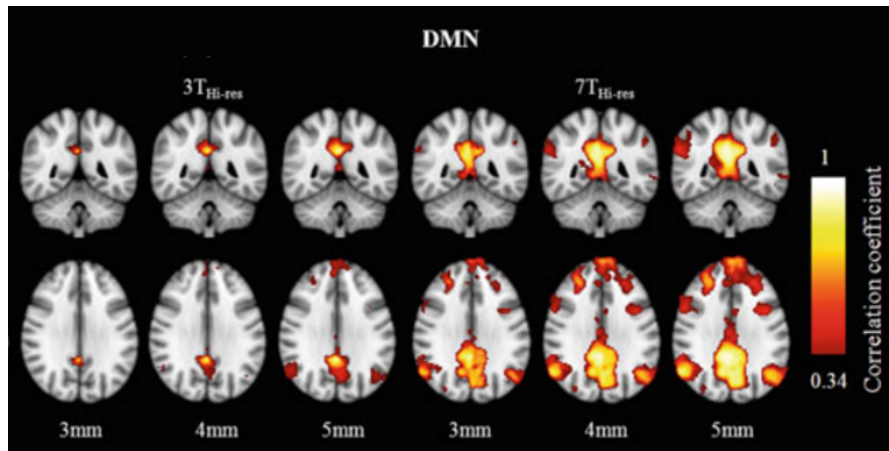

Figure 2.1: Functional connectivity maps of the default mode network (DMN) of a representative subject, overlaid on the standard MNI brain. 3, 4 and 5mm denote the FWHM of the spatial smoothing kernel applied prior to correlation computation. 3Thigh-res represents data acquired with 3T and 7Thigh-res with 7T, with the same spatial resolution (for comparison). Figure adapted with permission from [73].

The main advantage of ultra-high field fMRI is the availability of higher spatial specificity through higher spatial resolution, which facilitates the interpretation of the functional maps with respect to the underlying neuronal activity. When smaller imaging units (i.e. voxels) are sampled, partial volume effects decrease [25], but also the SNR and functional CNR (fCNR) are reduced. Ultra-high fields are advantageous because of the linear dependency of the SNR on the magnetic field [26, 27] and the supralinear gains in BOLD fCNR [25, 29]. These combined effects greatly improve signal detection, allowing higher spatial resolution, and a better spatial accuracy of the fMRI maps. However, higher spatial resolution implies longer TR, as a larger number of slices is required to cover the brain. Resting state studies need whole-brain measurements to detect functional networks completely, as these are largely distributed across the brain, including the cerebellum [74]. By combining a relatively standard 2D-EPI acquisition with parallel imaging at 7T, De Martino and colleagues [75] showed that enough sensitivity can be retained to extract the typical resting state networks, even at high spatial resolutions of 1mm isotropic voxels, without sacrificing whole brain coverage or temporal resolution (2s). The smaller voxel volumes reduce partial volume effects and leads to more distinct spatial features, allowing improved localization of the resting state networks [76].

High fields present several technical and methodological challenges, such as inhomogeneous B_0, receive and transmit RF coil sensitivity profiles [77, 78]. The advent of multi-channel receive coils and parallel imaging techniques [79], along

15

with improved gradient performances and correction for field inhomogeneities [77, 80] now allow large volume fMRI acquisition at high fields (see also section 2.3). Novel analysis approaches can improve the analysis of ultra-high fields resting state fMRI, such as using a cluster-based physiological noise correction [81], or connective field mapping [82].

Physiological noise mitigation, which is especially important at higher fields [83], will be discussed in the fast imaging section as it is somewhat sequence dependent.

As the technical challenges associated with ultra-high field are being solved, fMRI becomes possible beyond 7T also, which should further increase the SNR and CNR gains. For example, [84] used a 10.5T scanner to acquire resting state data in macaques. They demonstrate that the combination of multi-channel transmit and receiver arrays, optimized pulse sequences, and a careful anesthesia regime allows for detailed single-subject resting state analysis at high resolutions (0.75 mm isotropic), and they detected robust resting state networks across individual macaques, which closely resembled human findings.

Despite the advantages of ultra-high field fMRI in terms of SNR, CNR and parallel imaging performance, fMRI applications are hindered by the quadratically-increasing Specific Absorption Rate (SAR). SAR limitations can restrict fMRI EPIs when using multiband pulses, refocusing pulses as in SE-EPI, high spatial - or temporal - resolution, fat saturation or parallel transmit systems (pTX). SAR efficiency can be improved by new coil designs [85–87], SAR-optimizing pTX techniques [88], advanced multiband pulses, such as PINS [89, 90] and lower-SAR fat saturation [91]. More specifically for resting state measurements, in 2012 Koopmans et al. implemented a low-SAR PINS pulse with which they could perform a whole-brain spin-echo resting-state experiment [92]. A group-level independent component analysis (ICA) revealed several resting-state networks, highlighted by the higher specificity and sensitivity in higher susceptibility regions. Today, high SAR techniques are regularly used in ultra-high field fMRI [93–96].

By now, many resting state studies have been conducted using ultra-high field MRI. Some of these will be discussed in other sections because of the advanced sequences or contrast used. The higher SNR and better spatial resolution provided by ultra-high field strengths are well suited to assess the temporal reliability of mapping results, and to determine if resting-state fMRI can be applied in a clinical setting. For example, Branco et al. [97] used resting state fMRI at 7T to examine two functional networks of major importance in preoperative planning (sensorimotor and language networks) and assessed their intrasession and intersession temporal reliability. Torrisi et al. [98] used 7T rs-fMRI to map the habenula resting state network at high resolution in humans, to investigate its involvement in disorders such as anxiety, pathophysiology of depression and addiction disorders. Ebneabbasi et al. [99] assessed the brain–behavior correlations between the emotion processing-

and emotion regulation-related areas and the level of depression severity.

Ultra-high field resting state MRI also may offers insights in fundamental neuroscience, for example to map connectivity within the human visual cortex [100, 101], as well as in studying layer specific connections, which will be discussed in section 2.8.

2.4   Other hardware

Gradient-echo EPI, the most common acquisition method for fMRI, is sensitive to magnetic susceptibility, which results in signal dephasing and local distortions as well as BOLD sensitivity [102]. Hence, the high SNR and BOLD sensitivity at high field are accompanied by increased distortions. Higher-order shimming is now routinely used to reduce susceptibility effects, though distortions and dropout are typically still evident in the inferior part of the brain. In 2D EPI, decreasing the slice thickness further reduces through-plane dephasing [96, 102]. Distortion and blurring can be reduced with the careful manipulation of phase-encoding directions depending on the intended usage (e.g. in the L-R direction to minimize the Field-of-View in the phase-encoding direction, as was done in the Human Connectome Project [53]). Respiration or participant motion may additionally alter the B_0 homogeneity during the scan and induce dynamic dephasing and distortions as well as spin history effects [103]. These can bias functional connectivity metrics towards short-distance correlations in resting state [104]. Online tracking of B_0 with field cameras [105] or navigators [106], and a dynamic update of the shim can reduce distortions, improve temporal signal to noise ratio (tSNR) [106] and result in robust resting-state network correlations [105]. Motion can be further mitigated with head molds [107] or with prospective motion correction approaches to naturally complement dynamic B_0-shimming. Prospective motion correction approaches based on camera trackers or motion estimates from the fMRI data itself have been shown to reduce the negative correlation between motion and BOLD (e.g. due to signal dropouts), increase tSNR and resting-state sensitivity, particularly for slower, higher-resolution acquisitions [108–111].

Besides B_0 inhomogeneity, B_1 tends to destructively interfere at higher fields [112]. This is particularly an issue for high-flip angle techniques, but can also decrease BOLD functional connectivity in resting state (e.g. with a typical Human Connectome protocol, see Figure 2.2 [113]). RF homogeneity can be passively improved with the usage of dielectric pads [114], as was done for the 7T fMRI acquisitions of the Human Connectome project [53], or with the combination of parallel RF transmit (pTX) either statically (i.e. by calculating an individual- and channel-specific phase or amplitude offset to optimize B_1 homogeneity) or dynamically (for example by further modulating the RF for each slice in a SMS protocol) [115]. Such RF optimizations can be time-consuming, but have been shown to be robust between individuals, so that non-individual-specific weightings still result in good excitation homogeneity [116] and produce BOLD functional connectivity gains [113]. pTX further naturally lends itself to the so-called zoomed-EPI approaches that al-

low very fast fMRI acquisition [117, 118]. pTX is becoming less expensive and better supported by scanner vendors and may become the norm for ultra-high field fMRI in the future [93]. For fMRI techniques such as ASL and VASO that depend on longitudinal inversion, adiabatic pulses are also now commonly used due to their insensitivity to B_1 inhomogeneity [94, 95, 119].
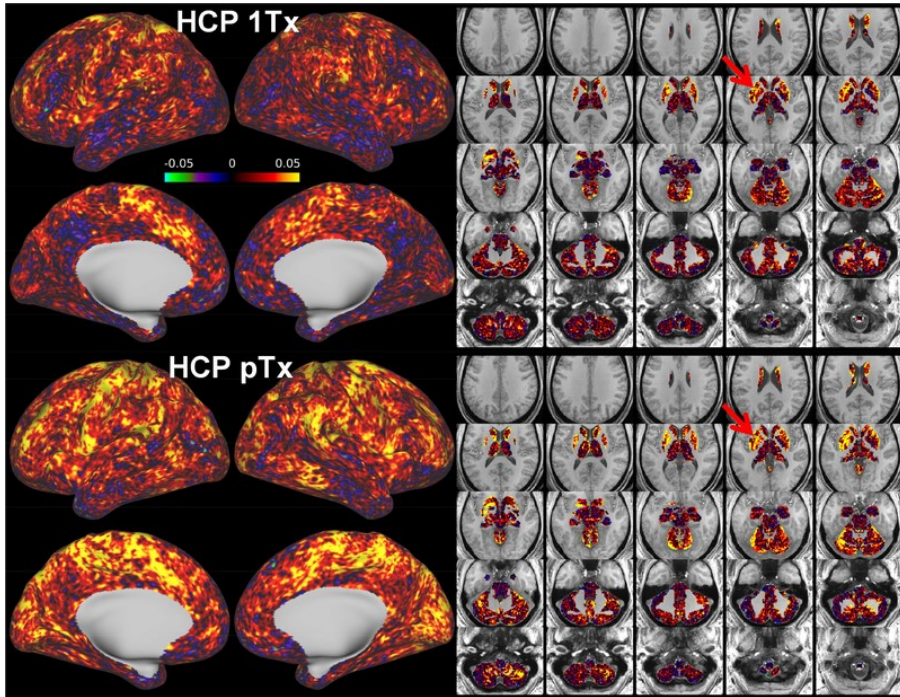

Figure 2.2: Seed-based dense connectome with a Human Connectome-like protocol at 7 T (seed in putamen as highlighted by a red arrow). Top, single transmit coil with dielectric pads. Bottom, 8 transmit coil with pTX multiband pulses. The pTX protocol shows stronger functional connectivity between the seed and the rest of the brain especially the cortical regions, as a result of improved flip angle homogeneity. Figure adapted from (Wu et al., 2019).

Most of the gains in fMRI sampling rate and image quality are due to the development of receive arrays with multiple smaller receive elements in a 3D arrangement. Smaller receives show higher SNR [120, 121] with improvements in fMRI sensitivity [122, 123]. Crucially, the multiple receivers constitute an additional spatial-encoding mechanism due to their differential sensitivity fields (an effect accentuated at higher field). This permits extensive undersampling of the k-space, thus allowing fast volume acquisitions, high spatial-resolution and reduced susceptibility artifacts in fMRI. Parallel imaging techniques have been shown to produce resting state networks with higher sensitivity or in less scanning time [124–128] leading to the development of even higher count receive arrays [129, 130]. Note that the intrinsic SNR gains of these arrays are largely in the periphery of the brain, but due to their improved parallel imaging performance (e.g. in SENSE techniques) they also

tend to show better SNR in the center of the brain with high-acceleration acquisitions [96, 131]. fMRI improvements are further fueled by the successful integration of high-amplitude and slew-rate gradients (for example, the Human Connectome project used a gradient coil capable of producing fields up to 300 mT/m with 200 T/m/s [96, 132]).

High-performance gradients are critical for the usage of advanced multiband pulses for highly-accelerated imaging [133] and further allow a shorter echo spacing, thus resulting in reduced distortions and drop-out in the EPI image [134]. The current limitations on gradient performance are largely set by the peripheral nervous stimulation that the fast-slewing gradients induce, rather than by hardware limitations. Dedicated head-only gradient coils or physiological modeling may reduce nervous stimulation further in the future and allow the usage of even stronger/faster gradients [135, 136].

2.5 Fast fMRI

Aided by the advent of parallel imaging, fast fMRI is increasingly prevalent in resting state studies, despite the hemodynamic response being relatively sluggish. At low sampling rates, physiological noise from respiration and cardiac pulsation aliases to the lower, brain function-relevant frequency bands [137]. This physiological effect is particularly critical in resting state, since there is no assumption of a task timeseries. Increasing the sampling rate can reduce the spectral overlap of these physiological processes on resting state [138] and/or facilitate the removal of structured noise from fMRI timeseries [139]. Fast fMRI can also allow us to examine how brain function at rest relates to other processes such as cardiact pulsation and respiration [87, 140, 141] or CSF flow [142]. The faster readouts can increase the sensitivity of multivariate approaches [143] and potentially achieve the same sensitivity in less time in the scanner, which is important for clinical populations [126], though this is still controversial [138, 143–145]. Furthermore, while most of the power of the resting state BOLD fluctuations is in the slower 0.01-0.1Hz band, higher frequencies may also hold brain function-relevant information that may be interesting to sample [146]. Finally, there is an ongoing discussion about the stationarity characteristics of fMRI resting state timeseries [147, 148], but fast fMRI has provided evidence for distinct brain connectivity states that change dynamically, a phenomenon that is gathering increasing attention [149, 150].

As noted in section 2.4, fast fMRI was popularized with the advent of multiple-receiver coils, that allow the unfolding of simultaneously-acquired but spatially-distinct data through the differential spatial sensitivity profiles of the receivers. While several techniques have been developed, the two most popular are the Multiband (or Simultaneous Multislice) and 3D-EPI. Multiband imaging has probably experienced the widest uptake of all methods mentioned here, greatly benefitting from the development and distribution by the Human Connectome Project. Multiband pulses excite several slices simultaneously that can then be unfolded, providing that there are enough distinct receives per unit distance [133]. The typ-

ical number of simultaneously-excited slices is MB2-4 (Multiband factor), up to MB8 for the popular CMRR protocol of the Human Connectome project [38, 53], thus allowing an equally reduced TR and potentially improved network detection and shorter scan times [126, 128]. When the multiband factor is increased beyond the decoding capabilities of the rf-coil, signal leakage between slices may occur [151]. However, the multiband factor, and fMRI sampling rate, can be further increased if the overlap between slices is artificially minimized with approaches like CAIPIRINHA [152, 153]. The acquisition can additionally be accelerated by combining with other sparse-sampling schemes, such as partial Fourier, to reduce the TR and potentially the echo time [154]. Nowadays, fast online reconstructions are available from all major vendors, greatly simplifying workflows and data handling. One aspect to take into account for high temporal resolution data is that the conventional auto-correlation models might not be sufficient for data acquired with faster TRs [155]. Higher-degree temporal autocorrelation models are advised for task-related GLM fast fMRI, but they may be beneficial also in resting-state analysis, for example when fitting nuisance regressors [156].

In 3D-EPI, the slice direction is also defined with a phase encoding gradient. As the entire imaging volume is excited every TR, much smaller flip angles are used, which can be an advantage over the more SAR-intensive multiband pulses. The second phase encoding gradient also means that the acquisition can be accelerated in the slab-direction, while keeping the echo time and BOLD contrast constant [157]. This feature has been used to achieve very high spatial resolution [158]. A 2D-CAIPIRINHA scheme can also be used here to permit higher acceleration factors [159]. The biggest difference between 3D-EPI and multiband 2D-EPI is the sensitivity to physiological noise (in 3D-EPI) and spin-history artefacts (in MB-EPI). The longer effective averaging time in 3D-EPI leads to both higher SNR and higher sensitivity to system instabilities, including physiological noise [40]. At moderate spatiotemporal resolutions, this necessitates physiological noise removal [160]. However, in faster acquisitions, with a volume TR of ~0.5s, 3D-EPI and multiband are equivalent in terms of detection of resting state networks [161]. When profiting from the volumetric acquisition to introduce fast water excitation and elliptical sampling, 3D-EPI was found to outperform a matched MB-EPI sequence [162].

Even faster approaches include the Magnetic Resonance Electroencephalography (MREG). In its typical implementation, MREG traverses the k-space in a stack-of-spirals trajectory [163]. This allows for extensive undersampling and a subsequent whole-brain acquisition at < 100 ms at low spatial resolutions (e.g. a nominal spatial resolution of 3x3x3 mm^3) [164]. This has allowed the detection of resting state networks at frequencies above 0.1 Hz [144], improved individual level network detection [52] as well as the extraction of resting-state networks from sub-minute fMRI segments, thus greatly facilitating dynamic functional connectivity analyses [144, 165]. A drawback, besides the limited spatial resolution, is the computationally intensive reconstruction.

Similar to the MREG, inverse imaging (InI) increases the sampling rate of traditional functional MRI due to the minimal time required to traverse k-space, at a cost of a moderate reduction in spatial resolution [166]. InI derives spatial information by solving inverse problems using data simultaneously acquired from all channels in the array, leading to whole-brain coverage at ~100 ms and 5 mm spatial resolution. The spectral characteristics of resting state networks with generalized inverse imaging (GIN) have been investigated by Boyacioglu at al. [167] with 50 ms TR and 3.5 mm isotropic resolution.

Keyhole techniques also allow significantly improved temporal resolution [168], while keeping the same spatial resolution. A combination of the keyhole concept with EPI sequences (EPIK) [169], has proven to be more robust against susceptibility and chemical-shift artifacts than single-shot EPI. The performance of EPIK, in term of BOLD sensitivity and functional connectivity, have been evaluated by Yun et al. [170] through a visually-guided finger-tapping task.

These acquisition advances promise that fast fMRI will become a mainstay of rs-fMRI, with increasing usage. To further establish fast imaging, dedicated data processing may be beneficial, such as avoiding the typically-applied low-pass filter that removes statistical degrees-of-freedom and may insert high-frequency noise [145] and accounting for the higher-degree temporal autocorrelation where relevant [139, 156].

2.6   Multi-echo fMRI and connectomics

Multi-echo fMRI acquisition is an extension of the standard 2D BOLD EPI, which involves acquisition of images at multiple TEs instead of only one [171–173]. The use of multi-echo fMRI in the study of connectomics has emerged as a strategy for contending with artifacts from head motion, imaging, and non-neuronal physiology in fMRI datasets. Having signal time series at multiple echo times (TEs), enables evaluation of both BOLD contrast dynamics and time series activity concurrently [171, 174, 175]. The advantages of the multi-echo fMRI approach are most evident when assumptions regarding BOLD contrast and time series dynamics deviate from ideal conditions, which occurs when imaging patients, at high-field and deep brain regions [176]. In these cases, multi-echo fMRI can separate BOLD signal from artifacts in the time series [177]. Specifically, BOLD percent signal changes scale linearly with TE, whereas artifactual signals from hardware instabilities, motion, or physiology do not exhibit this dependence, and are thus TE-independent. Nevertheless, the advantages of ME-fMRI are largest when data is acquired at moderate spatial resolution and at low to moderate field strength, on a system with high-performing gradients. If these ingredients are not present, sampling multiple echoes before TE=T_2* can only be achieved with detrimentally high acceleration factors, which counteracts the benefits of acquiring multiple echoes [61, 178].
Hence, typical multi-echo fMRI acquisition parameters at 3.0 T involve voxel sizes from 2.0 mm to 3.5 mm isotropic, R=2 to 3 in-plane acceleration, three to five TEs usually spanning 10-60 ms, and TR ranging from 800 ms to 3.0 s with and without

multi-band acceleration.

2

Reconstructing multi-echo fMRI results in separate 3D+time datasets corresponding to the different acquired TEs. Combining the separate 4D datasets into a single time series through averaging with BOLD-sensitive weights has been shown as a reliable means of mitigating susceptibility artifacts, increasing BOLD contrast, and reducing thermal noise across the brain volume. Implementing a matched filter by averaging with voxel-wise weights based on voxel-wise T_2^* estimates and TE yields optimum contrast at all voxels by approximating acquisition at TE=T_2^* at each voxel [172, 179]. This enhancement leads to appreciable improvements in resting state fMRI functional connectivity mapping (and task activation) in deep brain regions with low signal amplitude and susceptibility artifacts such as the orbitofrontal cortex and inferior temporal cortex [180, 181].

The TE-dependence of linear components of spatiotemporal datasets can also be evaluated. After decomposition of multi-echo datasets with principal component analysis (PCA) or ICA, a weighted average of goodness of fit statistics provides a summary statistic for component-level TE-dependence, κ, and TE-independence, ρ. This strategy is the basis for the analysis and denoising technique called multi-echo independent components analysis (ME-ICA) [171].

Spatial ICA of the dimensionally reduced dataset produces components with κ and ρ values that indicate subsets of component in two separable regimes. The first shows high BOLD weighting (high κ) and low non-BOLD weighting (low ρ), and the second has low κ, and high or low ρ (Figure 2.3). Removing components of the low-κ regime by linear projection results in time series denoising of numerous artifacts related to subject head motion, cardiac pulsation, in-plane and through-plane acceleration, and even baseline signal drifts [182].

The advantages of multi-echo fMRI acquisition and analysis have been demonstrated in a wide range of connectomic studies across field strengths, experimental conditions, and at subject and population levels. Task-based analysis of multi-echo fMRI shows increases in sensitivity to individual events, and with concomitant resting state fMRI, intra- and inter-subject variability of task activation and connectivity patterns is decreased [183]. Resulting increases in statistical power lead to two- to four-fold reductions in required sample size to achieve significant findings in key connectivity patterns, particularly across cortical and subcortical areas and in precision connectomics [184–187].
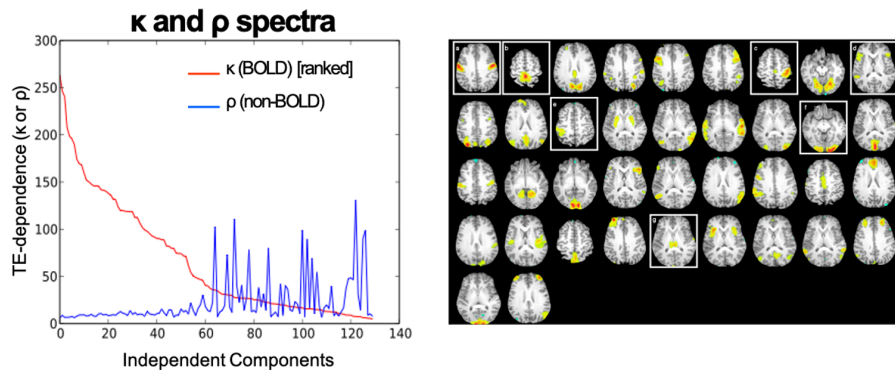
Figure 2.3: (left) κ and ρ spectra of an individual multi-echo dataset differentiating BOLD and non-BOLD components. (right) Boxes highlight high-κ components in the motor cortex, hand area of motor cortex, Broca's area network, lateralized sensory cortex, primary visual cortices and thalamic resting state network.

Other notable areas of functional neuroscience are also seeing novel applications of ME-ICA, particularly neuropsychopharmacology. A recent study using multi-echo fMRI acquisition at 3 T MRI on the response of patients with major depressive disorder to the recently FDA-approved antidepressant ketamine showed that, after a 40-minute infusion, patients had increased functional connectivity between the hippocampus and subgenual anterior cingulate cortex proportional to their performance and activation on the incentive flanker task [188].

Because ME-ICA makes no assumptions on the number or characteristics of functional networks in a given dataset, it can be used to study variations in component number with condition. Multi-echo fMRI data acquired in a cohort of healthy volunteers aged 40 to 80 showed a consistent reduction in the number of resting state components 1-hour after emerging from general anesthesia [189]. A study on multi-echo fMRI across the age range showed an exponential decrease in component number with age from age 8 to 40, alongside increasing functional connectivity in cortical networks [190]. The age-dependence of functional connectivity network integration has also been demonstrated in a larger neurodevelopmental study [191].

2.7 Other contrasts

Despite its high sensitivity to deoxyhemoglobin variations and widespread availability, rs-fMRI based on GE has several drawbacks: 1.) The spatial specificity is limited, as the BOLD signal is predominantly driven by the large draining vessels. 2.) Images contain geometric distortions because of the long EPI readout and are sensitive to signal dropout in regions near air cavities. 3.) BOLD signal does not provide a direct or quantitative measure of brain function.

2.7.1 SE-EPI

Although less sensitive, spin-echo EPI (SE-EPI) can also be used for BOLD imaging, with the advantage of an increased localization of the neuronal activity [92, 192] and higher robustness against signal dropouts[192–195]. The benefit of conducting an fMRI experiment with SE at 3T is usually low, as the gain in specificity is not that large, susceptibility-induced distortions remain and the sensitivity loss in some regions is quite high [92, 192]. Nevertheless, two studies showed that SE-EPI based rs-fMRI at 3T provides higher sensitivity, specificity, and inter-subject reproducibility in high-susceptibility regions [194, 195] and see Figure 2.4.
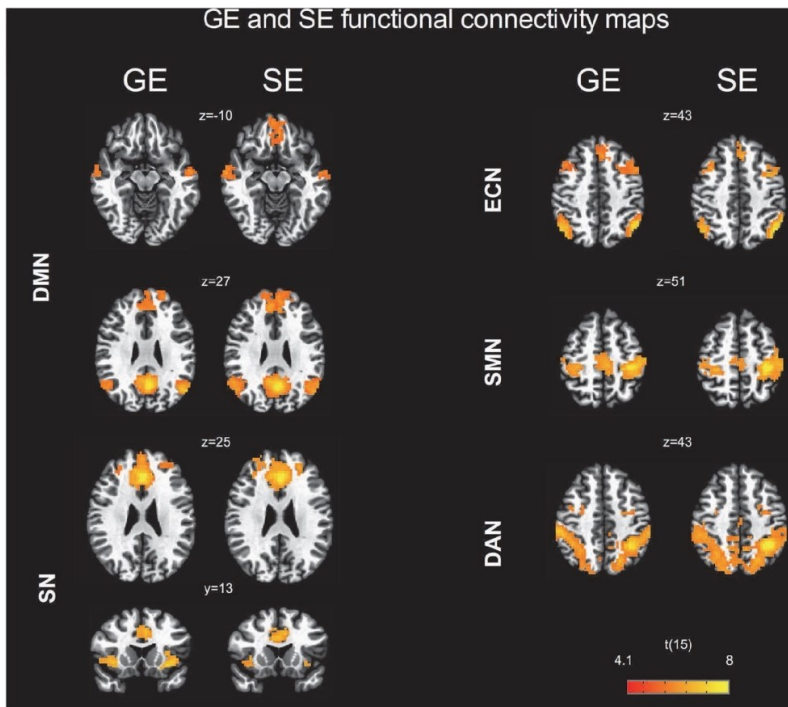

Figure 2.4: GE and SE functional connectivity maps. A seed-based connectivity map for Gradient echo (GE) and Spin echo (SE) obtained from random effects group analysis showing the following resting state networks: default mode network (DMN), executive control network (ECN), salience network (SN), dorsal attention network (DAN), sensorimotor network (SMN). Differences are especially large in the inferior frontal areas of the DMN. Figure adapted from [194].

High spatial resolution is easier at high field (see section 2.2), but there are fundamental difficulties for SE BOLD data acquisition at 7T. First, the TE needs to match the longer gray matter T_2, rather than the T_2^*, making it challenging to acquire whole-brain data quickly. Another problem is SAR deposition because of the refocusing pulse (see section 2.4 and [196]). Although challenging, the 7T implementation of SE-EPI with PINS is a compelling alternative because it can achieve fair spatial and temporal resolution [92]. Nevertheless, the sensitivity penalties are

high, the requirements for this implementation are challenging, and the sequence is not yet widely available.

2.7.2 ASL-CBF

With recent technical advances, Arterial Spin Labeling (ASL) is gradually becoming a more feasible alternative to BOLD fMRI [197–199]. ASL is a non-invasive method that uses the water present in the arterial blood as a freely diffusible intrinsic tracer to measure tissue perfusion. Quantitative CBF maps can be obtained using Buxton's General Kinetic Model [200]. Similar to BOLD rs-fMRI, functional ASL experiments are performed with a timeseries acquisition where a pairwise acquisition (label-control) is acquired [197].

There are several possible labelling implementation schemes for ASL. Due to its straightforward implementation and relatively high SNR, pseudocontinuous (pCASL) labelling has become the method of choice for most ASL experiments [201]. Although the typical readout is 2D GE EPI, the timing differences between slices mean that for a whole-brain resting state connectivity measurement, 3D acquisitions are usually preferable. BOLD contamination can be quite pronounced because of the GE-EPI readout. Hence, a 3D Gradient and Spin-Echo (GRASE) readout [202] emerged as an alternative to the 2D readout [203], providing higher SNR and more brain coverage. The 3D GRASE acquisition, in combination with pCASL and Background Suppression (BS) [204] seems to be the current optimal protocol for both static and dynamic resting state ASL, though it is not yet widely available [198, 201]. Another motivation for an ASL acquisition at high field is the prolonged blood T_1, which can amplify the perfusion signal. There are not many ASL fMRI experiments at 7T but an interesting study employed Turbo-Flash (Fast Low Angle Shot) ASL (both pCASL and PASL) and showed its feasibility in a 7T resting state experiment [205].

Compared to GE-EPI, ASL offers a direct and quantifiable CBF measure, and increased spatial specificity to neuronal activity due to the capillary signal origin of ASL. The main drawbacks of ASL are its intrinsic low signal-to-noise ratio (SNR), and the temporal resolution, which is usually much lower than BOLD GE rs-fMRI protocols. Despite its disadvantages, ASL has gained considerable attention. Several studies demonstrated the viability of characterizing intrinsic brain activity with ASL maps [198, 206–209]. The recently improved post-processing methods for subtraction and filtering have also contributed to the rising number of resting-state functional connectivity studies using ASL [51, 210–213].

ASL has been used as an alternative to rs-BOLD in several clinical investigations in Schizophrenia [214–216], chronic fatigue [217], epilepsy [218, 219], healthy ageing [220] and psychosis [221]. Recent studies show that ASL provides enough statistical power, reproducibility and low-frequency variations comparable to BOLD [207, 222], but it is still limited by partial brain coverage in the majority of the sequences used.

2.7.3 VASO-CBV

Similarly, spontaneous fluctuation in CBV-weighted signal can also be used for resting state functional connectivity [44, 223–225]. The Vascular Space Occupancy (VASO) sequence takes advantage of the T_1 differences between blood and the surrounding tissue to null blood signal and measure CBV changes [226]. Recently, VASO fMRI gained attention because it offers higher spatial specificity than GE BOLD [227, 228]. Similar to ASL, much smaller coverage is achieved in VASO than in BOLD fMRI experiments. Also, VASO is less sensitive than GE BOLD fMRI [229]. The first study that showed VASO-CBV resting-state functional connectivity was conducted by Miao et al. [224], using a 3T scanner. For a whole-brain acquisition, a single-shot 3D GRASE readout was used [230], which also yields increased SNR, minimum BOLD contamination and low sensitivity to susceptibility artefacts. Their functional connectivity analysis consisted of a thorough comparison between VASO-CBV and BOLD using ICA and seed-based analysis, identifying the DMN, salience-, executive control-, visual-, auditory-, and sensorimotor networks. Another exciting study was published by Zhang et al. [225], comparing GE BOLD, CBF and CBV resting-state functional connectivity metrics within the same group of subjects using a seed-based approach. Both VASO and ASL were more specific and less sensitive than GE-BOLD (Figure 2.5). These differences are at least partially biologically driven [225].
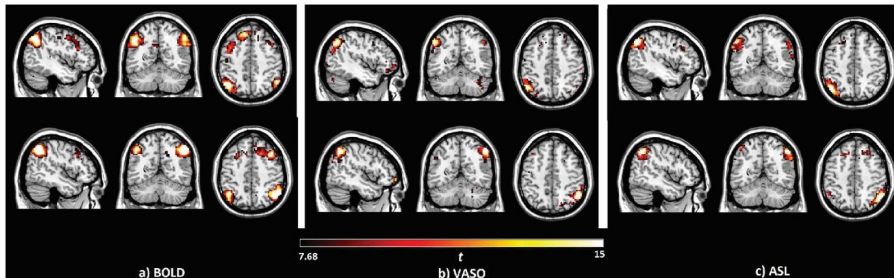

Figure 2.5: Left/Right executive control networks identified with a seed-based analysis of the A) blood oxygen level dependent (BOLD), B) vascular space occupancy (VASO) and C) Arterial Spin Labeling (ASL) data. Figure adapted from [225].

A recent VASO variant was used for resting state connectivity analysis at high spatial resolution (< 1mm) in a small slab covering M1 [231] and will be described in section 2.8 below. A Slice Selective Slab Inversion VASO [232] was employed to acquire VASO-CBV and BOLD simultaneously using an interleaved acquisition. Recent technical improvements with Multiple Acquisitions with Global Excitation Cycling (MAGEC) [223] allow whole-brain coverage and detection of a larger number of networks.

2.8 Laminar connectivity

Ultra-high magnetic fields open up novel avenues in the mapping of functional specialization and the flow of information between and across the cortex [5, 8].

The thickness of the human cerebral cortex ranges from 1-4 mm [3] and is highly convoluted. As we cannot distinguish the six layers of the neocortical microcircuit [233], the BOLD signals are typically described in terms of cortical depth [5], which relates loosely to the different cortical layers: feedforward projections arrive in the granular layer (L4), feedback projections terminate in the more superficial supra-granular layer (L2/3) and the deeper infragranular (L5/6), while lateral fibers target all areas [233]. Increasing the spatial resolution results in more accurate sampling of the signals arising across depth [234]. In other words, a conventional 3T fMRI protocol with a voxel dimension of 3 mm practically samples 2 "layers" of the cortex, rendering interpretability at mesoscopic level pointless due to partial voluming; signals from multiple layers/sources are sampled as one [227, 235]. With sub-millimeter fMRI, multiple cortical depths can be separated [236].

While promising, high-resolution (sub-millimeter) laminar fMRI also faces challenges [5]. The cortical vascular architecture poses a difficulty for the interpretation of the BOLD signal across depth, as BOLD signal originates primarily from field distortions resulting from deoxygenated blood draining via venules and intracortical veins to larger pial veins at the cortical surface [42, 45, 237]. While this problem is inherent to the GE-BOLD-contrast, its consequence is magnified while interpreting signals across depth [236, 238]. The vascular architecture means that venous blood from deeper layers contributes to the BOLD signal in upper layers as it flows towards the pial surface [42, 239]. Advanced modeling strategies capturing the contribution of venous effects [42, 239–242] might enhance interpretability of laminar signals [243]. Given that extravascular contamination from the veins at the pial surface decreases rapidly away from the cortical surface [244] and signals from central layers can be distinguished from those of pial veins [245], issues inherent to GE-BOLD at the laminar level can, to some extent, be mitigated.

Recognizing these challenges, efforts to map connectivity using resting-state fMRI across and between layers and to develop analysis-strategies are only slowly appearing [223, 235, 246, 247]. One of the most prominent examples of laminar rs-fMRI with seed-based connectivity showed that the primary motor area (M1) received somatosensory and premotor input in superficial layers and cortico-spinal motor output in deep layers using a slab-selective VASO contrast with 0.75mm isotropic resolution [231]. Though challenging, the feasibility of probing laminar connectivity with gradient-echo approaches is increasingly being recognized [248]; using a TR-external GE-EPI with keyhole (EPIK) sequence with 0.63mm isotropic resolution, Pais et al. were able to show that during rest, the superficial layers show high coherence (a measure of "similarity in frequency content", rather than "correlation in the time domain", thought to be less affected by draining vein effects [248]). The scope of laminar connectivity has also been broadened towards task-related processes. Depth-dependent connectivity patterns were observed during motor [248] [0.63 mm isotropic], language [0.943x0.9 mm] [249], and auditory [1.5 mm isotropic] [250] processing; all showing the contribution of deeper layers to task performance using a GE-EPI acquisition scheme. These early studies high-

light the impact of laminar connectivity, adding an additional dimension to our understanding of the brain using non-invasive methods [223].

2.9   White matter

Although the overwhelming majority of connectivity studies are targeting gray matter networks, there is a recent interest in white matter functional connectivity based on resting state BOLD data. These signals are much smaller than those in gray matter, as both the blood flow [251] and blood volume [252] are much lower in white matter than in gray matter. Hence, reports of BOLD responses in white matter are relatively rare. The existing literature of task-based responses is mostly focused on the large white matter bundles in the corpus callosum [253]. Nevertheless, the signal fluctuations found in the white matter in resting state data do show consistent networks [254]. These networks can be found with similar analysis approaches as used to identify the cortical resting state networks, such as ICA or clustering approaches [255, 256] and white matter voxels have been shown to contribute at least a little to brain-wide networks [257].

In terms of acquisition, the same T_2* weighted EPI images are acquired for white matter network identification as for cortical resting state analysis. Images tend to be acquired at 3T with a modest spatial resolution of 3.5 mm and TE of ~T_2*. For the post-processing, a masking step is added to remove the gray matter, so as to avoid signal swamping from the large BOLD responses. This suffices to make the further post-processing analysis sensitive to the signal correlations in the white matter networks.

In 2016, Ding et al [255] showed that the resting state connectivity found in white matter is indeed BOLD-like and TE-dependent, and, hence, separate from physiological effects that are S_0-based [171]. The same group showed that a hemodynamic response function, HRF, can be derived for white matter [258]. This white matter HRF has a reduced peak amplitude and delayed peak times compared to the gray matter HRF.

These findings have recently led to the publication of a few papers specifically investigating white matter resting state connectivity, for example observing differences in these networks during baseline or movie watching [256] or differences in clinical populations, such as patients suffering from epilepsy [259] and mild cognitive impairment [260].

2.10   Conclusions

In this review, we presented the most common and recent approaches for different resting state studies, specifically focusing on acquisitions and hardware improvements. In each section, applications have been discussed, to show the potential of rs-fMRI and its growing availability and usage for both fundamental neuroscience and clinical investigations.

In Table 2.1, we summarize the most common approaches in terms of imaging

sequence, spatial and temporal resolution, required field strength and subject behavior, for different purposes, depending on which subject population or specific brain activity is the object of the study.

Overall, we can conclude that lower field strength (3T) is more suitable for large patient studies, where whole brain coverage is required, while extremely high spatial resolution is not essential. For this kind of investigations, multi-band or 3D EPI methods can be used, with a sub-second acquisition time, as well as 2D EPI or 2D pCASL EPI, with TR_{acq} ranging from 3 to 5 s. For most of these applications, subjects are instructed to keep their eyes open and fixate on a fixation cross, except for multi-center studies, where eyes close condition is best to avoid differences in stimulus displays.

Instead, when specific brain regions are targeted (such as when studying deep gray matter, or connectivity within layers for a certain gray matter area), higher field strengths or alternative acquisitions (ME-EPI, VASO/ASL) are more suitable. 7T is essential to reach sub-millimeter spatial resolutions, and this is usually combined with smaller brain coverage.

In conclusion, the exact acquisition parameters will depend on the objective of the study at hand. Nevertheless, this review and Table 2.1 can guide the new rs-fMRI user to make an informed choice from the possible acquisition schemes currently available for rs-fMRI for functional connectomics.

2

2

Application	Magnetic Field	Spatial Information	Acquisition Approach	Subject's Condition
Large groups of patients, single-center study	3T	Whole brain coverage (14cm) moderate spatial resolution (2-3mm); Cerebrum coverage Spatial resolution (3-4mm); quantitative CBF also acquired	Multiband EPI or 3D-EPI, TR_{acq} sub-second; 2D pCASL EPI TR_{acq} 3-5s (use ASL for qCBF and connectivity)	Eyes open, fixation cross
Large groups of patients, multi-center study	3T	Whole brain coverage (14 cm) moderate spatial resolution (2-3mm)	2D-EPI, TR_{acq} 2-3s to avoid differences between vendors	Eyes closed
Individual subject or moderately powered patient studies, seed-based analysis of subcortical structures	3T, 7T	Whole brain coverage (14 cm) moderate spatial resolution (2-3mm)	Multi-echo EPI, 3-4 TEs, TR_{acq}=2.5s (single-band) TR_{acq}=1.0s (multi-band); ME-ICA	Eyes open, fixation cross
Changes within a network upon task-related activation	7T	Coverage of network of interest, higher spatial resolution (1.5 mm)	Multiband EPI or 3D-EPI, TR_{acq} ~2s	Eyes open, fixation cross/ task
Connectivity within layers of a specific gray matter area	7T	Coverage of area of interest; Sub-millimeter resolution (0.7-0.8 mm)	VASO with TR_{acq} 3s or T_2*-w 3D-EPI, TR_{acq} ~2s	Eyes open, fixation cross

Table 2.1: Common resting state fMRI acquisition approaches for different study's goals.
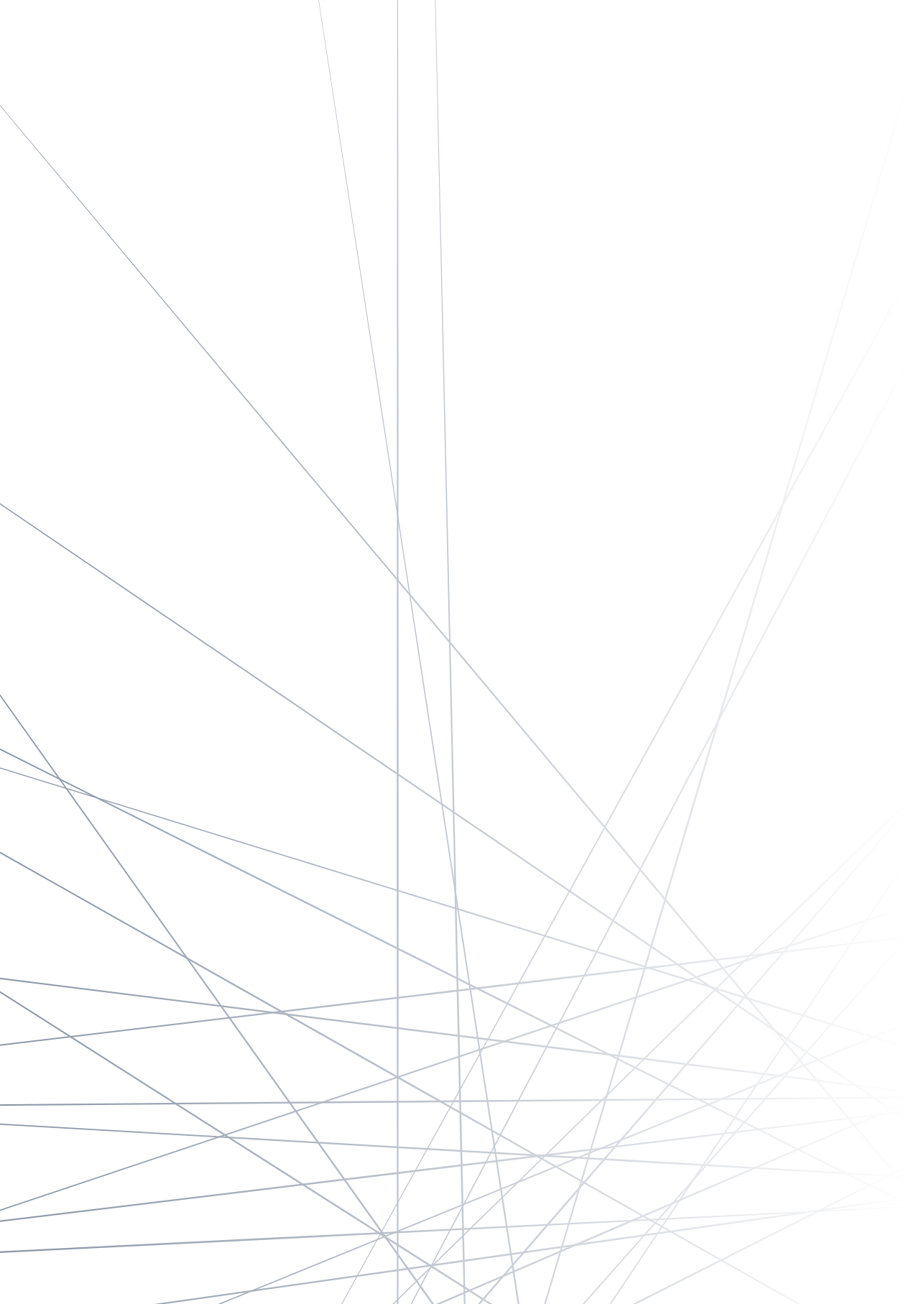
3

A LINE THROUGH THE BRAIN: IMPLEMENTATION OF HUMAN LINE-SCANNING AT 7T FOR ULTRA-HIGH SPATIOTEMPORAL RESOLUTION FMRI

Luisa Raimondo, Tomas Knapen, Icaro A.F. de Oliveira , Xin Yu, Serge O. Dumoulin, Wietske van der Zwaag, and Jeroen C.W. Siero

3

Abstract

Functional magnetic resonance imaging (fMRI) is a widely used tool in neuro-science to detect neurally evoked responses, e.g. the blood oxygenation level- dependent (BOLD) signal. Typically, BOLD fMRI has millimeter spatial resolution and temporal resolution of one to few seconds. To study the sub-millimeter structures and activity of the cortical gray matter, the field needs an fMRI method with high spatial and temporal resolution. Line-scanning fMRI achieves very high spatial resolution and high sampling rate, at the cost of a sacrifice in volume coverage.

Here, we present a human line-scanning implementation on a 7T MRI system. First, we investigate the quality of the saturation pulses that suppress MR signal outside the line. Second, we established the best coil combination for reconstruction. Finally, we applied the line-scanning method in the occipital lobe during a visual stimulation task, showing BOLD responses along cortical depth, every 250 μm with a 200 ms repetition time (TR).

We found a good correspondence of t-statistics values with 2D gradient-echo echo planar imaging (GE-EPI) BOLD fMRI data with the same temporal resolution and voxel volume (R = 0.6 ± 0.2).
In summary, we demonstrate the feasibility of line-scanning in humans and this opens line-scanning fMRI for applications in cognitive and clinical neuroscience.

3.1   Introduction

Functional magnetic resonance imaging (fMRI) is a widely used tool in neuroscience, where most fMRI studies are based on blood oxygenation level-dependent (BOLD) contrast weighted imaging [22]. fMRI data are typically acquired using Echo Planar Imaging (EPI). EPI is an efficient sampling method, with up to submillimeter spatial resolution and a temporal resolution usually in the order of seconds. Spatially, the neurons, however, are organized in columnar and laminar structures measuring in the hundreds of micrometers [5]. Temporally, neurons communicate at the microsecond level. The BOLD response features carry information in the range of hundreds of microseconds [32, 159]. A subsecond, preferably ~100ms sampling rate in fMRI is necessary to detect temporal features of the hemodynamic response function (HRF) that specify how the hemodynamic signal propagates through the functional at the mesoscopic scale (cortical layers).
Advances in fMRI methodology have been aimed at increasing both the spatial and the temporal resolution of fMRI, with the final goal being sub-millimeter spatial resolution and sub-second sampling rate.

Ultra-high magnetic field strength MRI systems allow fMRI data acquisition with high spatial resolutions [261] because of the increases in signal-to-noise ratio (SNR) [26] and contrast-to-noise ratio (CNR) [29, 58] with the magnetic field strength B_0. In general, different spatial resolutions are required, depending on the functional unit which are the study object. Human cortical thickness varies between 1 and 4.5 mm, with an overall average of approximately 2.5 mm [3]. Within the cortex, different layers can be distinguished; hence sub-millimeter spatial resolution is a prerequisite in terms of spatial resolution for layer resolved fMRI studies. Here, we specifically focused on the human visual cortex which has a cortical thickness around 2 mm, and is composed of 6 layers. In this context and region, we believe that a spatial resolution of 250 μm is the minimal resolution to detect functional organization both at columnar (~500 μm) and laminar level (~500 μm) [5, 8]. Other regions of human cortex, such as motor cortex, are slightly thicker, and contain fewer discernable layers. Here a spatial resolution of 500 μm might be adequate to resolve signals at different cortical depths, corresponding to the cortical layers. Similar voxel sizes are required for macaque (ocular dominance columns ~400 μm and laminae ~100–500 μm) [262] and other primates. However, in rodents, cortical thickness ranges from 900 μm to 3400 μm [263], so higher spatial resolution is required to distinguish these layers with sufficient accuracy.

Animal experiments have demonstrated cortical layer specific fMRI activations with spatial resolutions as high as ~100-200 μm [264–266]. Cortical depth-dependent BOLD fMRI activations in humans have also been shown in the primary visual, auditory and motor cortices, typically with spatial resolutions in the range of 750-1300 μm [236, 267, 268]. However, an increase in spatial resolution usually comes at the cost of temporal resolution and longer scan times as more points have to be sampled to obtain the same brain coverage.

Different methods have been developed to achieve higher temporal resolutions;

undersampling techniques such as partial Fourier (PF) [33] and parallel imaging (PI) [35, 36], as well as compressed sensing [269] are now widely available. These can also be applied to EPI sequences, but the gain in temporal resolution is not very high because of the requirement to keep the echo time (TE) close to the tissue T_2^*. Strongly accelerated SMS-EPI (15-fold total acceleration) sequences using a custom 32-channel coil for 7 T can lead to 1.5 mm isotropic resolution with sampling rate of 1.2 s and all brain coverage [157].

Larger speed gains can be obtained for 3D acquisition schemes, where the third dimension can be undersampled in order to obtain shorter scan time [40, 157], similar to what has been achieved successfully with simultaneous multislice imaging [38, 161]. All these methods allow whole-brain coverage.

Other strategies need to be adopted to reach a combination of very high temporal and spatial resolution for BOLD fMRI studies, since all high-resolution EPI-based methods are still relatively slow due to the slice phase-encoding steps or multiple slice acquisitions. Acquiring only single-slice data allows a very fast acquisition, with repetition times (TR) down to ~200 ms. In order to simultaneously increase the spatial resolution, one could reduce the in-plane field-of-view (FOV), in combination with an outer volume suppression (OVS) scheme, similar to so-called zoomed imaging [270]. The smaller FOV allows sub-millimeter resolution and a faster sampling as a smaller imaging matrix is acquired [271]. Specific FOVs have been adapted to map different brain regions with high in-plane spatial resolution. [43, 272] focused on ocular dominance columns in the visual cortex with elongated voxels, while Huber et al. [231] studied the laminar activity of motor cortex with similar anisotropic voxels. Kashyap et al. [45] achieved unprecedented 0.1 mm in-plane spatial resolution to resolve laminar activation in human visual cortex with even more anisotropic 'pancake' voxels, optimized for the sampling of cortical depth.

The sampling time can be further shortened if the phase-encoding steps are completely skipped. This extreme approach is dubbed line-scanning and, as the name suggests, involves the acquisition of only one line of interest. A single-slice is excited and the signal outside the line of interest can be suppressed through saturation (OVS) pulses. The phase-encoding in the direction perpendicular to the line is omitted, and the line signal is then acquired after every excitation pulse. Line-scanning fMRI has been successfully implemented by pioneering studies conducted by X. Yu et al. [50] in rodents on a 11.7 T MRI system. Line-scanning fMRI data were acquired in rodents with 50 ms temporal resolution and 50 μm spatial resolution along the line. They managed to extract high-fidelity BOLD hemodynamic response functions (HRF) of cortical laminae. Specifically, the laminar position of BOLD fMRI onsets were mapped according to the neural input applied in somatosensory and motor cortices of rats. Other preliminary studies have shown the feasibility of line-scanning in humans at 3T [273] and promising results for neuroscience applications at 7T [274]. Specifically, Morgan et al. showed preliminary results identifying cortical layers in the human primary visual cortex through multi-

echo line-scanning.

In this study, we investigated gradient-echo line-scanning fMRI for human applications, with in-line spatial resolution of 250 μm and temporal resolution of 200 ms. We discuss the implemented pulse sequence, data reconstruction and analysis. We compared the BOLD sensitivity of line-scanning with a fast single-slice gradient-echo BOLD EPI sequence using a block-design visual task. We previously presented initial findings on these investigations [275, 276].

3.2 Materials and Methods

3.2.1 Data acquisition

Nine healthy volunteers (4 male, 30±5 years old) participated in this study after providing written informed consent as approved by the medical ethics committee of the Amsterdam University Medical Centre. The guidelines of the Helsinki Declaration were followed throughout the study. All participants were screened prior to the experiments, to ensure MR compatibility.

All volunteers were scanned on a 7T MRI system (Philips, Netherlands) equipped with a 2 channel transmit, 32 channel receive head coil (Nova Medical, USA). We acquired line-scanning data using a modified 2D gradient-echo (GE) sequence, depicted in Figure 3.1a.

To suppress the signal outside the targeted area in the line of interest, we applied two slab-selective spatial radiofrequency (RF) saturation pulses for outer volume suppression (OVS), before slice excitation. The spatial saturation pulses had a pulse duration of 7.16 ms, a pulse flip angle of 97° , RF amplitudes of 4.85 μT and 4.67 μT respectively, related gradients with 0.27 mT/m gradient strength and duration of 7.76 ms (note this includes the slope time). Fat suppression was applied before the OVS using the vendor implementation of spectral presaturation with inversion recovery (SPIR), adjusting the frequency offset to 250 Hz and bandwidth to 1000 Hz. All the prepulses (including fat suppression and OVS) were repeated every TR. The phase-encoding gradients were turned off so that the signal collapses along the phase-encoding direction into a line profile. The different 'phase-encoding steps' hence become time points in a functional experiment. The equivalent in k-space is the acquisition of one line, crossing the center k-space point ($k_{PE} = 0$), every TR (Figure 3.1b), which represents mainly the signal coming from the region between the two saturation slabs, i.e. the "line". The parameters of the functional acquisitions were as follows: readout direction, line resolution: 250 μm, array size: 720 points along the line, line thickness in the 'slice' direction: 2.5 mm. The nominal in-plane line width, or gap between the two OVS slabs, was 4 mm, TR 200 ms and flip angle of 16°, with a total of 520 timepoints per run. The readout was performed with a gradient duration of 22.28 ms and strength of 4.26 mT/m, resulting in a readout bandwidth of 45.4 Hz/pixel. No SAR restrictions were encountered, vendor SAR level estimation never exceeded 47% of the local SAR limit. A TE of 13 ms was used for the first 3 subjects. In these subjects, we investigated the

optimal coil combination approach, line-scanning temporal SNR and BOLD sensitivity. A TE of 22 ms was used for the other subjects, where we compared the BOLD sensitivity between the line-scanning and a fast single-slice GE-EPI sequence (see below).

In each session, one phase-encoded scan (without OVS) was acquired as an anatomical reference for the line-scanning data. Moreover, one phase-encoded scan (with OVS) was acquired before and one after the functional scans, to assess possible subject motion and to generate coil sensitivity maps. Subjects' motion across different runs was evaluated through frame-wise displacement [277]. Scan parameters matched that of the line as much as possible: voxel size 250x250 μm^2, matrix size 720x180, slice thickness=2.5 mm, TR=103 ms, flip angle=16° and TE=13 ms.
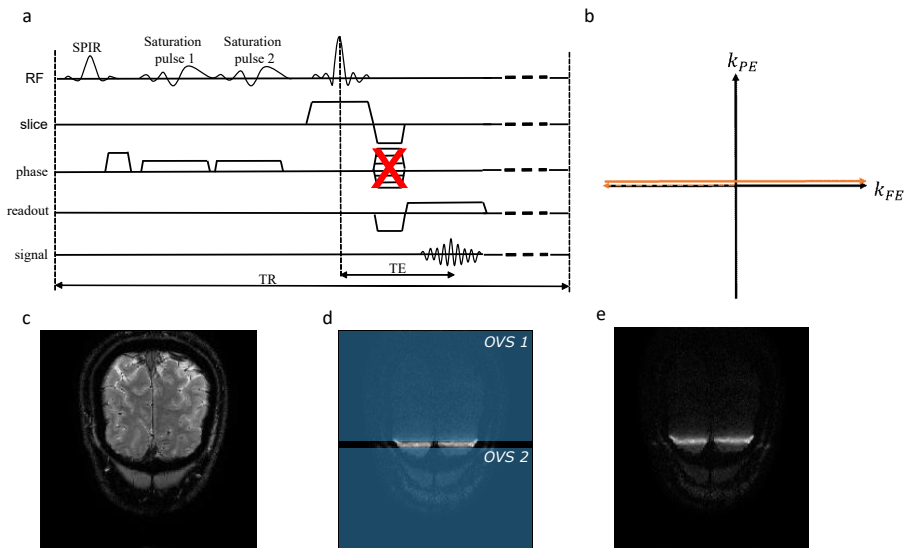

Figure 3.1: (a) Schematic of the gradient echo line-scanning (GE-line) sequence. Phase-encoding gradients are removed so that signal collapses along the phase-encoding direction into the line profile. Two saturation pulses suppress the signal outside the relevant cortical area, i.e. acting as outer volume suppression slabs. (b) The line-scanning k-space sampling pattern: acquisition of the same k_{FE} line every TR. (c) Acquired slice. (d) outer volume suppression (OVS): placement of saturation slabs to suppress unwanted signal outside the line of interest, depicted by the gap (4mm) between the saturation slabs, in right/left direction across visual cortex. (e) effect of the OVS on the phase-encoded slice, i.e. LSD image.

The line-scanning signal is defined as the projection of all the signals originating from the slice with OVS, which we here dub the line signal distribution image (LSD image, see Figure 3.1c). Therefore, voxels can only be assigned to a certain tissue type if the signal is homogeneous along the phase-encoding direction, otherwise a mixture of tissue types is likely present due to partial volume effects. Hence, the line was, wherever possible, positioned orthogonal to the cortical ribbon across the two hemispheres, along the right-left axis and crossing the visual cortex. In Figure 3.1c, an anatomical scan of the acquired slice is shown. Figure 3.1b and c indicate the positions of the OVS slabs and give a visual impression of their signal

saturation effect outside the line (Figure 3.1e).

We acquired functional data using a block design visual task in 6 runs of 104 s each, using a strong visual stimulus to elicit robust BOLD responses in the occipital cortex. A full-field 20 Hz black and white flickering checkerboard was presented in blocks for 10 s on/off, starting with 4 s baseline and finishing with 10 s baseline. Subjects were asked to fixate on a fixation cross present during the OFF condition and in the center of the checkerboard during the ON condition.

To assess the line-scanning BOLD sensitivity, we acquired a phase-encoded fast single-slice EPI BOLD fMRI dataset in 5 volunteers for comparison. Here, fMRI data was recorded using a single-slice GE-EPI acquisition with a 1x1 mm^2 in-plane spatial resolution and 2.5 mm slice thickness to match voxel volume in the line data. Other parameters were: matrix size 176x176, TR=200 ms, TE=22 ms, flip angle=30°, SENSE factor 3, partial Fourier=0.8. One run of 520 timepoints was acquired, leading to a total acquisition time of 104 s. Note that the temporal resolution (200 ms) was matched to the line-scanning fMRI. The same functional stimulus was used as for the line-scanning acquisitions. For a more direct comparison the value used for the line-scanning acquisition and the single-slice GE-EPI are reposted in Table 3.1. Notice that TR and TE were chosen to be exactly the same, as well as the overall voxel volume. Note, the FA was slightly different (16° for line-scanning and 30° for GE-EPI). However, this discrepancy leads to a small relative signal difference and should not influence the final results (less than 1.1% using the signal equation for a spoiled gradient-echo acquisition and a T_1 of 1800 ms for gray matter tissue, see also the Discussion section).

	Line-scanning	2D GE-EPI
TR	200 ms	200 ms
TE	22 ms	22 ms
FA	16°	30°
Spatial resolution	0.25x4x2.5 mm^3	1x1x2.5 mm^3

Table 3.1: Acquisition parameters for the comparison between line-scanning and 2D GE-EPI.

3.2.2 Reconstruction

The reconstruction was performed offline using Matlab (Mathworks Inc, USA) and MRecon (Gyrotools, CH). Four different reconstruction methods to combine the multi-channel line-scanning data were compared.

1. Sum of squares (SoS)

2. Weighted SoS using the tSNR per coil element (tSNR)

3. Weighted SoS using the coil sensitivity maps (csm)

4. Combination of 2) and 3), as follows: $S(x) = \frac{\sum_{i=1}^{N_c} w_i(x) * S_i(x)}{\sqrt{\sum_{i=1}^{N_c} |w_i(x)|^2}}$ where S is the MRI signal, N_c is the number of channels of the receive coil (N_c=32), and $w_i(x) = conj(csm) * tSNR(x)$ per coil as the weighting factor.

Coil sensitivity maps (csm) were obtained from the phase-encoded reference scan that included OVS slabs ($Data_{py}$), according to the following formula:

$$csm = \frac{Re(Data_{py}) + i * Im(Data_{py})}{\sum_{i=1}^{N_c} |Data_{py}|^2}$$

Where Re and Im indicate the real and imaginary part of $Data_{py}$. $Data_{py}$ were first smoothed with a 2D Gaussian smoothing kernel, with a full-width-at-half-maximum (FWHM) of 7 mm. Finally, the 2D csm were summed along the phase-encoding direction over the region where the slice was positioned, so their dimensions matched that of the functional line-scanning data. The coil combination yielding the highest tSNR of the resulting time-series was used for subsequent analyses. tSNR was evaluated through:

$$tSNR = \frac{\overline{S(t)}}{\sigma(S(t))}$$

Where $\overline{S(t)}$ is the mean signal over time and $\sigma(S(t))$ is the standard deviation of the signal across time.

3.2.3 Analysis

We evaluated the performance of the OVS as the ratio of the mean signal intensity between a scan with and without OVS in regions of interest (ROI) inside and outside the line. We also report the signal leakage from outside the line into the equivalent line scan area. This line-scanning signal leakage is computed as the fraction of signal from outside the line and the total signal in an equivalent line scan (i.e. complex addition of all signals in the phase-encoding direction). In the same way we evaluated the signal coming from inside the line. The mean signal profile perpendicular to the line was also computed and the FWHM was used to estimate the effective line width.

Subject motion across different runs was estimated for all sessions through the framewise displacement evaluation of the LSD images acquired in the beginning and at the end of the scan session. Additionally, the motion within single runs was evaluated through the displacement of the line center of mass (root mean square displacement). Data from one subject, presenting an average root mean squared displacement across runs higher than 0.6 mm, were excluded from the analysis.

Functional data were analyzed using a general linear model (GLM) approach to assess the line-scanning and 2D GE-EPI BOLD sensitivity. T-statistics values (t-stats) were computed to select active voxels. For the computation of line-scanning t-stats

we averaged over the 6 runs, while to have a proper comparison with the GE-EPI we considered each line-scanning run separately, in order to have the same degrees of freedom (only one run of GE-EPI fMRI was acquired).

To compare line-scanning and single-slice GE-EPI fMRI acquisitions we modified the GE-EPI data in two ways, to make the 2D data comparable to line data. This double approach was chosen to confirm that the performance of the OVS was adequate for fMRI experiments and that any leaked signal from outside the line of interest did not influence the final results of the GLM analysis. First, we multiplied the LSD image by the single-slice BOLD time-series data after matching the spatial resolution of the LSD image to the one of the single slice GE-EPI (CASE1-LSD). The resulting image was summed along the phase-encoding direction to obtain "line data" for the GE-EPI, prior to computation of t-stats, giving rise to an activation profile along the line. For the second approach (CASE2-NOM), we selected the region where the line was nominally positioned in the GE-EPI scan and again summed along the phase-encoding direction in that region, before the GLM analysis. For a better understanding of the two approaches, see also Figure 3.6 in the supplementary material. In both cases, we manually aligned the line-scanning data to the 1D versions of the image data and averaged the line-scanning data every 4 voxels in the readout (line) direction, in order to match the spatial resolutions of the two acquisitions. Then we calculated the Spearman's correlation (R) between the t-stats in brain tissue regions of every line-scanning run and the GE-EPI CASE1-LSD t-stats and the CASE2-NOM t-stats, yielding two correlation values ($R_{CASE1-LSD}$ and $R_{CASE2-NOM}$). Comparing $R_{CASE1-LSD}$ and $R_{CASE2-NOM}$ will allow us to quantify the out-of-line BOLD contamination. We also estimated the correlation of the t-stats between CASE1-LSD and CASE2-NOM ($R_{CASE1,2}$). In addition, we evaluated the correlation coefficients between t-stats of every run of line-scanning with respect to each other, to estimate the stability over time. Kolmogorov-Smirnov test was performed on the distributions of t-stats for the line-scanning, CASE1-LSD and CASE2-NOM data, and it rejected the null hypothesis at the 5% significance level for all cases. For this reason, we used the non-parametric Spearman's correlation coefficient for the correlation analyses.

Finally, we report an example of cortical depth profile in a small line segment (9 voxels), as well as the temporal behavior of the same voxels. We chose a region where the line was perpendicular to the cortical surface. We averaged the signal across runs and across trials to get the signal profile in percentage signal change (PSC) across 20 s of visual stimulus.

3.3 Results

Figure 3.2a shows the tSNR along the line-scan direction for the four different coil combinations, for one run of line-scanning data of a representative subject. All weighted combinations resulted in an increase in tSNR compared to the simple SoS coil combination for reconstruction. Importantly, the weighted combination of both tSNR and csm outperformed the other approaches in terms of tSNR in all individual datasets. In pilot experiments, this result was consistent across volun-

teers and runs. Hence, this coil combination was used for all subsequent analyses.
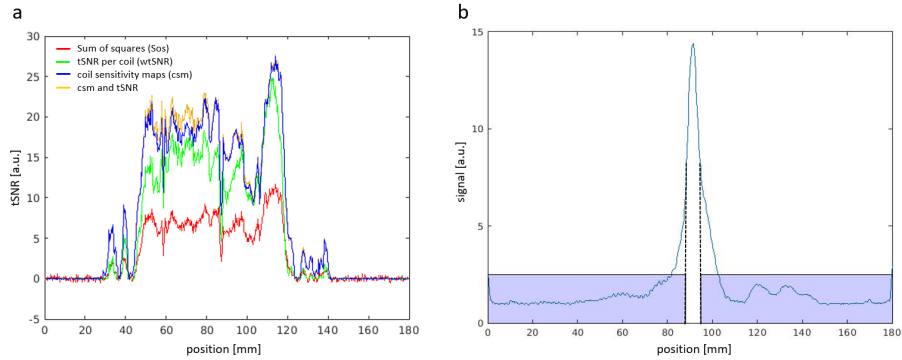

Figure 3.2: (a) tSNR for different coil combinations for an example dataset: sum of squares (red curve, SoS) and weighted combinations using tSNR per single channel (green curve, tSNR per coil), synthetic coil sensitivity maps (evaluated from data acquired with the phase-encoding enabled and applied saturation pulses for OVS (blue curve, csm) and merged combinations of the previous two methods (yellow curve, csm and tSNR). (b) Signal profile perpendicular to the line for a representative subject, to assess the signal suppression outside the region of interest, OVS slabs are indicated by the purple rectangles. The line-width is measured as the FWHM of the signal profile, represented by the dashed black lines.

Figure 3.2b shows the signal profile perpendicular to the line to assess the signal suppression outside the region of interest. Note that the magnitude values are shown in this plot, hence noise in the suppressed regions is amplified due to the imaging data being complex.

Data are shown for a representative subject. The signal within the line of interest has a peaked profile, i.e. it does not reach a plateau between the two OVS slabs. The OVS slabs are nominally spaced 4 mm apart, hence 16×0.25 mm phase-encoded voxels would be contributing signal if the OVS profile were an ideal step-function. Experimentally, on average across all subjects, the mean line width (FWHM) was 6.9±1.0 mm (mean ± std), hence more phase-encoded voxels are effectively contributing to the line-scanning signal.

Table 3.2 contains the FWHM and OVS values for all subjects, as well as the % of the signal coming from the line and the % signal leakage.

The performance of the OVS was adequate (see also Figure 3.1e). On average, the suppression of undesired signal outside the region of interest (i.e. where saturations slabs were positioned) was 94.3±1.3 % (mean ± std over subjects). This equals to 5.7±1.3 % (mean ± std over subjects) of signal that was still present outside the region of interest. The signal within the line of interest is also reduced due to saturation slabs, but the residual signal inside the line is on average 61.5±11.8 % (mean ± std over subjects).

Regarding the estimation of signal coming from inside and outside the line, compared to the signal coming from the all the LSD image, we estimated that, on average across subjects, 42±5 % (mean ± std over subjects), of the signal is coming from the line, while 58±5 % (mean ± std over subjects) is originating from outside

the line.

Subject	Saturated signal outside line [%]	Residual signal inside line [%]	FWHM [mm]	Signal coming from the line [%]	Signal leakage [%]
1	92.0	83.5	6.7	39.9	60.1
2	94.8	57.8	6.5	37.1	62.9
3	95.0	54.3	7.0	44.7	55.3
4	94.9	55.3	8.3	40.3	59.7
5	94.2	63.2	5.9	48.9	51.1
6	96.3	51.7	5.6	49.2	50.8
7	92.8	75.2	8.5	40.0	60.0
8	94.3	51.1	6.8	36.3	63.7
mean	94.3	61.5	6.9	42.0	58.0
std	1.3	11.8	1.0	5.0	5.0

Table 3.2: Percentage of saturated signal outside the line, residual signal inside the line and full-width-at-half maximum of the line profile, signal originating from the line and signal leakage, for all subjects.

An example line-scanning dataset of a representative subject, averaged over 6 runs, is shown in Figure 3.3a. The color map represents the signal intensity as a function of position (vertical axis) and time (horizontal axis). The stability over time and the limited effect of subject motion in the left-right direction is clear from the stability of the horizontal bands of signal in Figure 3.3a. The motion in the left-right direction, estimated for every run and subject through the root mean square displacement of the line center of mass, was on average 0.32±0.14 mm (mean ± std over runs and subjects), apart from one subject which was rejected from the analysis, since the averaged root mean square displacement across runs was 0.85±0.22 mm (mean ± std over runs).

Subject motion estimated from LSD images acquired before and after each run showed that the average displacement over the whole scan session (around 40 minutes) was 0.71±0.65 mm (mean ± std over subjects). Figure 3.3b shows the mean signal intensity profile along this line through the occipital lobe. This mean signal also represents the anatomical profile along the line.

Figure 3.3c shows t-stats overlaid on the anatomical scan for a representative subject. The white arrows indicate the voxels with highest activation. Note that there is good spatial correspondence between the positive BOLD t-stats and the grey matter ribbon in the depicted dataset. In Figure 3.3d, an example time course for a single voxel (t-stat = 25) is plotted, showing a strong BOLD response along with the predicted BOLD response from the GLM in blue.
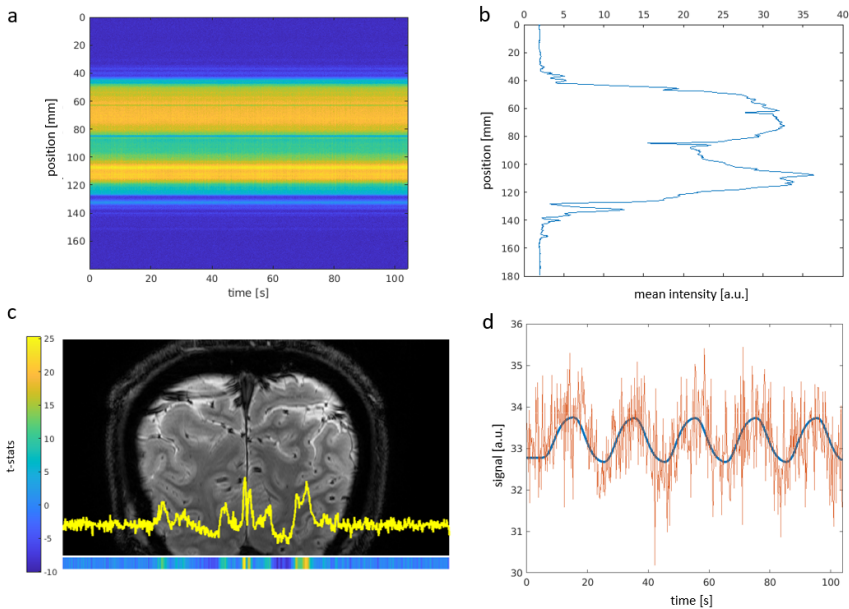
3

Figure 3.3: (a) line-scanning data, averaged over 6 runs and (b) mean intensity signal over the line for a representative subject. (c) t-stats (plot in yellow and colormap on the bottom) superimposed on the anatomical scan for the acquired slice. In the color map, yellow colors represent the highest t-stats and dark blue colors negative t-stats. The position of the line is indicated with a blue box. White arrows indicate voxels with highest activity. (d) time course for a voxel with the raw time-series in orange and the predicted BOLD responses from the GLM in blue.

Figure 3.4 shows the comparison of line-scanning (3.4a) and single-slice, TR-matched, GE-EPI BOLD fMRI (3.4b). To compare the single-slice GE-EPI and line-scanning data along the line, the GE-EPI scan was multiplied by the LSD image, in order to obtain a version of GE-EPI with the same line profile as the line-scanning dataset. The signal was then summed in the phase-encoding direction in order to obtain the activation profile for the GE-EPI data (grey lines). Using a perfect step function to select the line signal in the GE-EPI (black line, Figure 3.4b), a similar activation pattern is found.

Figure 3.4c shows a scatter plot of the t-stats of the single-slice GE-EPI and line-scanning BOLD fMRI data, resampled to match the spatial resolution of the GE-EPI scan. Data is shown for all runs of a representative subject.

Figure 3.4d shows the GLM results over the whole slice for the GE-EPI acquisition, demonstrating that the bulk of activation in the slice is located inside the line of interest.
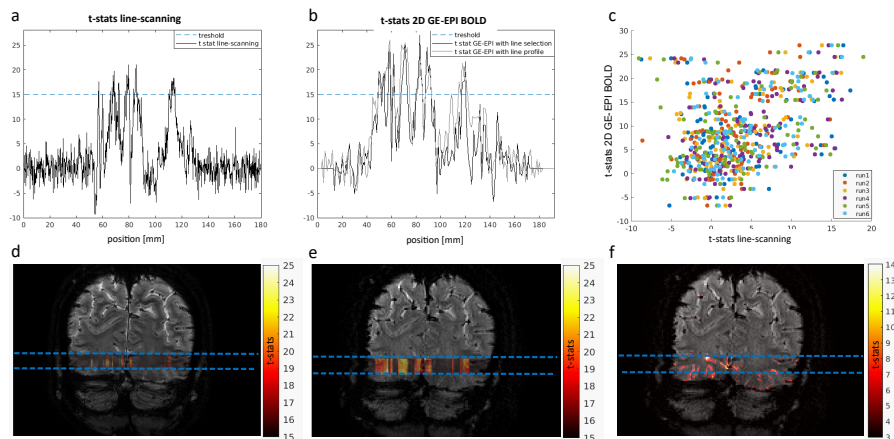
Figure 3.4: (a) t-stats profile for the line-scanning BOLD data (mean over 6 runs). Blue dashed lines indicate the thresholds (here t-stats that are greater than 15) for showing active voxels in (d) coronal slice (anatomical reference) shown with phase-encoding and without OVS applied. Overlaid on the slice are t-stats of the line scanning data plotted in hot colors (red to yellow). Light blue lines highlight the position of the line-scanning data. (b) t-stats profile for the GE-EPI BOLD data obtained in the two ways: GLM approach considering the line profile (multiplication of LSD prior to functional analysis, gray) and mean signal over the nominal line of interest (black). (e) t-stats obtained with line profile, overlaid on the GE-EPI. Light blue lines highlight the position of the line-scanning data. (c) correlation between t-stats of line-scanning acquisition and 2D GE-EPI with line profile approach for all runs, for the same representative subject. (f) 2D t-stats for the GE EPI acquisition, showing that most of the activation is coming from the region inside the line, marked with light blue lines.

The similarity of line-scanning t-stats and GE-EPI BOLD t-stats obtained with the line profile (CASE1-LSD) is quantified for all subjects in Table 3.3 of the supplementary material, through the correlation between the t-stats for the two scans. The mean value of correlation over all runs and subjects was $R_{CASE1-LSD} = 0.59 \pm 0.17$ (mean $\pm$ std).

Similar results were obtained with the second approach of comparison (CASE2-NOM), selection of the nominal line location in the GE-EPI prior to GLM analysis. In this case the mean correlation coefficient across runs and subjects was $R_{CASE2-NOM} = 0.49 \pm 0.21$ (mean $\pm$ std, see Table 3.3 in the supplementary material, and Figure 3.7 for the t-stats comparison of the same representative subject of Figure 3.4. The correlation coefficients of the t-stats sampled from the GE-EPI in the two approaches were $R_{CASE1,2} = 0.81 \pm 0.12$ (mean $\pm$ std) on average over subjects, indicating very little differences between the two approaches (see Figure 3.8).

Further analysis has been reported in the supplementary material, where Figure 3.9 shows the power spectra of the line-scanning sequence (Figure 3.9a) and the adapted GE-EPI to have one dimensional data using the line profile, i.e. multiplication of LSD image (Figure 3.9b). The time-series data was first averaged over all voxels in the line contains data before computing the power spectrum. In both cases the physiological contributions from the heart rate and respiration are visible.

To evaluate the stability over time of the six different line-scanning runs, we report in Figure 3.10 the correlation between t-stats of line-scanning runs (Spearman's

correlation coefficient, R), averaged across subjects. Averaging across all runs and subjects we find that the mean correlation coefficient is R = 0.77±0.04 (mean ± std), hence t-stats are stable over time across the 6 different runs, facilitating averaging over runs.

In order to show the potential of line-scanning for assessment across cortical layers, we show in Figure 3.5 an example of a layer dependent profile for a small portion of visual cortex located on the edge of the calcarine sulcus, intersected perpendicularly by the line.
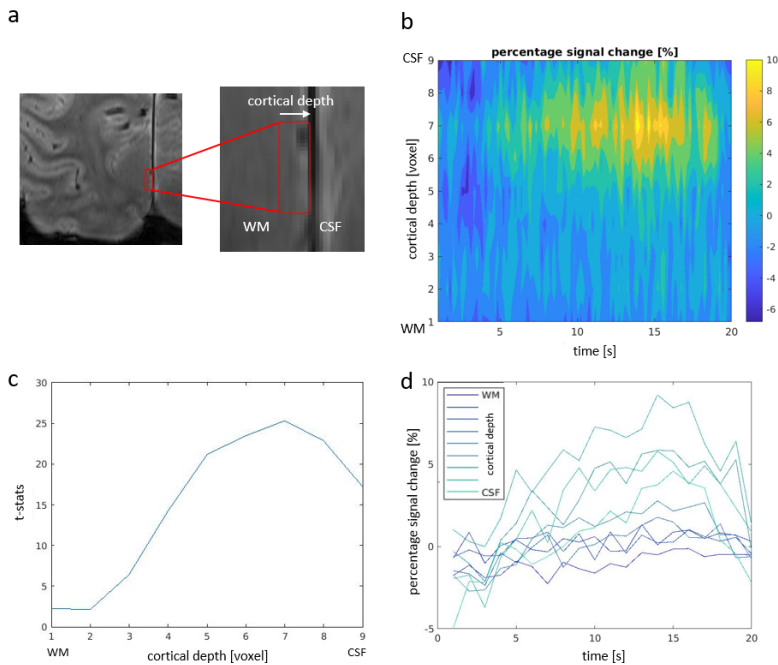

Figure 3.5: Line-scanning cortical depth analysis; (a) the region of interest (ROI) is depicted by the red box on top of the anatomical image. (b) The BOLD response amplitude (PSC) across cortical depth and time is shown for the ROI. (c) t-stats values for the same voxels. Highest t-stats are found for voxels containing gray matter. (d) mean PSC every 5 timepoints versus time, showing different behaviour in time, depending on cortical depth. PSC stands for percentage signal change.

In Figure 3.5a, the region of interest is highlighted through the red box and the percentage signal change is plotted for the same region across time (Figure 3.5b). Figure 3.5c shows the t-statistic values for the same portion of brain, while in Figure 3.5d the PSC versus time is plotted for every voxel separately.

3.4 Discussion

In this paper, we report line-scanning fMRI results in humans combining very high spatial and temporal resolution. Line-scanning has unique potential for laminar fMRI due to its ability to map the BOLD signal response at the mesoscopic scale

in humans, with a temporal resolution of a few hundred milliseconds. We demonstrate that line-scanning can detect BOLD activation in human visual cortex, with similar results as standard single-slice GE-EPI, but with a much higher spatial resolution.

We first focused on the optimization of coil combinations for the reconstruction of line-scanning data. A coil combination including coil sensitivity maps and coil channel tSNR for the reconstruction shows the best temporal stability, with resulting tSNR values that are comparable to sub-milllimeter 3D imaging and sufficient for BOLD signal detection [161].

The line-scanning method demonstrated here relies on the use of saturation pulses that aim to suppress the signal outside the line of interest. The saturation pulses resulted in a good OVS but also reduced the signal inside the line. Considering the signal coming from the line only, with respect to the total signal of the whole LSD image, we estimate that there is, on average, 58% of signal coming from outside the line. For future studies we will investigate whether the rotation of the slice would reduce signal leakage from outside the line, as we could diminish the amount of tissue orthogonal to the line. Future line-scanning efforts could also benefit from sharper saturation profiles or spin-echo based line-scanning (i.e. beam excitation using orthogonal 90° and 180° selective RF pulses [278] to improve the sharpness of the line profile. At present, however, we argue that the strong correlations of t-stats between dimension-adjusted planar (2D-EPI) obtained through CASE1-LSD and CASE2-NOM ($R=0.81\pm0.12$) indicate that line-scanning can be used for fMRI with very limited within slice, out-of-line BOLD signal contributions. As quantification of the out-of-line BOLD signal contribution we calculated the difference between $R_{2CASE1\text{-}LSD}$ and $R_{2CASE2\text{-}NOM}$, $R_{2CASE1\text{-}LSD}$ - $R_{2CASE2\text{-}NOM}$ = 10.8%, which indicates a variance mismatch of 10.8% between the actual obtained LS activation profile CASE1-LSD and the ideal CASE2-NOM.

Motion correction of fMRI data usually requires spatial information from the images themselves. In line-scanning data, these spatial references are severely reduced when phase-encoding gradients are removed. For this reason, subjects' movements have to be limited. To prevent motion, subjects were secured in place using foam pads between the ears and the head coil. Moreover, movement in left-right direction is directly visible in the line-scanning data as an instability of the horizontal bands of signal (cfr Figure 3.3a), as well as quantifiable by the displacement of the line center of mass. In these datasets, data from one subject were rejected due to excessive movement. As described in the methods section, a phase-encoded scan containing a 2D image with OVS slabs was repeated before and after the functional scans, to evaluate the subject's total displacement. All subjects showed little displacement (mean framewise displacement 0.71±0.65 mm, over the 40 minute scan session), apart from the aforementioned rejected dataset. Future studies may investigate subjects' motion through a multi-slice acquisition repeated multiple times during the scan session, in order to better quantify the exact

location of the imaged line in 3D – perhaps in conjunction with a bite-bar to minimize head motion. Moreover multi-echo acquisitions can be used to retrospectively remove physiological noise contributions [176]. Finally, prospective motion correction through external cameras or fat-navigators could be introduced to correct the position of the line during line-scanning acquisition, without increasing the number of scans needed in our protocol [111].

In this study, we examined line-scanning sensitivity to BOLD activity using a simple block design visual task. BOLD responses can be detected in the human primary visual cortex, with similar sensitivity to a matched GE-EPI BOLD acquisition and the potential of extraordinary temporal and spatial resolution along the line of interest. The parameters of the two scans were matched as much as possible and the only difference was the FA (16° vs 30°). The difference in FA will result in a 1.1% difference for the inherent SNR between the two scans. This can lead to small differences in the BOLD contrast weighting and image contrast. Differences in flip angles will also lead to different sensitivity to the inflow effect. However, from literature [168, 279], we know that at ultra-high field strengths the inflow effect for BOLD imaging is already minor because of the largely diminished intravascular contribution due to the shortened blood T_2*. Previous work by Gao et al. [279] compared BOLD signals with different flip angles (30°, 60° and 90°) at 3T. They found that even with such large differences in flip angles, the BOLD percentage signal change is only slightly affected by different in-flow effects. For these reasons, we believe that in our acquisitions a difference of only 14° in flip angle should not affect the interpretation of our results.

The comparison of single-slice GE-EPI BOLD and functional line-scanning ensured that the proposed technique offers similar BOLD sensitivity to conventional approaches. Note that for the current conservative data analysis no temporal filtering was applied, meaning that the raw signal shows the robustness of the proposed approach. Effective signal to noise ratios may also be improved by examining and removing contributions of physiological and movement-related noise sources, a strategy facilitated by the very high sampling rates of our line scanning approach. Moreover, the stability of signals across different runs guarantee that our method is stable over time and can be used for longer tasks. This opens up the possibility of using line-scanning for cognitive neuroscience experiments. Here, the promise is that the spatial and temporal specificities of line-scanning will allow us to investigate time-resolved cognitive computations with laminar precision. In this paper, we describe a line-scanning implementation and assessed its reliability in detecting the BOLD signal changes upon a visual stimulus. Line-scanning was primarily developed for layer fMRI investigations, for which we presented a preliminary example of cortical depth profile where the line was positioned perpendicular to the cortical ribbon in the calcarine sulcus. The cortical depth profile shown here is affected by additional blurring not related to the finite readout gradients, which was estimated to be on the order of 3% (for a T_2* value of 25 ms for gray matter), i.e. ~8 μm. Future work could focus on the unexplained blurring which we attribute

to biological point-spread function [280].

Line-scanning fMRI is a promising technique for neuroscience and (patho) physiological research on cerebrovascular and related disorders. Line-scanning fMRI capitalizes on the high spatial and temporal information from BOLD responses across the cortical depth that can yield important insight on microvessel function in health and disease. More specifically, a wide range of neuroscientific questions may be addressed by studying the dynamics of the BOLD response across cortical depth, for example, in integration of visual information across the "blind spot" [281]; the dynamics of BOLD responses in higher order areas compared to lower input ones (e.g. output of V1 becoming input in V2 or MT) or the timing of signals in the somatosensory cortex on self-touch, that prevent ticklishness. Regarding elucidating cerebrovascular (patho)physiology, the benefits of line scanning fMRI can be very valuable in identifying and separating microvessels signal features from large vessel signals. Impaired microvessel function directly feeding the neurons as opposed to those draining from the neurons may have very different implications on the nature and origin of cerebrovascular and neurodegenerative diseases [282–285]. Commonly obtained BOLD signals are usually a mixture from the tissue-feeding microvessels, directly part of the neurovascular network engaged in brain tissue functioning, and signals from the larger venous vessels that drain the cortical tissue. Unfortunately, signals from larger vessels generally obscure signals from the microvasculature, hampering the identification of impaired microvessel function. Nascent high-resolution techniques such as line-scanning will open new methodological avenues to isolate and characterize microvessel spatiotemporal behaviour, i.e. acting as a hemodynamic probe. For example, microvascular flow patterns and transit time estimates in response to neuronal or vascular (i.e. hypercapnia, hyperoxia) challenges could be studied in relation to, for example, small vessel diseases [286], and the proposed capillary transtit time heterogeneity model [287–290]. Finally, characterizing the microvascular hemodynamics by line-scanning could potentially provide more insights in neurovascular coupling and supply input to computational BOLD models [291, 292].

3.5   Conclusion

Overall, we demonstrate the feasibility of line-scanning in humans at 7T. We show reliable BOLD responses at sub-millimeter and sub-second resolution using the line-scanning fMRI technique, revealing high spatial specificity for a visual task. We demonstrate the robustness of the line-scanning technique by the comparison with a standard method (2D GE-EPI).

Supplementary Material

3
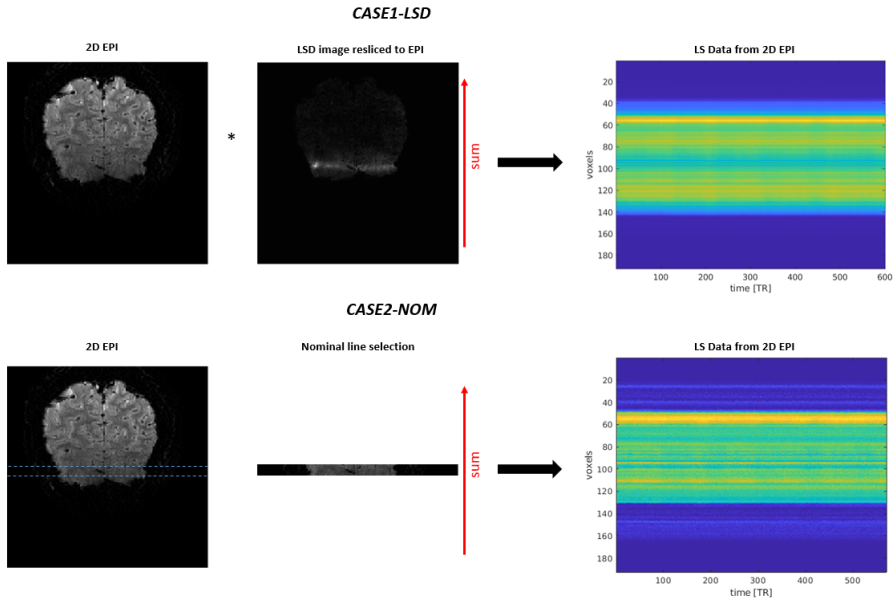
CASE1-LSD

CASE2-NOM

Figure 3.6: Graphical explanation of CASE1-LSD and CASE2-NOM. (top row) 2D EPI multiplied by LSD image, before summing in the phase encoding direction leads to a line-scanning profile for CASE1-LSD. (bottom row) nominal selection of the line, before summing in the phase encoding direction and related line-scanning profile for CASE2-NOM.
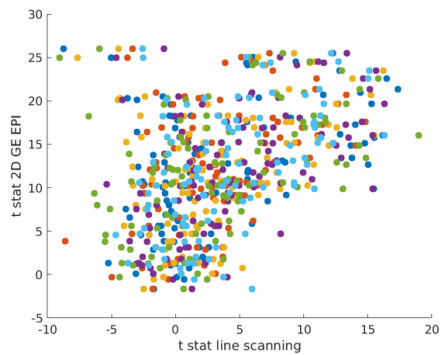
Figure 3.7: correlation between t stats of line-scanning acquisition and 2D GE-EPI with line selection approach for all runs, for the same representative subject of Figure 8.
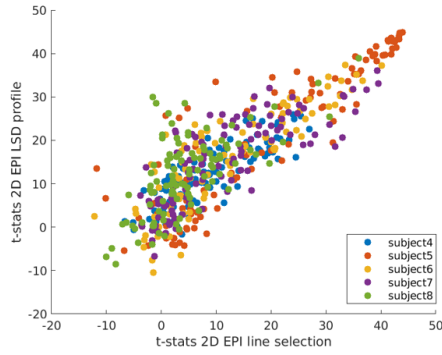
Figure 3.8: correlation between t stats of 2D GE-EPI evaluated with the two different approaches (line selection and LSD image profile).
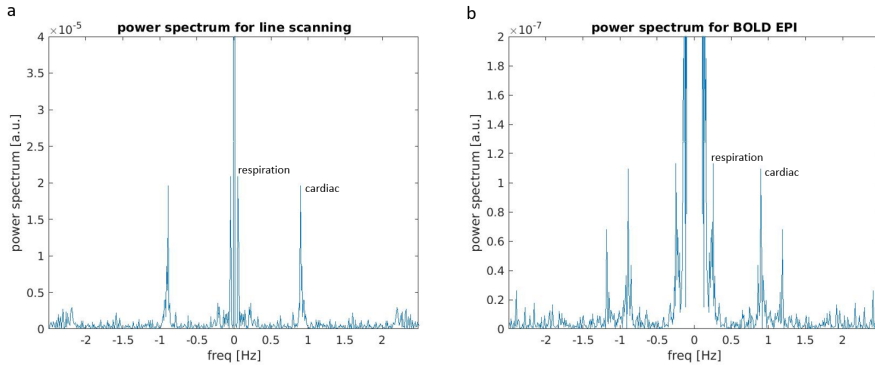
Figure 3.9: (a) power spectrum of line-scanning, and (b) power spectrum of the 1D version of GE-EPI obtained through multiplication with the LSD image/ and averaged over all line. For both the line-scanning and GE-EPI power spectra, the timeseries data was first averaged over all voxels in the line before computing the power spectrum.

Figure 3.10: Run-by-run line-scanning t-statistic correlation matrix, averaged across subjects.

Subject	4	5	6	7	8
run1	0.38	0.82	0.72	0.54	0.47
run2	0.36	0.86	0.72	0.63	0.43
run3	0.37	0.83	0.74	0.56	0.50
run4	0.52	0.84	0.54	0.52	0.52
run5	0.45	0.83	0.64	0.53	0.43
run6	0.48	0.87	0.69	0.55	0.50
mean	0.43	0.84	0.68	0.56	0.48
std	0.07	0.02	0.08	0.04	0.04

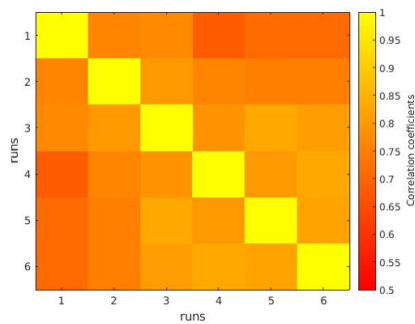Table 3.3: Correlation between line-scanning and BOLD GE-EPI t-stats evaluated after multiplying the GE-EPI and the LSD image, Spearman correlation coefficients (R) are reported for each run and subject.

Subject	4	5	6	7	8
run1	0.30	0.80	0.64	0.43	0.46
run2	0.30	0.83	0.65	0.55	0.16
run3	0.30	0.79	0.64	0.53	0.28
run4	0.42	0.79	0.45	0.35	0.19
run5	0.39	0.80	0.56	0.45	0.27
run6	0.43	0.79	0.58	0.41	0.25
mean	0.36	0.80	0.59	0.45	0.27
std	0.06	0.01	0.08	0.07	0.11

Table 3.4: Correlation between line-scanning and BOLD GE-EPI t-stats evaluated after manual line selection in the GE-EPI, Pearson correlation coefficients (R) are reported for each run and subject.

4

Robust high spatio-temporal line-scanning fMRI in humans at 7T using multi-echo readouts, denoising and prospective motion correction

Luisa Raimondo, Nikos Priovoulos, Catarina Passarinho, Jurjen Heij, Tomas Knapen, Serge O. Dumoulin, Jeroen C.W. Siero and Wietske van der Zwaag

Abstract

Background: Functional magnetic resonance imaging (fMRI), typically using blood oxygenation level-dependent (BOLD) contrast weighted imaging, allows the study of brain function with millimeter spatial resolution and temporal resolution of one to a few seconds. At a mesoscopic scale, neurons in the human brain are spatially organized in structures with dimensions of hundreds of micrometers, while they communicate at the millisecond timescale. For this reason, it is important to develop an fMRI method with simultaneous high spatial and temporal resolution. Line-scanning promises to reach this goal at the cost of volume coverage.

New method: Here, we release a comprehensive update to human line-scanning fMRI. First, we investigated multi-echo line-scanning with five different protocols varying the number of echoes and readout bandwidth while keeping the TR constant. In these, we compared different echo combination approaches in terms of BOLD activation (sensitivity) and temporal signal-to-noise ratio. Second, we implemented an adaptation of NOise reduction with DIstribution Corrected principal component analysis (NORDIC) thermal noise removal for line-scanning fMRI data. Finally, we tested three image-based navigators for motion correction and investigated different ways of performing fMRI analysis on the timecourses which were influenced by the insertion of the navigators themselves.

Results: The presented improvements are relatively straightforward to implement; multi-echo readout and NORDIC denoising together, significantly improve data quality in terms of tSNR and t-statistical values, while motion correction makes line-scanning fMRI more robust.

Comparison with existing methods: Multi-echo acquisitions and denoising have previously been applied in 3D magnetic resonance imaging. Their combination and application to 1D line-scanning is novel. The current proposed method greatly outperforms the previous line-scanning acquisitions with single-echo acquisition, in terms of tSNR (4.0 for single-echo line-scanning and 36.2 for NORDIC-denoised multi-echo) and t-statistical values (3.8 for single-echo line-scanning and 25.1 for NORDIC-denoised multi-echo line-scanning).

Conclusions: Line-scanning fMRI was advanced compared to its previous implementation in order to improve sensitivity and reliability. The improved line-scanning acquisition could be used, in the future, for neuroscientific and clinical applications.

4.1   Introduction

In the human brain, neurons with similar functions cluster together in spatial structures with an extent of hundreds of micrometers, i.e. mesoscopic scale, while they communicate at the millisecond timescale [5, 10]. For example, in the cortex neurons are organized in columnar and layer structures [4, 6, 293]. Cortical layers differ in neuronal content, but also in their connectivity to other parts of the brain. Brodmann [4] used differences in cortical layers to define distinct cortical areas. Thus, cortical layers are considered a basic anatomical and physiological unit of the cortex and for this reason it is interesting to study responses at the mesoscopic scale.

Functional magnetic resonance imaging (fMRI) plays an important role in the study of brain function [22], allowing detection of brain activity through the changes in blood flow and oxygenation. Blood oxygenation level-dependent (BOLD) contrast weighted imaging is one of the primarily used contrast mechanisms in both cognitive [23] and clinical [294] neuroscience. BOLD imaging has two important advantages: it is non-invasive and readily available at any MRI scanner. For BOLD fMRI, high spatial and temporal (<1mm, ~100ms) resolutions are required to detect spatiotemporal features of the hemodynamic response function (HRF) which describes how the hemodynamic signal propagates through the cortex at the mesoscopic scale, in particular across cortical layers.

However, functional MRI is an inherently noisy acquisition method [295]. As a result, most fMRI data are denoised in some form before statistical testing, usually by applying a spatial smoothing step [296–298]. For high-resolution acquisitions, smoothing is not appropriate because of the concurrent loss in spatial definition [299], even though noise levels increase at these higher resolutions. This means that other techniques have to be applied to increase the signal-to-noise-ratio (SNR) and decrease the noise [300].

Advances in fMRI methodology have been aimed at increasing both the spatial and the temporal resolution, with the ultimate goal of recording at sub-millimeter spatial resolution and sub-second sampling rate. In the past decade, line-scanning fMRI in rodents achieved very high resolution across cortical depth (50 μm) and time (50 ms) by scanning only a single line of data, sacrificing volume coverage and resolution along the cortical surface in the process [50]. Line-scanning fMRI in rodents has also been used in combination with other techniques such as fiber-based optogenetic stimulation [301] and diffusion-sensitizing gradients [302], to investigate the fast BOLD onset times at high spatial resolution. Line-scanning fMRI in rats has been extended towards a multi-line implementation, acquiring line profiles from different cortical regions to investigate laminar-specific functional connectivity mapping under both evoked and resting-state conditions [303].

Recently, line-scanning was employed in human studies, for microstructural investigations [304, 305] and with the goal of isolating microvessel responses and characterizing the distribution of blood flow and laminar functional MRI profiles

across cortical depth, at high spatiotemporal resolution [274, 306]. Our first human line-scanning implementation [306] achieved resolutions of 250 μm and 200 ms and demonstrated its utility for measuring BOLD responses along cortical depth, in the visual cortex, during a visual stimulation task. The sequence was a modified 2D gradient-echo (GE) sequence employing a single-echo readout, with low bandwidth for increased SNR, but still with some deadtime within the repetition time (TR). Here, we propose several ways to improve this line-scan sequence for increased sensitivity. This increased sensitivity is necessary to make line-scanning a more robust and generalizable technique, which could be used for future neuroscientific and clinical applications. Specifically, diseases such as small vessel or sickle cell diseases [286, 307–309] would benefit from high spatial and temporal resolutions to gain insights about the altered hemodynamic responses in patients across cortical depths.

First, the unused deadtime within the TR permits the acquisition of additional echo readouts without increasing the TR. The BOLD contrast is known to be maximal when the echo time (TE) is equal to the local tissue T_2^* relaxation rate [310]. With multi-echo imaging, we can measure the T_2^* signal decay curve and reach optimal readout efficiency and BOLD sensitivity. In addition, the T_2^* signal decay curve can be used to disentangle BOLD-like (T_2^*) changes from non-BOLD signal changes [171]. Non-BOLD signals can be caused by drift, motion, physiological noise or other contaminating signals that impact the initial signal intensity (S_0) of the T_2^* decay curve sensitivity [172, 300, 311].

Second, thermal noise dominates at the high spatial and temporal resolution of line-scanning. The "MR signal" can be specifically defined as an electrical current induced in the receiver coil by the precession of the net magnetization during resonance, as the manifestation of Faraday's Law of Induction [12]. However, the definition of noise in an fMRI time series is more complex, due to the different noise sources [312]. Thermal noise, classified as a zero-mean Gaussian distributed noise, is generated either from the electronics or from the sample being imaged and depends on a range of parameters including the static magnetic field strength, the electronics, the readout bandwidth and sampling scheme [313, 314]. It becomes predominant when small voxel sizes are used. Other sources of signal variance include subject motion and physiological noise through respiration and heartbeat [315]. For denoising, the final goal is to decrease noise without compromising any physiological aspects of the data, but, generally, some information has to be sacrificed. Many denoising techniques [316–318] are based on a trade-off between the removal of unwanted signal and the preservation of the data quality, such as spatial and temporal resolution, as well as the underlying biological processes. In a newly described approach from Vizioli et al. [319], thermal noise is selectively suppressed from high-resolution fMRI data while preserving the amplitude of the hemodynamic response, the spatial resolution and the functional point-spread function.

Finally, line-scanning is highly sensitive to subjects' motion. Generally in fMRI,

participant movement leads to inconsistencies in the fMRI timecourse. These are typically corrected by coregistering the volume timepoints [298, 320]. Motion is even more problematic in high-resolution MRI, where the impact of smaller movements is amplified [321–323]. In the case of line-scanning, the 1-dimensional nature of the data only allows motion detection in the line direction, whereas rotations or displacements perpendicular to the line lead to spin-history artifacts or line acquisition outside the area of interest. These effects cannot be corrected by post-hoc motion correction in line scans; therefore, a prospective motion correction scheme (PMC) is required [324]. This can be achieved with external hardware [322, 323, 325] or with image-based navigators [326, 327]. Here we use an image-based navigator implementation.

In this work, we aim to improve the line-scanning acquisition in three ways: first, we investigated five different multi-echo protocols varying the numbers of echoes and readout bandwidth while keeping the TR — and thus the overall scan time — constant. We compared different echo combination approaches in terms of BOLD activation (sensitivity) and temporal signal-to-noise ratio. Second, we implemented an adaptation of the NORDIC thermal noise removal for line-scanning fMRI data, and finally, we tested three image-based navigators for motion correction.

4.2 Methods

4.2.1 Participants

Our pool of participants is composed of two groups: multi-echo section: 6 participants (3 male, 32 ± 6 years old (mean $\pm$ standard deviation)), noise removal section: 4 participants (4 male, 28 ± 4 years old) and for the motion correction section: 8 participants dataset (7 male, 31 ± 8 years old, including the individuals participating in the noise removal section). All the participants were healthy individuals who provided written informed consent as approved by the medical ethics committee of the Amsterdam University Medical Centre. The guidelines of the Helsinki Declaration were followed throughout the study, and all participants were screened for MRI compatibility prior to the experiments.

Note that the line-scanning method allows a high sampling rate within the participant, hence we can reach statistical power without the need to average over many participants.

In addition, we aimed to find an effect in every single participant, which is easily achieved with the strong visual task we employed across the study. The number of participants can be seen as replication of the same effect rather than a way to measure the effect itself [328, 329]. Ultimately, for clinical research it is essential to maximize signal and minimize noise to have information in individuals [330].

4.2.2 Selection of multi-echo acquisition and echo combination version

The 7T MRI (Philips Healthcare, Best, NL) was equipped with a 2 channel transmit and 32 channel local receive surface coil [122], positioned close to the visual cortex.

Line-scanning acquisition used a modified 2D multi-echo gradient-echo sequence where the phase-encoding in the direction perpendicular to the line, needed for conventional 2D imaging, was omitted: line resolution=250 μm, TR=105 ms (108 ms for one participant), flip angle=16°, array size=720, line thickness=2.5 mm, in-plane line width=4 mm, fat suppression using SPIR. Two saturation pulses (7.76 ms pulse duration) suppressed the signal outside the line of interest. Five different multi-echo schemes (including 3, 5, 7, 9 and 11 echoes) were compared by adapting the readout bandwidth for the different schemes. The longest echo time for all schemes was 38 ms. The order of acquisitions was randomized across participants; details are provided in Table 4.1.

	N echoes	TE1 [ms]	echo spacing [ms]	Readout BW [Hz/pixel]
acq1	3	9.2	14.4	71.7
acq2	5	6	8	131.4
acq3	7	5	5.5	197.6
acq4	9	4.4	4.2	264.2
acq5	11	4	3.4	337.6

Table 4.1: parameters for the 5 multi-echo line-scan acquisitions. N-echoes is the number of echoes, TE1 is the first acquired echo, echo spacing is the time difference between echoes acquisitions and readout BW is the readout bandwidth per pixel. The last echo time in the series always was 38 ms.

The line was manually positioned approximately perpendicularly to the medial gray matter sheet of the occipital lobe. We acquired one run of functional data with each protocol, using a block design visual task consisting of an 8 Hz flickering checkerboard presented on the entire screen for 10 s on/off. Runs lasted 5 minutes and 40 seconds. The total run duration for the 11 echoes acquisition runs was shortened for 3 participants due to technical constraints and skipped for one other participant. Reconstruction was performed offline (MatLab, Gyrotools).

We combined the multi-channel coil data with a temporal signal-to-noise ratio (tSNR) and coil sensitivity-weighted sum of squares (SoS) weighted scheme per echo in the data reconstruction as in [306]. The SoS was defined as:

$$S(t, TE) = \sqrt{\sum_{i=1}^{N} S_i(t, TE)^2} \tag{4.1}$$

where S_i is the MR signal for each receive coil channel and N is the number of channels. The resulting $S(t, TE)$ is the MR signal as a function of time and TE.

Multi-echo data were combined in 3 different ways: SoS (with the same formula as equation 4.1, but summing over echoes instead of channels), T_2^* fit and a tSNR weighted combination (wtSNR) based on Poser et al. [172]. 'T_2^* fit' fits the T_2^* decay per voxel with a linear fit of equation 4.2 in a least-squares way:

$$S(t, TE) = S_0 e^{-\frac{TE}{T_2^*}} \tag{4.2}$$

Functional data were analyzed in Matlab using a general linear model (GLM) approach. We used the SPM implementation of the canonical HRF [320] as block design experiments do not allow one to fit the HRF shape. T-statistic values (t-stats) were computed to identify active voxels. We also evaluated the tSNR for each voxel through:

$$tSNR = \frac{\overline{S(t)}}{\sigma(S(t))} \tag{4.3}$$

Where $\overline{S(t)}$ is the mean signal over time, across the whole timecourse and $\sigma(S(t))$ is the standard deviation of the signal across time for the whole timecourse. Note that the tSNR is computed across the whole timecourse, hence including voxels with functional activation due to the visual task. However, within the line, very few voxels contain task activation and task effects on the tSNR are minimal. We compared the mean and maximum t-stats in a region of interest (ROI) for the 5 different multi-echo acquisitions, the three echo-combination methods and the ROI average tSNR. The ROIs were defined as the 11 voxels, 11 x 0.25 mm = 2.75 mm, covering the gray matter (GM) ribbon (identified in a slice image centered on the line), surrounding the voxel showing the highest t-stats, for all acquisitions. For the tSNR comparison, we also defined a white matter ROI (WM ROI).

4.2.3 Noise removal

For the noise removal dataset, we acquired data using the 5 echoes acquisition with the same visual task as the previous section, adding 20 s baseline in the beginning.

In fMRI, it is common to perform some kind of noise reduction data processing to increase the SNR, with the final goal of maintaining signal integrity (including spatial and temporal resolutions). To achieve this purpose, for this section, we employed a thermal noise removal step in the reconstruction pipeline based on Noise reduction with Distribution Corrected (NORDIC) principal component analysis (PCA) [319]. The denoising was applied to k-space data before the coil and the echo combination (see Figure 4.1).

A singular value decomposition (SVD) of the data was submitted to "hard thresholding" that eliminates all components indistinguishable from zero-mean Gaussian distributed noise (Figure 4.1a). The singular value decomposition of our line-scanning k-space data matrix (for every channel and echo) was $\mathbf{U} \cdot \mathbf{S} \cdot \mathbf{V^H}$, where $\mathbf{U}$ and $\mathbf{V}$ are unitary matrices, and $\mathbf{S}$ is a diagonal matrix whose diagonals are the spectrum of ordered singular values. The singular values below a chosen threshold were replaced by 0, and the other singular values were unaffected. $\mathbf{S_{th}}$ is a new diagonal matrix generated as a result of thresholding, and the estimate of the NORDIC-denoised data was given as $\mathbf{U} \cdot \mathbf{S_{th}} \cdot \mathbf{V^H}$. The threshold was chosen from the elbow point of the 'scree plot' depicting the eigenvalues versus the number of components (see Figure 4.1) for every channel and every echo separately. Note that, during a pilot study we ensured that noise was preferentially removed, leaving task-driven signal variation, by verifying that t-values rose as a function of removed
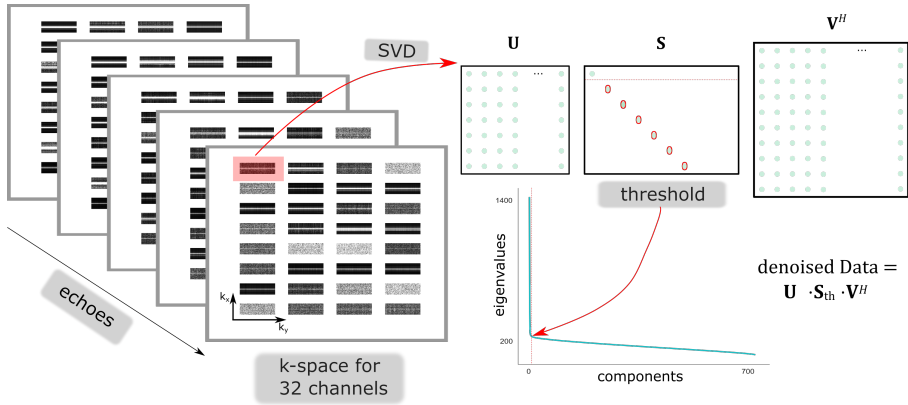
variance.

Figure 4.1: NORDIC implementation for multi-echo line-scan data, based on [319]. Line-scanning k-space data for every channel and echo separately were decomposed through singular value decomposition (SVD); the diagonal matrices containing the eigenvalues (**S**) were thresholded through the elbow (red arrow) of the scree plot depicting the eigenvalues versus the components.

4.2.4 Prospective motion correction

For the motion correction section, we combined line-scanning with prospective motion correction (PMC) using an interleaved scanning architecture (MISS, Philips) following [326]. We inserted a navigator at every dynamic (i.e. every 440 time-points = ~46 s) (Figure 4.2), as a trade-off between motion tracking and the resulting navigator-introduced signal transients in the time series (see below). Following every navigator acquisition, the navigator was reconstructed and registered to the previous one in the series in real-time.

The field of view (FOV) of both the navigator and target sequence was updated based on the estimated translation and rotation parameters (1s waiting time). The required time gap in the line-scanning acquisition for recording and real-time processing of the PMC navigator introduces a consistent transient signal due to the temporary loss of the steady-state of the transversal magnetization. This is observed as a T_1-driven return to steady-state, here dubbed 'T_1-transient'.

Three possible navigators were compared (Table 4.2): a highly-accelerated surface-coil-receive fat-navigator only covering the back of the head (surf fat-nav), a slower whole-head, transmit-coil-receive fat-navigator (vol fat-nav) and a surface-coil-receive water-excitation navigator (surf wat-nav), used to reduce the amplitude of the T_1-transient signal. The order of acquisitions was randomized across participants.
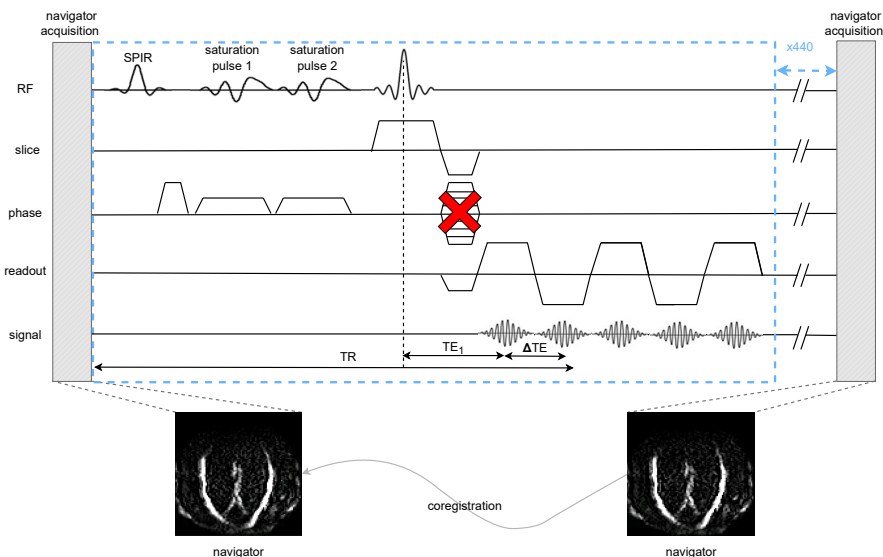
Figure 4.2: Sequence diagram for prospective motion correction.

Acquisition	surf wat-nav	vol fat-nav	surf fat-nav
sequence	3D EPI	3D EPI	3D EPI
excitation	water selective	fat selective	fat selective
TR [ms]	13	18	18
TE [ms]	3.5	5.1	4.1
FA [deg]	8	1	1
resolution [mm]	2 iso	2.5x3.12x2.5	2 iso
SENSE factor	4x1.1	1	4x1.1
duration/dyn [s]	0.546	1.7	0.751
receiver coils	surface, 32ch	transmit, 2ch	surface, 32ch

Table 4.2: Scan parameters of the interleaved navigators scans for the prospective motion correction during line-scanning acquisition, using the interleaved scanning architecture (MISS).

We acquired one run of functional data (6 min 20 s) using the 5-echo acquisition and the same visual task described above. For each scan, we applied the NORDIC-denoising step in the reconstruction of the data.

We investigated three ways of managing the gaps and T_1-transient:

1. Regressing out the T_1-transient during the GLM analysis (regressed): 30 points around every T_1-transient of each timecourse were averaged and fitted to an

exponential decay ($a - be^{-cx}$). Each voxel timecourse was then submitted to the T_1-transient regression in the GLM analysis;

2. Interpolating the points corresponding to the T_1-transient by substituting 30 point in correspondence of the T_1-transient with the average of the 10 points after it (imputed);

3. Analyzing the T_2* estimates which are implicitly non-sensitive to baseline T_1 effects (T_2*PMC fit);

The time points during which the navigators were acquired and the following pause were removed from the GLM's regressors that model the visual task.

We evaluated the t-stats and tSNR values along the line, to find the optimal acquisition and analysis strategy. Specifically, for our group comparison, we plotted the tSNR evaluated from the whole timecourse following the dummy acquisition, and the mean t-stats along the line for all the participants, for all the different ways of managing the T_1-transient and for every PMC navigator method. We compared those results using an ANOVA test, to check if the imputed data showed a significant improvement compared to the other methods and the echo combined data (raw).

The navigator method allows for motion measurements. Pilot experiments on four participants with different navigator acquisitions and length of the scans showed average frame wise displacement of ~0.2 mm. This results in motion patterns that are well within the range that can be corrected for using fat navigator-based motion correction [326, 331].

4.2.5 Comparison of denoised multi-echo with single-echo line-scanning

In the very last section, for one participant only, we acquired a functional scan with the same functional task as in section 4.2 to demonstrate the improvements we made to our previous implementation of line-scanning [306]. Here, we compared the single-echo gradient echo line-scanning sequence from Raimondo et al. and the 5-echo multi-echo version with SoS echo combination and NORDIC-denoising in terms of t-stats.

4.3 Results

4.3.1 Multi-echo acquisition and echo combination approach

Figure 4.3 shows a multi-echo line-scanning dataset for a representative participant: the position of the slice (4.3a), the placement of the saturation slabs (4.3b), the line signal distribution image (4.3c) and finally, an example of multi-echo line-scanning acquisition (for a 5-echo acquisition), for every echo separately (4.3d) and for the combined version (through SoS) (4.3e). Note the decreasing signal intensity with increasing TE in consecutive echoes.
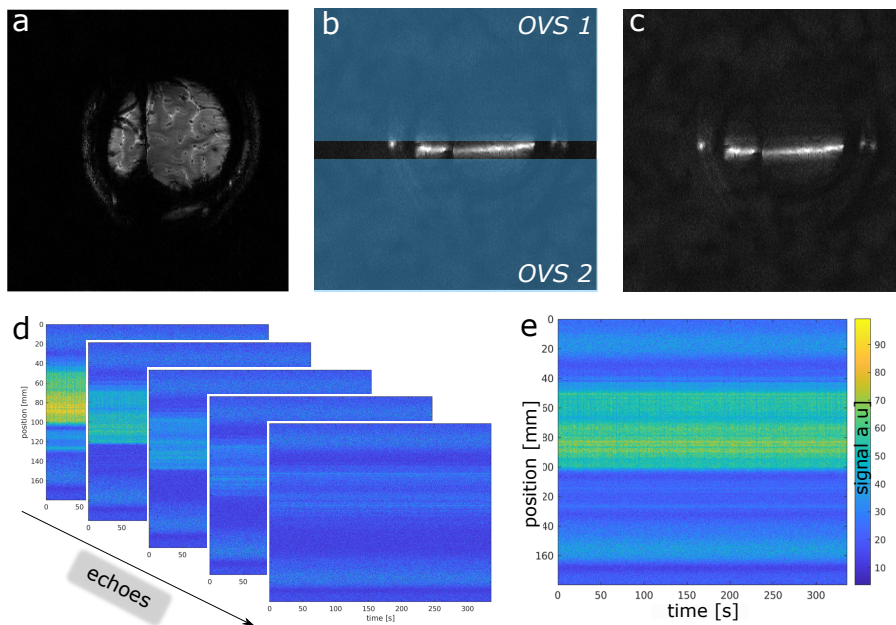
Figure 4.3: (a) Accompanying 2D reference slice before 1D line-scanning and (b) outer volume suppression (OVS): placement of saturation slabs to suppress unwanted signal outside the line of interest, depicted by the gap (4 mm) between the saturation slabs. (c) line signal distribution image, (d) example of multi-echo line-scanning acquisition (position of the voxels vs time) for every echo separately (5 echoes acquisition) and (e) resulting line-scan data after multi-echo combination.

We evaluated t-stats for every acquisition and echo combination method, and we averaged the maximum t-stat across participants (Figure 4.4a) and the mean value of t-stats in the 11-voxel gray matter (GM) ROI centered on that maximum (Figure 4.4b). As the echo combination methods used the same data, the variance was higher between acquisition types than between echo combination methods. There were no statistically significant differences for different numbers of acquired echoes, though visual inspection showed higher t-stats, both mean and peak, for the 5-echo acquisition.

We found significantly higher maximum and mean t-stats for SoS and wtSNR echo combination compared to the T_2^* fit method (Student t-test, $p < 0.05$). Regarding the tSNR (evaluated across the whole timecourse), we averaged the values of two different ROIs: GM ROI and white matter (WM) ROI (Figure 4.4c and d, respectively). In both ROIs, the SoS echo combination gave slightly higher tSNR compared to the other two methods. Considering that the second acquisition (5-echo) led to the highest mean and maximum t-stats across groups, we used this approach for the rest of the comparisons. For the reconstruction, we selected the SoS because of the slightly higher tSNR and ease of implementation.
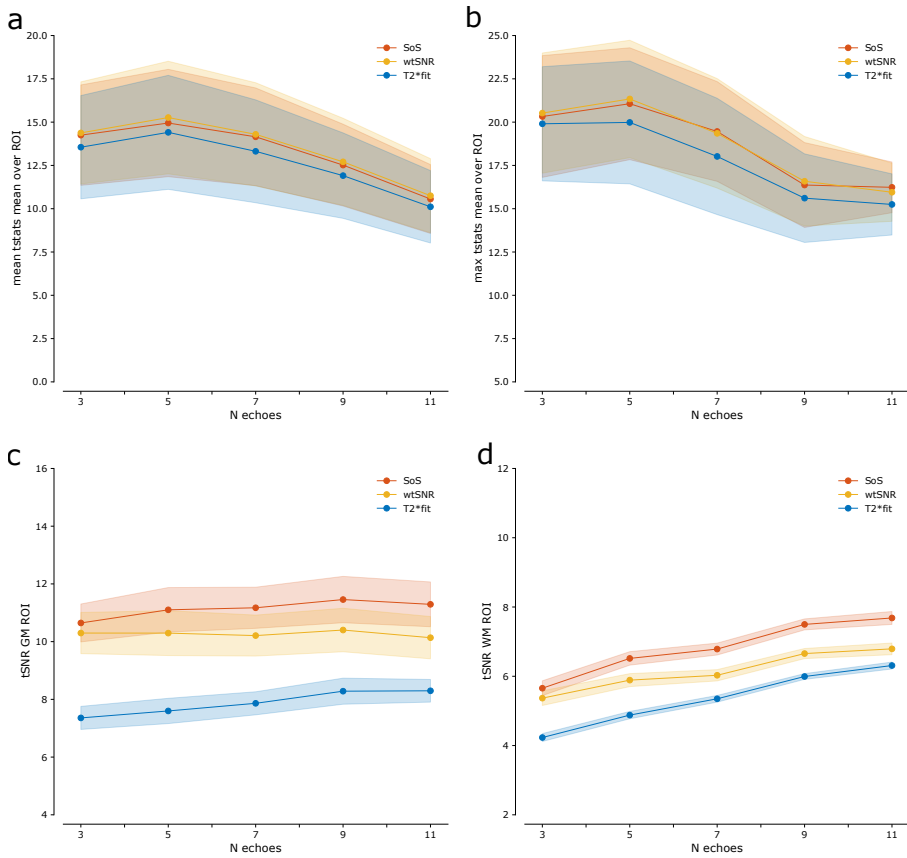
Figure 4.4: (a) mean value of t-stats within the GM ROI for every multi-echo (N echoes) line-scanning acquisition, averaged across participants; Shaded areas correspond to the standard error over participants. (b) maximum value of t-stats within the ROI, averaged across participants; (c) mean tSNR within a GM ROI for every acquisition, averaged across participants; (d) mean tSNR within a WM ROI for every acquisition, averaged across participants. We found significantly higher max and mean t-stats for SoS and wtSNR echo combination compared to the T_2^* fit method. The SoS echo combination gives slightly higher tSNR compared to the other two methods. The 5 echoes acquisition led to the highest mean and maximum t-stats.

4.3.2 NORDIC denoising for multi-echo line-scanning

In Figure 4.5, the comparison of line-scanning data without (a) ('Standard') and with (b) ('NORDIC') denoising are shown for one exemplar participant. Note that the signal found outside the brain (i.e. mostly resulting from thermal noise) was notably reduced after NORDIC denoising. The BOLD response to the visual task was preserved after NORDIC, as demonstrated for a single voxel time course in Figure 4.5c. NORDIC notably improves tSNR and the distribution of t-stats (Figure 4.5d and 4.5e, respectively). A scatter plot (Figure 4.5f) of the t-stats shown in Figure 4.5e, showed that the voxels with positive t-stats became more positive; they are found above the unity line on the positive x-axis (black line, Figure 4.5f). There are very few voxels for which the absolute t-stat became smaller. The effect

of denoising was highly consistent: in every individual participant, we saw a substantial improvement in both t-stats and tSNR by at least, 200%. Table 4.3 showed the group average of tSNR mean, t-stats mean and t-stats maximum, within an 11 voxel ROI surrounding the voxel showing the highest t-stats.
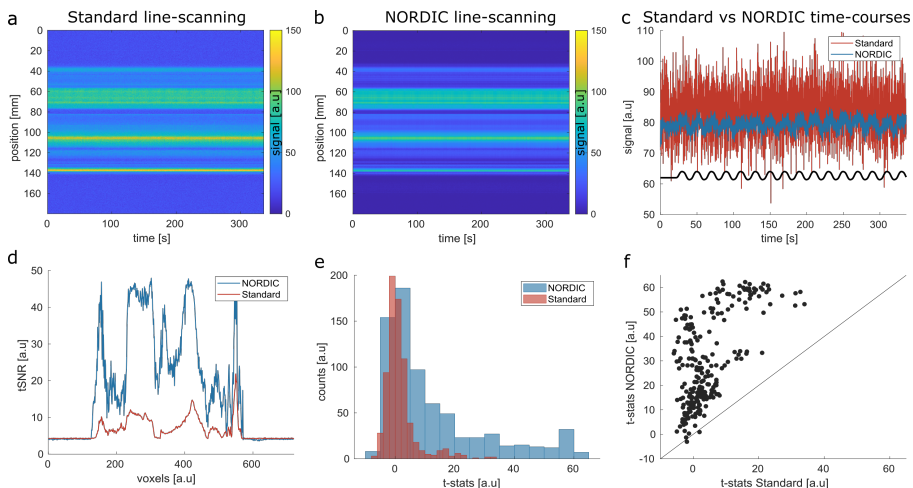
Figure 4.5: (a) Standard line-scanning fMRI data, (b) NORDIC denoised line-scanning fMRI data after noise removal, (c) single voxel timecourse for standard line-scanning data (red line) and NORDIC-denoised data (blue line), together with the GLM model following the visual task, (d) tSNR comparison of the standard line-scanning data (red line) and the NORDIC-denoised data (blue line), (e) t-stats distributions for the standard data (red) and for the NORDIC denoised data (blue), and (f) scatter plot of standard t-stats and NORDIC-denoised t-stats for one representative participant. The black line indicates the unity line. NORDIC denoising notably improves tSNR and increases the t-stats upon a visual task. The BOLD response to the visual task is preserved after NORDIC, while NORDIC notably improves tSNR and t-stats distribution.

	Standard line-scanning			NORDIC line-scanning		
	tSNR mean	t-stats mean	t-stats max	tSNR mean	t-stats mean	t-stats max
sub1	13	6	8	46	17	18
sub2	11	7	9	43	56	62
sub3	17	14	20	55	34	36
sub4	10	4	11	29	17	31
Mean±se	13±1	8±2	12±2	43±5	31±8	37±8

Table 4.3: Comparing NORDIC denoising to non-denoised (standard) line-scanning in terms of tSNR and t-stats upon a visual task, group results: average tSNR mean, mean t-stats and maximum t-stats in the 11 voxels ROI; mean and standard error over participants. We observe that NORDIC denoising improves tSNR and t-stats by >200% for line-scanning.

4.3.3 Prospective motion correction using water and fat excitation navigators

Figure 4.6a, b and c showed for a single voxel the raw data timecourse for the three acquisitions; surf wat-nav, vol fat-nav, and surf wat-nav. The T_1-transient signal

due to the time needed for navigator coregistration and acquisition update is highlighted in Figure 4.6a. The selected single voxel was at the same nominal location in the brain in an area with large task-driven responses. Note that the faster, more undersampled, navigators (surf wat-nav and surf fat-nav) resulted in reduced T_1-transient signal amplitude due to the shorter acquisition gap. The utilization of water excitation for the navigators reduced the T_1-transient signal amplitude even further. The regressed, imputed and T_2*PMC fit corrected data are shown in Figure 4.6d, e and f. For this particular voxel, BOLD responses were visible in all timecourses, despite the T_1-transient. For all acquisitions, the T_1-transient signal was much reduced after this GLM-based signal regression and completely disappeared in T_2*PMC fit corrected data. T_2*PMC fit data is plotted separately as the resulting T_2* time course has physical units in ms.
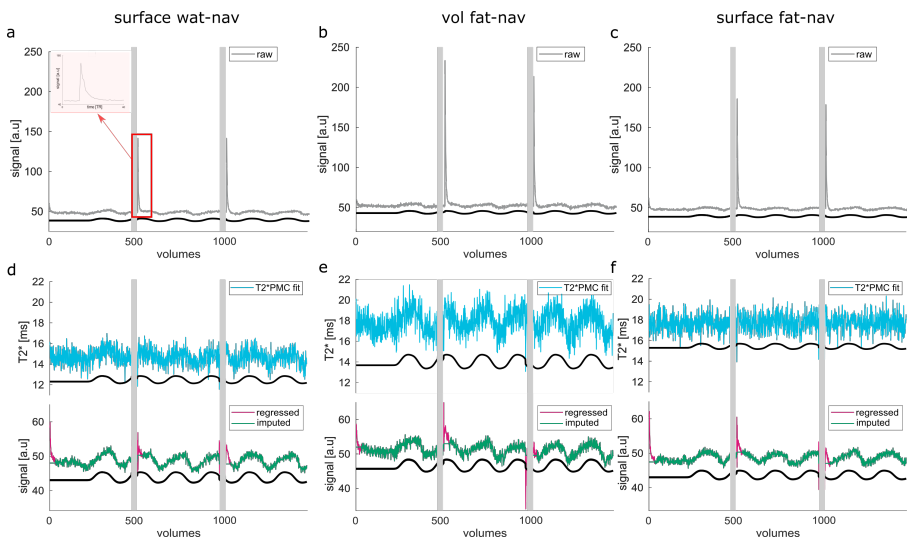
4

Figure 4.6: (a,b,c) single voxel timecourse (first 139 seconds) for an example participant, for the three PMC approaches, for raw data (grey line) and (d,e,f) T_2*PMC fit data (light blue line), regressed (red line) and imputed data around the T_1-transient (green line). The black curves depict the visual task for every time course, while the gray bars indicate the time during which the navigators were acquired. The inset in (a) highlights a region where the T_1-transient effect is visible. This is caused by the required time gap in the line-scan acquisition for the PMC navigator and introduces a consistent transient signal due to the temporary loss of steady-state of the transversal magnetization. surf wat-nav and surf fat-nav result in reduced T_1-transient signal amplitude. BOLD responses are visible in all timecourses, despite the T_1-transient. The T_1-transient signal appearance is much reduced after GLM-based signal regression (regressed) and completely disappears in T_2*PMC fit corrected data.

Figure 4.7 showed box plots for the mean tSNR across participants, evaluated on the whole timecourse, across the whole line, for the PMC-induced T_1-transient correction approaches. With each correction approach displayed separately: (a) the water navigators acquired with surface coils (surf wat-nav), (b) the fat navigators acquired with the transmit coils (vol fat-nav) and (c) the fat navigators acquired with surface coils (surf fat-nav).

Figure 4.8 showed the box plots for the mean t-stats across participants across the

whole line, for the PMC-induced T_1-transient correction approaches. As seen in Figure 4.6, the navigators acquired with surface coils (surf wat-nav and surf fat-nav) offered slightly higher tSNR (Figure 4.7) and t-stats (Figure 4.8) compared to the navigators acquired with the transmit coil (vol fat-nav).
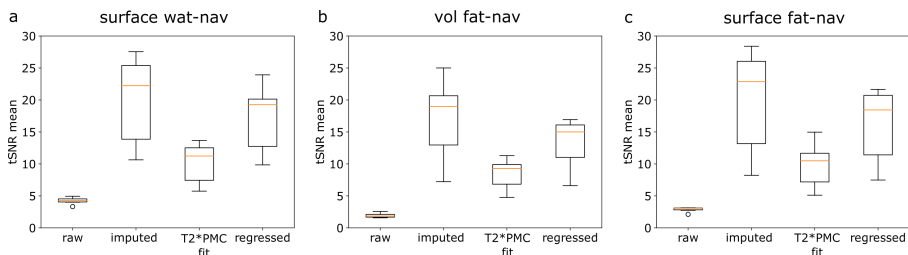

Figure 4.7: box plots showing the mean tSNR across participants, evaluated on the 20 s time baseline, across the whole line, for the PMC-induced T_1-transient correction approaches: (a) the water navigators acquired with surface coils (surf wat-nav), (b) the fat navigators acquired with the transmit coils (vol fat-nav) and (c) the fat navigators acquired with surface coils (surf fat-nav). The boxes extend from the first quartile (Q1) to the third quartile (Q3) of the data, with the orange line at the median. The whiskers extend from the box by 1.5 times the inter-quartile. Higher tSNR values are reached when surf wat-nav and surf fat-nav are used, and particularly when the imputed method is applied.
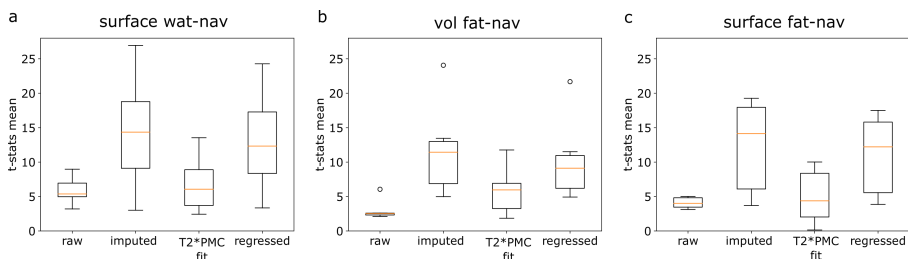

Figure 4.8: box plots showing the mean t-stats across participants, across the whole line, for the PMC-induced T_1-transient correction approaches: (a) the water navigators acquired with surface coils (surf wat-nav), (b) the fat navigators acquired with the transmit coils (vol fat-nav) and (c) the fat navigators acquired with surface coils (surf fat-nav). The boxes extend from the first quartile (Q1) to the third quartile (Q3) of the data, with the orange line at the median. The whiskers extend from the box by 1.5 times the inter-quartile range and the dot indicates an outlier. Higher t-stats values are reached when surf wat-nav and surf fat-nav are used, and particularly when the imputed method is applied.

Analysis of variance (ANOVA) test was used to assess whether one of the ways of dealing with the T_1-transient showed a significant improvement in either t-stats or tSNR compared to the other two and raw data. We found significant effects on t-stats for the surf wat-nav ($F_{3,15} = 7.4$, p = 0.03), vol fat-nav ($F_{3,15} = 12.8$, p = 0.01), and surf fat-nav ($F_{3,15} = 9.3$, p = 0.01). Using a pairwise post-hoc T-test, we found no significant contrasts.

Regarding the tSNR we found $F_{3,15} = 26.7$, p = 0.003 for surf wat-nav, $F_{3,15} = 31.9$, p = 0.002 for vol fat-nav and $F_{3,15} = 25.2$, p = 0.004 for surf fat-nav. The post-hoc T-test showed that the imputed and regressed methods resulted in higher tSNR values compared to the T_2*PMC fit method, as well as raw data, for every navigator acquisition strategy.

4.3.4 Comparison of denoised multi-echo line-scanning with previous single-echo line-scanning

As a final comparison, in Figure 4.9 we showed the line-scanning data acquired with single-echo (a), NORDIC-denoised multi-echo (b) as well as a single voxel timecourse for both acquisitions (c).
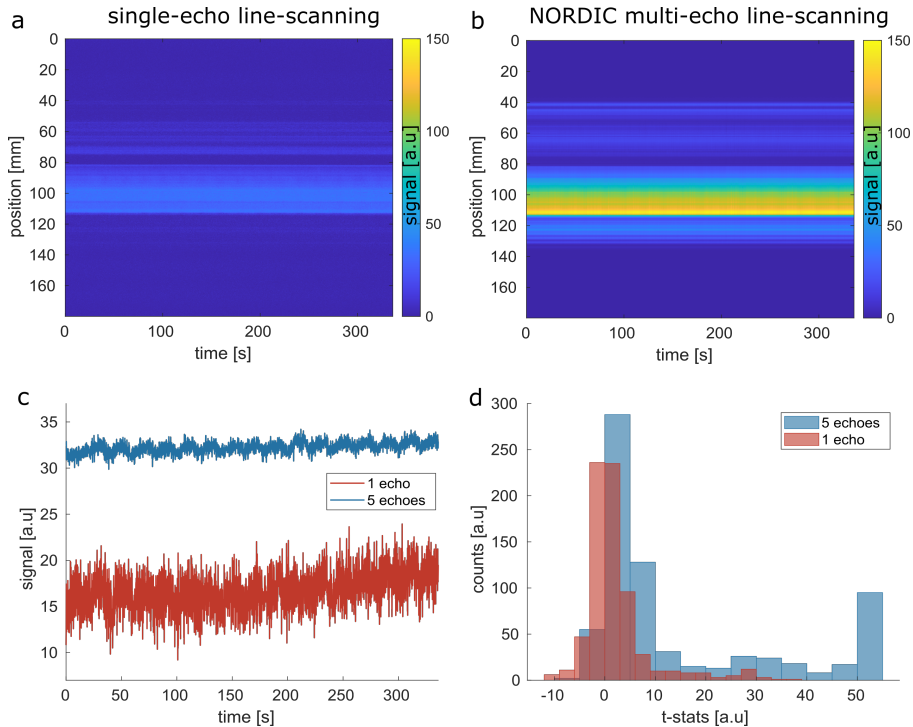

Figure 4.9: (a) Single-echo line-scanning fMRI data implemented in Raimondo et al [306], (b) NORDIC-denoised multi-echo line-scanning fMRI data (c) single voxel timecourse for single-echo line-scanning data (red line) and NORDIC-denoised multi-echo data (blue line), and (d) t-stats distributions for the single-echo data (red) and for the NORDIC denoised multi-echo data (blue). Substantial improvements in signal quality (tSNR single-echo = 4.0, tSNR NORDIC denoised multi-echo = 36.2; averaged across the line) and t-stats (t-stats single-echo = 3.8, t-stats NORDIC denoised multi-echo = 25.1; averaged across the line) upon a visual task is demonstrated for the NORDIC denoised multi-echo line-scanning.

We observed an increase in signal intensity when multi-echo data are acquired, compared to the single-echo acquisition, and a significant decrease of noise in the multi-echo denoised single voxel timecourse, as demonstrated from the averaged tSNR along the line, of 4.0 for the single-echo line-scanning and 36.2 for NORDIC-denoised multi-echo. Moreover, from Figure 4.9d where t-stats distributions are shown, we observed an improvement in t-stats when multi-echo NORDIC-denoised data are used. On average, across the line, a mean t-stats value of 3.8±8.4 (mean ± standard deviation) was found for single-echo line-scanning, and 25.1±20.5 for NORDIC-denoised multi-echo line-scanning.

4.4 Discussion

Line-scanning fMRI is a novel technique for high spatiotemporal resolution fMRI in humans with multiple potential applications such as cognitive neuroscience, including layer and columnar imaging, but also clinical studies on, for instance, small vessel disease. Here, we report on three improvements to our first implementation of line-scanning [306] to increase the sensitivity and flexibility of line-scanning and mitigate the effects of motion: 1) multi-echo acquisitions, 2) NORDIC denoising and 3) real-time motion correction using interleaved navigators.

Multi-echo fMRI is known to increase SNR and BOLD contrast-to-noise ratio (CNR) and decrease sensitivity to physiological noise [171, 172]. We found that a scheme with 5 echoes showed the highest sensitivity. This is likely the result of the known interplay between SNR (and tSNR) and TE-dependent BOLD CNR as reflected by the higher t-stats from the visual task. Other multi-echo studies have also opted for 5 echoes [172, 332], suggesting that this number of echoes is a suitable balance between exploiting the power of the multiple echo acquisition (in terms of T_2^* range broadening) while maximizing the readout length without too much time spent in the risetime of the readout gradients. Further increasing the number of echoes in the same readout-time pushed the first echo to earlier echo times, resulting in the highest tSNR for 9 echoes, albeit with reduced CNR (t-stats) compared to the other multi-echo schemes, possibly due to the increased gradient ramp time.

The tSNR weighted echo combination approach (wtSNR) showed a similar behavior of tSNR profile with increasing echoes compared to SoS (Figure 4.4c). The T_2^* fit echo combination approach consistently showed reduced t-stats and tSNR, reflecting the challenges of obtaining a good T_2^* fit while retaining the necessary bandwidth for our current spatiotemporal resolution. Note that the tSNR increase with respect to the increasing number of echoes appears larger in WM rather than the GM ROI (Figure 4.4d). WM is known to contain less physiological noise than GM [312], so the larger tSNR increase likely reflects a reduction in the contribution of thermal noise.

Regarding the echo combination methods, we investigated three echo combination strategies. Note that many other combination approaches exist, some of which might exploit the benefit of multi-echo acquisitions better [176, 333], though most do not solve the T_1-transient that we have to deal with in the motion-corrected data.

To further optimize line-scanning, we aimed to reduce thermal noise by adapting NORDIC denoising for multi-echo line-scanning [319]. High spatial resolution line-scanning data is likely dominated by thermal noise, as opposed to physiological noise. We observed that most of the principal components (99.7%, on average across participants) after SVD were removed from the data, suggesting that thermal noise is indeed dominant and needs to be removed. T-stats increased after denoising, with respect to the standard reconstruction (no denoising), for every participant. The "hard-thresholding" we used in the adapted NORDIC denoising is very liberal (due to the large number of components removed from the data), hence, as

for any denoising techniques, one should be wary of potential biases that can be introduced [319, 334]. This is particularly important when less strong stimuli (leading to smaller responses) are used. In these cases, other thresholding approaches can be adopted (such as approaches involving noise scans or g-factor maps when parallel imaging is used, or approaches involving cross-validation [335] to evaluate a threshold that allows removing specific noise sources while retaining signal components.

Importantly, besides the t-stats, the tSNR also strongly improved when NORDIC-denoising was applied, in agreement with the findings of [319]. Note that line-scanning presents some analogies with electroencephalography (EEG) data; both have a one-dimensional nature, high noise levels, and temporal resolution in the order of ms. This suggests that denoising methods used in EEG could also be investigated for line-scanning. Specifically, some non-linear approaches [336, 337], as well as ICA-based methods, particularly on short-time Fourier transforms of EEG signals [338], appear to efficiently denoise EEG data.

Line-scanning data are by definition 1D fMRI recordings in the spatial domain. The 1D nature renders line-scanning more susceptible to motion compared to standard fMRI, which is exacerbated by the fact that volume coregistration cannot be applied as a post-hoc correction method. Moreover, if motion occurs during the functional line-scanning acquisition, any drift out of the selected FOV is impossible to detect and fix. Here, we implemented a motion correction procedure using interleaved large FOV navigators to track and correct the acquisition in real-time, albeit at the temporary loss of both fMRI samples and the signal steady-state, which induces a consistent T_1-transient signal warranting the reported correction schemes. We employed three different navigators: two surface coil navigators (surf wat/fat-nav), which have the advantage of being faster due to the possibility of strong SENSE acceleration by parallel imaging, at the cost of brain coverage and possibly reduced coregistration quality, and one transmit coil navigator (vol wat/fat-nav), which was much slower (2-3 times slower than surface coils navigators), but whole brain movements could be tracked, favoring the coregistration. The T_1-transient on the timecourse can be minimized by reducing the navigator acquisition time, i.e. by employing high-undersampling afforded by dense surface receive arrays. Surface-array-recorded navigators (surf wat/fat-nav) provided large gains in t-stats and tSNR compared to a whole-head but slower navigator (vol wat/fat-nav), acquired with the transmit coil. Using water excitation rather than a fat-based excitation navigator leads to lower T_1-transient amplitudes, as the excitation of the navigator counteracts the T_1-driven magnetization recovery. Note that the water-based navigator images are less sparse than fat images, resulting in potentially increased SENSE artifacts. However, our current undersampling factor of four in an array of 32 receive coils, did not prove to be problematic. In terms of signal analysis, large gaps and a T_1-transient signal are introduced to the timecourse. From the analysis of all participants, we found that a simple interpolation of the points corresponding to the T_1-transient was the optimal option for managing the issue, in terms of both tSNR and t-stats. Even though the interpolation method

is the simplest, it completely removes the T_1-transient distortions, (unlike our regression method, which only reduces the T_1-transient signal), hence enhancing both the tSNR and t-stats. The T_2*PMC fit method yielded noisy timecourses and, while the T_1-transient signal is fully eliminated, it does not fulfil the requirement of high tSNR. A more sophisticated regression might bring the results closer to the imputed data quality while retaining more of the original timecourse. However, the limited tSNR of linescan acquisitions and the sharp peak of the T_1-transients to be removed would complicate such regressions.

We already acknowledged that the presence of the T_1-transient is a limiting factor in the motion-corrected data, but it is a great tool when scanning specific groups, such as patients, young adults and non-trained participants (i.e. participants that are completely naive to scanning), as well as to validate the sensitivity of the method to motion. In general, considering the necessary pause for navigator acquisition and the resulting T_1-transient effect to perform PMC, we recommend using image-based prospective motion correction only when non-trained participants are involved. Highly trained participants are capable of staying still within 250 μm for remarkably long periods of time [339], if necessary supported externally, such as through head fixation.

From our last comparison, on a single participant, we observed a substantial improvement in data quality and obtained functional responses for NORDIC denoised multi-echo line-scanning compared to the original single-echo line-scanning [306], in terms of both t-stats and tSNR. The NORDIC-denoising proved to be a great tool for decreasing thermal noise, while the use of multi-echo data per se offers an increase in MR signal and more freedom in the processing of the data, such as different possibilities of echo combination strategies or physiological noise regression. We decided not to add the PMC in the comparison with the single-echo line-scanning version to avoid the T_1-transient, which would bias the comparison.

The presented improvements are relatively straightforward ways to increase the data quality and make line-scanning fMRI more generalizable and open for new neuroscientific questions, as well as possible clinical research. Specifically, with a double session approach we would aim for a subject-specific line planning, in order to investigate the hemodynamic responses function across cortical depth in patients with small vessel and sickle cell diseases, compared to healthy participants [286, 307–309].

4.5 Conclusion

Line-scanning is a powerful fMRI technique to detect BOLD responses at ultra-high spatial and temporal resolutions. Here, we added multi-echo readouts, NORDIC denoising, and real-time motion correction. We suggest a 5-echo multi-echo acquisition with NORDIC-denoising for line-scanning fMRI in the visual cortex. For non-trained participants, we recommend using prospective motion correction and we suggest interpolating the time points corresponding to the T_1-transient time in

order to correct for it. Using multi-echo readouts and NORDIC denoising for line-scanning, we found a substantial increase in tSNR and t-stats upon a visual task compared to the original single-echo line-scanning protocol.

4
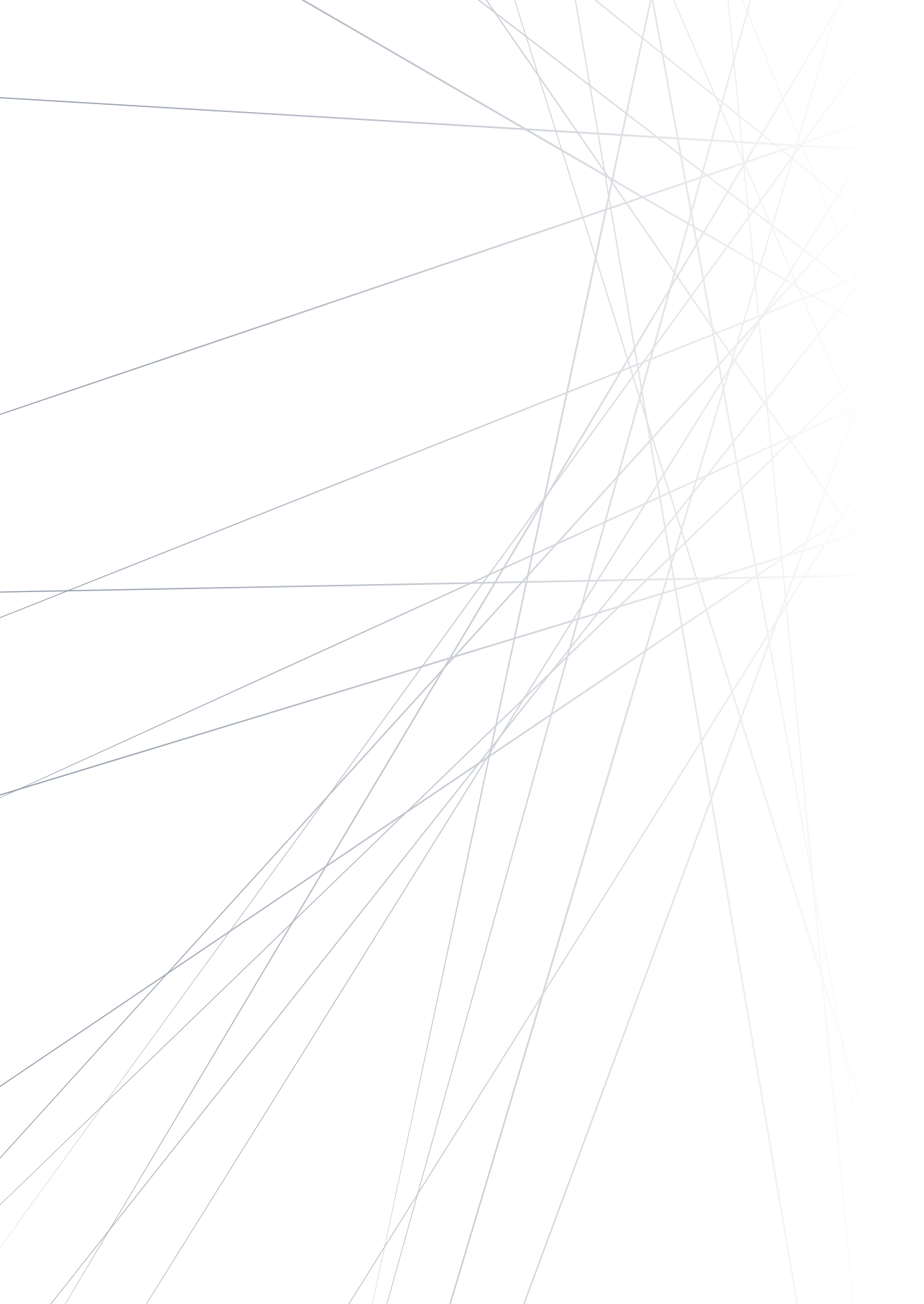
5

TOWARDS FUNCTIONAL SPIN-ECHO BOLD LINE-SCANNING IN HUMANS AT 7T

Luisa Raimondo, Jurjen Heij, Tomas Knapen, Serge O. Dumoulin, Wietske van der Zwaag and Jeroen C.W. Siero

Abstract

Objective: Neurons cluster into sub-millimeter spatial structures and neural activity occurs at millisecond resolutions; hence, ultimately, high spatial and high temporal resolutions are required for functional MRI. In this work, we implemented a spin-echo line-scanning (SELINE) sequence to use in high spatial and temporal resolution fMRI.

Materials and Methods: A line is formed by simply rotating the spin-echo refocusing gradient to a plane perpendicular to the excited slice and by removing the phase-encoding gradient. This technique promises a combination of high spatial and temporal resolution (250 μm, 500 ms) and microvascular specificity of functional responses. We compared SELINE data to a corresponding gradient-echo version (GELINE).

Results: We demonstrate that SELINE showed much-improved line selection (i.e. a sharper line profile) compared to GELINE, albeit at the cost of a significant drop in functional sensitivity.

Discussion: This low functional sensitivity needs to be addressed before SELINE can be applied for neuroscientific purposes.

5

5.1 Introduction

Functional magnetic resonance imaging (fMRI) is a powerful tool in neuroscience to detect brain activity, particularly based on the blood oxygenation level-dependent (BOLD) signal [22]. Neurons cluster into sub-millimeter columnar and laminar structures, and neural activity occurs at millisecond resolution; hence, when investigating brain activation differences across layers, high spatial and high temporal resolution is required. The recently described gradient-echo line-scanning (GELINE) sequence achieved very high resolution in humans [274, 306] across cortical depth (250 μm) and time (~200 ms), by sacrificing volume coverage and resolution along the cortical surface. This method is based on very early MRI experiments [47, 49] and was more recently implemented in rodents [50] and for relaxometry and diffusion MRI in humans [304]. Gradient-echo (GE) BOLD is highly sensitive to changes in the local T_2^* relaxation time and is the most commonly used contrast in fMRI experiments. However, it suffers from non-specific signal contributions from large veins [234, 340, 341]. This is even more problematic when high spatial resolution is involved since confounds caused by signals from non-capillary vessels impact the localizational fidelity of GE BOLD fMRI signal [32, 241]. Hence, more specific functional imaging techniques have recently gained much attention [223, 229, 342–344]. Spin-echo (SE) functional responses are expected to be much better localized to the site of neuronal activation, because of the strong micro-vascular weighting which can be achieved with SE for field strengths larger than 3T [32, 192, 262, 341, 345]. In fact, this technique offers a better localization of the signal coming from the capillaries, particularly at ultra-high magnetic field strength (7T and above) and presents the advantage of furnishing an optimal sensitivity with a single echo readout, due to the little variation in T_2 of gray matter (GM) through the brain (unlike the considerable variation of T_2^*, in case of GE BOLD) [192]. Although spin-echo imaging is long established for fMRI [196, 346, 347], the technique continues to be developed to improve sensitivity and acquisition efficiency [343, 348–352].

The high spatiotemporal resolution reached with line-scanning, when combined with a functional contrast more specific to the microvasculature than GE BOLD, would allow us to isolate microvessel responses and to characterize the distribution of blood flow and laminar fMRI profiles across cortical depth with higher fidelity. Moreover, spin-echo line-scanning (SELINE) offers beam excitation without the need for the outer-volume suppression (OVS) pulses, which are necessary in the case of GELINE and lead to imperfect RF saturation performance, hence poor line boundary definition [47]. SELINE capitalizes on a simple rotation of the plane for the refocusing pulse to a perpendicular plane. This intrinsic characteristic of SELINE allows us to minimise out-of-line signal contributions. Theoretically, it also results in lower specific absorption rate (SAR) limits, because of the absence of OVS pulses, even if SAR restrictions arise due to the presence of a refocusing pulse.

Besides the numerous advantages that SE would give to line-scanning, it also pre-

sents intrinsic problems when combining the formation of a SE with high resolution fMRI. First, the need for a relatively long TE (~50-55 ms) at 7T to match the T_2 of cortical gray matter [353]. This makes it more difficult to keep a short TR for fMRI studies; this aspect is even more important for line-scanning fMRI, which is characterized by a high temporal resolution. Second, the TR is limited by the need to have at least one refocusing radiofrequency pulse in the sequence, which can also reach the power limits (SAR) with very short TRs. Third, SE has an intrinsically lower BOLD sensitivity and tSNR compared to GE (approximately half the BOLD percentage signal change and tSNR for SE compared to GE) [32, 354, 355]. Finally, the signal-to-noise ratio (SNR) of SE is lower than GE, making small voxels more difficult and increasing the required measurement times.

Spin echo lines have been implemented for diffusion-weighted MRI, to show the laminar architecture of the primary somatosensory cortex and primary motor cortex at 250-500 μm spatial resolution [304]. Here, we present our implementation of SELINE for BOLD fMRI in humans at 7T. We compared the performance of SELINE with a GELINE acquisition in terms of temporal signal-to-noise ratio (tSNR), line specificity and BOLD sensitivity. We also guide the reader through specific technical issues we ran into during the implementation of the sequence.

5.2 Methods

We scanned 5 healthy participants at a 7T MRI system (Philips, Netherlands) equipped with a 2 channel transmit, 32 channels receive head coil (Nova Medical, USA) and 1 participant with an 8 channel transmit, 32 channels receive head coil (Nova Medical, USA). In addition, multiple pilots were conducted to optimize the parameters used here (Table 5.1). For pilot studies, we used a sphere phantom or healthy participants.

All participants provided written informed consent before participating, and the study was approved by the local ethical committee.

N transmit channels	TR [ms]	TE [ms]	FA [deg]	BW [Hz/pixel]	fat suppression
2	500	50	146	28.89	SPAIR
8	300	40	148	28.95	SPIR
8	200	50	154	28.95	SPIR
8	190	43	154	28.95	SPIR
8	190	40	154	28.95	SPIR
8	355	40	146	28.95	SPAIR
8	500	50	140	28.95	SPAIR

Table 5.1: Sequence parameters for pilot SELINE acquisition. FA = flip angle, BW = bandwidth.

We modified a 2D spin-echo sequence for the SELINE data acquisition (Figure 5.1a). The phase-encoding in the direction perpendicular to the line was turned

off. Other parameters: line resolution 250 µm, TR 500 ms, TE 50 ms, flip angle
146°, array size 720, line thickness 2.5 mm, in-plane line width 5 mm, fat suppres-
sion using the vendor implementration of SPectral Attenuated Inversion Recovery
(SPAIR), adjusting the frequency offset to 250 Hz and bandwidth (BW) to 1000 Hz.
Different 180° refocusing pulse shapes were tested, and the one leading to the best
results in terms of beam selection was a symmetric sinc pulse named 'echo2' in
the vendor software. It has a maximum B_1 of 18 µT and bandwidth-time product
of 4.4. Its slice-selection gradient was moved to the phase-encoding direction to
refocus only a single beam of the excited slice (Figure 5.1b). Note that with "beam
selection" we mean the formation of the line as a result of the intersection between
the excited plane and the refocusing of the perpendicular plane.

Pairs of crusher gradients (strength=25 mT/m, duration=1.9 ms) were added around
the refocusing gradient in every direction to avoid free induction decay (FID) arte-
facts while spoilers (strength=3.3 mT/m, duration=21.6 ms) were introduced at the
end of the sequence to eliminate residual transverse magnetization. The readout
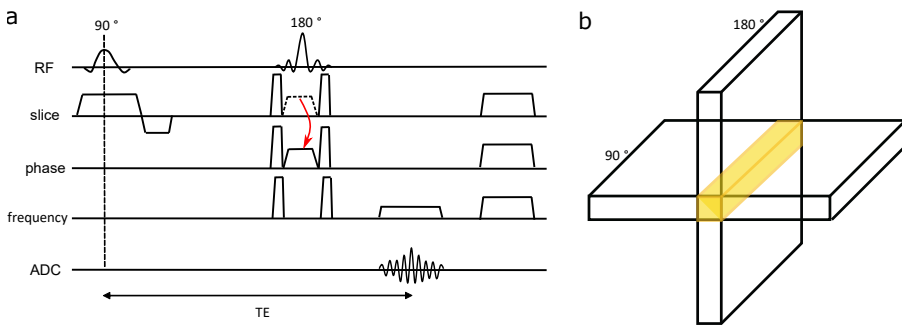was performed with a gradient duration of 19.5 ms and a strength of 2.6 mT/m.

Figure 5.1: (a) SELINE sequence. Note the absence of phase-encoding gradients and the two different orientations of
the 90° and 180° gradients to excite and refocus perpendicular planes. The gradient was moved from the slice-selection
direction to the phase-encoding direction, as indicated by the red arrow. Pairs of crusher gradients were added around
the refocusing gradient in every direction to avoid free induction decay artefacts, while spoilers were introduced at the
end of the sequence to eliminate residual transverse magnetization. (b) Excitation and refocusing of 2 perpendicular
planes, leading to a signal coming from a beam, indicated in yellow.

GELINE data acquisition was based on the method described previously [306].
Briefly, line-scanning data using a modified 2D gradient-echo (GE) sequence, where
the phase-encoding gradients were turned off. Before slice excitation, the signal
outside the line of interest was suppressed through two slab-selective spatial ra-
diofrequency (RF) saturation pulses for outer volume suppression (OVS). The spa-
tial saturation pulses had a pulse duration of 7.16 ms, a pulse flip angle of 97° RF
amplitudes of 4.85 mT and 4.67 mT, respectively, and selection gradients with 0.27
mT/m gradient strength and duration of 7.76 ms. Fat suppression was applied be-
fore the OVS using the vendor implementation of spectral presaturation with in-
version recovery (SPIR), adjusting the frequency offset to 250 Hz and bandwidth
to 1000 Hz. The other parameters were: line resolution of 250 µm, array size 720
points along the line, and line thickness in the 'slice' direction 2.5 mm. The nomi-

nal in-plane line width was 4 mm, flip angle of 16° and TE 22 ms. This TE was used to achieve an optimal GE BOLD contrast. We used a slightly lower TE than the T_2^* of gray matter at 7T [356] to compensate for T_2^*-shortening by B_0 inhomogeneities and to increase the SNR. The readout gradient duration of 22.28 ms and strength of 4.26 mT/m, resulting in a readout bandwidth of 45.4 Hz/pixel. A TR of 500 ms, however, was used here to match that of the SELINE acquisition in terms of temporal resolution and degrees of freedom in the GLM for assessing significant task activation.

Regarding the line position, since GELINE and SELINE are scanned in the same session, it is possible to use exactly the same geometry for both acquisitions. In fact, the slice parameters were copied from one acquisition to the other, while the lines end up in the middle of the slice in both cases (either through the rotation of planes or through the placement of saturation slabs).

SELINE and GELINE data were reconstructed offline using Matlab (Mathworks Inc, USA) and MRecon (Gyrotools, CH). Multi-channel line data were combined with a weighted sum of squares (SoS), based on tSNR and coil sensitivity maps (csm) per channel:

$$S(x) = \frac{\sum_{i=1}^{N_c} w_i(x) * S_i(x)}{\sqrt{\sum_{i=1}^{N_c} |w_i(x)|^2}} \tag{5.1}$$

where S is the MRI signal, Nc is the number of channels of the receive coil (N_c=32), and $w_i(x) = conj(csm) * tSNR(x)$ per coil as the weighting factor. Details for the reconstruction are reported in Raimondo et al. [306]. In addition to the previously described pipeline, we introduced a NORDIC-based denoising step to remove thermal noise prior to the coil combination step [319, 357].

For both acquisitions, the line was positioned perpendicular to the visual cortex as much as possible, considering the restrictions to the geometry, allowing only coronal acquisitions with the line positioned in the center of the slice and 45° angulation away from a coronal plane. The occipital lobe was identified from a low resolution whole brain scan, and a coronal slice covering a portion of visual cortex was scanned. From that slice, a portion of gray matter was selected and the left-to-right oriented line was placed in order to cover that region. Sometimes more than one slice was scanned, in order to make sure that the line intersected a suitably positioned portion of gray matter. The whole planning procedure took around 5 minutes. By design, the line was centered in the middle of the slice for both SELINE and GELINE, hence, in the absence of gross subject motion, further registration of the line to the slice was unnecessary.

We acquired one run of functional data with each protocol, using a block design visual task consisting of an 8Hz flickering checkerboard presented for 10s on/off. Runs lasted 6 minutes and 20 s, starting with a 10 s baseline period. For one subject, 2 GELINE runs and 4 SELINE runs were acquired to further increase the functional SNR, when averaging more runs. Note that we scanned a highly experienced participant when we acquired more runs to make sure that motion was not degrading the data quality; for this reason we did not perform any kind of registration between lines. Functional data were analyzed using a general linear model (GLM)

approach, and t statistical values (t-stats) were evaluated to identify active voxels. We also ran an independent component analysis (ICA) on both GELINE and SE-LINE data. This validation is useful when there is no certainty that the temporal autocorrelation is handled properly [358].

We also calculated the tSNR across the line, as well as in an 11 voxels ROI containing gray matter, through

$$tSNR = \frac{\overline{S(t)}}{\sigma(S(t))} \tag{5.2}$$

where $\overline{S(t)}$ is the mean signal over the whole timecourse, and $\sigma(S(t))$ is the standard deviation of the signal across time for the whole timecourse. For each subject, we acquired a Line Signal Distribution (LSD) image with the same parameters used for the SELINE acquisition but without the removal of the phase-encoding gradient. The LSD image describes the imaged line, hence the line-scanning sequence without the removal of the phase-encoding gradients. Additionally, for one subject, we acquired matched 2D gradient-echo (GE) and SE EPI fMRI at a lower spatiotemporal resolution (1.5 mm isotropic, TR=2.5 s, but with the same TE, and 'coverage' as the line images) to compare functional runs in terms of t-stats of single slices with line scanning fMRI. In addition, we acquired LSD images (with the same parameters) with the same visual task to investigate the effect of line selection on functional sensitivity in both acquisitions.

5.2.1 Design considerations

Here, we summarize minor technical constraints we encountered during the implementation of the sequence:

- Spoiler gradients were added at the end of the TR loop on all 3 gradient axes to avoid phase artifacts in the center of the slice image (see Figure 5.7a and b). Those spoiler gradients of 3.3 mT/m strength and 21.6 ms duration completely eliminated the residual signal after the readout and the associated ripples in the line (Figure 5.7b).

- Pairs of crusher gradients (strength=25 mT/m, duration=1.9 ms) were added around the refocusing pulse, again on all the three gradient axes. These crushers were necessary to eliminate the frees artefacts resulting from the refocusing pulse. Those artefacts are visible as well in the slice image (see Figure 5.8).

- From the pilots reported in Table 5.1, we noted that the 8-channel transmit coil provided more B_1 and offered acceptable fat suppression with SPIR instead of SPAIR, which allowed the use of shorter TRs. However, very short TRs (<350 ms) lead to low signal (Figure 5.10 of the supplementary material). With both 8-channel and 2 channel transmit coils, SPAIR furnished better fat suppression than SPIR. Different excitation flip angles (FA) were also investigated to optimize the SELINE signal. 146° was found to be the best option in terms of B_1 homogeneity and relative SNR, similar to what was suggested by

our simulation in Figure 5.9, evaluated according to Diiokio et al. [359], having the maximum signal intensity for a FA of 142°. We evaluated the optimal excitation flip angle for a given set of TR and T_1 by minimizing the following equation for the spin-echo transverse magnetization:

$$M_{xy} = \frac{\sin\alpha[1 - (\cos\beta)e^{-\frac{TR}{T_1}}) - (1 - \cos\beta)e^{-\frac{TR-TE/2}{T_1}}]}{[1 - \cos\alpha(\cos\beta)e^{-\frac{TR}{T_1}}]} \tag{5.3}$$

With α being the varied excitation angle, TR = 500 ms, TE = 50 ms, T_1 = 2100 ms (for gray matter at 7T), β = 180° (FA of the refocusing pulse).

Overall, a 2 channel transmit acquisition with TR = 500 ms, TE = 50 ms, fat suppression using SPAIR and FA of 146° proved to be the best option, together with the corresponding version with 8 channel transmit. Those sequences were used respectively for the 5 subjects acquisition on the 2 channel transmit, and 1 subject acquisition on 8 channel transmit with additional runs.

5.3   Results

Figure 5.2 shows an example coronal slice (a), the associated LSD image (b), with the signal coming from the intersection of excited and refocused planes, and an example line-scanning acquisition, depicting the evolution of the MR signal for each voxel (position), across time (c).
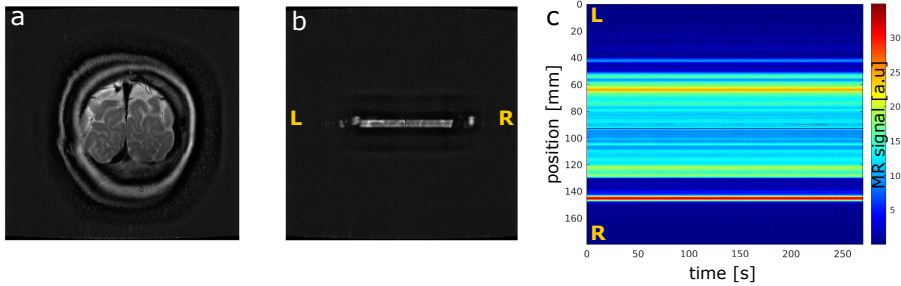
Figure 5.2: (a) acquired slice with spin-echo sequence. (b) LSD image for SELINE acquisition, resulting from the intersection of the excited and refocused planes. L and R indicates the left and right direction respectively. (c) SELINE acquisition, a plot of the MR signal for position and time.

In Figure 5.3a, a representative participant's LSD profile is shown for the SE and GE acquisitions, obtained by averaging over all the voxels in the readout direction of an LSD image. Note the much sharper profile of the SE acquisition compared to the GE version, where the effect of imperfect OVS pulses is clearly visible from the residual signal coming from outside the line. On average, across subjects, we found a full-width-at-half maximum (FWHM) of the LSD profile of (5.5±1.0) mm for SELINE and (9.2±3.2) mm for GELINE.

Figure 5.3b shows the tSNR for line acquisitions with SELINE and GELINE for the

same subject. SELINE tSNR values were consistently lower than GELINE tSNR, likely driven by the TE difference as well as the differences in the line profile. In this plot, we evaluated the tSNR after averaging 2 runs of GELINE and 4 runs of SELINE. Across subjects, we evaluated that tSNR was 2.4 times higher for 1 run of GELINE, compared to 1 run of SELINE, and 4 times higher in the 11 voxels ROI containing gray matter.

Results for all 5 participants scanned with the 2-channel transmit system can be found in Figure 5.11 showing LSD profiles, tSNR values and timecourses for both GE and SE.
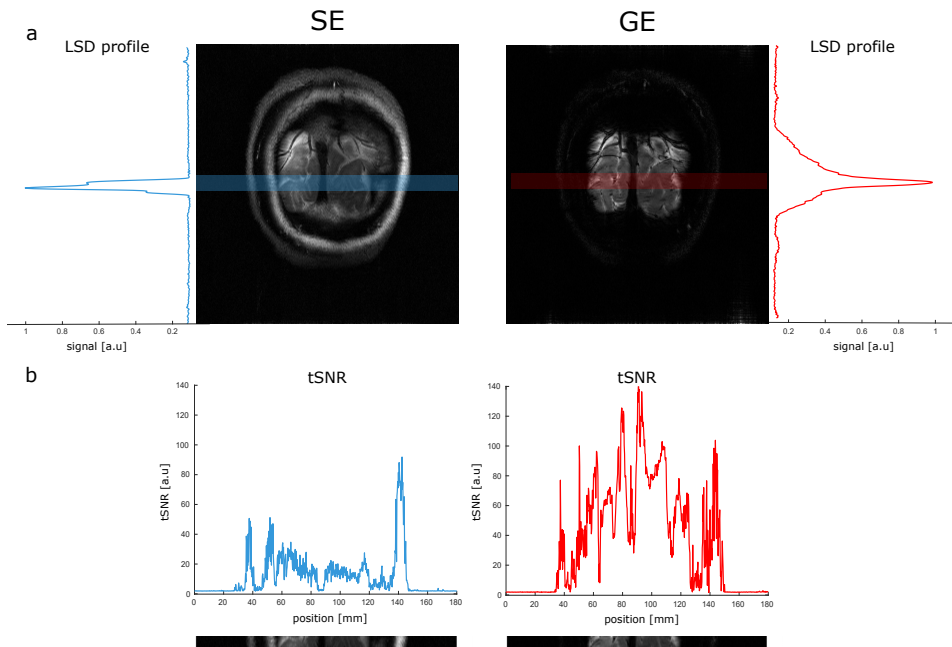
Figure 5.3: (a) normalized LSD profile for spin-echo (blue line) and gradient-echo (red line), plotted perpendicularly to the slice, where the region of the line is highlighted in the blue and red box. Note the improved line definition in SELINE. (b) tSNR for spin-echo line-scanning (blue line) and gradient-echo line-scanning (red line), with the anatomical references at the bottom (spatially matched).

As might be expected from the lower tSNR values, SELINE acquisitions also yielded low functional responses. Figure 5.4 shows the t-stats values obtained from the GLM of 1 run of SELINE (a) and GELINE (b) and for the average of respectively 4 and 2 runs (c and d), overlaid on the acquired slices for SE and GE. While one run of GELINE activation is visible, with relatively high t-stats in the gray matter areas of the line (yellow arrows), even the average of 4 runs of SELINE does not lead to easily detectable responses. Only small responses are visible in the gray matter areas.

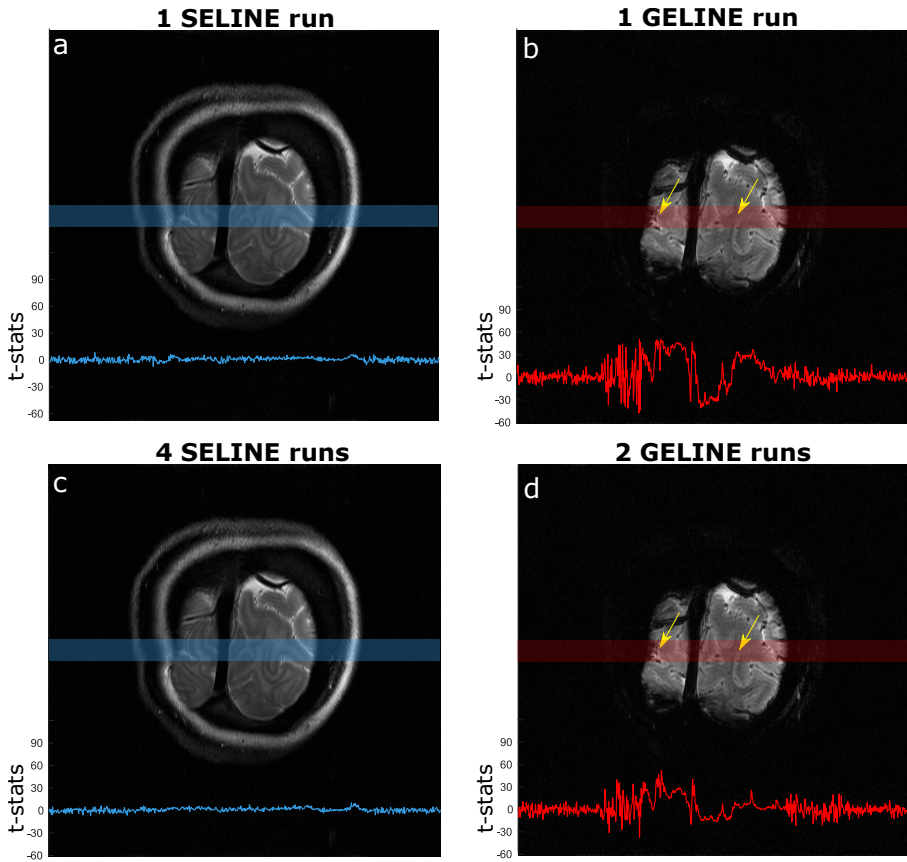**Figure 5.4:** (a) t-stats for 1 SELINE acquisition, (b) 1 GELINE acquisition, (c) 4 runs average SELINE acquisition and (d) 2 runs average GELINE acquisition, overlaid on the acquired slices, for the same representative participant. The light blue and red boxes indicate where the line was positioned, and the yellow arrows highlight gray matter regions.

On average, across subjects, we found that 1 run of GELINE furnished 3.9 times higher mean value of t-stats along the line, compared to 1 run of SELINE.

To investigate the sensitivity differences between the SELINE and GELINE protocols, independent from the line formation, we compared them in a limited resolution image format as well, for both the slices and LSD images. Figure 5.5 shows the activation maps of the SE and GE-EPI slices and the accompanying functional LSD images. The SE-EPI showed solid but lower functional responses than GE-EPI. All functional responses were well within the gray matter areas in both SE-EPI and GE-EPI slice acquisitions. Note the different scales for GE-EPI and SE-EPI t-stats. The difference in functional sensitivity between SE-EPI and GE-EPI appeared to be larger in the LSD images (Figure 5.5c and d). LSD functional images confirmed good line selection in SELINE, but also highlighted the limited available functional signal in SELINE. Note that these voxels were larger than those used in the SELINE

and GELINE acquisitions.

SE-EPI slice   **GE-EPI slice**

SE-EPI LSD   **GE-EPI LSD**
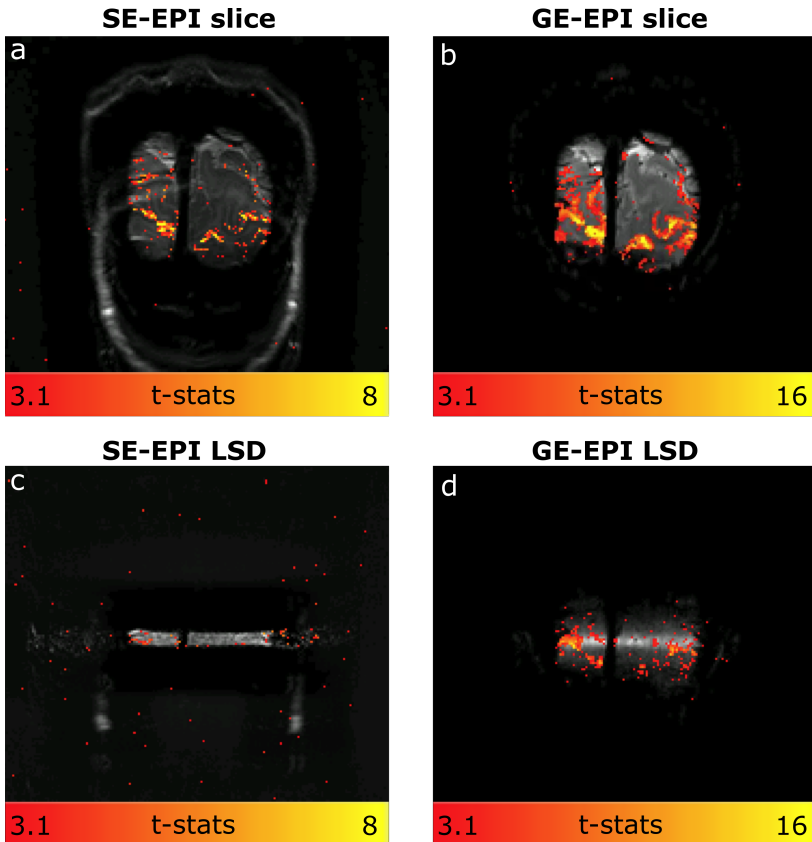
Figure 5.5: (a) t-stats for SE-EPI slice acquisition, (b) GE-EPI slice acquisition (c) SE LSD image acquisition and (d) GE LSD image. The spatial resolution is 1.5mm isotropic in all four acquisitions.

In Figure 5.6 we reported the results of the ICA for a representative participant. In GELINE data (a) the task component is observed in one of the ICA's first components as visible from the timecourse of the component and the power spectra with the peak at the task frequency (0.05 Hz, indicated by the light-blue dashed bar). For SELINE data (b) the task component was never properly detected by the ICA, indicating that the GLM analysis was not influenced by noisy temporal fluctuations.

Figure 5.6: first 5 components of the ICA analysis for GELINE (a) and SELINE (b) acquisition. For each row we represented the spatial profile, the component timecourse, the power spectra and the power spectra zoomed around the task frequency, indicated by the light-blue dashed bar. Note that the y-axis in the component timecourse is scaled differently for each component.

5.4 Discussion

In this paper, we reported the first implementation of SELINE for fMRI in humans at 7T. SELINE showed sharp line definition by rotat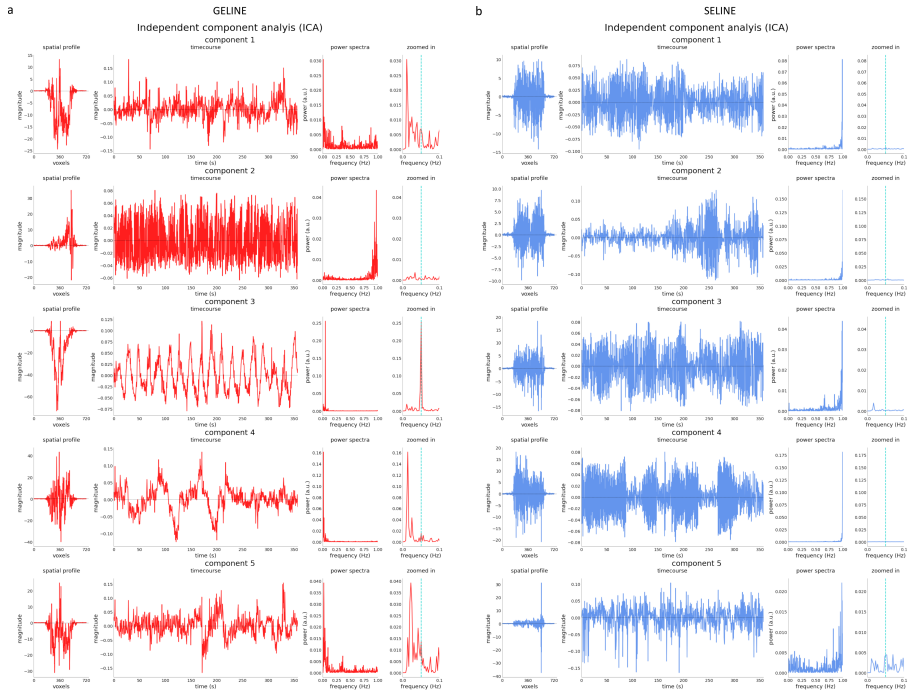ing of the refocusing plane relative to the slice acquisition. In SELINE, the line thickness can be easily adapted by simply changing the refocusing gradient strengths.

To achieve SELINE, we used a sinc-shaped refocusing pulse and an optimized gradient crusher and spoiler scheme to remove the signal from spurious echoes. In the vendor implementation of standard SE imaging, no crushers gradients are included, and FID artefacts are located on the edges of the slice; hence they do not interfere with the actual image being acquired. However, when the phase-encoding gradient is removed, in order to obtain line-scanning data, the artefact signals are concentrated in the line as well. Hence, the crusher gradients were essential for obtaining a clean line signal. Regarding the refocusing pulse shape, the default composite block pulse, used in the standard vendor implementation of SE imaging, resulted in coherence artifacts in the beam. The 'echo2' sinc pulse we chose was also used successfully in SE-EPI based functional acquisitions at 7T [345].

An optimal excitation FA for short TR SELINE was simulated and validated to ob-

tain maximal SELINE signal (Figure 5.9). We assessed the SELINE fMRI performance by comparing it to GELINE fMRI and image-based comparisons to 2D SE and GE EPI.

We found that within the SE LSD image, it was possible to observe anatomical features of the brain; hence the signal in the line was not affected by the line creation through the rotation of refocusing gradient. On the contrary, the OVS pulses used here for GELINE are positioned in close proximity, and result in some signal deterioration within the line, visible from the decrease of the line-selection fidelity (see also [306]). However, the improved line definition for SELINE leads to a smaller area yielding signal and hence lower tSNR and functional sensitivity. This is in addition to the inherently lower sensitivity of SE-BOLD. The combination of these two effects leads to much lower tSNR and t-stats for SELINE than GELINE.

Regarding the BOLD activation, smaller responses are expected in SE-BOLD weighted data [343]. Much work is undertaken to improve SE-based acquisition for functional imaging [343, 348, 350–352]. Here, we used a single-echo acquisition. We could not detect significant task-driven activation in the SELINE, while GELINE consistently showed clear activation patterns in the visual cortex (on average across participants, t-stats were 3.9 times higher for 1 run of GELINE compared to SE-LINE). In the image-based comparison presented in Figure 5.5, SE-EPI images have clearly defined functional responses located within the gray matter, though at lower t-stats values than GE-EPI. Functional activation is barely detectable on the SE-LSD images, while a clear activation is observed in the corresponding GE-EPI LSD functional images. This difference suggests that there is an additional loss in sensitivity in SE-EPI when generating a line rather than exciting and refocusing an entire slice, possible due to the small size of the target line. The data in Figure 5.5 is drawn from a single individual, so it can only show a general trend and is not precise enough to measure effect sizes. Taken into account that the SELINE acquisition has even lower SNR than the SE-EPI LSD due to the smaller voxel volume (1.8 times smaller) and bigger sampling rate (5 times higher), the SELINE acquisition is currently not suitable for fMRI visual experiments.

Note that we do not expect that inflow effects are more prominent in SELINE compare to GELINE. In fact, in GE sequences, inflow effects arise when the blood within an imaged slice is replaced during the TR, hence, here, in 500 ms. In case of SE sequences, the critical time during which unwanted inflow effects can occur is shorter because it corresponds to the time between the excitation and the refocusing pulse (TE/2), which is, here, only 25 ms. For fast flowing blood, the blood will not experience the refocusing pulse and will result in a blood signal reduction effect (wash-out); this is opposite for GE where one will observe a blood signal increase (inflow effect). For this reason, we may expect (if any) inflow artefacts for GELINE rather than for SELINE.

NORDIC denoising could have an effect in removing task-driven signal from the

SELINE data. We also tested unfiltered data and we could not detect any responses due to task either, as visible from Figure 5.12 in the Supplementary material.

Another concern that line-scanning often raises is motion. In general, when using line-scanning, motion can be problematic. Although the multi-run data was acquired in a highly experienced individual, some motion is to be expected over the course of 4 5-minute runs. However, since GELINE and SELINE data were acquired in the same session and the same subjects, we would expect any motion problems to be similar in both acquisitions and hence conclude that motion is not the main cause for the observed differences in SELINE and GELINE. Moreover, the current setup does not allow for motion correction, but a prospective motion correction module could be introduced in future implementations [357].

Another theoretically easy source for improvement would be a change in the geometry of the excited and refocused plane when creating the line. In fact, we decided to excite coronally and refocus axially, not only to match the GELINE and SELINE acquisitions, but also due to experimental limitations which we should overcome to be able to perform SELINE acquisition outside of visual cortex. Being able to excite an axial slice and refocus coronally would lead to less tissue being affected by the refocusing RF, possibly minimizing the FID artefacts mentioned in the "Design considerations".

Finally, the SELINE sensitivity can be improved in future by incorporating a multi-echo readout [360], the use of high-density surface coils [122], as well as using higher field strengths. Massive averaging across runs is a widely employed strategy in neuroscience to improve the SNR and recover activation from specific tasks or low-sensitivity acquisitions [231, 361–365]. For SELINE data, we can speculate that averaging across more than 4 runs would help to improve the sensitivity and recover activation detection, at least with a strong block-design visual task. However, such long acquisition times render the data sensitive to motion, especially so at the line-scanning spatial resolution. Prospective motion correction would allow scanning people for a very long time. However, the current implementation of SELINE does not include prospective motion correction [357]. For this reason, at this stage we cannot provide the reader with an estimate of how long one would need to scan to see activation in SELINE data.

The use of a strongly asymmetric spin-echo optimized for BOLD fMRI might also help to increase the detectability of functional activation [366]. Another approach often used to overcome some of the technical limitations of SE is GRASE [347, 367], which has already been suggested for line-scanning purposes at lower resolution [368]. Moreover, shorter TRs should be properly investigated in order to fully exploit the power of line-scanning, which promises, at the same time, high spatial and temporal resolution. So far, we noticed that fat suppression using SPIR allows shorter TRs, however, SPIR only suppresses fat adequately when an 8-channel transmit coil is used.

5.5   Conclusion

In this study, we presented our first attempts to implement spin-echo line-scanning in humans at 7T. We demonstrated a much-improved line definition compared to the corresponding gradient-echo version at the cost of lower tSNR and BOLD sensitivity. Due to the non-detectability of active voxels in visual cortex after a very strong visual task, we conclude that the implementation of spin-echo line-scanning currently lacks adequate sensitivity for line-scanning fMRI. Still, we argue that spin-echo has a high potential for line-scanning applications due to its innate properties of sharp line selection and the microvascular selective functional contrast. We believe that several improvements can be performed to further develop the current implementation, which can be considered a starting point for future development. We propose multiple directions for improvement: regarding the SNR increase, high-density surface coils array and higher field strengths, as well as averaging across more runs and a more suitable geometry for the excitation and refocusing plane could play a relevant role. Moreover, the sequence could be optimized with a multi-echo readout (GRASE), asymmetric spin-echo for increased SNR and reduced B_1 sensitivity [369, 370], and the addition of prospective motion correction.

5

Supplementary material
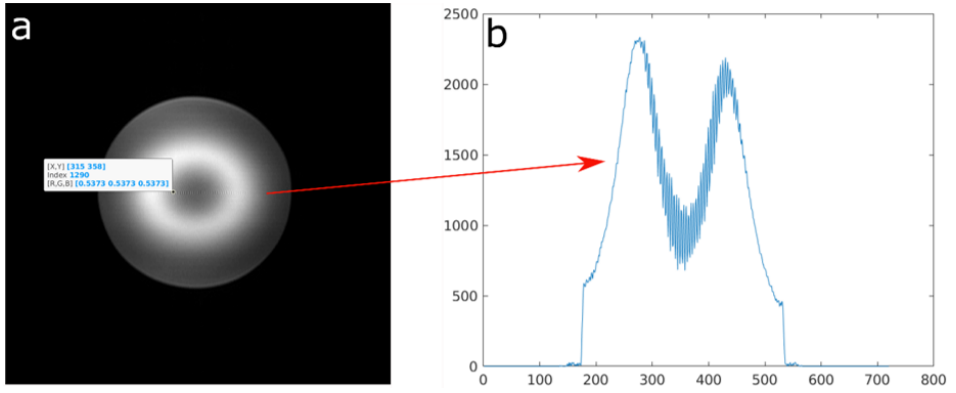
Figure 5.7: Example, on a sphere phantom, of (a) phase artifacts in the slice image and (b) profile of the line artifacts.
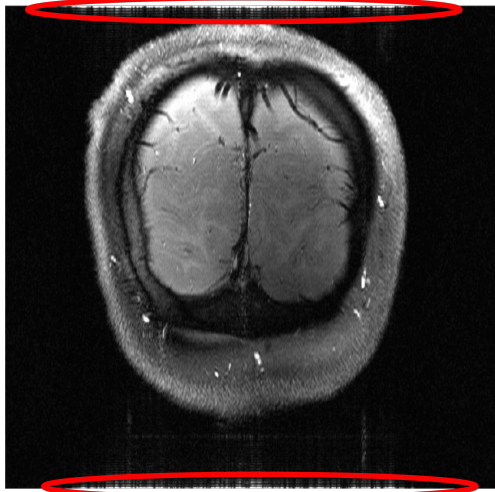
Figure 5.8: Example, on a brain slice, of FID artefacts that would be projected into the line, when the phase encoding gradient is removed. Artefacts are highlighted in the red ellipses.
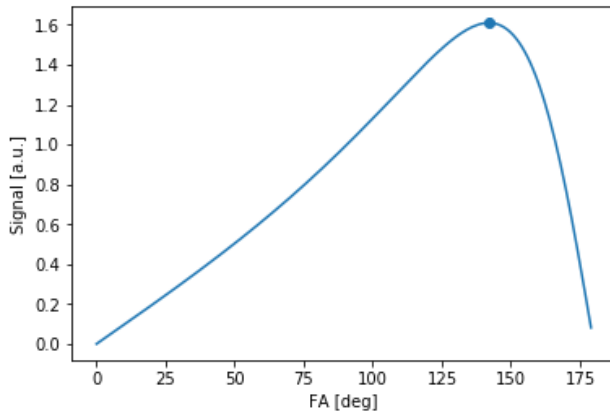
Figure 5.9: Simulation of signal intensity for different flip angles (FA). The maximum signal is obtained for FA = 142°.

5
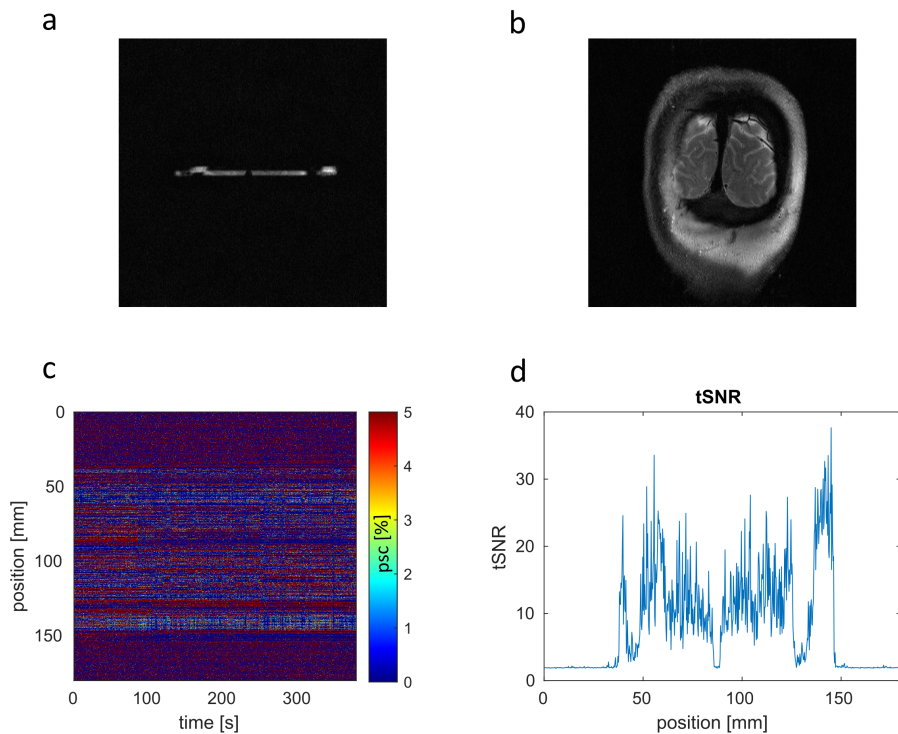
Figure 5.10: (a) LSD image for SE acquisition, (b) slice image, (c) SELINE data in psc and (d) tSNR for the acquisition with TR = 190 ms, acquired on an 8-channel transmit system.
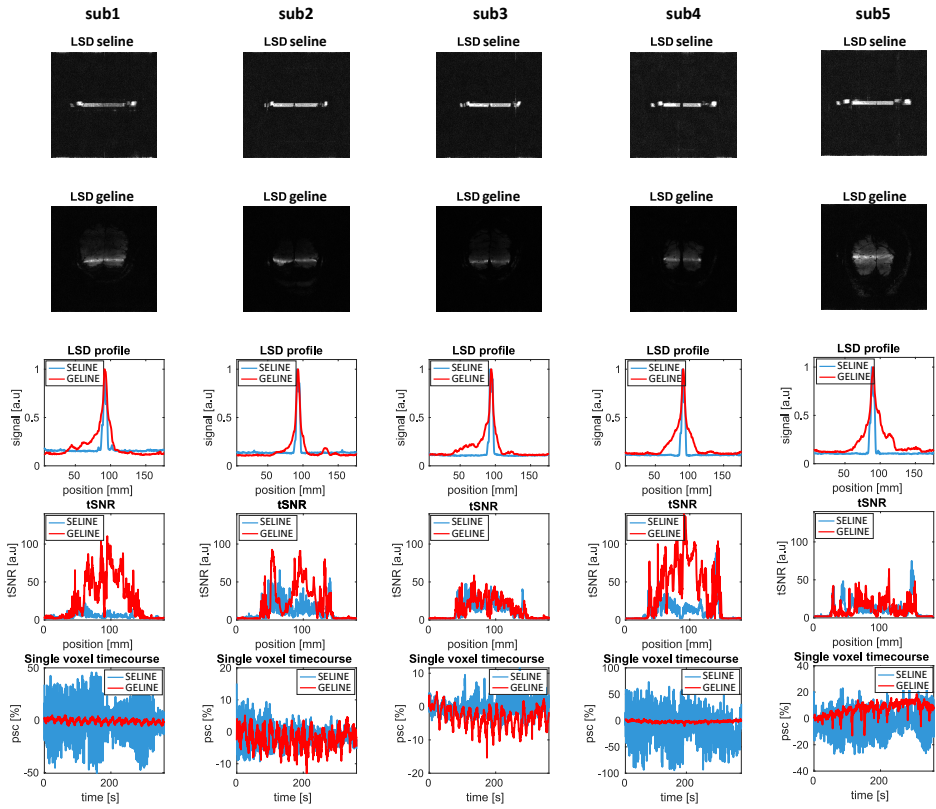
Figure 5.11: Schematic representation of the results for the five subjects scanned with the 2-channel transmit system: LSD images for the SELINE and GELINE acquisition (row 1 and 2 respectively), LSD profiles (row 3), tSNR values along the line (row 4) and single voxel timecourses expressed in psc (row 5), for both GE (red line) and SE (blue line).
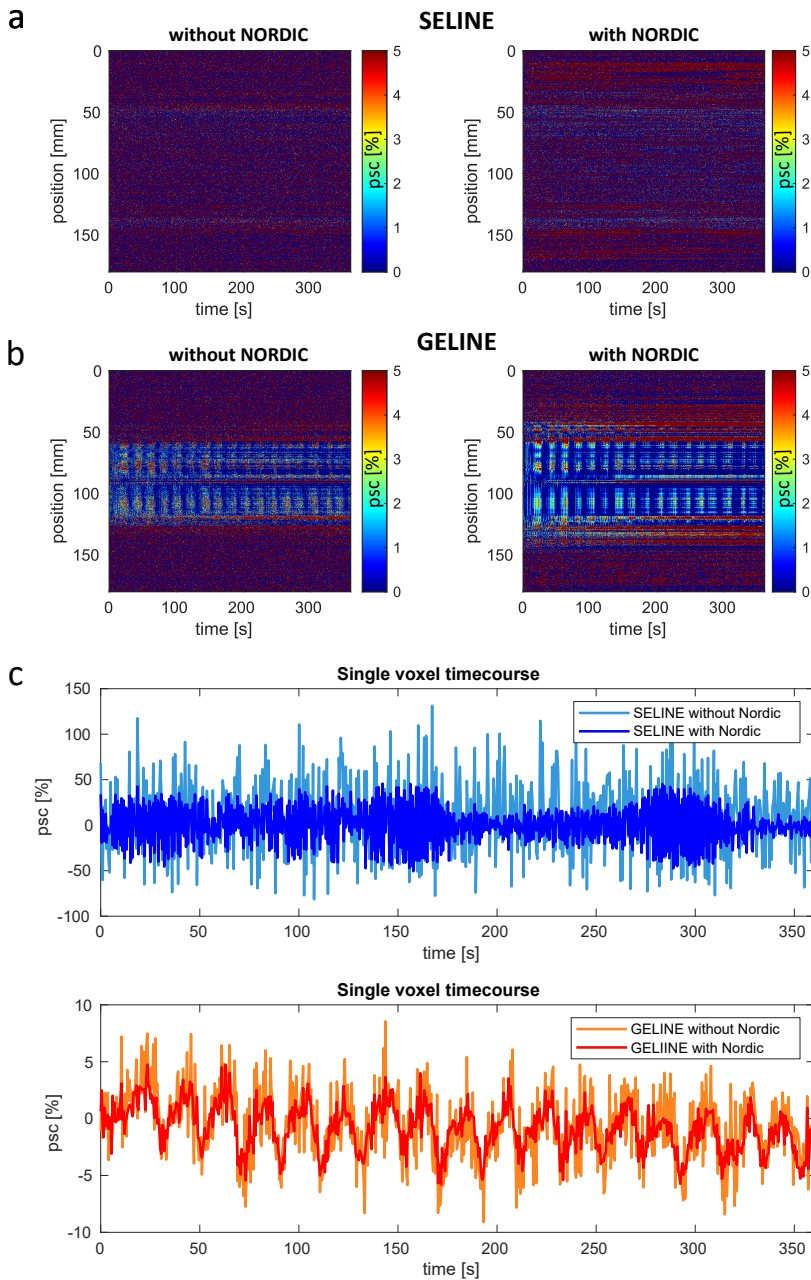
Figure 5.12: Carpet plot in psc for SELINE (a) and GELINE (b) with and without NORDIC-denoising and timecourses in psc with and without NORDIC-denoising for SELINE (c) and GELINE (d), for a representative voxel.

6

DOES THE HEMODYNAMIC RESPONSE FUNCTION IN VISUAL CORTEX DIFFER BETWEEN AGE GROUPS? A HIGH SPATIO-TEMPORAL RESOLUTION FMRI STUDY WITH CORTICAL DEPTH DEPENDENCY INSIGHTS

Luisa Raimondo*, Jurjen Heij*, Tomas Knapen, Jeroen C.W. Siero, Wietske van der Zwaag and Serge O. Dumoulin
*shared first authorship.

Abstract

Functional magnetic resonance imaging (fMRI) is a widely used tool to investigate in vivo functional brain responses in humans. Valid comparisons of fMRI results across age groups depend on consistency of the blood-oxygen-level-dependent (BOLD)-driven hemodynamic response function (HRF). Although common statistical approaches assume a single HRF across the entire brain, HRF differences can be observed across individuals, regions of the brain, and even across cortical depth. Several attempts have been made to map these differences to the process of aging, but these efforts have not led to a consensus view.

Here, we expand previous research in visual cortex using 7T fMRI as well as ultra-high spatiotemporal resolution line-scanning (250 μm in laminar direction, sampled every 105 ms), which allowed us to investigate age-related changes in the HRF across cortical depth. Eleven young healthy participants (23±2 years old, 6 males) and 11 healthy middle-aged participants (6±4 years old, 9 males) participated in HRF-mapping experiment. HRFs were estimated using a smooth basis function deconvolution approach at each cortical depth separately. From these HRFs, we extracted properties related to response magnitude and temporal dynamics.

We found that the these properties of the HRF in the two age groups are similar in primary visual cortex for both the high-resolution whole-brain fMRI acquisition and the line-scanning acquisitions, suggesting that middle-aged individuals can participate in neuroscientific studies free of bias in HRF characteristics.

6

6.1 Introduction

Aging causes a broad set of anatomical and functional changes in the brain. For example, thinning and atrophy of the cortex are observable in later stages of life, starting from middle aged [371]. Functional changes are also reported, such as a reduction in cerebral blood flow (CBF) and alterations in cerebral metabolic rate of oxygen (CMRO2) and blood supply [372, 373]. Magnetic resonance imaging (MRI) is a powerful tool, since it allows for measurements of structure and function in the living human brain. Particularly, functional MRI (fMRI) is a non-invasive method that is sensitive to changes in the blood oxygenation level-dependent (BOLD) signal as a consequence of tasks [22]. With respect to ageing brains, fMRI allows to detect the hemodynamic response function (HRF) changes, which can reflect changes in the vasculature, particularly when sufficient high spatiotemporal resolution is employed.

Several studies investigated the age-dependence of fMRI responses, but there is no clear consensus on whether, and if so how, the HRF changes in healthy aging. On the one hand, some studies reported a decrease in the amplitude of the BOLD response following a visual stimulus in elderly individuals compared to a young group (66-89 and 18-24 years old and 57-84 and 20-36 years old) [374, 375]. On the other hand, Huettel et al. [376] found similar BOLD response amplitudes. West et al. [377] suggested the small sample sizes, analysis techniques, and physiological mechanisms could cause between-study discrepancies. Using large sample sizes and minimal analysis assumptions, they aimed to disentangle age-related changes in HRF parameters from other sources of variability and link them solely to alterations in one or more components of the neural-vascular coupling system. This approach yielded a delayed response with decreased amplitude, reduced undershoot and longer return to baseline in elderly (54-74 years old) compared to younger (18-30 years old) participants in response to a visual-motor task, in the occipital cortex. Moreover, the older group exhibited higher variability in response shape compared to the younger group. However, in an earlier study, a lower amplitude and SNR were not linked to shape and or variability differences between age groups [378].

Despite the discrepancies reported above, some common points of those studies can be highlighted: relatively low magnetic fields (1.5 and 3T), low spatial and temporal resolutions (>3 mm isotropic) and long repetition times (TR) of 1-2 s were used, which were standard for fMRI at the time [23, 24]. These acquisitions are thus likely biased to sample BOLD signals from larger, draining veins [237]. In contrast, contemporary hardware (e.g. UHF-MRI) and methodological (modelling approaches) advances are likely bring relevant insights in HRF characterization in the aging brain. Particularly, increased field strengths can be employed to reach higher spatial and temporal resolution. This, in turn, would allow a more spatially localized detection of changes in the HRF through reduction of partial voluming [5, 9, 30, 342]. Using a higher sampling rate allows more frequent sampling along the HRF, which aids in estimation of shape and timing parameters.

This study aims to expand existing literature by employing state of the art acquisition and modelling approaches. Line-scanning fMRI is such an approach. In contrast to conventional whole-brain acquisition, line-scanning allows extremely high spatial (250 μm) and temporal (~100 ms) resolution in line direction by sacrificing volume coverage [50, 303, 306]. This is done by exciting a slice and suppressing the signal outside the line of interest through outer volume suppression (OVS). The phase-encoding gradient in the direction perpendicular to the line is omitted, and the line signal is then acquired after every excitation pulse. This method is suitable to yield highly detailed HRFs in humans across cortical depth by positioning the line perpendicularly to the cortex, thereby reducing the mixing of signal from different depth stages. We also included a relatively high-resolution whole-brain fMRI acquisition (1.8 mm isotropic spatial resolution and repetition time of 1.32 s). The same visual task was performed in both acquisition schemes. We selected two age groups (19-25 and 57-69 years old) to compare the HRF obtained both in a large extent of primary visual cortex (V1) and across depth within a specific patch.

6.2 Materials and Methods

6.2.1 Participants

11 young healthy participants (23±2 years old, 6 males) and 11 middle aged healthy participants (63±4 years old, 9 males) were scanned with a 7T MRI system (Philips, Netherlands) equipped with a 2-channel transmit and 32 channel receive head coil (Nova Medical, USA). Following the Helsinki Declaration, all participants provided written informed consent before participating. This study was approved by the local ethical committee of the Vrije Universiteit Amsterdam. Participants were screened prior to the experiments to ensure MR compatibility. We carefully instructed participants to lay still in the scanner and motion was limited by fixing the head using foam pads.

6.2.2 Stimulus and task

The visual stimulus was presented on a screen placed at the end of the scanner bore, visible through a mirror positioned on the top of the coil. To independently localize responses visual cortex [379], a 12 seconds ON/OFF "localizer" task of 2.5 minutes was presented. During the ON-period, objects flickering at 8 Hz were presented on a scrambled grey background, while during the OFF-period a grey screen was displayed. For estimation of HRF shapes [380–382], an event-related visual task was employed (see Figure 6.1). The inter-stimulus intervals (ISIs) were generated following a negative exponential decay [383, 384]. We optimized the ISI distribution in two stages. First, we generated 1000 ISI distributions ($ISI_{min}/ISI_{max}/ISI_{mean}$ = 3s/18s/6s) and obtained the predicted time course using a canonical HRF and a stimulus duration of 3 s. The ISI distribution that resulted in the prediction with the highest variance ($ISI_{optimized}$) was entered in stage 2. Here, we optimized the order of ISIs by selecting the predicted time course with the highest variance generated from all possible ISI orders in $ISI_{optimized}$. To ensure participants' engagement, we introduced contrast-inverted presentations of flickering images (target) lasting

~0.3 s in half of the trials and instructed participants to press a button whenever they detected a target. A baseline consisting of 20 s of grey screen was added in the beginning of the task.
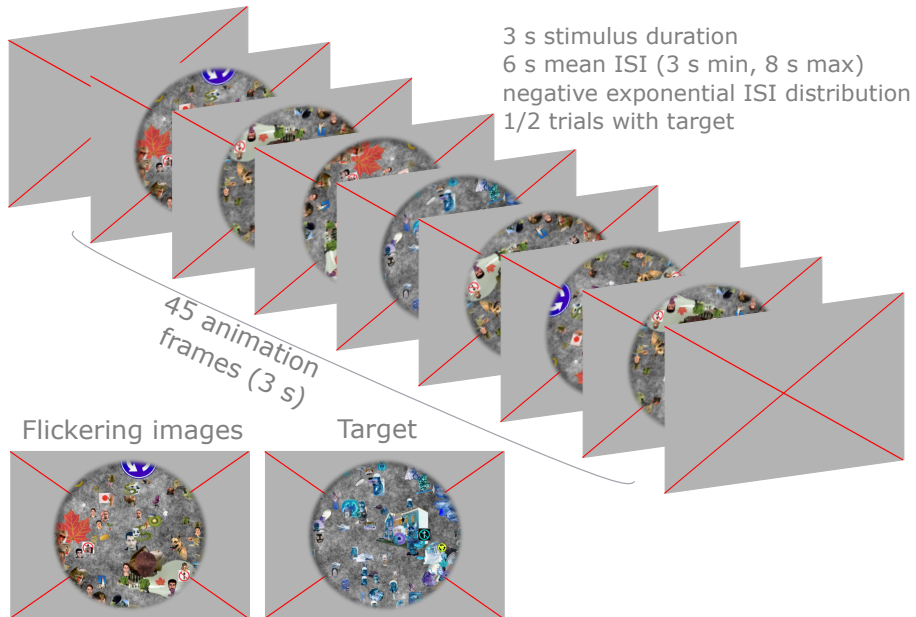
Figure 6.1: Schematic representation of the event-related visual task. Images selected from the HCP retinotopy dataset [385] were flickering at 15 Hz on a scrambled grey background, in an event-related manner: 3 s stimulus duration (i.e. 45 animation frames), 6 s mean inter-stimulus interval (ISI), 3 s minimum ISI, 18 s maximum ISI, following a negative exponential ISI distribution. In half of the trial negative images (target) were introduced to keep the participants focused. The participants were instructed to press a bottom whenever a target was displayed.

6.2.3 Data acquisition - whole brain data

We acquired anatomical scans with a magnetization-prepared 2 rapid acquisition gradient echo (MP2RAGE) sequence [386, 387]: matrix size = 344x344, spatial resolution = 0.64 mm isotropic, TR = 6.2 ms, TE = 2.3 ms, TI1/TI2 = 0.8/2.7 s, flip angle = 8°/5°. The MP2RAGE sequence was used for segmentation and co-registration purposes. A fluid-attenuated inversion recovery (FLAIR) sequence with the following parameters was acquired to aid in pial surface segmentation: matrix size = 220x220 spatial resolution = 1 mm isotropic, TR/TI = 8/2.2 s, TE = 234 ms, flip angle = 90°. Whole brain functional data were acquired using a 3D GE-EPI sequence with the following parameters: matrix size = 112x112, spatial resolution = 1.8 mm isotropic, TR = 1.32 s, TE = 17 ms, flip angle = 13°. Each run was followed by 4 volumes acquired in the opposite phase-encoding direction to correct for susceptibility distortions [388]. The localizer run consisted of 124 volumes (2.5 mins), while 230 volumes per event-related run were acquired (5 min 11 s). Note that for the whole-brain acquisitions, the ISI distribution was different for every run.

A schematic representation of the overall whole brain data acquisition can be seen

in the top part of Figure 6.2.
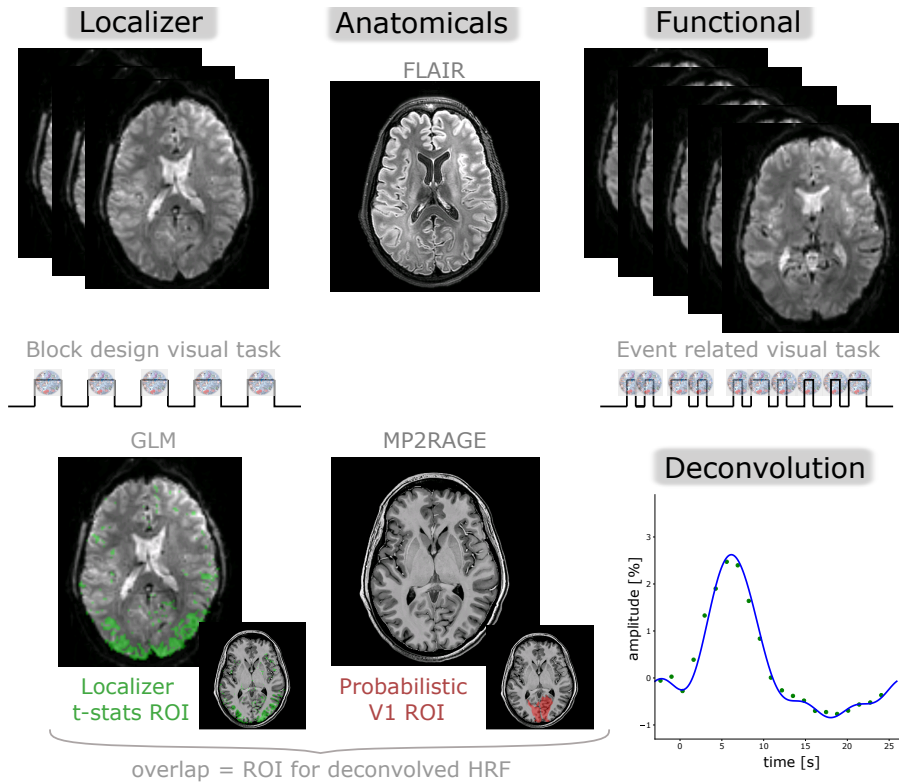
Figure 6.2: Schematic representation of the whole brain data acquisition and analysis. From the localizer with the block design task, a localizer ROI was created with voxels with t-stats>2.3 following the GLM analysis. A probabilistic V1 ROI (pV1) was derived from the Julich Histological Atlas [389] as implemented in FSL [298] and transformed to the functional space. The overlap of localizer ROI and pV1 ROI resulted in voxels eligible for the deconvolution approach from the functional runs with event-related task.

6.2.4   Data acquisition - line-scanning data

The line-scanning acquisition was based on [306, 357]: starting with a single slice gradient-echo acquisition (matrix size = 720x180, in-plane spatial resolution = 0.25x1 mm, slice thickness = 2.5 mm, TR = 106 ms, TE = 12 ms, flip angle = 22°), a line-signal distribution (LSD) image: same as the slice acquisition, with the addition of 2 saturation pulses (7.76 ms pulse duration) to suppress the signal outside the line of interest, and 3 runs of functional line-scanning acquisition: modified 2D multi-echo gradient-echo sequence (5 echoes), where the phase-encoding in the direction perpendicular to the line, needed for conventional 2D imaging, was omitted; line resolution = 250 μm, TR = 105 ms, TE1 = 6 ms, ΔTE = 8 ms, flip angle = 16°, array size = 720, line thickness = 2.5 mm, in-plane line width = 4 mm, fat suppression using SPIR and 2 saturation pulses (OVS bands), identical to the LSD image, with 7.76 ms pulse duration. The left part of Figure 6.3 shows a schematic representa-

tion of the line-scanning data acquisition.

Regarding the planning procedure, the slice was positioned coronally, crossing the visual cortex. By design, the line, located in the middle of the slice, was positioned approximately perpendicular to the medial grey matter sheet of the occipital lobe to avoid partial volume effects. A second criterion for the line planning was the proximity to V1. Finally, we tried to avoid voxels which clearly included big veins (visible form the single slice gradient-echo acquisition).
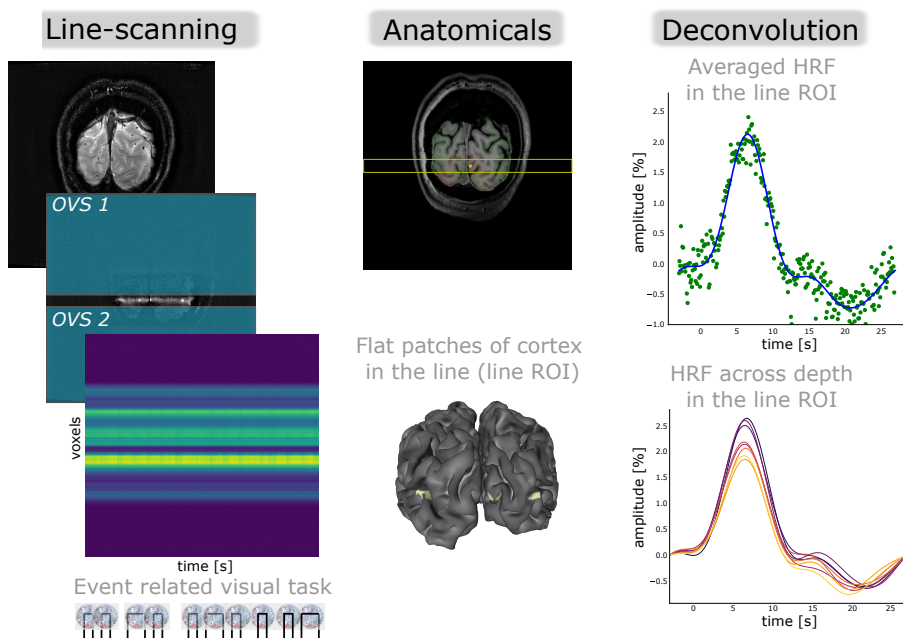
Figure 6.3: Schematic representation of line-scanning data acquisition and analysis. A gradient-echo slice with and without OVS bands was acquired, followed by the line-scanning runs with the event-related visual task. The slice was coregistered to the whole brain anatomical scan (MP2RAGE) and a patch of cortex relatively perpendicular to the line was selected (line ROI). The deconvolved HRF was extracted across cortical depth along the line ROI, as well as averaged across the line ROI.

6.2.5   Estimation of shape using deconvolution

Deconvolution was performed using Nideconv (github-nideconv). A finite impulse response model with a regressor per TR (time period/TR) was applied to capture shapes without any assumptions regarding HRF shape. The time period included 3 seconds before stimulus onset until 27 seconds after stimulus onset. The large number of regressors used with FIR inflates variability, as fewer samples contribute to each parameter estimate [390]. To deal with this, we complemented the analysis with a deconvolution using Fourier basis set. Such an approach imposes some shape, but is still flexible because different linear combinations allow for larger variety of HRF shapes than a single canonical basis function [390]. The following

parameters were derived from the response estimations: response magnitude (amplitude), time-to-peak, full-width-at-half-maximum (FWHM), rising slope (i.e. the angulation of the rising part of the HRF; evaluated from the derivative), positive area under the curve, and post-stimulus undershoot area.

6.2.6 Data analysis - whole brain data

The T_1-weighted (T_1w) anatomical image from the MP2RAGE sequence was processed as follows: first, a spatial-adaptive Non-Local Means (SANLM-) filter implemented in CAT12 was applied to filter noise while maintaining edges [391]. The denoised image was segmented into cerebrospinal fluid (CSF), white-matter (WM) and grey-matter (GM) using CAT12 and corrected for intensity non-uniformity with N4BiasFieldCorrection [392], distributed with ANTs 2.3.3. A mask representing the sagittal sinus was created by hand. The voxels in the mask were set to zero in the denoised T_1w image to limit the necessity for manual intervention after surface reconstruction. The final masked image was then skull-stripped with a Nipype implementation of the antsBrainExtraction.sh workflow (from ANTs), using OASIS30ANTs as target template. Brain tissue segmentation of CSF, WM and GM was performed on the brain-extracted T_1w image using FSL's FAST [393]. FreeSurfer 7.2 recon-all [394] was used to obtain native cortical surface reconstructions. The software makes use of the FLAIR image to refine the segmentation obtained by T_1w image alone, particularly in the exclusion of sinus and at the pial surface border.

Using the Julich histological atlas [389], we defined a probabilistic V1 region of interest (pV1 ROI) on the anatomical data, using FSL. The data from the block design localizer were analysed with a general linear model (GLM) analysis, assuming a gaussian HRF shape and t statistical values (t-stats) were estimated. The voxels with t-stats $\geq$ 2.3 were used to make a localizer ROI. The timecourses from overlapping voxels of the pV1 ROI and localizer ROI were converted in percentage signal change and averaged, from the baseline at the beginning of the visual task.

6.2.7 Data analysis - line-scanning data

The reconstruction of line-scanning data was performed offline using MatLab, Gyrotools. We combined the multi-channel coil data with a temporal signal-to-noise ratio (tSNR) and coil sensitivity-weighted sum of squares (SoS) weighted scheme per echo as in [357]. Prior to channel combination, we applied a NOise reduction with DIstribution corrected PCA (NORDIC) denoising step, while multi-echo data were combined with a sum of squares [319, 357].

We averaged the 3 runs of line-scanning data to increase the signal-to-noise ratio (SNR). To select a region in the line where the line was mostly perpendicular to the cortex (line ROI), we defined perpendicularity as the area where normal vectors of the surface aligned most with the coronal vector (because of the coronal slice positioning and the orthogonal nature of normal vectors). We obtained the normal vectors in the line by projecting the nominal line image to the surface and minimized the angle between the coronal vector and each normal vector in the line.

The voxels surrounding the most perpendicular vertex were selected to cover the pial surface to the white matter boundary to form the line ROI. The Supplementary material (Figure 6.8) shows each participant's line ROI after coregistration to the anatomical MP2RAGE. We also highlighted on the same slices the pV1 ROI and the localizer ROI to confirm that the line ROI ended up in an active region of V1 for each participant. Since the number of voxels that we selected for the line ROI differed across participants, we converted the number of voxels to percentage of distance from the cortex in order to pool the values of the HRF parameters across participants. We also averaged all the HRFs across cortical depth for a closer comparison with whole brain data in visual cortex. Note that the post stimulus undershoot was computed only for the averaged data across cortical depth, since the single HRF for each cortical depth was too noisy to perform this estimation.

Finally, we had to exclude 2 participants of the "middle aged" group for the line-scanning dataset due to misplacement of the line (i.e. the line was positioned far from V1) (1) and excessive motion (1).

6.3 Results

6.3.1 Similar HRF shapes between age-groups extracted from whole brain ROI

Figure 6.4 shows the deconvolved HRFs extracted from the ROI from the whole brain data. The deconvolved HRF using Fourier basis sets is superimposed on the points from the FIR model for a representative participant (for all participants please see supplementary material Figure 6.9), showing good agreement between the Fourier basis sets and FIR model. The deconvolved HRFs are shown together for all participants in Figure 6.4b (light lines), along with the averages (darker lines) for the young (red) and middle-aged group (blue).

Individual differences aside, group-average HRF shapes between age-groups were remarkably similar, as confirmed by the analysis of the main HRFs parameters (Figure 6.4c). No significant differences were found for amplitude ($t_{20} = -0.287$, $p = 0.777$), time to peak ($t_{20} = -0.257$, $p = 0.800$), FWHM ($t_{20} = 0.339$, $p = 0.738$), rising slope ($t_{20} = 0.199$, $p = 0.845$), positive area under the curve ($t_{20} = -0.088$, $p = 0.931$), and post stimulus undershoot area ($t_{20} = 0.611$, $p = 0.538$).

Furthermore, we compared the HRF parameters among the 2 age groups using a Bayesian independent samples T-test to estimate evidence in favor of the alternative hypothesis. We found moderate evidence that all the parameters are identical across groups ($BF_{01,\text{amplitude}} = 2.523$, $BF_{01,\text{time-to-peak}} = 2.538$, $BF_{01,\text{FWHM}} = 2.494$, $BF_{01,\text{rising slope}} = 2.563$, $BF_{01,\text{positive area}} = 2.592$, $BF_{01,\text{post stimulus undershoot area}} = 2.272$).
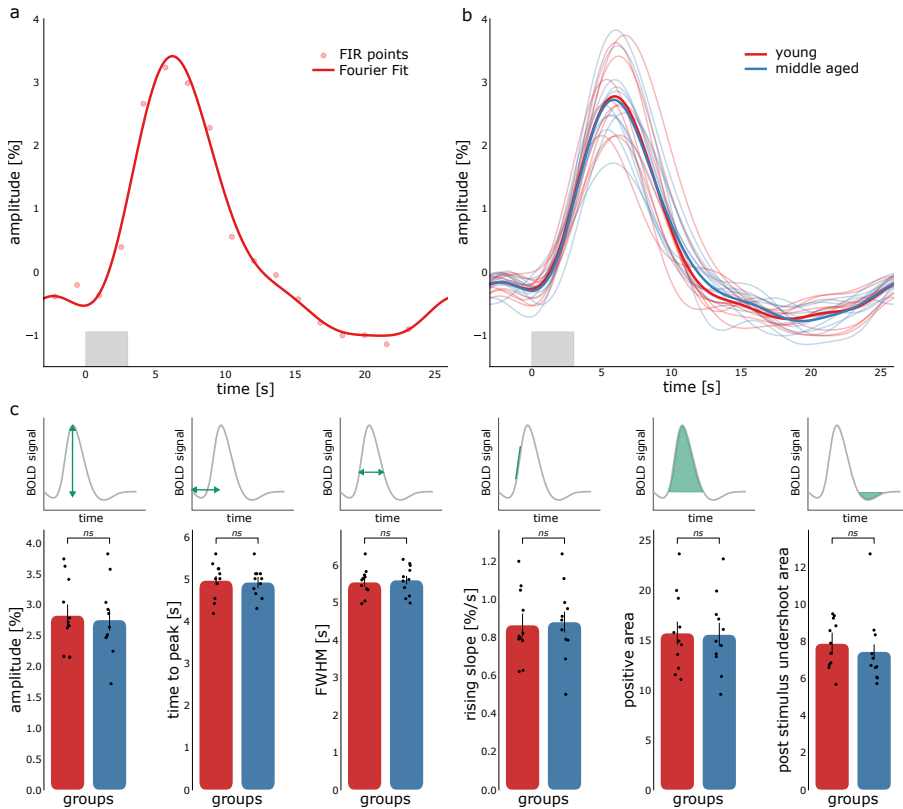
Figure 6.4: (a) Extracted HRF from whole brain data (with FIR points and Fourier basis set), for a representative participant. (b) HRFs for all participants in the young (red) and middle-aged (blue) group (thin lines) and averaged HRF for both groups (thick lines). The light gray box indicates the period when the task was shown. (c) HRF parameters from whole brain data for the 2 age groups (red young and blue middle aged).

6.3.2 Average HRF parameters across cortical depth from line-scanning data

Before analyzing line-scanning data we checked the results of the line planning procedure by plotting the pV1 mask on the slice on which the line was acquired, together with the localizer ROI from the whole brain functional localizer (Figure 6.8 of the Supplementary material). We selected the voxels along the line crossing the cortex from pial surface to WM boundary, as perpendicular as possible (line ROI). The angle between line and surface was calculated a posteriori, and was on average $(18\pm12)°$ for the young group and $(22\pm6)°$ for the middle aged group).

Figure 6.5 follows a similar layout compared to Figure 6.4, but results are derived from the line-scanning acquisition. Figure 6.5a shows the deconvolved HRF for the same representative participant as Figure 6.4a, together with the FIR points. Note the drastic increase in samples compared to the whole brain data in Figure 6.4. This is because the TR used for line-scanning is ~13 times shorter than the TR of whole brain data acquisition (0.105 s vs 1.32 s). In the Supplementary material (Figure 6.10) the deconvolved HRF with FIR points is reported for every participant. The

deconvolved HRFs are also represented for all participants in Figure 6.5b, together with the averages for the age groups (with the same colour coding as in Figure 6.4). The deconvolved HRFs follow similar trends, but they present slightly more variability compared to whole brain data. Again, no differences were found for amplitude (t_{18} = -0.308, p = 0.762), time-to-peak (t_{18} = -0.345, p = 0.734), FWHM (t_{18} = 0.429, p = 0.673), rising slope (t_{18} = 0.085, p = 0.933), positive area (t_{18} = -0.070, p = 0.945), and post stimulus undershoot area (t_{18} = -1.131, p = 0.273). When comparing the spatiotemporal HRF parameters among age groups with a Bayesian independent samples T-test, we found moderate or weak evidence that the parameters are identical between groups ($BF_{01, amplitude}$ = 2.425, $BF_{01, time\text{-}to\text{-}peak}$ = 2.404, $BF_{01, FWHM}$ = 2.350, $BF_{01, rising slope}$ = 2.501, $BF_{01, positive area}$ = 2.504, $BF_{01, post stimulus undershoot area}$ = 1.609).

6
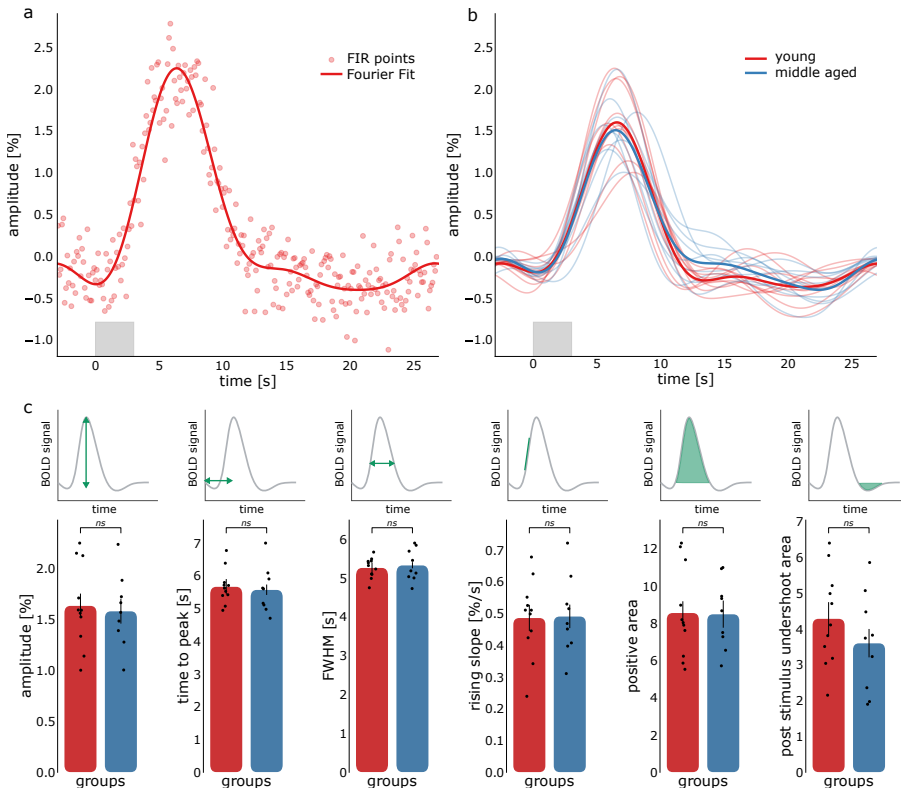
Figure 6.5: (a) Extracted HRF from line-scanning data averaged across cortical depths (with FIR points and Fourier basis set), for a representative participant. (b) HRFs averaged across cortical depth for all participants (red young group and blue middle aged group) and respective averaged HRF across the 2 age groups (ticker red and blue lines). The light gray box indicates the period when the task was shown. (c) HRF parameters from averaged across cortical depth line-scanning data for the 2 age groups (red young and blue middle aged). Note that the line-scanning data for 2 participants were excluded from plot (b) and (c) as well as from the analysis.

6.3.3 Similar cortical depth dependent HRFs in V1

Figure 6.6 shows the deconvolved HRF extracted for each cortical depth within the line ROI for a young representative participant (Figure 6.6a) and a middle aged representative participant (Figure 6.6c). The corresponding amplitude across cortical depth is reported in Figure 6.6bc, together with the line ROI from the gradient-echo slice acquisition.
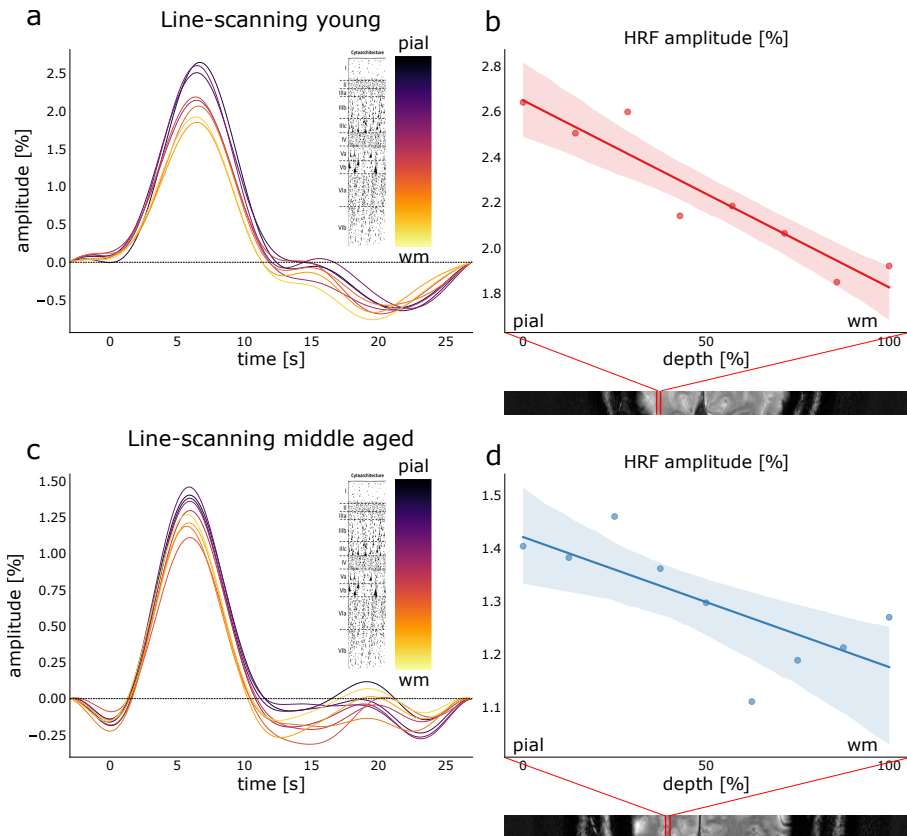
Figure 6.6: (a) Extracted HRF from line-scanning data across cortical depths for a representative young participant, and (b) corresponding amplitude across cortical depth with line ROI location reported on top of the gradient-echo slice. (c) Extracted HRF from line-scanning data across cortical depths for a representative middle aged participant and (d) corresponding amplitude across cortical depth with line ROI location reported on top of the gradient-echo slice.

The HRF across cortical depths show similar behaviours, with a consistent decrease in amplitude from the pial surface to the WM boundary. Note that the return to baseline looks rather noisy, as expected from deconvolution in line-scanning data, which are noisier than whole brain data. For this reason, we did not compute the post stimulus undershoot area for the HRFs across cortical depths. All the other HRF parameters were estimated across cortical depths and reported in Figure 6.7a

for all the individual participants and averaged across groups (Figure 6.7b).
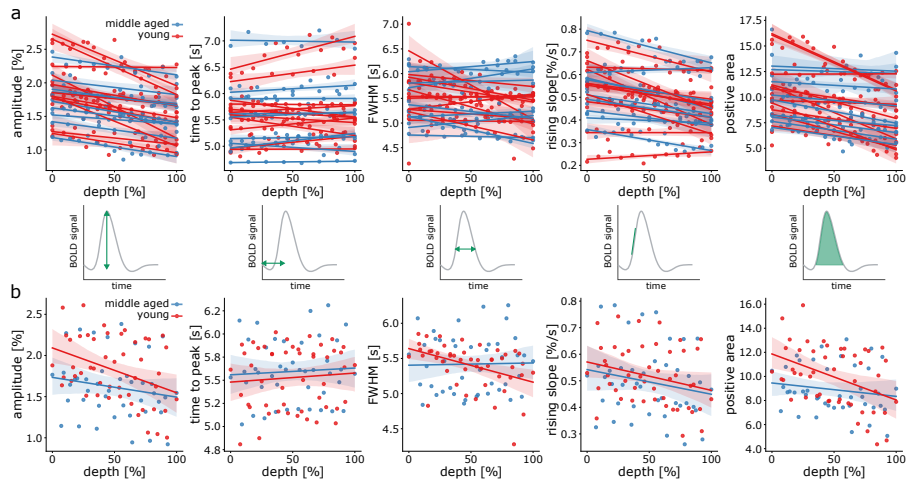
Figure 6.7: (a) HRF parameters from line-scanning data across cortical depth for all the individual participants (apart from the 2 excluded ones) and (b) for the averaged parameters across young and middle aged groups. Red indicate the young participants and blue the middle aged ones.

For both young and middle aged groups, the BOLD signal showed the canonical pattern of signal evolution; BOLD signals increased towards the pial surface. To test differences across depth formally, we assessed the different HRF parameters as the intercept at 50% of cortical depth and slope of the linear regression fit averaged across the 2 age groups (Figure 6.7b).

For the slopes of amplitude, time-to-peak, and positive area, the assumption of normality using Levene's test was violated ($p < 0.001$, $p = 0.021$, and $p = 0.002$, respectively). A Mann-Whitney U-test for independent samples was used to assess differences in these parameters across groups. We found a significant effect for the positive area ($W = 79.00$, $p = 0.025$), where young participants ($M = -0.030$, SD = 0.020) had a steeper slope compared to middle aged participants ($M = -0.012$, SD = 0.006, effect size = 0.596). No significant effects were found for the slope of the amplitude and time-to-peak ($W = 75.00$, $p = 0.046$ and $W = 52.00$, $p = 0.882$, respectively). The parameters that did not break the assumption of normality were assessed using a Student's T-test (FWHM and rising slope). No significant effects were found for these parameters ($t_{18} = 1.877$, $p = 0.770$ and $t_{18} = 0.634$, $p = 0.534$, respectively).

Regarding the slopes of the parameters which were not significantly different (amplitude, time to peak, FWHM and rising slope), from the Bayesian independent samples T-test we found weak evidence that the amplitude and FWHM are identical across groups ($BF_{01} = 0.624$, $BF_{01} = 0.775$ respectively), while for time-to-peak and rising slope showed the evidence for this was stronger ($BF_{01} = 2.506$, $BF_{01} =$

2.177 respectively).

The intercept at 50% of the cortical depth of the linear for all the parameters was assessed with a Student's T-test. None of the slopes of the parameters was significantly different in the young and middle-aged group (t_{18} = -0.579, p = 0.569 for amplitude, t_{18} = -0.339, p = 0.739 for time to peak, t_{18} = -0.030, p = 0.977 for FWHM, t_{18} = 0.068, p = 0.947 for rising slope and t_{18} = -0.278, p = 0.784 for the positive area). From the Bayesian independent samples T-test, we found moderate evidence that the intercept at 50% of cortical depth for all the parameters was identical across groups ($BF_{01, \text{amplitude}}$ = 2.227, $BF_{01, \text{time-to-peak}}$ = 2.408, $BF_{01, \text{FWHM}}$ = 2.507, $BF_{01, \text{rising slope}}$ = 2.504, $BF_{01, \text{positive area}}$ = 2.440).

6.4   Discussion

Age related changes in the HRF have been reported in the literature with diverging findings. We deduced some common aspects of the previous studies that we used as a starting point for improvements in the study of HRF shapes in two groups of people of different ages. Specifically, relatively low magnetic field strengths were used previously (1.5 and 3T), as well as standard fMRI spatial and temporal resolutions (>3 mm isotropic and repetition time of 1-2 s) and various tasks difficulties (flickering checkerboards, pattern recognition, Oddball task, bimodal audio/visual tasks). Here, we exploited the power of high-field MRI (7T) to boost the SNR and be able to increase both spatial and temporal resolution (1.78 mm isotropic and 1.32 s TR for whole brain data).

Moreover, we used a detection task on the stimulus in order to maintain vigilance and ensure that participant's attention was focused on the visual stimuli, all while keeping the changes to the visual stimulus minimal. Over a single run, the participants performed with d' values of 1.2±0.4 (mean±standard error) for the middle-aged group and 2.1±0.3 (mean±standard error) for the young group.

Our results show that, averaged across the activate V1 patch sampled in the whole-brain acquisitions, there is no significant difference in the HRF shape in visual cortex between the young and middle aged group, in accordance with previous findings that include larger sample sizes [395]. The discrepancies with the literature that showed a decrease in HRF amplitude in older age groups [374, 375, 377] could be due to the selection of the ROI where the timecourses were averaged in order to extract the HRF. This is a predominant source of variability as in most cases the ROI was based on anatomical information (from standard templates) and/or functional information (only voxels which showed activation higher than a certain threshold). The anatomical selection of the ROI has the disadvantage that voxels are included which do not show a task response (or, also highly prevalent in the visual cortex, showed a negative response), hence decreasing the HRF amplitude and possibly distorting its shape (see also [396] for a discussion on this regard). On the other hand, a functional ROI made from active voxels means that the voxels which best follow the model are the same ones used to estimate the HRF shape. As in any

standard GLM approach, certain assumptions on the HRF shape are made; this makes the HRF estimate based on functional ROI a circular problem. In our study, we combined anatomical and independent functional information to select the voxels on which the HRF estimate was performed. Particularly, we disentangled the functional ROI from the scan on which the deconvolved HRF was extracted by introducing an additional localizer scan with a block design task, which is much less sensitive to the HRF shape and can safely be analyzed using a canonical HRF. The combination of the localizer ROI with the anatomical V1 region based on the MNI template (pV1 ROI) to create the final ROI on which the deconvolved HRF was extracted ensured to avoid the circularity problem on the HRF estimation and minimize the assumptions on the HRF shape.

Moreover, since the laminar differences in the HRF response relate to the properties of the vasculature, changes in the BOLD response can reflect changes in the vasculature properties. For this reason, we also introduced a novel acquisition that has never been used before for age-related studies. Line-scanning fMRI brings the advantage of being able to investigate the HRF response across cortical depth (0.25 mm spatial resolution) at an extremely high temporal resolution (0.105 s). This high sampling rate allows more detailed estimation of the HRF shape and variations of the HRF across cortical depth. Before analysing the line-scanning results we checked the selection of a proper ROI from which to extract the HRF for the line-scanning dataset (line ROI). In this case, we used multiple criteria for the voxel selection. First, a certain level of line perpendicularity with respect to the cortex to avoid partial voluming effects across depths, resulting in a degree of perpendicularity of the line ROI of $(18\pm12)°$ for the young group and $(22\pm6)°$ for the middle aged group. The second criterion was the proximity to V1: we confirmed that the line ROI was falling in the pV1 ROI or nearby for all included subjects (see Figure 6.8 in the Supplementary material). Finally, we tried to avoid voxels which clearly included big veins, exploiting the high resolution of the line-scanning fMRI to detect BOLD responses from microvessels. The planning procedure could have been improved with the introduction of a separate scan session and line planning a priori to minimize partial voluming effects, as suggested by Heij et al. [397]. However, logistical constraints on the participant group meant that a single MRI session was preferable. Only one subject was excluded due to wrong planning, which was felt to be acceptable in this cohort (n=22), hence the planning procedure did not seem to be problematic for this specific study.

Another limitation of line-scanning is subject motion, which cannot be corrected with the implementation of line-scanning we used for this study. A way to reduce motion artefacts is to introduce prospective motion correction as in [326, 357]. However, we decided not to include motion correction in this study because the interruptions in the time series necessary to acquire motion navigators would have complicated our deconvolution approach and the T_1 decays after every navigator acquisition would have introduced undesired signal fluctuations in the time courses, further complicating the deconvolution. Since only one subject was ex-

cluded from the line-scanning dataset due to excessive motion, we confirmed that the addition of prospective motion correction was not necessary for this study.

Regarding the results across cortical depths, we found that the HRF amplitudes derived from line-scanning data are consistent with existing literature, showing an increase in the HRF amplitude from the WM boundary to the pial surface [9]. This increase is caused by the draining and pooling of blood by the upper layers and pial veins, which cause an increase of the BOLD response to the cortical surface [241]. The increases in area under the peak and steepness of the rising slope most likely also reflect this effect. The line-scanning data showed a small effect for differences in the slope of the positive area, with signal draining more clearly towards the cortical surface in the young cohort. This could be caused by differences in partial voluming originating from the angle of the line or the cortical thickness. Considering the cortical thinning with age [371], it is of paramount importance to have a spatial resolution that allows to see laminar responses. In fact, a high spatial resolution guarantees that the HRF differences are due to vascular effects rather than anatomical changes. On the other hand, if the resolution is low, the difference in the HRF shapes in young and older groups could be due to the mixing of different tissues. For example, if the pial layers become thinner with age, an insufficient resolution could lead to the finding of a lower HRF amplitude, but this effect would be solely due to the anatomy rather than the actual vasculature).

To our knowledge, this is the first time that age related differences across cortical depth were shown, so we could not compare our finding with previous literature. The main finding across cortical depth is a significant steeper slope of the positive area in the young group, compared to the middle-aged group. All the other parameters were not significantly different, and when considering whole brain data and averaged line-scanning data over the line ROI we observed striking similarities. This finding can have potential implications for the inclusion criteria of participants in neuroscientific studies, as well as the number of participants needed for this kind of applications.

6.5   Conclusion

This work studied the hemodynamic response function in the visual cortex in two age groups (young and middle aged). We exploited the potential of high field MRI to increase the spatial and temporal resolutions, particularly when using the line-scanning method, which allowed to look at HRF properties also across cortical depth, in individual participants. We showed that there is a significant steeper slope of the positive area in the young group, compared to the middle aged one, while there are no significant differences in the other parameters of the HRF in the two age groups in visual cortex. This means that when non behaviourally challenging or cognitively demanding memory tasks are employed, there are no differences in scanning young or middle aged individuals.

Supplementary material
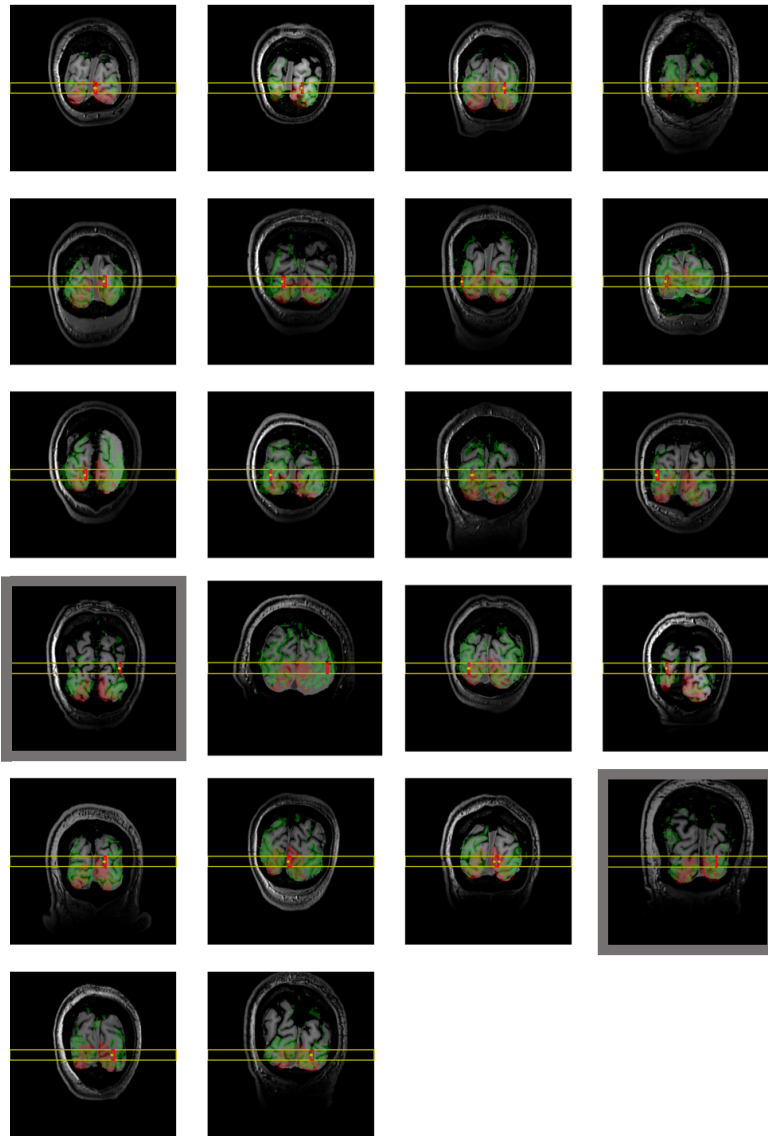
Figure 6.8: (a) Line-scanning planning: anatomical slice and lien positioning (yellow box). Yellow dots indicate voxels perpendicular to the surface. The red box is the selected line ROI, where we estimated the HRFs across cortical depth. The Red mask is the pV1 ROI and the green mask is the localizer ROI projected on the anatomical slice. The gray boxes indicate the 2 excluded subjects.
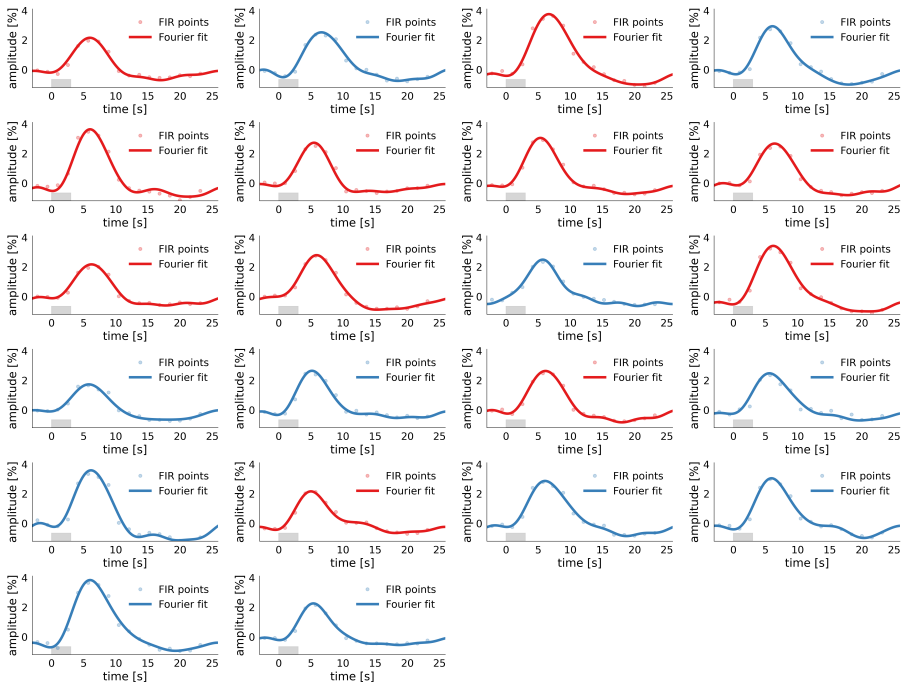
Figure 6.9: (a) Extracted HRF from whole brain data (with FIR points and Fourier basis set), for all the participants (red is used for young participants and blue for middle age participants).
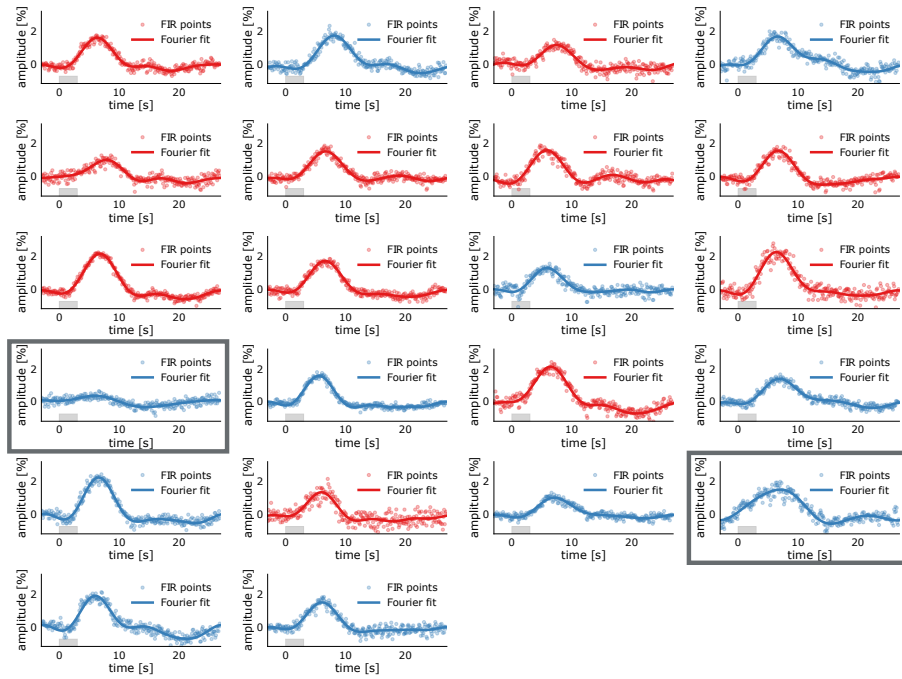
Figure 6.10: (a) Extracted HRF from line-scanning data, averaged across cortical depth (with FIR points and Fourier basis set), for all the participants (red is used for young participants, blue for middle age participants). The gray boxes indicate the 2 excluded subjects).

6

7

SUMMARY AND GENERAL DISCUSSION

7.1   Objective

The main aim of this thesis was to implement an extreme fMRI method, with ultra-high spatiotemporal resolution and severely reduced FOV, in order to gain more insights on the human brain hemodynamics at different cortical depths. Line-scanning is a one dimensional fMRI recording, which relies on the repeated acquisition of a single line of k-space after making sure that the signal projected into that k-space line derives from a small region where the line is positioned. The creation of this reduced FOV can be achieved either through saturation bands such as in the gradient-echo implementation or with a rotation of the refocusing plane in the spin-echo version. To acquire a single k-space line, the gradients in the phase-encoding direction are omitted, allowing a very fast sampling rate (~100 ms) and an ultra-high spatial resolution along the line (250 μm).

In this thesis, I implemented different line-scanning sequences for humans at 7T, and I tested the line-scanning performance in the context of fMRI (Chapter 3 and 5). Several improvements were proposed over the first implementation (Chapter 4), to increase the SNR (multi-echo readouts), remove thermal noise (NORDIC denoising) and correct for motion (prospective motion correction). The most suitable version of line-scanning was then used for a neuroscientific fMRI experiment (Chapter 6). The relevance of line-scanning was also contextualized with other more standard fMRI approaches such as whole brain acquisitions (Chapter 6) and resting-state fMRI (rs-fMRI) for functional connectomics (Chapter 2).

7.2   Summary of main findings

Advances in resting state fMRI for functional connectomics (Chapter 2)

This chapter offers an example of how the overall aim of gaining further insights on the human brain functions can be achieved through multiple ways, even in the context of fMRI itself. Instead of using ultra-high spatiotemporal resolution in a very specific region of the brain (such as with line-scanning), I focused on the opposite: connectivity-aimed resting-state fMRI (rs-fMRI), which requires a large FOV, and investigates spontaneous fluctuations in the BOLD signal, which occur simultaneously in different brain regions. I presented some common and recent approaches for different types of resting state studies, to show the potential of rs-fMRI and its growing availability in the study of the human brain.

Implementation of gradient-echo line-scanning in humans at 7T (Chapter 3)

Inspired by the work of Xin Yu et al. [50], I implemented a human version of line-scanning, based on a single slice (2D) gradient-echo sequence. I used two saturation pulses to suppress the signal outside the line of interest, and I evaluated the performance of the saturation. I then found the best coil combination strategy for the data reconstruction. Finally, I tested the power of line-scanning with a visual experiment and showed the BOLD responses along cortical depth, with resolutions of 250 μm and 200 ms. To prove the reliability of the first implementation of human line-scanning I also compared the t-stats results with a single slice (2D)

gradient-echo echo planar imaging (GE-EPI) BOLD fMRI data with the same temporal resolution and voxel volume, and found a good correspondence among the two.

Directions for improvements (Chapter 4)

The first implementation of line-scanning suffered from some challenges concerning different aspects. Thermal noise is definitely one of the major issues when small voxels are being imaged [319, 398]. To address this issue, I tried to improve the SNR both by using a multi-echo readout and by implementing an adaptation of NORDIC for one dimensional data. Together, those improvements furnished a much higher tSNR and t-statistical values with respect to the single-echo non-denoised version. Moreover, I added the possibility to include prospective motion correction to the multi-echo line-scanning, which rendered the line-scanning method more robust and suitable for different kind of experiments (such as when scanning specific groups of people, such as patients).

Implementation of spin-echo line-scanning in humans at 7T (Chapter 5)

An extremely natural approach for line-scanning is using a spin-echo sequence. This has a double advantage; on the one hand saturation pulses are not needed, since the line signal is created from the rotation of the refocusing plane with respect to the excited one. On the other hand, spin-echo offers a contrast (T_2w) more specific to the microvasculature [192] rather than the macrovasculature (as the T_2^* signal from gradient-echo), but contains an overall reduced sensitivity to the BOLD effect. I found that the creation of the line is extremely sharp compared to the gradient-echo version. However, when it comes to the detection of activation, I found that this implementation of spin-echo line-scanning was not sensitive enough to detect any activation. Despite its great potential, further improvement is needed to make this sequence useful for fMRI experiments.

A line-scanning fMRI application, together with a standard acquisition at 7T (Chapter 6)

To prove that line-scanning carries the potential to be a valuable fMRI technique for neuroscientific experiments, when the focus is on cortical depth dependencies of the functional signal, I evaluated the HRF behaviour in visual cortex after an event related visual task in two age groups. I found an overall similar behaviour in the two age groups both when using line-scanning and a whole brain acquisition.

7.3 Limitations and future prospective

I often compare the PhD path to a marathon. In short words, it requires time, energy and dedication. Time is limited to 4 years (a bit more if your PhD ends up in the middle of a pandemic). Energy is also limited (particularly if you are not good at running). And dedication has huge fluctuations, often due to external agents (including the Dutch weather). Together, those three factors contributed to multiple limitations to the projects I carried out during my PhD. In the following I will

discuss some of the limitations and propose some directions for improvement, as well as future prospective of line-scanning.

Gradient-echo line-scanning relies on the use of saturation pulses to null the signal outside the line of interest. The saturation pulses used in this thesis have an asymmetric sinc pulse. As reported in Chapter 3, they are far from being perfect: the suppression of undesired signal from outside the region of interest is ~94%, so there is still ~6% of signal present outside the region of interest. Moreover, also the signal inside the line is partially saturated (~62% of residual signal inside the line), because of the not ideal profile of the OVS bands. The gradient-echo version of line-scanning would benefit from OVS pulses with sharper saturation profiles, which would be an interesting focus point in future work on improving the line-scanning method. Morgan et al. proposed several strategies for the saturation, which includes the superimposition of two saturation bands (dual-saturation), for an optimized line profile [274]. Another approach would be to use adiabatic pulses, which are relatively insensitive to B_1 inhomogeneity and frequency offsets. For example, the B_1-Insensitive Rotation (BIR-4) pulse is a promising pulse, commonly used in spectroscopy, to localize the signal from a specific region [399].

The line-scanning data used in this thesis definitely suffers from thermal noise, which can be much reduced through NORDIC denoising, showing a significant increase in t-stats and tSNR values. However, thermal noise is not the only source of noise. The voxel volume is 2.5 mm^3, hence physiological noise is also present, as well as noise due to subjects' motion. A component based noise correction method (CompCor) [400] proves to be efficient to reduce noise due to physiological fluctuations and other sources, and could be applied to line-scanning data, as in [397]. The timecourses of voxels in the white matter and cerebrospinal fluid along the line can be also selected and used as input for principal component analysis (PCA), and the resulting timecourses from the PCA can be high-pass filtered below the respiratory frequency (~0.18Hz). These high-pass filtered time courses can then be used as nuisance regressors to clean the data from physiological noise, specifically at the respiration and cardiac frequencies.

Another limitation of the projects presented in this thesis is the absence of an accurate planning procedure. In fact, in every study, the line was manually positioned, during the scan session, along the right-left axis, in the occipital lobe, covering a region in visual cortex, with a coronal orientation of the slice. This kind of planning simplified the process of hitting a perpendicular piece of cortex with respect to the line, since the line ended up orthogonally to the cortical ribbon either side of the intra-hemispheric cleft. The perpendicular orientation relative to the cortex is necessary when the goal is to investigate the laminar dimension of the cortex. Moreover, when the phase encoding gradients are removed, all the signal coming from the gap in between the two saturation pulses is projected into the line. This means that the ideal target for the line is a flat piece of cortex, to make sure that there is no contamination from different tissues. Together, those two requirements (perpendicularity to the cortex and absence of curvature) made the online

planning procedure suboptimal. A more advanced planning is necessary when performing neuroscientific experiments. In Heij et al. [397], we proposed a double session approach: in the first scan session the anatomical scans are used to extract a vertex corresponding to a flat piece of cortex. During the second session, a quicker anatomical scan is acquired and coregistered to the first session, to extract the coordinate of the line, to make sure that the line is positioned perpendicularly to that specific target vertex. The anatomical information from the first session can be combined to additional functional information tuned to the specific experiment that is performed. This extensive planning procedure would definitely allow to be more specific in the voxels selection, and the outcomes of this thesis would have benefited from its use, particularly in the application presented in Chapter 6. However, due to logistical difficulties in recruiting the middle aged cohort, we opted for a single session approach.

In Chapter 4, we implemented an alternative contrast for the line-scanning technique, being a T_2w contrast with a spin-echo sequence. Despite the partially unsuccessful implementation for fMRI purposes, this was also the only attempt to implement a T_2w contrast version of line-scanning. In addition to the possible improvements which were discussed in Chapter 4 to improve the spin-echo line-scanning sequence, Choi et al. [368] also proposed a gradient- and spin-echo (GRASE) [347] implementation of line-scanning, which is a valuable addition for human line-scanning. This technique allows the evaluation of the fMRI signal evolutions along the echo trains by simultaneously acquiring both gradient-echo and spin-echo based fMRI responses with high spatiotemporal resolution. In this case, the low specificity and high sensitivity of gradient-echo BOLD (T_2*w) can be seen together with the low sensitivity but high specificity of the spin-echo signal (T_2w).

Moreover, the line-scanning method suffers from the extremely reduced field of view. This problem can be partially overcome when using a bilateral or a multi line approach [401, 402]. Those methods allow exploitation of the ultra-high spatiotemporal resolution of line-scanning to detect laminar-specific fMRI signals from adjacent cortical regions, and open the way for connectivity studies (Chapter 2). If similar techniques can be implemented for human studies as well, they could pave the way for resting state and functional connectivity human line-scanning studies.

7

Finally, line-scanning proved to have great potential and could be extended to many specific application studies, which have not been investigated in this thesis. For example, regarding clinical applications, it could be used to target a specific lesion. Alternatively, when the vasculature is compromised, as with sickle cell disease [307, 308], line-scanning could be used to track the changes in the hemodynamic responses at high spatiotemporal resolution in diseases condition. From a neuroscientific prospective, line-scanning could give more insights about the BOLD responses during specific experiments which require high spatial and temporal resolutions together.

7.4   Conclusion

The non-invasive investigation of the information processed along the cortical depth requires fMRI methods that simultaneously allow high spatial and temporal resolutions. Line-scanning can provide unique high resolutions at the cost of spatial coverage and standard processing. In this work, the line-scanning method was implemented in humans, at 7T. After introducing general methods for resting-state fMRI for functional connectomics (Chapter 2), I presented a gradient-echo line-scanning implementation in humans (Chapter 3), followed by some improvements regarding the readout, thermal noise removal and motion correction (Chapter 4). I also presented some efforts on the implementation of a spin-echo version (Chapter 5), which proved to be not yet applicable for fMRI purposes. Finally, I showed an example of line-scanning application to detect hemodynamic responses across cortical depth in two age groups (Chapter 6) and measured how line-scanning compares with a standard whole brain acquisition in the same populations.

Overall, line-scanning proved to be an extremely powerful method for layer dependent fMRI studies. Careful consideration should be taken in the beginning of a study to make sure that the best acquisition strategy is selected. The ultra-high spatiotemporal resolution of line-scanning is associated with several challenges in the acquisition and analysis strategies. As shown in Chapter 2, other fMRI approaches can be considered for experiments where the spatial or temporal resolution can be slightly decreased.

7
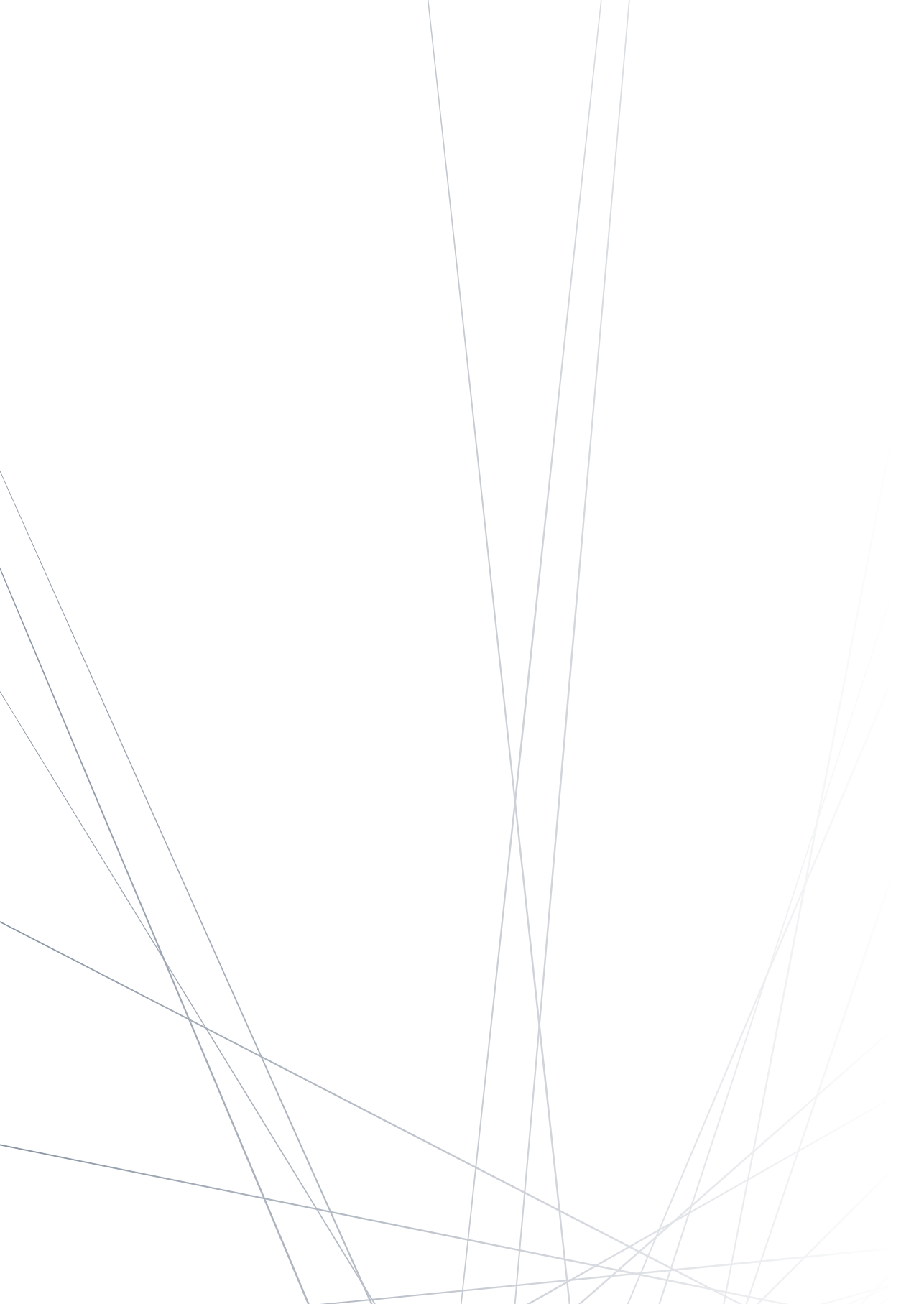
8

BIBLIOGRAPHY

References

[1] A. Minagar, J. Ragheb, and R. E. Kelley, "The Edwin Smith Surgical Papyrus: Description and Analysis of the Earliest Case of Aphasia," *J Med Biogr*, vol. 11, pp. 114–117, May 2003. doi: 10.1177/096777200301100214.

[2] D. Liewald, R. Miller, N. Logothetis, H.-J. Wagner, and A. Schüz, "Distribution of axon diameters in cortical white matter: an electron-microscopic study on three human brains and a macaque," *Biol Cybern*, vol. 108, pp. 541–557, Oct. 2014. doi: 10.1007/s00422-014-0626-2.

[3] B. Fischl and A. M. Dale, "Measuring the thickness of the human cerebral cortex from magnetic resonance images," *Proceedings of the National Academy of Sciences*, vol. 97, pp. 11050–11055, Sept. 2000. doi: 10.1073/pnas.200033797.

[4] K. Brodmann, *Vergleichende Lokalisationslehre der Grosshirnrinde in ihren Prinzipien dargestellt auf Grund des Zellenbaues.* Leipzig : Barth, 1909.

[5] S. O. Dumoulin, A. Fracasso, W. van der Zwaag, J. C. Siero, and N. Petridou, "Ultra-high field MRI: Advancing systems neuroscience towards mesoscopic human brain function," *NeuroImage*, vol. 168, pp. 345–357, Mar. 2018. doi: 10.1016/j.neuroimage.2017.01.028.

[6] D. H. Hubel and T. N. Wiesel, "Receptive fields and functional architecture of monkey striate cortex," *The Journal of Physiology*, vol. 195, no. 1, pp. 215–243, 1968. doi: 10.1113/jphysiol.1968.sp008455.

[7] E. M. Hillman, "Coupling Mechanism and Significance of the BOLD Signal: A Status Report," *Annu Rev Neurosci*, vol. 37, pp. 161–181, July 2014. doi: 10.1146/annurev-neuro-071013-014111.

[8] N. Petridou and J. C. W. Siero, "Laminar fMRI: What can the time domain tell us?," *NeuroImage*, vol. 197, pp. 761–771, Aug. 2019. doi: 10.1016/j.neuroimage.2017.07.040.

[9] J. C. Siero, N. Petridou, H. Hoogduin, P. R. Luijten, and N. F. Ramsey, "Cortical Depth-Dependent Temporal Dynamics of the BOLD Response in the Human Brain," *J Cereb Blood Flow Metab*, vol. 31, pp. 1999–2008, Oct. 2011. doi: 10.1038/jcbfm.2011.57.

[10] B. L. Sabatini and W. G. Regehr, "Timing of neurotransmission at fast synapses in the mammalian brain," *Nature*, vol. 384, pp. 170–172, nov 1996. doi: 10.1038/384170a0.

[11] L. G. Hanson, "Is quantum mechanics necessary for understanding magnetic resonance?," *Concepts in Magnetic Resonance Part A*, vol. 32A, no. 5, pp. 329–340, 2008. doi: 10.1002/cmr.a.20123.

[12] E. L. Hahn, "Free nuclear induction," *Physics Today*, vol. 6, pp. 4–9, Nov. 1953. doi: 10.1063/1.3061075.

[13] D. Cammoun, K. A. Davis, and W. R. Hendee, "Clinical Applications of Magnetic Resonance Imaging—Current Status," *West J Med*, vol. 143, pp. 793–803, Dec. 1985.

[14] L. C. Jordan and M. R. DeBaun, "Cerebral hemodynamic assessment and neuroimaging across the lifespan in sickle cell disease," *J Cereb Blood Flow Metab*, vol. 38, pp. 1438–1448, Sept. 2018. doi: 10.1177/0271678X17701763.

[15] C. Ledig, A. Schuh, R. Guerrero, R. A. Heckemann, and D. Rueckert, "Structural brain imaging in Alzheimer's disease and mild cognitive impairment: biomarker analysis and shared morphometry database," *Sci Rep*, vol. 8, p. 11258, July 2018. doi: 10.1038/s41598-018-29295-9.

[16] M. E. MacDonald and R. Frayne, "Cerebrovascular MRI: a review of state-of-the-art approaches, methods and techniques," *NMR in Biomedicine*, vol. 28, no. 7, pp. 767–791, 2015. doi: 10.1002/nbm.3322.

8

[17] F. J. Meijer, B. Goraj, B. R. Bloem, and R. A. Esselink, "Clinical Application of Brain MRI in the Diagnostic Work-up of Parkinsonism," *J Parkinsons Dis*, vol. 7, no. 2, pp. 211–217, 2017. doi: 10.3233/JPD-150733.

[18] J. Van Heerden, P. M. Desmond, and P. M. Phal, "Functional MRI in clinical practice: A pictorial essay: Functional MRI in clinical practice," *Journal of Medical Imaging and Radiation Oncology*, vol. 58, pp. 320–326, June 2014. doi: 10.1111/1754-9485.12158.

[19] C.-L. Wu, T.-J. Lin, G.-L. Chiou, C.-Y. Lee, H. Luan, M.-J. Tsai, P. Potvin, and C.-C. Tsai, "A Systematic Review of MRI Neuroimaging for Education Research," *Frontiers in Psychology*, vol. 12, 2021. doi: 10.3389/fpsyg.2021.617599.

[20] G. H. Glover, "Overview of Functional Magnetic Resonance Imaging," 2011. doi: 10.1016/j.nec.2010.11.001.

[21] S. Petcharunpaisan, J. Ramalho, and M. Castillo, "Arterial spin labeling in neuroimaging," *World J Radiol*, vol. 2, pp. 384–398, Oct. 2010. doi: 10.4329/wjr.v2.i10.384.

[22] S. Ogawa, T. M. Lee, A. R. Kay, and D. W. Tank, "Brain magnetic resonance imaging with contrast dependent on blood oxygenation.," *Proceedings of the National Academy of Sciences*, vol. 87, pp. 9868–9872, Dec. 1990. doi: 10.1073/pnas.87.24.9868.

[23] N. K. Logothetis, "What we can do and what we cannot do with fMRI," *Nature*, vol. 453, pp. 869–878, June 2008. doi: 10.1038/nature06976.

[24] R. Turner, "Uses, misuses, new uses and fundamental limitations of magnetic resonance imaging in cognitive science," *Philosophical Transactions of the Royal Society B: Biological Sciences*, vol. 371, p. 20150349, Oct. 2016. doi: 10.1098/rstb.2015.0349.

[25] E. Yacoub, A. Shmuel, J. Pfeuffer, P.-F. Van De Moortele, G. Adriany, P. Andersen, J. T. Vaughan, H. Merkle, K. Ugurbil, and X. Hu, "Imaging brain function in humans at 7 Tesla," *Magnetic Resonance in Medicine*, vol. 45, no. 4, pp. 588–594, 2001. doi: 10.1002/mrm.1080.

[26] R. Pohmann, O. Speck, and K. Scheffler, "Signal-to-noise ratio and MR tissue parameters in human brain imaging at 3, 7, and 9.4 tesla using current receive coil arrays," *Magnetic Resonance in Medicine*, vol. 75, no. 2, pp. 801–809, 2016. doi: 10.1002/mrm.25677.

[27] J. Vaughan, M. Garwood, C. Collins, W. Liu, L. DelaBarre, G. Adriany, P. Andersen, H. Merkle, R. Goebel, M. Smith, and K. Ugurbil, "7T vs. 4T: RF power, homogeneity, and signal-to-noise comparison in head images," *Magnetic Resonance in Medicine*, vol. 46, no. 1, pp. 24–30, 2001. doi: 10.1002/mrm.1156.

[28] W. van der Zwaag, J. P. Marques, M. Hergt, and R. Gruetter, "Investigation of high-resolution functional magnetic resonance imaging by means of surface and array radiofrequency coils at 7 T," *Magnetic Resonance Imaging*, vol. 27, pp. 1011–1018, Oct. 2009. doi: 10.1016/j.mri.2009.01.013.

[29] W. van der Zwaag, S. Francis, K. Head, A. Peters, P. Gowland, P. Morris, and R. Bowtell, "fMRI at 1.5, 3 and 7 T: Characterising BOLD signal changes," *NeuroImage*, vol. 47, pp. 1425–1434, Oct. 2009. doi: 10.1016/j.neuroimage.2009.05.015.

[30] W. van der Zwaag, A. Schäfer, J. P. Marques, R. Turner, and R. Trampel, "Recent applications of UHF-MRI in the study of human brain function and structure: a review," *NMR in Biomedicine*, vol. 29, no. 9, pp. 1274–1288, 2016. doi: 10.1002/nbm.3275.

[31] E. Yacoub, T. Q. Duong, P.-F. Van De Moortele, M. Lindquist, G. Adriany, S.-G. Kim, K. Ugurbil, and X. Hu, "Spin-echo fMRI in humans using high spatial resolutions and high magnetic fields," *Magn. Reson. Med.*, vol. 49, pp. 655–664, Apr. 2003. doi: 10.1002/mrm.10433.

[32] J. C. W. Siero, N. F. Ramsey, H. Hoogduin, D. W. J. Klomp, P. R. Luijten, and N. Petridou, "BOLD Specificity and Dynamics Evaluated in Humans at 7 T: Comparing Gradient-

8

Echo and Spin-Echo Hemodynamic Responses," *PLoS ONE*, vol. 8, p. e54560, Jan. 2013. doi: 10.1371/journal.pone.0054560.

[33] A. Jesmanowicz, P. A. Bandettini, and J. S. Hyde, "Single-shot half k-space high-resolution gradient-recalled EPI for fMRI at 3 tesla," *Magnetic Resonance in Medicine*, vol. 40, no. 5, pp. 754–762, 1998. doi: 10.1002/mrm.1910400517.

[34] F. A. Breuer, M. Blaimer, M. F. Mueller, N. Seiberlich, R. M. Heidemann, M. A. Griswold, and P. M. Jakob, "Controlled aliasing in volumetric parallel imaging (2D CAIPIRINHA)," *Magnetic Resonance in Medicine*, vol. 55, no. 3, pp. 549–556, 2006. doi: 10.1002/mrm.20787.

[35] M. A. Griswold, P. M. Jakob, R. M. Heidemann, M. Nittka, V. Jellus, J. Wang, B. Kiefer, and A. Haase, "Generalized autocalibrating partially parallel acquisitions (GRAPPA)," *Magnetic Resonance in Medicine*, vol. 47, no. 6, pp. 1202–1210, 2002. doi: 10.1002/mrm.10171.

[36] K. P. Pruessmann, M. Weiger, M. B. Scheidegger, and P. Boesiger, "SENSE: Sensitivity encoding for fast MRI," *Magnetic Resonance in Medicine*, vol. 42, no. 5, pp. 952–962, 1999. doi: 10.1002/(SICI)1522-2594(199911)42:5<952::AID-MRM16>3.0.CO;2-S.

[37] S. Geethanath, R. Reddy, A. S. Konar, S. Imam, R. Sundaresan, R. B. D R, and R. Venkatesan, "Compressed sensing MRI: a review," *Crit Rev Biomed Eng*, vol. 41, no. 3, pp. 183–204, 2013. doi: 10.1615/critrevbiomedeng.2014008058.

[38] S. Moeller, E. Yacoub, C. A. Olman, E. Auerbach, J. Strupp, N. Harel, and K. Ugurbil, "Multiband multislice GE-EPI at 7 tesla, with 16-fold acceleration using partial parallel imaging with application to high spatial and temporal whole-brain fMRI," *Magnetic Resonance in Medicine*, vol. 63, no. 5, pp. 1144–1153, 2010. doi: 10.1002/mrm.22361.

[39] B. Poser, P. Koopmans, T. Witzel, L. Wald, and M. Barth, "Three dimensional echo-planar imaging at 7 Tesla," 2010. doi: 10.1016/j.neuroimage.2010.01.108.

[40] W. van der Zwaag, J. P. Marques, T. Kober, G. Glover, R. Gruetter, and G. Krueger, "Temporal SNR characteristics in segmented 3D-EPI at 7T," *Magnetic Resonance in Medicine*, vol. 67, no. 2, pp. 344–352, 2012. doi: 10.1002/mrm.23007.

[41] D. G. Norris and J. R. Polimeni, "Laminar (f)MRI: A short history and future prospects," *NeuroImage*, vol. 197, pp. 643–649, Aug. 2019. doi: 10.1016/j.neuroimage.2019.04.082.

[42] J. A. van Dijk, A. Fracasso, N. Petridou, and S. O. Dumoulin, "Linear systems analysis for laminar fMRI: Evaluating BOLD amplitude scaling for luminance contrast manipulations," *Sci Rep*, vol. 10, p. 5462, Mar. 2020. doi: 10.1038/s41598-020-62165-x.

[43] K. Cheng, R. A. Waggoner, and K. Tanaka, "Human Ocular Dominance Columns as Revealed by High-Field Functional Magnetic Resonance Imaging," *Neuron*, vol. 32, pp. 359–374, Oct. 2001. doi: 10.1016/S0896-6273(01)00477-9.

[44] L. Huber, D. A. Handwerker, D. C. Jangraw, G. Chen, A. Hall, C. Stüber, J. Gonzalez-Castillo, D. Ivanov, S. Marrett, M. Guidi, J. Goense, B. A. Poser, and P. A. Bandettini, "High-Resolution CBV-fMRI Allows Mapping of Laminar Activity and Connectivity of Cortical Input and Output in Human M1," *Neuron*, vol. 96, pp. 1253–1263.e7, Dec. 2017. doi: 10.1016/j.neuron.2017.11.005.

[45] S. Kashyap, D. Ivanov, M. Havlicek, S. Sengupta, B. A. Poser, and K. Uludağ, "Resolving laminar activation in human V1 using ultra-high spatial resolution fMRI at 7T," *Sci Rep*, vol. 8, p. 17063, Nov. 2018. doi: 10.1038/s41598-018-35333-3.

[46] J. Pfeuffer, P.-F. van de Moortele, E. Yacoub, A. Shmuel, G. Adriany, P. Andersen, H. Merkle, M. Garwood, K. Ugurbil, and X. Hu, "Zoomed Functional Imaging in the

8

Human Brain at 7 Tesla with Simultaneous High Spatial and High Temporal Resolution," *NeuroImage*, vol. 17, pp. 272–286, Sept. 2002. doi: 10.1006/nimg.2002.1103.

[47] P. Mansfield and A. A. Maudsley, "Line scan proton spin imaging in biological structures by NMR," *Phys. Med. Biol.*, vol. 21, pp. 847–852, Sept. 1976. doi: 10.1088/0031-9155/21/5/013.

[48] P. Mansfield and A. A. Maudsley, "Planar spin imaging by NMR," *Journal of Magnetic Resonance (1969)*, vol. 27, pp. 101–119, July 1977. doi: 10.1016/0022-2364(77)90197-4.

[49] A. A. Maudsley, "Multiple-line-scanning spin density imaging," *Journal of Magnetic Resonance (1969)*, vol. 41, pp. 112–126, Oct. 1980. doi: 10.1016/0022-2364(80)90207-3.

[50] X. Yu, C. Qian, D.-y. Chen, S. J. Dodd, and A. P. Koretsky, "Deciphering laminar-specific neural inputs with line-scanning fMRI," *Nat Methods*, vol. 11, pp. 55–58, Jan. 2014. doi: 10.1038/nmeth.2730.

[51] K. Jann, R. X. Smith, E. A. Rios Piedra, M. Dapretto, and D. J. Wang, "Noise reduction in arterial spin labeling based functional connectivity using nuisance variables," *Frontiers in Neuroscience*, vol. 10, no. AUG, 2016. doi: 10.3389/fnins.2016.00371.

[52] M. H. Lee, C. D. Smyser, and J. S. Shimony, "Resting-state fMRI: A review of methods and clinical applications," *American Journal of Neuroradiology*, vol. 34, no. 10, pp. 1866–1872, 2013. doi: 10.3174/ajnr.A3263.

[53] S. M. Smith, C. F. Beckmann, J. Andersson, E. J. Auerbach, J. Bijsterbosch, G. Douaud, E. Duff, D. A. Feinberg, L. Griffanti, M. P. Harms, M. Kelly, T. Laumann, K. L. Miller, S. Moeller, S. Petersen, J. Power, G. Salimi-Khorshidi, A. Z. Snyder, A. T. Vu, M. W. Woolrich, J. Xu, E. Yacoub, K. Ugurbil, D. C. Van Essen, and M. F. Glasser, "Resting-state fMRI in the Human Connectome Project," *NeuroImage*, vol. 80, pp. 144–168, 2013. doi: 10.1016/j.neuroimage.2013.05.039.

[54] B. Biswal, F. Zerrin Yetkin, V. M. Haughton, and J. S. Hyde, "Functional connectivity in the motor cortex of resting human brain using echo-planar mri," *Magnetic Resonance in Medicine*, vol. 34, no. 4, pp. 537–541, 1995. doi: 10.1002/mrm.1910340409.

[55] M. P. van den Heuvel and H. E. Hulshoff Pol, "Exploring the brain network: A review on resting-state fMRI functional connectivity," *European Neuropsychopharmacology*, vol. 20, no. 8, pp. 519–534, 2010. doi: 10.1016/j.euroneuro.2010.03.008.

[56] J. Yang, S. Gohel, and B. Vachha, "Current methods and new directions in resting state fMRI," *Clinical Imaging*, vol. 65, pp. 47–53, 2020. doi: 10.1016/j.clinimag.2020.04.004.

[57] B. T. Thomas Yeo, F. M. Krienen, J. Sepulcre, M. R. Sabuncu, D. Lashkari, M. Hollinshead, J. L. Roffman, J. W. Smoller, L. Zöllei, J. R. Polimeni, B. Fisch, H. Liu, and R. L. Buckner, "The organization of the human cerebral cortex estimated by intrinsic functional connectivity," *Journal of Neurophysiology*, vol. 106, no. 3, pp. 1125–1165, 2011. doi: 10.1152/jn.00338.2011.

[58] E. Yacoub, P. F. Van De Moortele, A. Shmuel, and K. Ugurbil, "Signal and noise characteristics of Hahn SE and GE BOLD fMRI at 7 T in humans," *NeuroImage*, vol. 24, no. 3, pp. 738–750, 2005. doi: 10.1016/j.neuroimage.2004.09.002.

[59] K. R. Van Dijk, T. Hedden, A. Venkataraman, K. C. Evans, S. W. Lazar, and R. L. Buckner, "Intrinsic functional connectivity as a tool for human connectomics: Theory, properties, and optimization," *Journal of Neurophysiology*, vol. 103, no. 1, pp. 297–321, 2010. doi: 10.1152/jn.00783.2009.

[60] H. Jahanian, S. Holdsworth, T. Christen, H. Wu, K. Zhu, A. B. Kerr, M. J. Middione, R. F. Dougherty, M. Moseley, and G. Zaharchuk, "Advantages of short repetition time resting-state functional MRI enabled by simultaneous multi-slice

8

imaging," *Journal of Neuroscience Methods*, vol. 311, pp. 122–132, 2019. doi: 10.1016/j.jneumeth.2018.09.033.

[61] M. P. Harms, L. H. Somerville, B. M. Ances, J. Andersson, D. M. Barch, M. Bastiani, S. Y. Bookheimer, T. B. Brown, R. L. Buckner, G. C. Burgess, T. S. Coalson, M. A. Chappell, M. Dapretto, G. Douaud, B. Fischl, M. F. Glasser, D. N. Greve, C. Hodge, K. W. Jamison, S. Jbabdi, S. Kandala, X. Li, R. W. Mair, S. Mangia, D. Marcus, D. Mascali, S. Moeller, T. E. Nichols, E. C. Robinson, D. H. Salat, S. M. Smith, S. N. Sotiropoulos, M. Terpstra, K. M. Thomas, M. D. Tisdall, K. Ugurbil, A. van der Kouwe, R. P. Woods, L. Zöllei, D. C. Van Essen, and E. Yacoub, "Extending the Human Connectome Project across ages: Imaging protocols for the Lifespan Development and Aging projects," *NeuroImage*, vol. 183, pp. 972–984, 2018. doi: 10.1016/j.neuroimage.2018.09.060.

[62] E. C. Caparelli, T. J. Ross, H. Gu, and Y. Yang, "Factors Affecting Detection Power of Blood Oxygen-Level Dependent Signal in Resting-State Functional Magnetic Resonance Imaging Using High-Resolution Echo-Planar Imaging," *Brain Connectivity*, vol. 9, no. 8, pp. 638–648, 2019. doi: 10.1089/brain.2019.0683.

[63] M. Pannunzi, R. Hindriks, R. G. Bettinardi, E. Wenger, N. Lisofsky, J. Martensson, O. Butler, E. Filevich, M. Becker, M. Lochstet, S. Kühn, and G. Deco, "Resting-state fMRI correlations: From link-wise unreliability to whole brain stability," *NeuroImage*, vol. 157, no. December 2016, pp. 250–262, 2017. doi: 10.1016/j.neuroimage.2017.06.006.

[64] C. D. Hacker, J. L. Roland, A. H. Kim, J. S. Shimony, and E. C. Leuthardt, "Resting-state network mapping in neurosurgical practice: A review," *Neurosurgical Focus*, vol. 47, no. 6, pp. 1–9, 2019. doi: 10.3171/2019.9.FOCUS19656.

[65] M. J. Donahue, H. Hoogduin, S. M. Smith, J. C. Siero, M. Chappell, N. Petridou, P. Jezzard, P. R. Luijten, and J. Hendrikse, "Spontaneous blood oxygenation level-dependent fMRI signal is modulated by behavioral state and correlates with evoked response in sensorimotor cortex: A 7.0-T fMRI study," *Human Brain Mapping*, vol. 33, no. 3, pp. 511–522, 2012. doi: 10.1002/hbm.21228.

[66] T. Jao, P. E. Vértes, A. F. Alexander-Bloch, I. N. Tang, Y. C. Yu, J. H. Chen, and E. T. Bullmore, "Volitional eyes opening perturbs brain dynamics and functional connectivity regardless of light input," *NeuroImage*, vol. 69, pp. 21–34, 2013. doi: 10.1016/j.neuroimage.2012.12.007.

[67] P. Xu, R. Huang, J. Wang, N. T. Van Dam, T. Xie, Z. Dong, C. Chen, R. Gu, Y. F. Zang, Y. He, J. Fan, and Y. jia Luo, "Different topological organization of human brain functional networks with eyes open versus eyes closed," *NeuroImage*, vol. 90, pp. 246–255, 2014. doi: 10.1016/j.neuroimage.2013.12.060.

[68] O. Agcaoglu, T. W. Wilson, Y. P. Wang, J. M. Stephen, and V. D. Calhoun, "Dynamic Resting-State Connectivity Differences in Eyes Open Versus Eyes Closed Conditions," *Brain Connectivity*, vol. 10, no. 9, pp. 504–519, 2020. doi: 10.1089/brain.2020.0768.

[69] O. Agcaoglu, T. W. Wilson, Y. P. Wang, J. Stephen, and V. D. Calhoun, "Resting state connectivity differences in eyes open versus eyes closed conditions," *Human Brain Mapping*, vol. 40, no. 8, pp. 2488–2498, 2019. doi: 10.1002/hbm.24539.

[70] R. Patriat, E. K. Molloy, T. B. Meier, G. R. Kirk, V. A. Nair, M. E. Meyerand, V. Prabhakaran, and R. M. Birn, "The effect of resting condition on resting-state fMRI reliability and consistency: A comparison between resting with eyes open, closed, and fixated," *NeuroImage*, vol. 78, pp. 463–473, 2013. doi: 10.1016/j.neuroimage.2013.04.013.

[71] Q. Zou, X. Miao, D. Liu, D. J. Wang, Y. Zhuo, and J. H. Gao, "Reliability comparison of spontaneous brain activities between BOLD and CBF contrasts in eyes-

8

open and eyes-closed resting states," *NeuroImage*, vol. 121, pp. 91–105, 2015. doi: 10.1016/j.neuroimage.2015.07.044.

[72] Y. Weng, X. Liu, H. Hu, H. Huang, S. Zheng, Q. Chen, J. Song, B. Cao, J. Wang, S. Wang, and R. Huang, "Open eyes and closed eyes elicit different temporal properties of brain functional networks," *NeuroImage*, vol. 222, no. August, p. 117230, 2020. doi: 10.1016/j.neuroimage.2020.117230.

[73] J. R. Hale, M. J. Brookes, E. L. Hall, J. M. Zumer, C. M. Stevenson, S. T. Francis, and P. G. Morris, "Comparison of functional connectivity in default mode and sensori-motor networks at 3 and 7T," *Magnetic Resonance Materials in Physics, Biology and Medicine*, vol. 23, no. 5-6, pp. 339–349, 2010. doi: 10.1007/s10334-010-0220-0.

[74] R. L. Buckner, F. M. Krienen, A. Castellanos, J. C. Diaz, and B. T. Thomas Yeo, "The organization of the human cerebellum estimated by intrinsic functional connectivity," *Journal of Neurophysiology*, vol. 106, no. 5, pp. 2322–2345, 2011. doi: 10.1152/jn.00339.2011.

[75] F. De Martino, F. Esposito, P. F. van de Moortele, N. Harel, E. Formisano, R. Goebel, K. Ugurbil, and E. Yacoub, "Whole brain high-resolution functional imaging at ultra high magnetic fields: An application to the analysis of resting state networks," *NeuroImage*, vol. 57, no. 3, pp. 1031–1044, 2011. doi: 10.1016/j.neuroimage.2011.05.008.

[76] A. T. Newton, B. P. Rogers, J. C. Gore, and V. L. Morgan, "Improving measurement of functional connectivity through decreasing partial volume effects at 7T," *NeuroImage*, vol. 59, no. 3, pp. 2511–2517, 2012. doi: 10.1016/j.neuroimage.2011.08.096.

[77] P. F. Van de Moortele, E. J. Auerbach, C. Olman, E. Yacoub, K. Ugurbil, and S. Moeller, "T1 weighted brain images at 7 Tesla unbiased for Proton Density, T2* contrast and RF coil receive B1 sensitivity with simultaneous vessel visualization," *NeuroImage*, vol. 46, no. 2, pp. 432–446, 2009. doi: 10.1016/j.neuroimage.2009.02.009.

[78] Q. X. Yang, J. Wang, X. Zhang, C. M. Collins, M. B. Smith, H. Liu, X. H. Zhu, J. T. Vaughan, K. Ugurbil, and W. Chen, "Analysis of wave behavior in lossy dielectric samples at high field," *Magnetic Resonance in Medicine*, vol. 47, no. 5, pp. 982–989, 2002. doi: 10.1002/mrm.10137.

[79] K. Setsompop, D. A. Feinberg, and J. R. Polimeni, "Rapid brain MRI acquisition techniques at ultra-high fields," *NMR in Biomedicine*, vol. 29, no. 9, pp. 1198–1221, 2016. doi: 10.1002/nbm.3478.

[80] H. Togo, J. Rokicki, K. Yoshinaga, T. Hisatsune, H. Matsuda, N. Haga, and T. Hanakawa, "Effects of field-map distortion correction on resting state functional connectivity MRI," *Frontiers in Neuroscience*, vol. 11, no. DEC, pp. 1–10, 2017. doi: 10.3389/fnins.2017.00656.

[81] J. Pinto, S. Nunes, M. Bianciardi, A. Dias, L. M. Silveira, L. L. Wald, and P. Figueiredo, "Improved 7 Tesla resting-state fMRI connectivity measurements by cluster-based modeling of respiratory volume and heart rate effects," *NeuroImage*, vol. 153, pp. 262–272, 2017. doi: 10.1016/j.neuroimage.2017.04.009.

[82] T. Knapen, "Topographic connectivity reveals task-dependent retinotopic processing throughout the human brain," *Proceedings of the National Academy of Sciences of the United States of America*, vol. 118, no. 2, pp. 1–6, 2021. doi: 10.1073/pnas.2017032118.

[83] C. Triantafyllou, J. R. Polimeni, and L. L. Wald, "Physiological noise and signal-to-noise ratio in fMRI with multi-channel array coils," *NeuroImage*, vol. 55, no. 2, pp. 597–606, 2011. doi: 10.1016/j.neuroimage.2010.11.084.

[84] E. Yacoub, M. D. Grier, E. J. Auerbach, R. L. Lagore, N. Harel, G. Adriany, A. Zilverstand, B. Y. Hayden, S. R. Heilbronner, K. Ugurbil, and J. Zimmermann, "Ultra-high

8

field (10.5 T) resting state fMRI in the macaque," *NeuroImage*, vol. 223, no. September, 2020. doi: 10.1016/j.neuroimage.2020.117349.

[85] M. A. Ertürk, A. J. Raaijmakers, G. Adriany, K. Ugurbil, and G. J. Metzger, "A 16-channel combined loop-dipole transceiver array for 7 Tesla body MRI," *Magn Reson Med*, vol. 77, no. 2, pp. 884–894, 2017. doi: 10.1002/mrm.26153.

[86] J. Lee, M. Gebhardt, L. L. Wald, and E. Adalsteinsson, "Local SAR in parallel transmission pulse design," *Magn Reson Med*, vol. 67, no. 6, pp. 1566–1578, 2012. doi: 10.1002/mrm.23140.

[87] G. R. Wu and D. Marinazzo, "Sensitivity of the resting-state haemodynamic response function estimation to autonomic nervous system fluctuations," *Philos Trans A Math Phys Eng Sci*, vol. 374, no. 2067, 2016. doi: 10.1098/rsta.2015.0190.

[88] B. A. Poser, R. J. Anderson, B. Guérin, K. Setsompop, W. Deng, A. Mareyam, P. Serano, L. L. Wald, and V. A. Stenger, "Simultaneous multislice excitation by parallel transmission," *Magn Reson Med*, vol. 71, no. 4, pp. 1416–1427, 2014. doi: 10.1002/mrm.24791.

[89] B. A. Hargreaves, C. H. Cunningham, D. G. Nishimura, and S. M. Conolly, "Variable-rate selective excitation for rapid MRI sequences," *Magn Reson Med*, vol. 52, no. 3, pp. 590–597, 2004. doi: 10.1002/mrm.20168.

[90] D. G. Norris, P. J. Koopmans, R. Boyacioğlu, and M. Barth, "Power Independent of Number of Slices (PINS) radiofrequency pulses for low-power simultaneous multislice excitation," *Magn Reson Med*, vol. 66, no. 5, pp. 1234–1240, 2011. doi: 10.1002/mrm.23152.

[91] R. Stirnberg, D. Brenner, T. Stöcker, and N. J. Shah, "Rapid fat suppression for three-dimensional echo planar imaging with minimized specific absorption rate," *Magn Reson Med*, vol. 76, no. 5, pp. 1517–1523, 2016. doi: 10.1002/mrm.26063.

[92] P. J. Koopmans, R. Boyacioğlu, M. Barth, and D. G. Norris, "Whole brain, high resolution spin-echo resting state fMRI using PINS multiplexing at 7T," *NeuroImage*, vol. 62, no. 3, pp. 1939–1946, 2012. doi: 10.1016/j.neuroimage.2012.05.080.

[93] V. Gras, B. A. Poser, X. Wu, R. Tomi-Tricot, and N. Boulant, "Optimizing BOLD sensitivity in the 7T Human Connectome Project resting-state fMRI protocol using plug-and-play parallel transmission," *NeuroImage*, vol. 195, no. March, pp. 1–10, 2019. doi: 10.1016/j.neuroimage.2019.03.040.

[94] L. Huber, D. H. Y. Tse, C. J. Wiggins, K. Uludağ, S. Kashyap, D. C. Jangraw, P. A. Bandettini, B. A. Poser, and D. Ivanov, "Ultra-high resolution blood volume fMRI and BOLD fMRI in humans at 9.4T: Capabilities and challenges," *Neuroimage*, vol. 178, pp. 769–779, 2018. doi: 10.1016/j.neuroimage.2018.06.025.

[95] D. Ivanov, A. Gardumi, R. A. M. Haast, J. Pfeuffer, B. A. Poser, and K. Uludag, "Comparison of 3T and 7T ASL techniques for concurrent functional perfusion and BOLD studies," *Neuroimage*, vol. 156, pp. 363–376, 2017. doi: 10.1016/j.neuroimage.2017.05.038.

[96] L. L. Wald, "The future of acquisition speed, coverage, sensitivity, and resolution," *Neuroimage*, vol. 62, no. 2, pp. 1221–1229, 2012. doi: 10.1016/j.neuroimage.2012.02.077.

[97] P. Branco, D. Seixas, and S. L. Castro, "Temporal reliability of ultra-high field resting-state MRI for single-subject sensorimotor and language mapping," *NeuroImage*, vol. 168, no. November 2016, pp. 499–508, 2018. doi: 10.1016/j.neuroimage.2016.11.029.

[98] S. Torrisi, C. L. Nord, N. L. Balderston, J. P. Roiser, C. Grillon, and M. Ernst, "Resting state connectivity of the human habenula at ultra-high field," *NeuroImage*, vol. 147, pp. 872–879, 2017. doi: 10.1016/j.neuroimage.2016.10.034.

8

[99] A. Ebneabbasi, M. Mahdipour, V. Nejati, M. Li, T. Liebe, L. Colic, A. L. Leutritz, M. Vogel, M. Zarei, M. Walter, and M. Tahmasian, "Emotion processing and regulation in major depressive disorder: A 7T resting-state fMRI study," *Human Brain Mapping*, no. April 2020, pp. 797–810, 2020. doi: 10.1002/hbm.25263.

[100] J. Heinzle, T. Kahnt, and J. D. Haynes, "Topographically specific functional connectivity between visual field maps in the human brain," *NeuroImage*, vol. 56, no. 3, pp. 1426–1436, 2011. doi: 10.1016/j.neuroimage.2011.02.077.

[101] M. Raemaekers, W. Schellekens, R. J. van Wezel, N. Petridou, G. Kristo, and N. F. Ramsey, "Patterns of resting state connectivity in human primary visual cortical areas: A 7T fMRI study," *NeuroImage*, vol. 84, pp. 911–921, 2014. doi: 10.1016/j.neuroimage.2013.09.060.

[102] R. Deichmann, O. Josephs, C. Hutton, D. R. Corfield, and R. Turner, "Compensation of susceptibility-induced BOLD sensitivity losses in echo-planar fMRI imaging," *Neuroimage*, vol. 15, no. 1, pp. 120–135, 2002. doi: 10.1006/nimg.2001.0985.

[103] S. E. Yancey, D. J. Rotenberg, F. Tam, M. Chiew, S. Ranieri, L. Biswas, K. J. Anderson, S. N. Baker, G. A. Wright, and S. J. Graham, "Spin-history artifact during functional MRI: potential for adaptive correction," *Med Phys*, vol. 38, no. 8, pp. 4634–4646, 2011. doi: 10.1118/1.3583814.

[104] K. R. Van Dijk, M. R. Sabuncu, and R. L. Buckner, "The influence of head motion on intrinsic functional connectivity MRI," *Neuroimage*, vol. 59, no. 1, pp. 431–438, 2012. doi: 10.1016/j.neuroimage.2011.07.044.

[105] A. Fillmer, S. J. Vannesjo, M. Pavan, M. Scheidegger, K. P. Pruessmann, and A. Henning, "Fast iterative pre-emphasis calibration method enabling third-order dynamic shim updated fMRI," *Magn Reson Med*, vol. 75, no. 3, pp. 1119–1131, 2016. doi: 10.1002/mrm.25695.

[106] T. E. Wallace, J. R. Polimeni, J. P. Stockmann, W. S. Hoge, T. Kober, S. K. Warfield, and O. Afacan, "Dynamic distortion correction for functional MRI using FID navigators," *Magn Reson Med*, vol. 85, no. 3, pp. 1294–1307, 2021. doi: 10.1002/mrm.28505.

[107] J. D. Power, B. M. Silver, M. R. Silverman, E. L. Ajodan, D. J. Bos, and R. M. Jones, "Customized head molds reduce motion during resting state fMRI scans," *Neuroimage*, vol. 189, pp. 141–149, 2019. doi: 10.1016/j.neuroimage.2019.01.016.

[108] P. Huang, J. D. Carlin, A. Alink, N. Kriegeskorte, R. N. Henson, and M. M. Correia, "Prospective motion correction improves the sensitivity of fMRI pattern decoding," *Human Brain Mapping*, vol. 39, no. 10, pp. 4018–4031, 2018. doi: 10.1002/hbm.24228.

[109] P. Lanka and G. Deshpande, "Combining Prospective Acquisition CorrEction (PACE) with retrospective correction to reduce motion artifacts in resting state fMRI data," *Brain and Behavior*, vol. 9, no. 8, pp. 1–21, 2019. doi: 10.1002/brb3.1341.

[110] D. Maziero, C. Rondinoni, T. Marins, V. A. Stenger, and T. Ernst, "Prospective motion correction of fMRI: Improving the quality of resting state data affected by large head motion," *NeuroImage*, vol. 212, no. December 2019, p. 116594, 2020. doi: 10.1016/j.neuroimage.2020.116594.

[111] M. Zaitsev, B. Akin, P. LeVan, and B. R. Knowles, "Prospective motion correction in functional MRI," *Neuroimage*, vol. 154, pp. 33–42, 2017. doi: 10.1016/j.neuroimage.2016.11.014.

[112] M. V. Vaidya, C. M. Collins, D. K. Sodickson, R. Brown, G. C. Wiggins, and R. Lattanzi, "Dependence of B1+ and B1- Field Patterns of Surface Coils on the Electrical Properties of the Sample and the MR Operating Frequency," *Concepts Magn Reson Part B Magn Reson Eng*, vol. 46, no. 1, pp. 25–40, 2016. doi: 10.1002/cmr.b.21319.

8

[113] X. Wu, E. J. Auerbach, A. T. Vu, S. Moeller, P. F. Van de Moortele, E. Yacoub, and K. Ugurbil, "Human Connectome Project-style resting-state functional MRI at 7 Tesla using radiofrequency parallel transmission," *Neuroimage*, vol. 184, pp. 396–408, 2019. doi: 10.1016/j.neuroimage.2018.09.038.

[114] Q. X. Yang, W. Mao, J. Wang, M. B. Smith, H. Lei, X. Zhang, K. Ugurbil, and W. Chen, "Manipulation of image intensity distribution at 7.0 T: passive RF shimming and focusing with dielectric materials," *J Magn Reson Imaging*, vol. 24, no. 1, pp. 197–202, 2006. doi: 10.1002/jmri.20603.

[115] C. M. Deniz, "Parallel Transmission for Ultrahigh Field MRI," *Top Magn Reson Imaging*, vol. 28, no. 3, pp. 159–171, 2019. doi: 10.1097/rmr.0000000000000204.

[116] V. Gras, M. Boland, A. Vignaud, G. Ferrand, A. Amadon, F. Mauconduit, D. Le Bihan, T. Stöcker, and N. Boulant, "Homogeneous non-selective and slice-selective parallel-transmit excitations at 7 Tesla with universal pulses: A validation study on two commercial RF coils," *PLoS One*, vol. 12, no. 8, p. e0183562, 2017. doi: 10.1371/journal.pone.0183562.

[117] D. A. Feinberg and E. Yacoub, "The rapid development of high speed, resolution and precision in fMRI," *Neuroimage*, vol. 62, no. 2, pp. 720–725, 2012. doi: 10.1016/j.neuroimage.2012.01.049.

[118] W. van der Zwaag, O. Reynaud, M. Narsude, D. Gallichan, and J. P. Marques, "High spatio-temporal resolution in functional MRI with 3D echo planar imaging using cylindrical excitation and a CAIPIRINHA undersampling pattern," *Magn Reson Med*, vol. 79, no. 5, pp. 2589–2596, 2018. doi: 10.1002/mrm.26906.

[119] J. Bause, P. Ehses, C. Mirkes, G. Shajan, K. Scheffler, and R. Pohmann, "Quantitative and functional pulsed arterial spin labeling in the human brain at 9.4 T," *Magn Reson Med*, vol. 75, no. 3, pp. 1054–1063, 2016. doi: 10.1002/mrm.25671.

[120] A. Kumar, W. A. Edelstein, and P. A. Bottomley, "Noise figure limits for circular loop MR coils," *Magn Reson Med*, vol. 61, no. 5, pp. 1201–1209, 2009. doi: 10.1002/mrm.21948.

[121] P. B. Roemer, W. A. Edelstein, C. E. Hayes, S. P. Souza, and O. M. Mueller, "The NMR phased array," *Magn Reson Med*, vol. 16, no. 2, pp. 192–225, 1990. doi: 10.1002/mrm.1910160203.

[122] N. Petridou, M. Italiaander, B. L. van de Bank, J. C. W. Siero, P. R. Luijten, and D. W. J. Klomp, "Pushing the limits of high-resolution functional MRI using a simple high-density multi-element coil design," *Nmr in Biomedicine*, vol. 26, no. 1, pp. 65–73, 2013. doi: 10.1002/nbm.2820.

[123] N. Priovoulos, T. Roos, Ö. Ipek, E. F. Meliado, R. O. Nkrumah, D. W. Klomp, and W. van der Zwaag, "A local multi-transmit coil combined with a high-density receive array for cerebellar fMRI at 7 T," *NMR in Biomedicine*, no. September 2020, pp. 1–13, 2021. doi: 10.1002/nbm.4586.

[124] S. A. Anteraper, S. Whitfield-Gabrieli, B. Keil, S. Shannon, J. D. Gabrieli, and C. Triantafyllou, "Exploring functional connectivity networks with multichannel brain array coils," *Brain Connect*, vol. 3, no. 3, pp. 302–315, 2013. doi: 10.1089/brain.2012.0113.

[125] M. Narsude, W. van der Zwaag, D. Gallichan, R. Gruetter, and J. Marques, "Resting state networks detection, the importance of high temporal resolution: a comparison study between 2D-EPI, SMS 2D-EPI and 3D-EPI-CAIPI acquisitions," in *Proc. Intl. Soc. Mag. Reson. Med*, vol. 22, p. 4325, 2014.

[126] C. Preibisch, G. J. Castrillon, M. Buhrer, and V. Riedl, "Evaluation of Multiband EPI Acquisitions for Resting State fMRI," *PLoS One*, vol. 10, no. 9, p. e0136961, 2015. doi: 10.1371/journal.pone.0136961.

8

[127] R. Salomon, J. Darulova, M. Narsude, and W. van der Zwaag, "Comparison of an 8-channel and a 32-channel coil for high-resolution FMRI at 7 T," *Brain Topogr*, vol. 27, no. 2, pp. 209–212, 2014. doi: 10.1007/s10548-013-0298-6.

[128] K. A. Smitha, K. M. Arun, P. G. Rajesh, S. E. Joel, R. Venkatesan, B. Thomas, and C. Kesavadas, "Multiband fMRI as a plausible, time-saving technique for resting-state data acquisition: Study on functional connectivity mapping using graph theoretical measures," *Magn Reson Imaging*, vol. 53, pp. 1–6, 2018. doi: 10.1016/j.mri.2018.06.013.

[129] A. D. Hendriks, F. D'Agata, L. Raimondo, T. Schakel, L. Geerts, P. R. Luijten, D. W. Klomp, and N. Petridou, "Pushing functional MRI spatial and temporal resolution further: High-density receive arrays combined with shot-selective 2D CAIPIRINHA for 3D echo-planar imaging at 7 T," *NMR in Biomedicine*, vol. 33, no. 5, pp. 1–13, 2020. doi: 10.1002/nbm.4281.

[130] G. C. Wiggins, J. R. Polimeni, A. Potthast, M. Schmitt, V. Alagappan, and L. L. Wald, "96-Channel receive-only head coil for 3 Tesla: design optimization and evaluation," *Magn Reson Med*, vol. 62, no. 3, pp. 754–762, 2009. doi: 10.1002/mrm.22028.

[131] S. Bollmann and M. Barth, "New acquisition techniques and their prospects for the achievable resolution of fMRI," *Prog Neurobiol*, p. 101936, 2020. doi: 10.1016/j.pneurobio.2020.101936.

[132] J. A. McNab, B. L. Edlow, T. Witzel, S. Y. Huang, H. Bhat, K. Heberlein, T. Feiweier, K. Liu, B. Keil, J. Cohen-Adad, M. D. Tisdall, R. D. Folkerth, H. C. Kinney, and L. L. Wald, "The Human Connectome Project and beyond: initial applications of 300 mT/m gradients," *Neuroimage*, vol. 80, pp. 234–245, 2013. doi: 10.1016/j.neuroimage.2013.05.074.

[133] M. Barth, F. Breuer, P. J. Koopmans, D. G. Norris, and B. A. Poser, "Simultaneous multi-slice (SMS) imaging techniques," *Magn Reson Med*, vol. 75, no. 1, pp. 63–81, 2016. doi: 10.1002/mrm.25897.

[134] E. T. Tan, S. K. Lee, P. T. Weavers, D. Graziani, J. E. Piel, Y. Shu, J. Huston 3rd, M. A. Bernstein, and T. K. Foo, "High slew-rate head-only gradient for improving distortion in echo planar imaging: Preliminary experience," *J Magn Reson Imaging*, vol. 44, no. 3, pp. 653–664, 2016. doi: 10.1002/jmri.25210.

[135] M. Davids, B. Guerin, A. Vom Endt, L. R. Schad, and L. L. Wald, "Prediction of peripheral nerve stimulation thresholds of MRI gradient coils using coupled electromagnetic and neurodynamic simulations," *Magn Reson Med*, vol. 81, no. 1, pp. 686–701, 2019. doi: 10.1002/mrm.27382.

[136] E. C. Wong, "Local head gradient coils: window(s) of opportunity," *Neuroimage*, vol. 62, no. 2, pp. 660–664, 2012. doi: 10.1016/j.neuroimage.2012.01.025.

[137] J. E. Chen, L. D. Lewis, C. Chang, Q. Tian, N. E. Fultz, N. A. Ohringer, B. R. Rosen, and J. R. Polimeni, "Resting-state "physiological networks"," *Neuroimage*, vol. 213, p. 116707, 2020. doi: 10.1016/j.neuroimage.2020.116707.

[138] N. Huotari, L. Raitamaa, H. Helakari, J. Kananen, V. Raatikainen, A. Rasila, T. Tuovinen, J. Kantola, V. Borchardt, V. J. Kiviniemi, and V. O. Korhonen, "Sampling Rate Effects on Resting State fMRI Metrics," *Front Neurosci*, vol. 13, p. 279, 2019. doi: 10.3389/fnins.2019.00279.

[139] U. Agrawal, E. N. Brown, and L. D. Lewis, "Model-based physiological noise removal in fast fMRI," *Neuroimage*, vol. 205, p. 116231, 2020. doi: 10.1016/j.neuroimage.2019.116231.

[140] H. I. Jacobs, N. Priovoulos, B. A. Poser, L. H. Pagen, D. Ivanov, F. R. Verhey, and K. Uludag, "Dynamic behavior of the locus coeruleus during arousal-related mem-

8

ory processing in a multi-modal 7T fMRI paradigm," *Elife*, vol. 9, 2020. doi: 10.7554/eLife.52059.

[141] V. Napadow, R. Dhond, G. Conti, N. Makris, E. N. Brown, and R. Barbieri, "Brain correlates of autonomic modulation: combining heart rate variability with fMRI," *Neuroimage*, vol. 42, no. 1, pp. 169–177, 2008. doi: 10.1016/j.neuroimage.2008.04.238.

[142] N. E. Fultz, G. Bonmassar, K. Setsompop, R. A. Stickgold, B. R. Rosen, J. R. Polimeni, and L. D. Lewis, "Coupled electrophysiological, hemodynamic, and cerebrospinal fluid oscillations in human sleep," *Science*, vol. 366, no. 6465, pp. 628–631, 2019. doi: 10.1126/science.aax5440.

[143] L. Demetriou, O. S. Kowalczyk, G. Tyson, T. Bello, R. D. Newbould, and M. B. Wall, "A comprehensive evaluation of increasing temporal resolution with multiband-accelerated protocols and effects on statistical outcome measures in fMRI," *Neuroimage*, vol. 176, pp. 404–416, 2018. doi: 10.1016/j.neuroimage.2018.05.011.

[144] B. Akin, H. L. Lee, J. Hennig, and P. LeVan, "Enhanced subject-specific resting-state network detection and extraction with fast fMRI," *Hum Brain Mapp*, vol. 38, no. 2, pp. 817–830, 2017. doi: 10.1002/hbm.23420.

[145] J. E. Chen, J. R. Polimeni, S. Bollmann, and G. H. Glover, "On the analysis of rapidly sampled fMRI data," *Neuroimage*, vol. 188, pp. 807–820, 2019. doi: 10.1016/j.neuroimage.2019.02.008.

[146] S. R. Gohel and B. B. Biswal, "Functional integration between brain regions at rest occurs in multiple-frequency bands," *Brain Connect*, vol. 5, no. 1, pp. 23–34, 2015. doi: 10.1089/brain.2013.0210.

[147] M. Dai, Z. Zhang, and A. Srivastava, "Testing Stationarity of Brain Functional Connectivity Using Change-Point Detection in fMRI Data," in *2016 IEEE Conference on Computer Vision and Pattern Recognition Workshops (CVPRW)*, pp. 981–989, 2016. doi: 10.1109/CVPRW.2016.126.

[148] D. T. Jones, P. Vemuri, M. C. Murphy, J. L. Gunter, M. L. Senjem, M. M. Machulda, S. A. Przybelski, B. E. Gregg, K. Kantarci, D. S. Knopman, B. F. Boeve, R. C. Petersen, and C. R. Jack Jr., "Non-stationarity in the "resting brain's" modular architecture," *PLoS One*, vol. 7, no. 6, p. e39731, 2012. doi: 10.1371/journal.pone.0039731.

[149] M. G. Preti, T. A. Bolton, and D. V. Ville, "The dynamic functional connectome: State-of-the-art and perspectives," *Neuroimage*, 2016. doi: 10.1016/j.neuroimage.2016.12.061.

[150] A. Zalesky, A. Fornito, L. Cocchi, L. L. Gollo, and M. Breakspear, "Time-resolved resting-state brain networks," *Proc Natl Acad Sci U S A*, vol. 111, no. 28, pp. 10341–10346, 2014. doi: 10.1073/pnas.1400181111.

[151] N. Todd, S. Moeller, E. J. Auerbach, E. Yacoub, G. Flandin, and N. Weiskopf, "Evaluation of 2D multiband EPI imaging for high-resolution, whole-brain, task-based fMRI studies at 3T: Sensitivity and slice leakage artifacts," *NeuroImage*, vol. 124, pp. 32–42, 2016. doi: 10.1016/j.neuroimage.2015.08.056.

[152] F. A. Breuer, M. Blaimer, R. M. Heidemann, M. F. Mueller, M. A. Griswold, and P. M. Jakob, "Controlled aliasing in parallel imaging results in higher acceleration (CAIPIRINHA) for multi-slice imaging," *Magn Reson Med*, vol. 53, no. 3, pp. 684–691, 2005. doi: 10.1002/mrm.20401.

[153] K. Setsompop, B. A. Gagoski, J. R. Polimeni, T. Witzel, V. J. Wedeen, and L. L. Wald, "Blipped-controlled aliasing in parallel imaging for simultaneous multislice echo planar imaging with reduced g-factor penalty," *Magn Reson Med*, vol. 67, no. 5, pp. 1210–1224, 2012. doi: 10.1002/mrm.23097.

8

[154] D. A. Feinberg, J. D. Hale, J. C. Watts, L. Kaufman, and A. Mark, "Halving MR imaging time by conjugation: demonstration at 3.5 kG.," *Radiology*, vol. 161, pp. 527–531, nov 1986. doi: 10.1148/radiology.161.2.3763926.

[155] S. Bollmann, A. M. Puckett, R. Cunnington, and M. Barth, "Serial correlations in single-subject fMRI with sub-second TR," *NeuroImage*, vol. 166, no. October 2017, pp. 152–166, 2018. doi: 10.1016/j.neuroimage.2017.10.043.

[156] M. G. Bright, C. R. Tench, and K. Murphy, "Potential pitfalls when denoising resting state fMRI data using nuisance regression," *NeuroImage*, vol. 154, no. December 2016, pp. 159–168, 2017. doi: 10.1016/j.neuroimage.2016.12.027.

[157] B. A. Poser, P. J. Koopmans, T. Witzel, L. L. Wald, and M. Barth, "Three dimensional echo-planar imaging at 7 Tesla," *Neuroimage*, vol. 51, no. 1, pp. 261–266, 2010. doi: 10.1016/j.neuroimage.2010.01.108.

[158] M. A. Batson, N. Petridou, D. W. Klomp, M. A. Frens, and S. F. Neggers, "Single session imaging of cerebellum at 7 Tesla: obtaining structure and function of multiple motor subsystems in individual subjects," *PLoS One*, vol. 10, no. 8, p. e0134933, 2015. doi: 10.1371/journal.pone.0134933.

[159] M. Narsude, D. Gallichan, W. van der Zwaag, R. Gruetter, and J. P. Marques, "Three-dimensional echo planar imaging with controlled aliasing: A sequence for high temporal resolution functional MRI," *Magn Reson Med*, vol. 75, no. 6, pp. 2350–2361, 2016. doi: 10.1002/mrm.25835.

[160] J. Jorge, P. Figueiredo, W. van der Zwaag, and J. P. Marques, "Signal fluctuations in fMRI data acquired with 2D-EPI and 3D-EPI at 7 Tesla," *Magn Reson Imaging*, vol. 31, no. 2, pp. 212–220, 2013. doi: 10.1016/j.mri.2012.07.001.

[161] O. Reynaud, J. Jorge, R. Gruetter, J. P. Marques, and W. van der Zwaag, "Influence of physiological noise on accelerated 2D and 3D resting state functional MRI data at 7 T," *Magn Reson Med*, vol. 78, no. 3, pp. 888–896, 2017. doi: 10.1002/mrm.26823.

[162] R. Stirnberg, W. Huijbers, D. Brenner, B. A. Poser, M. Breteler, and T. Stocker, "Rapid whole-brain resting-state fMRI at 3 T: Efficiency-optimized three-dimensional EPI versus repetition time-matched simultaneous-multi-slice EPI," *Neuroimage*, vol. 163, pp. 81–92, 2017. doi: 10.1016/j.neuroimage.2017.08.031.

[163] B. Zahneisen, T. Hugger, K. J. Lee, P. LeVan, M. Reisert, H. L. Lee, J. Asslander, M. Zaitsev, and J. Hennig, "Single shot concentric shells trajectories for ultra fast fMRI," *Magn Reson Med*, vol. 68, no. 2, pp. 484–494, 2012. doi: 10.1002/mrm.23256.

[164] J. Hennig, V. Kiviniemi, B. Riemenschneider, A. Barghoorn, B. Akin, F. Wang, and P. LeVan, "15 Years MR-encephalography," *MAGMA*, 2020. doi: 10.1007/s10334-020-00891-z.

[165] J. Jacobs, J. Stich, B. Zahneisen, J. Asslander, G. Ramantani, A. Schulze-Bonhage, R. Korinthenberg, J. Hennig, and P. LeVan, "Fast fMRI provides high statistical power in the analysis of epileptic networks," *Neuroimage*, vol. 88, pp. 282–294, 2014. doi: 10.1016/j.neuroimage.2013.10.018.

[166] F. H. Lin, K. W. Tsai, Y. H. Chu, T. Witzel, A. Nummenmaa, T. Raij, J. Ahveninen, W. J. Kuo, and J. W. Belliveau, "Ultrafast inverse imaging techniques for fMRI," *NeuroImage*, vol. 62, no. 2, pp. 699–705, 2012. doi: 10.1016/j.neuroimage.2012.01.072.

[167] R. Boyacioğlu and M. Barth, "Generalized inverse imaging (GIN): Ultrafast fMRI with physiological noise correction," *Magnetic Resonance in Medicine*, vol. 70, no. 4, pp. 962–971, 2013. doi: 10.1002/mrm.24528.

[168] J.-h. Gao, J. Xiong, S. Lai, E. M. Haacke, M. G. Woldorff, J. Li, and P. T. Fox, "Improving the Temporal Resolution," *Magn Reson Med*, vol. 35, no. 6, pp. 854–860, 1996.

8

[169] M. Zaitsev, K. Zilles, and N. J. Shah, "Shared κ-space echo planar imaging with keyhole," *Magnetic Resonance in Medicine*, vol. 45, no. 1, pp. 109–117, 2001. doi: 10.1002/1522-2594(200101)45:1<109::AID-MRM1015>3.0.CO;2-X.

[170] S. D. Yun, R. Weidner, P. H. Weiss, and N. J. Shah, "Evaluating the Utility of EPIK in a Finger Tapping fMRI Experiment using BOLD Detection and Effective Connectivity," *Scientific Reports*, vol. 9, no. 1, pp. 1–11, 2019. doi: 10.1038/s41598-019-47341-y.

[171] P. Kundu, S. J. Inati, J. W. Evans, W. M. Luh, and P. A. Bandettini, "Differentiating BOLD and non-BOLD signals in fMRI time series using multi-echo EPI," *NeuroImage*, vol. 60, no. 3, pp. 1759–1770, 2012. doi: 10.1016/j.neuroimage.2011.12.028.

[172] B. A. Poser, M. J. Versluis, J. M. Hoogduin, and D. G. Norris, "BOLD contrast sensitivity enhancement and artifact reduction with multiecho EPI: Parallel-acquired inhomogeneity-desensitized fMRI," *Magnetic Resonance in Medicine*, vol. 55, no. 6, pp. 1227–1235, 2006. doi: 10.1002/mrm.20900.

[173] S. Posse, "Multi-echo acquisition," *NeuroImage*, vol. 62, no. 2, pp. 665–671, 2012. doi: 10.1016/j.neuroimage.2011.10.057.

[174] M. G. Bright and K. Murphy, "Removing motion and physiological artifacts from intrinsic BOLD fluctuations using short echo data," *NeuroImage*, vol. 64, no. 1, pp. 526–537, 2013. doi: 10.1016/j.neuroimage.2012.09.043.

[175] P. F. Buur, B. A. Poser, and D. G. Norris, "A dual echo approach to removing motion artefacts in fMRI time series," *NMR in Biomedicine*, vol. 22, no. 5, pp. 551–560, 2009. doi: 10.1002/nbm.1371.

[176] P. Kundu, V. Voon, P. Balchandani, M. V. Lombardo, B. A. Poser, and P. A. Bandettini, "Multi-echo fMRI: A review of applications in fMRI denoising and analysis of BOLD signals," *NeuroImage*, vol. 154, no. March, pp. 59–80, 2017. doi: 10.1016/j.neuroimage.2017.03.033.

[177] S. J. Peltier and D. C. Noll, "T2* Dependence of Low Frequency Functional Connectivity," *NeuroImage*, vol. 16, no. 4, pp. 985–992, 2002. doi: 10.1006/nimg.2002.1141.

[178] G. de Hollander, M. C. Keuken, W. van der Zwaag, B. U. Forstmann, and R. Trampel, "Comparing functional MRI protocols for small, iron-rich basal ganglia nuclei such as the subthalamic nucleus at 7 T and 3 T," *Human Brain Mapping*, vol. 38, pp. 3226–3248, jun 2017. doi: 10.1002/hbm.23586.

[179] L. S. Morris, P. Kundu, S. Costi, A. Collins, M. Schneider, G. Verma, P. Balchandani, and J. W. Murrough, "Ultra-high field MRI reveals mood-related circuit disturbances in depression: a comparison between 3-Tesla and 7-Tesla," *Translational Psychiatry*, vol. 9, no. 1, 2019. doi: 10.1038/s41398-019-0425-6.

[180] O. Dipasquale, A. Sethi, M. M. Lagan, F. Baglio, G. Baselli, P. Kundu, N. A. Harrison, and M. Cercignani, "Comparing resting state fMRI de-noising approaches using multi-and single-echo acquisitions," *PLoS ONE*, vol. 12, no. 3, pp. 1–25, 2017. doi: 10.1371/journal.pone.0173289.

[181] E. Kirilina, A. Lutti, B. A. Poser, F. Blankenburg, and N. Weiskopf, "The quest for the best: The impact of different EPI sequences on the sensitivity of random effect fMRI group analyses," *NeuroImage*, vol. 126, pp. 49–59, 2016. doi: 10.1016/j.neuroimage.2015.10.071.

[182] J. D. Power, M. Plitt, S. J. Gotts, P. Kundu, V. Voon, P. A. Bandettini, and A. Martin, "Ridding fMRI data of motion-related influences: Removal of signals with distinct spatial and physical bases in multiecho data," *Proceedings of the National Academy of Sciences of the United States of America*, vol. 115, no. 9, pp. E2105–E2114, 2018. doi: 10.1073/pnas.1720985115.

8

[183] J. Gonzalez-Castillo, P. Panwar, L. C. Buchanan, C. Caballero-Gaudes, D. A. Handwerker, D. C. Jangraw, V. Zachariou, S. Inati, V. Roopchansingh, J. A. Derbyshire, and P. A. Bandettini, "Evaluation of multi-echo ICA denoising for task based fMRI studies: Block designs, rapid event-related designs, and cardiac-gated fMRI," *NeuroImage*, vol. 141, pp. 452–468, 2016. doi: 10.1016/j.neuroimage.2016.07.049.

[184] K. Baek, L. S. Morris, P. Kundu, and V. Voon, "Disrupted resting-state brain network properties in obesity: Decreased global and putaminal cortico-striatal network efficiency," *Psychological Medicine*, vol. 47, no. 4, pp. 585–596, 2017. doi: 10.1017/S0033291716002646.

[185] M. V. Lombardo, B. Auyeung, R. J. Holt, J. Waldman, A. N. Ruigrok, N. Mooney, E. T. Bullmore, S. Baron-Cohen, and P. Kundu, "Improving effect size estimation and statistical power with multi-echo fMRI and its impact on understanding the neural systems supporting mentalizing," *NeuroImage*, vol. 142, pp. 55–66, 2016. doi: 10.1016/j.neuroimage.2016.07.022.

[186] C. J. Lynch, J. D. Power, M. A. Scult, M. Dubin, F. M. Gunning, and C. Liston, "Rapid Precision Functional Mapping of Individuals Using Multi-Echo fMRI," *Cell Reports*, vol. 33, no. 12, p. 108540, 2020. doi: 10.1016/j.celrep.2020.108540.

[187] L. S. Morris, P. Kundu, K. Baek, M. A. Irvine, D. J. Mechelmans, J. Wood, N. A. Harrison, T. W. Robbins, E. T. Bullmore, and V. Voon, "Jumping the gun: Mapping neural correlates of waiting impulsivity and relevance across alcohol misuse," *Biological Psychiatry*, vol. 79, no. 6, pp. 499–507, 2016. doi: 10.1016/j.biopsych.2015.06.009.

[188] L. S. Morris, S. Costi, A. Tan, E. R. Stern, D. S. Charney, and J. W. Murrough, "Ketamine normalizes subgenual cingulate cortex hyper-activity in depression," *Neuropsychopharmacology*, vol. 45, no. 6, pp. 975–981, 2020. doi: 10.1038/s41386-019-0591-5.

[189] T. Nir, Y. Jacob, K.-H. Huang, A. E. Schwartz, J. W. Brallier, H. Ahn, P. Kundu, C. Y. Tang, B. N. Delman, P. J. McCormick, M. Sano, S. Deiner, M. G. Baxter, and J. S. Mincer, "Resting-state functional connectivity in early postanaesthesia recovery is characterised by globally reduced anticorrelations," *British Journal of Anaesthesia*, vol. 125, pp. 529–538, oct 2020. doi: 10.1016/j.bja.2020.06.058.

[190] P. Kundu, B. E. Benson, D. Rosen, S. Frangou, E. Leibenluft, W. M. Luh, P. A. Bandettini, D. S. Pine, and M. Ernst, "The integration of functional brain activity from adolescence to adulthood," *Journal of Neuroscience*, vol. 38, no. 14, pp. 3559–3570, 2018. doi: 10.1523/JNEUROSCI.1864-17.2018.

[191] F. Váša, R. Romero-Garcia, M. G. Kitzbichler, J. Seidlitz, K. J. Whitaker, M. M. Vaghi, P. Kundu, A. X. Patel, P. Fonagy, R. J. Dolan, P. B. Jones, I. M. Goodyer, P. E. Vértes, and E. T. Bullmore, "Conservative and disruptive modes of adolescent change in human brain functional connectivity," *Proceedings of the National Academy of Sciences of the United States of America*, vol. 117, no. 6, pp. 3248–3253, 2020. doi: 10.1073/pnas.1906144117.

[192] D. G. Norris, "Spin-echo fMRI: The poor relation?," *NeuroImage*, vol. 62, no. 2, pp. 1109–1115, 2012. doi: 10.1016/j.neuroimage.2012.01.003.

[193] R. Boyacioğlu, J. Schulz, N. C. Müller, P. J. Koopmans, M. Barth, and D. G. Norris, "Whole brain, high resolution multiband spin-echo EPI fMRI at 7T: A comparison with gradient-echo EPI using a color-word Stroop task," *NeuroImage*, vol. 97, pp. 142–150, 2014. doi: 10.1016/j.neuroimage.2014.04.011.

[194] P. Chiacchiaretta and A. Ferretti, "Resting state BOLD functional connectivity at 3T: Spin echo versus gradient echo EPI," *PLoS ONE*, vol. 10, no. 3, 2015. doi: 10.1371/journal.pone.0120398.

8

[195] Y. B. Khatamian, A. M. Golestani, D. M. Ragot, and J. J. Chen, "Spin-Echo Resting-State Functional Connectivity in High-Susceptibility Regions: Accuracy, Reliability, and the Impact of Physiological Noise," *Brain Connectivity*, vol. 6, pp. 283–297, may 2016. doi: 10.1089/brain.2015.0365.

[196] B. A. Poser and D. G. Norris, "Fast spin echo sequences for BOLD functional MRI," *Magnetic Resonance Materials in Physics, Biology and Medicine*, vol. 20, no. 1, pp. 11–17, 2007. doi: 10.1007/s10334-006-0063-x.

[197] A. Borogovac and I. Asllani, "Arterial spin labeling (ASL) fMRI: Advantages, theoretical constrains and experimental challenges in neurosciences," *International Journal of Biomedical Imaging*, vol. 2012, 2012. doi: 10.1155/2012/818456.

[198] J. J. Chen, K. Jann, and D. J. Wang, "Characterizing Resting-State Brain Function Using Arterial Spin Labeling," *Brain Connectivity*, vol. 5, pp. 527–542, nov 2015. doi: 10.1089/brain.2015.0344.

[199] M. Vidorreta, Z. Wang, I. Rodriguez, M. A. Pastor, J. A. Detre, and M. A. Fernández-Seara, "Comparison of 2D and 3D single-shot ASL perfusion fMRI sequences," *NeuroImage*, vol. 66, pp. 662–671, 2013. doi: 10.1016/j.neuroimage.2012.10.087.

[200] R. B. Buxton, L. R. Frank, E. C. Wong, B. Siewert, S. Warach, and R. R. Edelman, "A general kinetic model for quantitative perfusion imaging with arterial spin labeling.," *Magnetic Resonance in Medicine*, vol. 40, no. 3, pp. 383–396, 1998. doi: 10.1002/mrm.1910400308.

[201] D. C. Alsop, J. A. Detre, X. Golay, M. Günther, J. Hendrikse, L. Hernandez-Garcia, H. Lu, B. J. Macintosh, L. M. Parkes, M. Smits, M. J. Van Osch, D. J. Wang, E. C. Wong, and G. Zaharchuk, "Recommended implementation of arterial spin-labeled Perfusion mri for clinical applications: A consensus of the ISMRM Perfusion Study group and the European consortium for ASL in dementia," *Magnetic Resonance in Medicine*, vol. 73, pp. 102–116, jan 2015. doi: 10.1002/mrm.25197.

[202] M. Günther, K. Oshio, and D. A. Feinberg, "Single-shot 3D imaging techniques improve arterial spin labeling perfusion measurements," *Magnetic Resonance in Medicine*, vol. 54, pp. 491–498, aug 2005. doi: 10.1002/mrm.20580.

[203] X. Liang, J. D. Tournier, R. Masterton, A. Connelly, and F. Calamante, "A k-space sharing 3D GRASE pseudocontinuous ASL method for whole-brain resting-state functional connectivity," *International Journal of Imaging Systems and Technology*, vol. 22, no. 1, pp. 37–43, 2012. doi: 10.1002/ima.22006.

[204] D. M. Garcia, G. Duhamel, and D. C. Alsop, "Efficiency of inversion pulses for background suppressed arterial spin labeling," *Magnetic Resonance in Medicine*, vol. 54, no. 2, pp. 366–372, 2005. doi: 10.1002/mrm.20556.

[205] Z. Zuo, R. Wang, Y. Zhuo, R. Xue, K. S. S. Lawrence, D. J. J. Wang, K. S. St. Lawrence, and D. J. J. Wang, "Turbo-FLASH Based Arterial Spin Labeled Perfusion MRI at 7 T," *PLoS ONE*, vol. 8, no. 6, pp. 1–9, 2013. doi: 10.1371/journal.pone.0066612.

[206] B. B. Biswal, J. V. Kylen, and J. S. Hyde, "Simultaneous assessment of flow and BOLD signals in resting-state functional connectivity maps," *NMR in Biomedicine*, vol. 10, no. 4-5, pp. 165–170, 1997. doi: 10.1002/(SICI)1099-1492(199706/08)10:4/5<165::AID-NBM454>3.0.CO;2-7.

[207] K. Jann, D. G. Gee, E. Kilroy, S. Schwab, R. X. Smith, T. D. Cannon, and D. J. J. Wang, "Functional connectivity in BOLD and CBF data: Similarity and reliability of resting brain networks," *NeuroImage*, vol. 106, pp. 111–122, feb 2015. doi: 10.1016/j.neuroimage.2014.11.028.

8

[208] X. Liang, A. Connelly, and F. Calamante, "Graph analysis of resting-state ASL perfusion MRI data: Nonlinear correlations among CBF and network metrics," *NeuroImage*, vol. 87, pp. 265–275, 2014. doi: 10.1016/j.neuroimage.2013.11.013.

[209] R. Viviani, I. Messina, and M. Walter, "Resting state functional connectivity in perfusion imaging: Correlation maps with Bold connectivity and resting state perfusion," *PLoS ONE*, vol. 6, no. 11, 2011. doi: 10.1371/journal.pone.0027050.

[210] K.-H. Chuang, P. van Gelderen, H. Merkle, J. Bodurka, V. N. Ikonomidou, A. P. Koretsky, J. H. Duyn, and S. L. Talagala, "Mapping resting-state functional connectivity using perfusion MRI," *NeuroImage*, vol. 40, pp. 1595–1605, may 2008. doi: 10.1016/j.neuroimage.2008.01.006.

[211] X. Liang, A. Connelly, and F. Calamante, "Voxel-Wise Functional Connectomics Using Arterial Spin Labeling Functional Magnetic Resonance Imaging: The Role of Denoising," *Brain Connectivity*, vol. 5, no. 9, pp. 543–553, 2015. doi: 10.1089/brain.2014.0290.

[212] J. P. S. Silva, L. d. M. Mônaco, A. M. Paschoal, Í. A. F. de Oliveira, and R. F. Leoni, "Effects of global signal regression and subtraction methods on resting-state functional connectivity using arterial spin labeling data," *Magnetic Resonance Imaging*, vol. 51, pp. 151–157, sep 2018. doi: 10.1016/j.mri.2018.05.006.

[213] Z. Wang, G. K. Aguirre, H. Rao, J. Wang, M. A. Fernández-Seara, A. R. Childress, and J. A. Detre, "Empirical optimization of ASL data analysis using an ASL data processing toolbox: ASLtbx," *Magnetic Resonance Imaging*, vol. 26, no. 2, pp. 261–269, 2008. doi: 10.1016/j.mri.2007.07.003.

[214] J. Kindler, K. Jann, P. Homan, M. Hauf, S. Walther, W. Strik, T. Dierks, and D. Hubl, "Static and dynamic characteristics of cerebral blood flow during the resting state in schizophrenia," *Schizophrenia Bulletin*, vol. 41, no. 1, pp. 163–170, 2015. doi: 10.1093/schbul/sbt180.

[215] Í. A. Oliveira, T. M. Guimarães, R. M. Souza, A. C. dos Santos, J. P. Machado-de Sousa, J. E. Hallak, and R. F. Leoni, "Brain functional and perfusional alterations in schizophrenia: an arterial spin labeling study," *Psychiatry Research: Neuroimaging*, vol. 272, pp. 71–78, feb 2018. doi: 10.1016/j.pscychresns.2017.12.001.

[216] J. Zhu, C. Zhuo, W. Qin, Y. Xu, L. Xu, X. Liu, and C. Yu, "Altered resting-state cerebral blood flow and its connectivity in schizophrenia," *Journal of Psychiatric Research*, vol. 63, pp. 28–35, 2015. doi: 10.1016/j.jpsychires.2015.03.002.

[217] J. Boissoneault, J. Letzen, S. Lai, M. E. Robinson, and R. Staud, "Static and dynamic functional connectivity in patients with chronic fatigue syndrome: Use of arterial spin labelling fMRI," *Clinical Physiology and Functional Imaging*, pp. 1–10, 2016. doi: 10.1111/cpf.12393.

[218] I. Boscolo Galazzo, S. F. Storti, A. Barnes, B. De Blasi, E. De Vita, M. Koepp, J. S. Duncan, A. Groves, F. B. Pizzini, G. Menegaz, and F. Fraioli, "Arterial spin labeling reveals disrupted brain networks and functional connectivity in drug-resistant temporal epilepsy," *Frontiers in Neuroinformatics*, vol. 12, no. March, pp. 1–18, 2019. doi: 10.3389/fninf.2018.00101.

[219] H. Xu, J. Li, K. Chen, H. Zhu, L. Luo, L. Yang, F. Chen, H. Ma, X. Qu, Z. Li, and R. Zhang, "Changes in resting-state cerebral blood flow and its connectivity in patients with focal to bilateral tonic-clonic seizures," *Epilepsy and Behavior*, vol. 115, p. 107687, 2021. doi: 10.1016/j.yebeh.2020.107687.

[220] A. Galiano, E. Mengual, R. García de Eulate, I. Galdeano, M. Vidorreta, M. Recio, M. Riverol, J. L. Zubieta, and M. A. Fernández-Seara, "Coupling of cerebral blood flow and functional connectivity is decreased in healthy aging," *Brain Imaging and Behavior*, vol. 14, no. 2, pp. 436–450, 2020. doi: 10.1007/s11682-019-00157-w.

8

[221] D. J. Overton, N. Bhagwat, J. D. Viviano, G. R. Jacobs, and A. N. Voineskos, "Identifying psychosis spectrum youth using support vector machines and cerebral blood perfusion as measured by arterial spin labeled fMRI," *NeuroImage: Clinical*, vol. 27, no. February, p. 102304, 2020. doi: 10.1016/j.nicl.2020.102304.

[222] A. Federspiel, T. J. Müller, H. Horn, C. Kiefer, and W. K. Strik, "Comparison of spatial and temporal pattern for fMRI obtained with BOLD and arterial spin labeling," *Journal of Neural Transmission*, vol. 113, pp. 1403–1415, oct 2006. doi: 10.1007/s00702-006-0434-5.

[223] L. Huber, E. S. Finn, Y. Chai, R. Goebel, R. Stirnberg, T. Stocker, S. Marrett, K. Uludag, S. G. Kim, S. Han, P. A. Bandettini, and B. A. Poser, "Layer-dependent functional connectivity methods," *Prog Neurobiol*, p. 101835, 2020. doi: 10.1016/j.pneurobio.2020.101835.

[224] X. Miao, H. Gu, L. Yan, H. Lu, D. J. Wang, X. J. Zhou, Y. Zhuo, and Y. Yang, "Detecting resting-state brain activity by spontaneous cerebral blood volume fluctuations using whole brain vascular space occupancy imaging," *NeuroImage*, vol. 84, pp. 575–584, 2014. doi: 10.1016/j.neuroimage.2013.09.019.

[225] K. Zhang, D. Huang, and N. J. Shah, "Comparison of Resting-State Brain Activation Detected by BOLD, Blood Volume and Blood Flow," *Frontiers in Human Neuroscience*, vol. 12, pp. 1–10, nov 2018. doi: 10.3389/fnhum.2018.00443.

[226] H. Lu, X. Golay, J. J. Pekar, P. C. M. van Zijl, P. C. M. V. Zijl, and P. C. M. van Zijl, "Functional magnetic resonance imaging based on changes in vascular space occupancy," *Magnetic Resonance in Medicine*, vol. 50, pp. 263–274, aug 2003. doi: 10.1002/mrm.10519.

[227] L. Huber, J. Goense, A. J. Kennerley, R. Trampel, M. Guidi, E. Reimer, D. Ivanov, N. Neef, C. J. Gauthier, R. Turner, and H. E. Moller, "Cortical lamina-dependent blood volume changes in human brain at 7 T," *NeuroImage*, vol. 107, pp. 23–33, 2015. doi: 10.1016/j.neuroimage.2014.11.046.

[228] T. Jin and S.-G. Kim, "Cortical layer-dependent dynamic blood oxygenation, cerebral blood flow and cerebral blood volume responses during visual stimulation," *NeuroImage*, vol. 43, pp. 1–9, oct 2008. doi: 10.1016/j.neuroimage.2008.06.029.

[229] Í. A. Oliveira, W. van der Zwaag, L. Raimondo, S. O. Dumoulin, and J. C. Siero, "Comparing hand movement rate dependence of cerebral blood volume and BOLD responses at 7T," *NeuroImage*, vol. 226, p. 117623, feb 2021. doi: 10.1016/j.neuroimage.2020.117623.

[230] B. A. Poser and D. G. Norris, "3D single-shot VASO using a maxwell gradient compensated GRASE sequence," *Magnetic Resonance in Medicine*, vol. 62, pp. 255–262, jul 2009. doi: 10.1002/mrm.22000.

[231] L. Huber, D. A. Handwerker, D. C. Jangraw, G. Chen, A. Hall, C. Stüber, J. Gonzalez-Castillo, D. Ivanov, S. Marrett, M. Guidi, J. Goense, B. A. Poser, and P. A. Bandettini, "High-Resolution CBV-fMRI Allows Mapping of Laminar Activity and Connectivity of Cortical Input and Output in Human M1," *Neuron*, vol. 96, no. 6, pp. 1253–1263.e7, 2017. doi: 10.1016/j.neuron.2017.11.005.

[232] L. Huber, D. Ivanov, S. N. Krieger, M. N. Streicher, T. Mildner, B. A. Poser, H. E. Möller, and R. Turner, "Slab-selective, BOLD-corrected VASO at 7 tesla provides measures of cerebral blood volume reactivity with high signal-to-noise ratio," *Magnetic Resonance in Medicine*, vol. 72, no. 1, pp. 137–148, 2014. doi: 10.1002/mrm.24916.

[233] D. J. Felleman and D. C. Van Essen, "Distributed hierarchical processing in the primate cerebral cortex," *Cereb Cortex*, vol. 1, no. 1, pp. 1–47, 1991. doi: 10.1093/cercor/1.1.1.

8

[234] K. Kay, K. W. Jamison, L. Vizioli, R. Zhang, E. Margalit, and K. Ugurbil, "A critical assessment of data quality and venous effects in sub-millimeter fMRI," *NeuroImage*, vol. 189, pp. 847–869, 2019. doi: 10.1016/j.neuroimage.2019.02.006.

[235] M. Guidi, L. Huber, L. Lampe, A. Merola, K. Ihle, and H. E. Moller, "Cortical laminar resting-state signal fluctuations scale with the hypercapnic blood oxygenation level-dependent response," *Hum Brain Mapp*, vol. 41, no. 8, pp. 2014–2027, 2020. doi: 10.1002/hbm.24926.

[236] J. R. Polimeni, B. Fischl, D. N. Greve, and L. L. Wald, "Laminar analysis of 7T BOLD using an imposed spatial activation pattern in human V1," *NeuroImage*, vol. 52, no. 4, pp. 1334–1346, 2010. doi: 10.1016/j.neuroimage.2010.05.005.

[237] R. Turner, "How much cortex can a vein drain? Downstream dilution of activation-related cerebral blood oxygenation changes," *NeuroImage*, vol. 16, no. 4, pp. 1062–1067, 2002. doi: 10.1006/nimg.2002.1082.

[238] K. Uludağ and P. Blinder, "Linking brain vascular physiology to hemodynamic response in ultra-high field MRI," *NeuroImage*, vol. 168, no. February 2017, pp. 279–295, 2018. doi: 10.1016/j.neuroimage.2017.02.063.

[239] J. Heinzle, P. J. Koopmans, H. E. M. den Ouden, S. Raman, and K. E. Stephan, "A hemodynamic model for layered BOLD signals," *NeuroImage*, vol. 125, pp. 556–570, 2016. doi: 10.1016/j.neuroimage.2015.10.025.

[240] K. Kay, K. W. Jamison, R. Y. Zhang, and K. Ugurbil, "A temporal decomposition method for identifying venous effects in task-based fMRI," *Nat Methods*, vol. 17, no. 10, pp. 1033–1039, 2020. doi: 10.1038/s41592-020-0941-6.

[241] I. Markuerkiaga, M. Barth, and D. G. Norris, "A cortical vascular model for examining the specificity of the laminar BOLD signal," *NeuroImage*, vol. 132, pp. 491–498, 2016. doi: 10.1016/j.neuroimage.2016.02.073.

[242] I. Marquardt, M. Schneider, O. F. Gulban, D. Ivanov, and K. Uludag, "Cortical depth profiles of luminance contrast responses in human V1 and V2 using 7 T fMRI," *Hum Brain Mapp*, vol. 39, no. 7, pp. 2812–2827, 2018. doi: 10.1002/hbm.24042.

[243] M. E. Larkum, L. S. Petro, R. N. S. Sachdev, and L. Muckli, "A Perspective on Cortical Layering and Layer-Spanning Neuronal Elements," *Frontiers in Neuroanatomy*, vol. 12, no. 56, 2018. doi: 10.3389/fnana.2018.00056.

[244] S. Ogawa, R. S. Menon, D. W. Tank, S. G. Kim, H. Merkle, J. M. Ellermann, and K. Ugurbil, "Functional brain mapping by blood oxygenation level-dependent contrast magnetic resonance imaging. A comparison of signal characteristics with a biophysical model," *Biophys J*, vol. 64, no. 3, pp. 803–812, 1993. doi: 10.1016/S0006-3495(93)81441-3.

[245] A. Fracasso, P. R. Luijten, S. O. Dumoulin, and N. Petridou, "Laminar imaging of positive and negative BOLD in human visual cortex at 7T," *NeuroImage*, vol. 164, pp. 100–111, 2018. doi: 10.1016/j.neuroimage.2017.02.038.

[246] A. R. Egbert, E. Lojek, B. Biswal, A. Pluta, and G. Harmonia, "The laminar pattern of resting state in human cerebral cortex," *Magn Reson Imaging*, vol. 76, pp. 8–16, 2021. doi: 10.1016/j.mri.2020.10.013.

[247] I. Shamir and Y. Assaf, "An MRI-Based, Data-Driven Model of Cortical Laminar Connectivity," *Neuroinformatics*, 2020. doi: 10.1007/s12021-020-09491-7.

[248] P. Pais-Roldán, S. D. Yun, N. Palomero-Gallagher, and N. J. Shah, "Cortical depth-dependent human fMRI of resting-state networks using EPIK," *bioRxiv*, p. 2020.12.07.414144, 2020. doi: 10.1101/2020.12.07.414144.

[249] D. Sharoh, T. van Mourik, L. J. Bains, K. Segaert, K. Weber, P. Hagoort, and D. G. Norris, "Laminar specific fMRI reveals directed interactions in distributed networks dur-

8

ing language processing," *Proceedings of the National Academy of Sciences*, vol. 116, no. 42, pp. 21185–21190, 2019. doi: 10.1073/pnas.1907858116.

[250] P.-Y. Wu, Y.-H. Chu, J.-F. L. Lin, W.-J. Kuo, and F.-H. Lin, "Feature-dependent intrinsic functional connectivity across cortical depths in the human auditory cortex," *Scientific Reports*, vol. 8, no. 1, p. 13287, 2018. doi: 10.1038/s41598-018-31292-x.

[251] M. J. Van Osch, W. M. Teeuwisse, M. A. Van Walderveen, J. Hendrikse, D. A. Kies, and M. A. Van Buchem, "Can arterial spin labeling detect white matter perfusion signal?," *Magnetic Resonance in Medicine*, vol. 62, no. 1, pp. 165–173, 2009. doi: 10.1002/mrm.22002.

[252] J. H. Jensen, H. Lu, and M. Inglese, "Microvessel density estimation in the human brain by means of dynamic contrast-enhanced echo-planar imaging," *Magnetic Resonance in Medicine*, vol. 56, no. 5, pp. 1145–1150, 2006. doi: 10.1002/mrm.21052.

[253] J. R. Gawryluk, E. L. Mazerolle, and R. C. D'Arcy, "Does functional MRI detect activation in white matter? A review of emerging evidence, issues, and future directions," *Frontiers in Neuroscience*, vol. 8, no. 8 JUL, pp. 1–12, 2014. doi: 10.3389/fnins.2014.00239.

[254] J. C. Gore, M. Li, Y. Gao, T. L. Wu, K. G. Schilling, Y. Huang, A. Mishra, A. T. Newton, B. P. Rogers, L. M. Chen, A. W. Anderson, and Z. Ding, "Functional MRI and resting state connectivity in white matter - a mini-review," *Magnetic Resonance Imaging*, vol. 63, no. July, pp. 1–11, 2019. doi: 10.1016/j.mri.2019.07.017.

[255] Z. Ding, R. Xu, S. K. Bailey, T. L. Wu, V. L. Morgan, L. E. Cutting, A. W. Anderson, and J. C. Gore, "Visualizing functional pathways in the human brain using correlation tensors and magnetic resonance imaging," *Magnetic Resonance Imaging*, vol. 34, no. 1, pp. 8–17, 2016. doi: 10.1016/j.mri.2015.10.003.

[256] L. Marussich, K. H. Lu, H. Wen, and Z. Liu, "Mapping white-matter functional organization at rest and during naturalistic visual perception," *NeuroImage*, vol. 146, pp. 1128–1141, 2017. doi: 10.1016/j.neuroimage.2016.10.005.

[257] M. Li, Y. Gao, F. Gao, A. W. Anderson, Z. Ding, and J. C. Gore, "Functional engagement of white matter in resting-state brain networks," *NeuroImage*, vol. 220, no. February, p. 117096, 2020. doi: 10.1016/j.neuroimage.2020.117096.

[258] T. Wang, D. M. Wilkes, M. Li, X. Wu, J. C. Gore, and Z. Ding, "Hemodynamic Response Function in Brain White Matter in a Resting State," *Cerebral Cortex Communications*, vol. 1, no. 1, pp. 1–13, 2020. doi: 10.1093/texcom/tgaa056.

[259] Y. Jiang, L. Song, X. Li, Y. Zhang, Y. Chen, S. Jiang, C. Hou, D. Yao, X. Wang, and C. Luo, "Dysfunctional white-matter networks in medicated and unmedicated benign epilepsy with centrotemporal spikes," *Human Brain Mapping*, vol. 40, no. 10, pp. 3113–3124, 2019. doi: 10.1002/hbm.24584.

[260] H. Lin, M. Li, Y. Zhan, L. Lin, K. Yang, S. Hu, and Y. Han, "Disrupted white matter functional connectivity in aMCI APOEϵ4 carriers: a resting-state study," *Brain Imaging and Behavior*, 2020. doi: 10.1007/s11682-020-00367-7.

[261] J. H. Duyn, "The future of ultra-high field MRI and fMRI for study of the human brain," *NeuroImage*, vol. 62, no. 2, pp. 1241–1248, 2012. doi: 10.1016/j.neuroimage.2011.10.065.

[262] J. B. Goense and N. K. Logothetis, "Laminar specificity in monkey V1 using high-resolution SE-fMRI," *Magnetic Resonance Imaging*, vol. 24, no. 4, pp. 381–392, 2006. doi: 10.1016/j.mri.2005.12.032.

[263] J. Lee, C. Ehlers, F. Crews, M. Niethammer, F. Budin, B. Paniagua, K. Sulik, J. Johns, M. Styner, and I. Oguz, "Automatic cortical thickness analysis on rodent

8

brain," *Medical Imaging 2011: Image Processing*, vol. 7962, p. 796248, 2011. doi: 10.1117/12.878305.

[264] Y. Hirano, B. Stefanovic, and A. C. Silva, "Spatiotemporal evolution of the functional magnetic resonance imaging response to ultrashort stimuli," *Journal of Neuroscience*, vol. 31, no. 4, pp. 1440–1447, 2011. doi: 10.1523/JNEUROSCI.3986-10.2011.

[265] A. J. Poplawsky, M. Fukuda, M. Murphy, and S. G. Kim, "Layer-specific fMRI responses to excitatory and inhibitory neuronal activities in the olfactory bulb," *Journal of Neuroscience*, vol. 35, no. 46, pp. 15263–15275, 2015. doi: 10.1523/JNEUROSCI.1015-15.2015.

[266] A. C. Silva and A. P. Koretsky, "Laminar specificity of functional MRI onset times during somatosensory stimulation in rat," *Proceedings of the National Academy of Sciences of the United States of America*, vol. 99, no. 23, pp. 15182–15187, 2002. doi: 10.1073/pnas.222561899.

[267] P. J. Koopmans, M. Barth, and D. G. Norris, "Layer-specific BOLD activation in human V1," *Human Brain Mapping*, vol. 31, no. 9, pp. 1297–1304, 2010. doi: 10.1002/hbm.20936.

[268] J. C. Siero, J. Hendrikse, H. Hoogduin, N. Petridou, P. Luijten, and M. J. Donahue, "Cortical depth dependence of the BOLD initial dip and poststimulus undershoot in human visual cortex at 7 Tesla," *Magnetic Resonance in Medicine*, vol. 73, no. 6, pp. 2283–2295, 2015. doi: 10.1002/mrm.25349.

[269] S. Geethanath, R. Reddy, A. S. Konar, S. Imam, R. Sundaresan, D. R. Ramesh Babu, and R. Venkatesan, "Compressed sensing MRI: A review," *Critical Reviews in Biomedical Engineering*, vol. 41, no. 3, pp. 183–204, 2013. doi: 10.1615/CritRevBiomedEng.2014008058.

[270] J. Pfeuffer, P. F. Van De Moortele, E. Yacoub, A. Shmuel, G. Adriany, P. Andersen, H. Merkle, M. Garwood, K. Ugurbil, and X. Hu, "Zoomed functional imaging in the human brain at 7 tesla with simultaneous high spatial and high temporal resolution," *NeuroImage*, vol. 17, no. 1, pp. 272–286, 2002. doi: 10.1006/nimg.2002.1103.

[271] T. Q. Duong, E. Yacoub, G. Adriany, X. Hu, K. Ugurbil, J. T. Vaughan, H. Merkle, and S. G. Kim, "High-resolution, spin-echo BOLD, and CBF fMRI at 4 and 7 T," *Magnetic Resonance in Medicine*, vol. 48, no. 4, pp. 589–593, 2002. doi: 10.1002/mrm.10252.

[272] E. Yacoub, N. Harel, and K. Ugurbil, "High-field fMRI unveils orientation columns in humans," *Proceedings of the National Academy of Sciences of the United States of America*, vol. 105, no. 30, pp. 10607–10612, 2008. doi: 10.1073/pnas.0804110105.

[273] D. Spitzer, J. Bauer, and C. Faber, "Feasibility of line scanning BOLD fMRI on human subjects," in *ISMRM 24th Annual Meeting Exhibition proceedings, Singapore*, pp. 16–18, 2016.

[274] A. T. Morgan, N. Nothnagel, L. S. Petro, J. Goense, and L. Muckli, "High-resolution line-scanning reveals distinct visual response properties across human cortical layers," *bioRxiv*, pp. 1–17, 2020. doi: 10.1101/2020.06.30.179762.

[275] J. Siero, I. de Oliveira, S. Choi, and X. Yu, "Human line-scanning fMRI: Initial results of ultra-high temporal and spatial resolution hemodynamic imaging," in *Journal of Cerebral Blood Flow Metabolism, BRAIN 2019, Yokahama, Japan*, 2019. doi: 10.1177/0271678x19850985.

[276] L. Raimondo, T. Knapen, I. de Oliveira, X. Yu, W. van der Zwaag, and J. C. Siero, "Preliminary results of functional line-scanning in humans: submillimeter, subsecond resolution evoked responses," in *Magn Reson Mater Phy , ESMRMB 2019, Rotterdam, NL*, 2019. doi: 10.1007/s10334-019-00755-1.

8

[277] J. D. Power, K. A. Barnes, A. Z. Snyder, B. L. Schlaggar, and S. E. Petersen, "Spurious but systematic correlations in functional connectivity MRI networks arise from subject motion," *NeuroImage*, vol. 59, no. 3, pp. 2142–2154, 2012. doi: 10.1016/j.neuroimage.2011.10.018.

[278] S. Choi, H. Zeng, R. Pohmann, K. Scheffler, and X. Yu, "Novel alpha-180 SE based LINE-scanning method (SELINE) for laminar-specific fMRI," in *ISMRM 27th Annual Meeting Exhibition proceedings, Montreal, Canada*, p. 1166, 2019.

[279] J. H. Gao and H. L. Liu, "Inflow effects on functional MRI," *NeuroImage*, vol. 62, no. 2, pp. 1035–1039, 2012. doi: 10.1016/j.neuroimage.2011.09.088.

[280] A. Fracasso, S. O. Dumoulin, and N. Petridou, "Point-spread function of the BOLD response across columns and cortical depth in human extra-striate cortex," *Progress in Neurobiology*, no. February 2020, p. 102034, 2021. doi: 10.1016/j.pneurobio.2021.102034.

[281] G. de Hollander, W. van der Zwaag, C. Qian, P. Zhang, and T. Knapen, "Ultra-high field fMRI reveals origins of feedforward and feedback activity within laminae of human ocular dominance columns," *NeuroImage*, vol. 228, no. November 2020, p. 117683, 2021. doi: 10.1016/j.neuroimage.2020.117683.

[282] M. D. Sweeney, K. Kisler, A. Montagne, A. W. Toga, and B. V. Zlokovic, "The role of brain vasculature in neurodegenerative disorders," *Nature Neuroscience*, vol. 21, no. 10, pp. 1318–1331, 2018. doi: 10.1038/s41593-018-0234-x.

[283] Y. Iturria-Medina, R. C. Sotero, P. J. Toussaint, J. M. Mateos-Pérez, A. C. Evans, M. W. Weiner, P. Aisen, R. Petersen, C. R. Jack, W. Jagust, J. Q. Trojanowki, A. W. Toga, L. Beckett, R. C. Green, A. J. Saykin, J. Morris, L. M. Shaw, Z. Khachaturian, G. Sorensen, L. Kuller, M. Raichle, S. Paul, P. Davies, H. Fillit, F. Hefti, D. Holtzman, M. M. Mesulam, W. Potter, P. Snyder, A. Schwartz, T. Montine, R. G. Thomas, M. Donohue, S. Walter, D. Gessert, T. Sather, G. Jiminez, D. Harvey, M. Bernstein, N. Fox, P. Thompson, N. Schuff, B. Borowski, J. Gunter, M. Senjem, P. Vemuri, D. Jones, K. Kantarci, C. Ward, R. A. Koeppe, N. Foster, E. M. Reiman, K. Chen, C. Mathis, S. Landau, N. J. Cairns, E. Householder, L. Taylor-Reinwald, V. Lee, M. Korecka, M. Figurski, K. Crawford, S. Neu, T. M. Foroud, S. Potkin, L. Shen, K. Faber, S. Kim, K. Nho, L. Thal, N. Buckholtz, M. Albert, R. Frank, J. Hsiao, J. Kaye, J. Quinn, B. Lind, R. Carter, S. Dolen, L. S. Schneider, S. Pawluczyk, M. Beccera, L. Teodoro, B. M. Spann, J. Brewer, H. Vanderswag, A. Fleisher, J. L. Heidebrink, J. L. Lord, S. S. Mason, C. S. Albers, D. Knopman, K. Johnson, R. S. Doody, J. Villanueva-Meyer, M. Chowdhury, S. Rountree, M. Dang, Y. Stern, L. S. Honig, K. L. Bell, B. Ances, M. Carroll, S. Leon, M. A. Mintun, S. Schneider, A. Oliver, D. Marson, R. Griffith, D. Clark, D. Geldmacher, J. Brockington, E. Roberson, H. Grossman, E. Mitsis, L. de Toledo-Morrell, R. C. Shah, R. Duara, D. Varon, M. T. Greig, P. Roberts, M. Albert, C. Onyike, D. D'Agostino, S. Kielb, J. E. Galvin, B. Cerbone, C. A. Michel, H. Rusinek, M. J. de Leon, L. Glodzik, S. De Santi, P. M. Doraiswamy, J. R. Petrella, T. Z. Wong, S. E. Arnold, J. H. Karlawish, D. Wolk, C. D. Smith, G. Jicha, P. Hardy, P. Sinha, E. Oates, G. Conrad, O. L. Lopez, M. Oakley, D. M. Simpson, A. P. Porsteinsson, B. S. Goldstein, K. Martin, K. M. Makino, M. S. Ismail, C. Brand, R. A. Mulnard, G. Thai, C. Mc-Adams-Ortiz, K. Womack, D. Mathews, M. Quiceno, R. Diaz-Arrastia, R. King, M. Weiner, K. Martin-Cook, M. DeVous, A. I. Levey, J. J. Lah, J. S. Cellar, J. M. Burns, H. S. Anderson, R. H. Swerdlow, L. Apostolova, K. Tingus, E. Woo, D. H. S. Silverman, P. H. Lu, G. Bartzokis, N. R. Graff-Radford, F. Parfitt, T. Kendall, H. Johnson, M. R. Farlow, A. Hake, B. R. Matthews, S. Herring, C. Hunt, C. H. van Dyck, R. E. Carson, M. G. MacAvoy, H. Chertkow, H. Bergman, C. Hosein, S. Black, B. Stefanovic, C. Caldwell, G.-Y. R. Hsiung, H. Feldman, B. Mudge, M. Assaly,

8

A. Kertesz, J. Rogers, C. Bernick, D. Munic, D. Kerwin, M.-M. Mesulam, K. Lipowski, C.-K. Wu, N. Johnson, C. Sadowsky, W. Martinez, T. Villena, R. S. Turner, K. Johnson, B. Reynolds, R. A. Sperling, K. A. Johnson, G. Marshall, M. Frey, B. Lane, A. Rosen, J. Tinklenberg, M. N. Sabbagh, C. M. Belden, S. A. Jacobson, S. A. Sirrel, N. Kowall, R. Killiany, A. E. Budson, A. Norbash, P. L. Johnson, J. Allard, A. Lerner, P. Ogrocki, L. Hudson, E. Fletcher, O. Carmichael, J. Olichney, C. DeCarli, S. Kittur, M. Borrie, T.-Y. Lee, R. Bartha, S. Johnson, S. Asthana, C. M. Carlsson, S. G. Potkin, A. Preda, D. Nguyen, P. Tariot, S. Reeder, V. Bates, H. Capote, M. Rainka, D. W. Scharre, M. Kataki, A. Adeli, E. A. Zimmerman, D. Celmins, A. D. Brown, G. D. Pearlson, K. Blank, K. Anderson, R. B. Santulli, T. J. Kitzmiller, E. S. Schwartz, K. M. Sink, J. D. Williamson, P. Garg, F. Watkins, B. R. Ott, H. Querfurth, G. Tremont, S. Salloway, P. Malloy, S. Correia, H. J. Rosen, B. L. Miller, J. Mintzer, K. Spicer, D. Bachman, E. Finger, S. Pasternak, I. Rachinsky, D. Drost, N. Pomara, R. Hernando, A. Sarrael, S. K. Schultz, L. L. B. Ponto, H. Shim, K. E. Smith, N. Relkin, G. Chaing, L. Raudin, A. Smith, K. Fargher, B. A. Raj, T. Neylan, J. Grafman, M. Davis, and T. A. D. N. Initiative, "Early role of vascular dysregulation on late-onset Alzheimer's disease based on multifactorial data-driven analysis," *Nature Communications*, vol. 7, no. 1, p. 11934, 2016. doi: 10.1038/ncomms11934.

[284] L. Pantoni, "Cerebral small vessel disease: from pathogenesis and clinical characteristics to therapeutic challenges," *The Lancet Neurology*, vol. 9, no. 7, pp. 689–701, 2010. doi: 10.1016/S1474-4422(10)70104-6.

[285] R. B. Nielsen, L. Egefjord, H. Angleys, K. Mouridsen, M. Gejl, A. Møller, B. Brock, H. Brændgaard, H. Gottrup, J. Rungby, S. F. Eskildsen, and L. Østergaard, "Capillary dysfunction is associated with symptom severity and neurodegeneration in Alzheimer's disease," *Alzheimer's and Dementia*, vol. 13, no. 10, pp. 1143–1153, 2017. doi: 10.1016/j.jalz.2017.02.007.

[286] J. J. Zwanenburg and M. J. Van Osch, "Targeting cerebral small vessel disease with MRI," *Stroke*, vol. 48, no. 11, pp. 3175–3182, 2017. doi: 10.1161/STROKEAHA.117.016996.

[287] H. Angleys, L. Østergaard, and S. N. Jespersen, "The effects of capillary transit time heterogeneity (CTH) on brain oxygenation," *Journal of Cerebral Blood Flow and Metabolism*, vol. 35, no. 5, pp. 806–817, 2015. doi: 10.1038/jcbfm.2014.254.

[288] L. Østergaard, R. Aamand, S. Karabegovic, A. Tietze, J. U. Blicher, I. K. Mikkelsen, N. K. Iversen, N. Secher, T. S. Engedal, M. Anzabi, E. G. Jimenez, C. Cai, K. U. Koch, E. T. Næss-Schmidt, A. Obel, N. Juul, M. Rasmussen, and J. C. H. Sørensen, "The role of the microcirculation in delayed cerebral ischemia and chronic degenerative changes after subarachnoid hemorrhage," *Journal of Cerebral Blood Flow and Metabolism*, vol. 33, no. 12, pp. 1825–1837, 2013. doi: 10.1038/jcbfm.2013.173.

[289] P. M. Rasmussen, S. N. Jespersen, and L. Østergaard, "The effects of transit time heterogeneity on brain oxygenation during rest and functional activation," *Journal of Perinatology*, vol. 35, no. 3, pp. 432–442, 2015. doi: 10.1038/jcbfm.2014.213.

[290] E. Gutiérrez-Jiménez, H. Angleys, P. M. Rasmussen, I. K. Mikkelsen, K. Mouridsen, and L. Østergaard, "The effects of hypercapnia on cortical capillary transit time heterogeneity (CTH) in anesthetized mice," *Journal of Cerebral Blood Flow and Metabolism*, vol. 38, no. 2, pp. 290–303, 2018. doi: 10.1177/0271678X17692598.

[291] M. Havlicek and K. Uludağ, "A dynamical model of the laminar BOLD response," *NeuroImage*, vol. 204, no. September 2019, 2020. doi: 10.1016/j.neuroimage.2019.116209.

[292] M. G. Báez-Yánez, J. C. Siero, and N. Petridou, "A statistical 3D model of the human cortical vasculature to compute the hemodynamic fingerprint of the BOLD fMRI signal," *bioRxiv*, vol. 31, no. 0, pp. 1–63, 2020.

8

[293] V. B. Mountcastle, "Modality and topographic properties of single neurons of cat's somatic sensory cortex," *Journal of Neurophysiology*, vol. 20, pp. 408–434, July 1957. doi: 10.1152/jn.1957.20.4.408.

[294] S. B. Eickhoff, M. Milham, and T. Vanderwal, "Towards clinical applications of movie fMRI," *NeuroImage*, vol. 217, p. 116860, Aug. 2020. doi: 10.1016/j.neuroimage.2020.116860.

[295] T. T. Liu, "Noise contributions to the fMRI signal: An overview," *NeuroImage*, vol. 143, pp. 141–151, Dec. 2016. doi: 10.1016/j.neuroimage.2016.09.008.

[296] J. Ashburner, "SPM: A history," *NeuroImage*, vol. 62, pp. 791–800, Aug. 2012. doi: 10.1016/j.neuroimage.2011.10.025.

[297] M. Jenkinson, C. F. Beckmann, T. E. Behrens, M. W. Woolrich, and S. M. Smith, "FSL," *NeuroImage*, vol. 62, pp. 782–790, Aug. 2012. doi: 10.1016/j.neuroimage.2011.09.015.

[298] S. M. Smith, M. Jenkinson, M. W. Woolrich, C. F. Beckmann, T. E. Behrens, H. Johansen-Berg, P. R. Bannister, M. De Luca, I. Drobnjak, D. E. Flitney, R. K. Niazy, J. Saunders, J. Vickers, Y. Zhang, N. De Stefano, J. M. Brady, and P. M. Matthews, "Advances in functional and structural MR image analysis and implementation as FSL," *NeuroImage*, vol. 23, pp. S208–S219, Jan. 2004. doi: 10.1016/j.neuroimage.2004.07.051.

[299] J. Stelzer, G. Lohmann, K. Mueller, T. Buschmann, and R. Turner, "Deficient approaches to human neuroimaging," *Front. Hum. Neurosci.*, vol. 8, July 2014. doi: 10.3389/fnhum.2014.00462.

[300] C. Caballero-Gaudes and R. C. Reynolds, "Methods for cleaning the BOLD fMRI signal," *NeuroImage*, vol. 154, pp. 128–149, July 2017. doi: 10.1016/j.neuroimage.2016.12.018.

[301] F. Albers, F. Schmid, L. Wachsmuth, and C. Faber, "Line scanning fMRI reveals earlier onset of optogenetically evoked BOLD response in rat somatosensory cortex as compared to sensory stimulation," *NeuroImage*, vol. 164, pp. 144–154, Jan. 2018. doi: 10.1016/j.neuroimage.2016.12.059.

[302] D. Nunes, R. Gil, and N. Shemesh, "A rapid-onset diffusion functional MRI signal reflects neuromorphological coupling dynamics," *NeuroImage*, vol. 231, p. 117862, May 2021. doi: 10.1016/j.neuroimage.2021.117862.

[303] S. Choi, H. Zeng, Y. Chen, F. Sobczak, C. Qian, and X. Yu, "Laminar-specific functional connectivity mapping with multi-slice line-scanning fMRI," preprint, Neuroscience, Mar. 2021. doi: 10.1101/2021.03.03.433376.

[304] M. Balasubramanian, R. V. Mulkern, J. J. Neil, S. E. Maier, and J. R. Polimeni, "Probing in vivo cortical myeloarchitecture in humans via line-scan diffusion acquisitions at 7 T with 250-500 micron radial resolution," *Magn Reson Med*, vol. 85, pp. 390–403, Jan. 2021. doi: 10.1002/mrm.28419.

[305] M. Balasubramanian, R. V. Mulkern, and J. R. Polimeni, "In vivo irreversible and reversible transverse relaxation rates in human cerebral cortex via line scans at 7 T with 250 micron resolution perpendicular to the cortical surface," *Magnetic Resonance Imaging*, vol. 90, pp. 44–52, July 2022. doi: 10.1016/j.mri.2022.04.001.

[306] L. Raimondo, T. Knapen, Í. A. Oliveira, X. Yu, S. O. Dumoulin, W. van der Zwaag, and J. C. Siero, "A line through the brain: implementation of human line-scanning at 7T for ultra-high spatiotemporal resolution fMRI," *J Cereb Blood Flow Metab*, p. 0271678X2110372, Aug. 2021. doi: 10.1177/0271678X211037266.

[307] L. Afzali-Hashemi, K. P. A. Baas, A. Schrantee, B. F. Coolen, M. J. P. van Osch, S. M. Spann, E. Nur, J. C. Wood, B. J. Biemond, and A. J. Nederveen, "Impairment of Cere-

8

brovascular Hemodynamics in Patients With Severe and Milder Forms of Sickle Cell Disease," *Front. Physiol.*, vol. 12, p. 645205, Apr. 2021. doi: 10.3389/fphys.2021.645205.

[308] M. R. DeBaun and F. J. Kirkham, "Central nervous system complications and management in sickle cell disease," *Blood*, vol. 127, pp. 829–838, Feb. 2016. doi: 10.1182/blood-2015-09-618579.

[309] H. van den Brink, F. N. Doubal, and M. Duering, "Advanced MRI in cerebral small vessel disease," *International Journal of Stroke*, p. 174749302210918, Apr. 2022. doi: 10.1177/17474930221091879.

[310] J. Olsrud, A. Nilsson, P. Mannfolk, A. Waites, and F. Ståhlberg, "A two-compartment gel phantom for optimization and quality assurance in clinical BOLD fMRI," *Magnetic Resonance Imaging*, vol. 26, pp. 279–286, Feb. 2008. doi: 10.1016/j.mri.2007.06.010.

[311] S. Posse, S. Wiese, D. Gembris, K. Mathiak, C. Kessler, M.-L. Grosse-Ruyken, B. Elghahwagi, T. Richards, S. R. Dager, and V. G. Kiselev, "Enhancement of BOLD-contrast sensitivity by single-shot multi-echo functional MR imaging," *Magn. Reson. Med.*, vol. 42, pp. 87–97, July 1999. doi: 10.1002/(SICI)1522-2594(199907)42:1<87::AID-MRM13>3.0.CO;2-O.

[312] G. Krüger and G. H. Glover, "Physiological noise in oxygenation-sensitive magnetic resonance imaging: Physiological Noise in MRI," *Magn. Reson. Med.*, vol. 46, pp. 631–637, Oct. 2001. doi: 10.1002/mrm.1240.

[313] W. A. Edelstein, G. H. Glover, C. J. Hardy, and R. W. Redington, "The intrinsic signal-to-noise ratio in NMR imaging," *Magn. Reson. Med.*, vol. 3, pp. 604–618, Aug. 1986. doi: 10.1002/mrm.1910030413.

[314] D. Hoult and R. Richards, "The signal-to-noise ratio of the nuclear magnetic resonance experiment," *Journal of Magnetic Resonance*, vol. 213, pp. 329–343, Dec. 2011. doi: 10.1016/j.jmr.2011.09.018.

[315] C. Triantafyllou, R. Hoge, G. Krueger, C. Wiggins, A. Potthast, G. Wiggins, and L. Wald, "Comparison of physiological noise at 1.5 T, 3 T and 7 T and optimization of fMRI acquisition parameters," *NeuroImage*, vol. 26, pp. 243–250, May 2005. doi: 10.1016/j.neuroimage.2005.01.007.

[316] M. H. Alkinani and M. R. El-Sakka, "Patch-based models and algorithms for image denoising: a comparative review between patch-based images denoising methods for additive noise reduction," *J Image Video Proc.*, vol. 2017, p. 58, Dec. 2017. doi: 10.1186/s13640-017-0203-4.

[317] L. Fan, F. Zhang, H. Fan, and C. Zhang, "Brief review of image denoising techniques," *Vis. Comput. Ind. Biomed. Art*, vol. 2, p. 7, Dec. 2019. doi: 10.1186/s42492-019-0016-7.

[318] P. Kaur, G. Singh, and P. Kaur, "A Review of Denoising Medical Images Using Machine Learning Approaches," *CMIR*, vol. 14, pp. 675–685, Sept. 2018. doi: 10.2174/1573405613666170428154156.

[319] L. Vizioli, S. Moeller, L. Dowdle, M. Akçakaya, F. De Martino, E. Yacoub, and K. Ugurbil, "Lowering the thermal noise barrier in functional brain mapping with magnetic resonance imaging," *Nat Commun*, vol. 12, p. 5181, Dec. 2021. doi: 10.1038/s41467-021-25431-8.

[320] K. J. Friston, P. Jezzard, and R. Turner, "Analysis of functional MRI time-series," *Hum. Brain Mapp.*, vol. 1, no. 2, pp. 153–171, 1994. doi: 10.1002/hbm.460010207.

[321] D. Gallichan, J. P. Marques, and R. Gruetter, "Retrospective correction of involuntary microscopic head movement using highly accelerated fat image navigators (3D FatNavs) at 7T," *Magn. Reson. Med.*, vol. 75, pp. 1030–1039, Mar. 2016. doi: 10.1002/mrm.25670.

8

[322] J. Maclaren, B. S. R. Armstrong, R. T. Barrows, K. A. Danishad, T. Ernst, C. L. Foster, K. Gumus, M. Herbst, I. Y. Kadashevich, T. P. Kusik, Q. Li, C. Lovell-Smith, T. Prieto, P. Schulze, O. Speck, D. Stucht, and M. Zaitsev, "Measurement and Correction of Microscopic Head Motion during Magnetic Resonance Imaging of the Brain," *PLoS ONE*, vol. 7, p. e48088, Nov. 2012. doi: 10.1371/journal.pone.0048088.

[323] J. Schulz, T. Siegert, E. Reimer, C. Labadie, J. Maclaren, M. Herbst, M. Zaitsev, and R. Turner, "An embedded optical tracking system for motion-corrected magnetic resonance imaging at 7T," *Magn Reson Mater Phy*, vol. 25, pp. 443–453, Dec. 2012. doi: 10.1007/s10334-012-0320-0.

[324] M. Zaitsev, J. Maclaren, and M. Herbst, "Motion artifacts in MRI: A complex problem with many partial solutions: Motion Artifacts and Correction," *J. Magn. Reson. Imaging*, vol. 42, pp. 887–901, Oct. 2015. doi: 10.1002/jmri.24850.

[325] D. Stucht, K. A. Danishad, P. Schulze, F. Godenschweger, M. Zaitsev, and O. Speck, "Highest Resolution In Vivo Human Brain MRI Using Prospective Motion Correction," *PLoS ONE*, vol. 10, p. e0133921, July 2015. doi: 10.1371/journal.pone.0133921.

[326] M. Andersen, I. M. Björkman-Burtscher, A. Marsman, E. T. Petersen, and V. O. Boer, "Improvement in diagnostic quality of structural and angiographic MRI of the brain using motion correction with interleaved, volumetric navigators," *PLoS ONE*, vol. 14, p. e0217145, May 2019. doi: 10.1371/journal.pone.0217145.

[327] G. H. Glover, T.-Q. Li, and D. Ress, "Image-based method for retrospective correction of physiological motion effects in fMRI: RETROICOR," *Magn. Reson. Med.*, vol. 44, pp. 162–167, July 2000. doi: 10.1002/1522-2594(200007)44:1<162::AID-MRM23>3.0.CO;2-E.

[328] M. P. Normand, "Less Is More: Psychologists Can Learn More by Studying Fewer People," *Frontiers in Psychology*, vol. 7, 2016. doi: 10.3389/fpsyg.2016.00934.

[329] P. L. Smith and D. R. Little, "Small is beautiful: In defense of the small-N design," *Psychon Bull Rev*, vol. 25, pp. 2083–2101, Dec. 2018. doi: 10.3758/s13423-018-1451-8.

[330] C. Gratton, S. M. Nelson, and E. M. Gordon, "Brain-behavior correlations: Two paths toward reliability," *Neuron*, vol. 110, pp. 1446–1449, May 2022. doi: 10.1016/j.neuron.2022.04.018.

[331] D. Gallichan and J. P. Marques, "Optimizing the acceleration and resolution of three-dimensional fat image navigators for high-resolution motion correction at 7T," *Magnetic Resonance in Medicine*, vol. 77, no. 2, pp. 547–558, 2017. doi: 10.1002/mrm.26127.

[332] C. W. Hesse, P. F. Buur, and D. G. Norris, "A Subspace Wiener Filtering Approach for Extracting Task-Related Brain Activity from Multi-Echo fMRI Data," in *4th European Conference of the International Federation for Medical and Biological Engineering*, vol. 22, pp. 705–708, 2009. doi: 10.1007/978-3-540-89208-3-168.

[333] S. Heunis, M. Breeuwer, C. Caballero-Gaudes, L. Hellrung, W. Huijbers, J. F. Jansen, R. Lamerichs, S. Zinger, and A. P. Aldenkamp, "The effects of multi-echo fMRI combination and rapid T*-mapping on offline and real-time BOLD sensitivity," *NeuroImage*, vol. 238, p. 118244, Sept. 2021. doi: 10.1016/j.neuroimage.2021.118244.

[334] K. Kay, "The risk of bias in denoising methods: Examples from neuroimaging," *PLOS ONE*, vol. 17, p. e0270895, July 2022. doi: 10.1371/journal.pone.0270895.

[335] K. N. Kay, A. Rokem, J. Winawer, R. F. Dougherty, and B. A. Wandell, "GLMdenoise: a fast, automated technique for denoising task-based fMRI data," *Front. Neurosci.*, vol. 7, 2013. doi: 10.3389/fnins.2013.00247.

8

[336] S. Aydın, "Tikhonov regularized solutions for improvement of signal-to-noise ratio in case of auditory-evoked potentials," *Med Biol Eng Comput*, vol. 46, pp. 1051–1056, Oct. 2008. doi: 10.1007/s11517-008-0385-0.

[337] S. Aydın, "A new combination: scale-space filtering of projected brain activities," *Med Biol Eng Comput*, vol. 47, pp. 435–440, Apr. 2009. doi: 10.1007/s11517-009-0450-3.

[338] A. Hyvärinen, P. Ramkumar, L. Parkkonen, and R. Hari, "Independent component analysis of short-time Fourier transforms for spontaneous EEG/MEG analysis," *NeuroImage*, vol. 49, pp. 257–271, Jan. 2010. doi: 10.1016/j.neuroimage.2009.08.028.

[339] J. Zimmermann, R. Goebel, F. De Martino, P.-F. van de Moortele, D. Feinberg, G. Adriany, D. Chaimow, A. Shmuel, K. Ugurbil, and E. Yacoub, "Mapping the Organization of Axis of Motion Selective Features in Human Area MT Using High-Field fMRI," *PLoS ONE*, vol. 6, p. e28716, Dec. 2011. doi: 10.1371/journal.pone.0028716.

[340] J. M. Oja, J. Gillen, R. A. Kauppinen, M. Kraut, and P. C. van Zijl, "Venous blood effects in spin-echo fMRI of human brain," *Magn. Reson. Med.*, vol. 42, pp. 617–626, Oct. 1999. doi: 10.1002/(SICI)1522-2594(199910)42:4<617::AID-MRM1>3.0.CO;2-Q.

[341] K. Uludag, B. Müller-Bierl, and K. Ugurbil, "An integrative model for neuronal activity-induced signal changes for gradient and spin echo functional imaging," *NeuroImage*, vol. 48, pp. 150–165, Oct. 2009. doi: 10.1016/j.neuroimage.2009.05.051.

[342] L. Raimondo, A. Oliveira, J. Heij, N. Priovoulos, P. Kundu, R. F. Leoni, and W. van der Zwaag, "Advances in resting state fMRI acquisitions for functional connectomics," *NeuroImage*, vol. 243, p. 118503, Nov. 2021. doi: 10.1016/j.neuroimage.2021.118503.

[343] S. Han, S. Eun, H. Cho, K. Uludağ, and S.-G. Kim, "Improvement of sensitivity and specificity for laminar BOLD fMRI with double spin-echo EPI in humans at 7 T," *NeuroImage*, vol. 241, p. 118435, Nov. 2021. doi: 10.1016/j.neuroimage.2021.118435.

[344] P. T. Toi, H. J. Jang, K. Min, S.-P. Kim, S.-K. Lee, J. Lee, J. Kwag, and J.-Y. Park, "In vivo direct imaging of neuronal activity at high temporospatial resolution," *Science*, vol. 378, pp. 160–168, Oct. 2022. doi: 10.1126/science.abh4340.

[345] R. M. S. Panchuelo, D. Schluppeck, J. Harmer, R. Bowtell, and S. Francis, "Assessing the Spatial Precision of SE and GE-BOLD Contrast at 7 Tesla," *Brain Topography*, vol. 28, pp. 62–65, Jan. 2015. doi: 10.1007/s10548-014-0420-4.

[346] E. Yacoub, A. Shmuel, N. Logothetis, and K. Ugurbil, "Robust detection of ocular dominance columns in humans using Hahn Spin Echo BOLD functional MRI at 7 Tesla," *NeuroImage*, vol. 37, pp. 1161–1177, Oct. 2007. doi: 10.1016/j.neuroimage.2007.05.020.

[347] K. Oshio and D. A. Feinberg, "GRASE (Gradient-and Spin-Echo) imaging: A novel fast MRI technique," *Magnetic Resonance in Medicine*, vol. 20, pp. 344–349, Aug. 1991. doi: 10.1002/mrm.1910200219.

[348] M. Moerel, F. De Martino, V. G. Kemper, S. Schmitter, A. T. Vu, K. Ugurbil, E. Formisano, and E. Yacoub, "Sensitivity and specificity considerations for fMRI encoding, decoding, and mapping of auditory cortex at ultra-high field," *NeuroImage*, vol. 164, pp. 18–31, Jan. 2018. doi: 10.1016/j.neuroimage.2017.03.063.

[349] F. De Martino, S. Schmitter, M. Moerel, J. Tian, K. Ugurbil, E. Formisano, E. Yacoub, and P.-F. v. de Moortele, "Spin echo functional MRI in bilateral auditory cortices at 7T: An application of B1 shimming," *NeuroImage*, vol. 63, pp. 1313–1320, Nov. 2012. doi: 10.1016/j.neuroimage.2012.08.029.

[350] F. Wang, Z. Dong, L. L. Wald, J. R. Polimeni, and K. Setsompop, "Simultaneous pure T2 and varying T2-weighted BOLD fMRI using Echo Planar Time-resolved Imaging for mapping cortical-depth dependent responses," *NeuroImage*, vol. 245, p. 118641, Dec. 2021. doi: 10.1016/j.neuroimage.2021.118641.

8

[351] A. Barghoorn, B. Riemenschneider, J. Hennig, and P. LeVan, "Improving the sensitivity of spin-echo fMRI at 3T by highly accelerated acquisitions," *Magnetic Resonance in Medicine*, vol. 86, no. 1, pp. 245–257, 2021. doi: 10.1002/mrm.28715.

[352] Y. Ye, Y. Zhuo, R. Xue, and X. J. Zhou, "BOLD fMRI using a modified HASTE sequence," *NeuroImage*, vol. 49, pp. 457–466, Jan. 2010. doi: 10.1016/j.neuroimage.2009.07.044.

[353] L. Leroi, V. Gras, N. Boulant, M. Ripart, E. Poirion, M. D. Santin, R. Valabregue, F. Mauconduit, L. Hertz-Pannier, D. Le Bihan, L. de Rochefort, and A. Vignaud, "Simultaneous proton density, T1 , T2 , and flip-angle mapping of the brain at 7 T using multiparametric 3D SSFP imaging and parallel-transmission universal pulses," *Magn Reson Med*, vol. 84, pp. 3286–3299, Dec. 2020. doi: 10.1002/mrm.28391.

[354] J. L. Boxerman, L. M. Hamberg, B. R. Rosen, and R. M. Weisskoff, "Mr contrast due to intravascular magnetic susceptibility perturbations," *Magn. Reson. Med.*, vol. 34, pp. 555–566, Oct. 1995. doi: 10.1002/mrm.1910340412.

[355] J. Harmer, R. M. Sanchez-Panchuelo, R. Bowtell, and S. T. Francis, "Spatial location and strength of BOLD activation in high-spatial-resolution fMRI of the motor cortex: a comparison of spin echo and gradient echo fMRI at 7 T," *NMR in Biomedicine*, vol. 25, no. 5, pp. 717–725, 2012. doi: 10.1002/nbm.1783.

[356] A. M. Peters, M. J. Brookes, F. G. Hoogenraad, P. A. Gowland, S. T. Francis, P. G. Morris, and R. Bowtell, "T2* measurements in human brain at 1.5, 3 and 7 T," *Magnetic Resonance Imaging*, vol. 25, pp. 748–753, July 2007. doi: 10.1016/j.mri.2007.02.014.

[357] L. Raimondo, N. Priovoulos, C. Passarinho, J. Heij, T. Knapen, S. O. Dumoulin, J. C. W. Siero, and W. van der Zwaag, "Robust high spatio-temporal line-scanning fMRI in humans at 7T using multi-echo readouts, denoising and prospective motion correction," *Journal of Neuroscience Methods*, vol. 384, p. 109746, Jan. 2023. doi: 10.1016/j.jneumeth.2022.109746.

[358] W. Olszowy, J. Aston, C. Rua, and G. B. Williams, "Accurate autocorrelation modeling substantially improves fMRI reliability," *Nat Commun*, vol. 10, p. 1220, Mar. 2019. doi: 10.1038/s41467-019-09230-w.

[359] G. Diiokio, J. J. Brown, J. A. Borrello, and H. Perman, "LARGE ANGLE SPIN-ECHO IMAGING," *Magnetic Resonance Imaging*, vol. 13, no. 1, p. 6, 1995.

[360] J. P. Mugler III, "Optimized three-dimensional fast-spin-echo MRI," *Journal of Magnetic Resonance Imaging*, vol. 39, no. 4, pp. 745–767, 2014. doi: 10.1002/jmri.24542.

[361] L. Huber, E. S. Finn, D. A. Handwerker, M. Bönstrup, D. R. Glen, S. Kashyap, D. Ivanov, N. Petridou, S. Marrett, J. Goense, B. A. Poser, and P. A. Bandettini, "Submillimeter fMRI reveals multiple topographical digit representations that form action maps in human motor cortex," *NeuroImage*, vol. 208, p. 116463, Mar. 2020. doi: 10.1016/j.neuroimage.2019.116463.

[362] Y. Cai, S. Hofstetter, J. van Dijk, W. Zuiderbaan, W. van der Zwaag, B. M. Harvey, and S. O. Dumoulin, "Topographic numerosity maps cover subitizing and estimation ranges," *Nat Commun*, vol. 12, p. 3374, Dec. 2021. doi: 10.1038/s41467-021-23785-7.

[363] T. O. Laumann, E. M. Gordon, B. Adeyemo, A. Z. Snyder, S. J. Joo, M.-Y. Chen, A. W. Gilmore, K. B. McDermott, S. M. Nelson, N. U. F. Dosenbach, B. L. Schlaggar, J. A. Mumford, R. A. Poldrack, and S. E. Petersen, "Functional System and Areal Organization of a Highly Sampled Individual Human Brain," *Neuron*, vol. 87, pp. 657–670, Aug. 2015. doi: 10.1016/j.neuron.2015.06.037.

[364] L. D. Lewis, K. Setsompop, B. R. Rosen, and J. R. Polimeni, "Fast fMRI can detect oscillatory neural activity in humans," *Proceedings of the National Academy of Sciences*, vol. 113, pp. E6679–E6685, Oct. 2016. doi: 10.1073/pnas.1608117113.

8

[365] J. Gonzalez-Castillo, Z. S. Saad, D. A. Handwerker, S. J. Inati, N. Brenowitz, and P. A. Bandettini, "Whole-brain, time-locked activation with simple tasks revealed using massive averaging and model-free analysis," *Proceedings of the National Academy of Sciences*, vol. 109, pp. 5487–5492, Apr. 2012. doi: 10.1073/pnas.1121049109.

[366] L. A. Stables, R. P. Kennan, and J. C. Gore, "Asymmetric spin-echo imaging of magnetically inhomogeneous systems: Theory, experiment, and numerical studies," *Magn. Reson. Med.*, vol. 40, pp. 432–442, Sept. 1998. doi: 10.1002/mrm.1910400314.

[367] F. De Martino, J. Zimmermann, L. Muckli, K. Ugurbil, E. Yacoub, and R. Goebel, "Cortical Depth Dependent Functional Responses in Humans at 7T: Improved Specificity with 3D GRASE," *PLoS ONE*, vol. 8, p. e60514, Mar. 2013. doi: 10.1371/journal.pone.0060514.

[368] S. Choi, X. Yu, and K. Sche, "Simultaneous acquisition of GRE- and SE-type resting-state fMRI signals with GRASE-based line-scanning in the human brain," *ISMRM 27th Annual Meeting & Exhibition proceedings, London, UK, 1105*, 2022.

[369] K. D. Brewer, J. A. Rioux, R. C. N. D'Arcy, C. V. Bowen, and S. D. Beyea, "Asymmetric spin-echo (ASE) spiral improves BOLD fMRI in inhomogeneous regions," *NMR in Biomedicine*, vol. 22, no. 6, pp. 654–662, 2009. doi: 10.1002/nbm.1380.

[370] M. Shrestha, U. Nöth, and R. Deichmann, "Improved signal-to-noise ratio in EPI sequences with highly asymmetric spin echo and highly asymmetric STEAM preparations (HASE-EPI and HASTEAM-EPI)," *Magn Reson Mater Phy*, vol. 32, pp. 549–558, Oct. 2019. doi: 10.1007/s10334-019-00749-z.

[371] D. H. Salat, R. L. Buckner, A. Z. Snyder, D. N. Greve, R. S. Desikan, E. Busa, J. C. Morris, A. M. Dale, and B. Fischl, "Thinning of the Cerebral Cortex in Aging," *Cerebral Cortex*, vol. 14, pp. 721–730, July 2004. doi: 10.1093/cercor/bhh032.

[372] J. J. Chen, H. D. Rosas, and D. H. Salat, "Age-associated reductions in cerebral blood flow are independent from regional atrophy," *NeuroImage*, vol. 55, pp. 468–478, Mar. 2011. doi: 10.1016/j.neuroimage.2010.12.032.

[373] H. Lu, F. Xu, K. M. Rodrigue, K. M. Kennedy, Y. Cheng, B. Flicker, A. C. Hebrank, J. Uh, and D. C. Park, "Alterations in Cerebral Metabolic Rate and Blood Supply across the Adult Lifespan," *Cerebral Cortex*, vol. 21, pp. 1426–1434, June 2011. doi: 10.1093/cercor/bhq224.

[374] R. L. Buckner, A. Z. Snyder, A. L. Sanders, M. E. Raichle, and J. C. Morris, "Functional Brain Imaging of Young, Nondemented, and Demented Older Adults," *Journal of Cognitive Neuroscience*, vol. 12, pp. 24–34, Nov. 2000. doi: 10.1162/089892900564046.

[375] M. H. Ross, D. A. Yurgelun-Todd, P. F. Renshaw, L. C. Maas, J. H. Mendelson, N. K. Mello, B. M. Cohen, and J. M. Levin, "Age-related Reduction in Functional MRI Response to Photic Stimulation," *Neurology*, vol. 48, pp. 173–176, Jan. 1997. doi: 10.1212/WNL.48.1.173.

[376] S. A. Huettel, J. D. Singerman, and G. McCarthy, "The Effects of Aging upon the Hemodynamic Response Measured by Functional MRI," *NeuroImage*, vol. 13, pp. 161–175, Jan. 2001. doi: 10.1006/nimg.2000.0675.

[377] K. L. West, M. D. Zuppichini, M. P. Turner, D. K. Sivakolundu, Y. Zhao, D. Abdelkarim, J. S. Spence, and B. Rypma, "BOLD hemodynamic response function changes significantly with healthy aging," *NeuroImage*, vol. 188, pp. 198–207, Mar. 2019. doi: 10.1016/j.neuroimage.2018.12.012.

[378] M. D'Esposito, E. Zarahn, G. K. Aguirre, and B. Rypma, "The Effect of Normal Aging on the Coupling of Neural Activity to the Bold Hemodynamic Response," *NeuroImage*, vol. 10, pp. 6–14, July 1999. doi: 10.1006/nimg.1999.0444.

8

[379] B. Maus, G. J. P. Van Breukelen, R. Goebel, and M. P. F. Berger, "Optimization of Blocked Designs in fMRI Studies," *Psychometrika*, vol. 75, pp. 373–390, June 2010. doi: 10.1007/s11336-010-9159-3.

[380] R. M. Birn, R. W. Cox, and P. A. Bandettini, "Detection versus Estimation in Event-Related fMRI: Choosing the Optimal Stimulus Timing," *NeuroImage*, vol. 15, pp. 252–264, Jan. 2002. doi: 10.1006/nimg.2001.0964.

[381] K. J. Friston, E. Zarahn, O. Josephs, R. N. A. Henson, and A. M. Dale, "Stochastic Designs in Event-Related fMRI," *NeuroImage*, vol. 10, pp. 607–619, Nov. 1999. doi: 10.1006/nimg.1999.0498.

[382] T. T. Liu, L. R. Frank, E. C. Wong, and R. B. Buxton, "Detection Power, Estimation Efficiency, and Predictability in Event-Related fMRI," *NeuroImage*, vol. 13, pp. 759–773, Apr. 2001. doi: 10.1006/nimg.2000.0728.

[383] A. M. Dale, "Optimal experimental design for event-related fMRI," *Human Brain Mapping*, vol. 8, no. 2-3, pp. 109–114, 1999. doi: 10.1002/(SICI)1097-0193(1999)8:2/3<109::AID-HBM7>3.0.CO;2-W.

[384] J. A. Mumford, J.-B. Poline, and R. A. Poldrack, "Orthogonalization of Regressors in fMRI Models," *PLOS ONE*, vol. 10, p. e0126255, Apr. 2015. doi: 10.1371/journal.pone.0126255.

[385] N. C. Benson, K. W. Jamison, M. J. Arcaro, A. T. Vu, M. F. Glasser, T. S. Coalson, D. C. Van Essen, E. Yacoub, K. Ugurbil, J. Winawer, and K. Kay, "The Human Connectome Project 7 Tesla retinotopy dataset: Description and population receptive field analysis," *Journal of Vision*, vol. 18, p. 23, Dec. 2018. doi: 10.1167/18.13.23.

[386] J. P. Marques, T. Kober, G. Krueger, W. van der Zwaag, P.-F. Van de Moortele, and R. Gruetter, "MP2RAGE, a self bias-field corrected sequence for improved segmentation and T1-mapping at high field," *NeuroImage*, vol. 49, pp. 1271–1281, Jan. 2010. doi: 10.1016/j.neuroimage.2009.10.002.

[387] A. F. Oliveira, T. Roos, S. O. Dumoulin, J. C. W. Siero, and W. van der Zwaag, "Can 7T MPRAGE match MP2RAGE for gray-white matter contrast?," *NeuroImage*, vol. 240, p. 118384, Oct. 2021. doi: 10.1016/j.neuroimage.2021.118384.

[388] J. L. R. Andersson, S. Skare, and J. Ashburner, "How to correct susceptibility distortions in spin-echo echo-planar images: application to diffusion tensor imaging," *NeuroImage*, vol. 20, pp. 870–888, Oct. 2003. doi: 10.1016/S1053-8119(03)00336-7.

[389] K. Amunts, A. Malikovic, H. Mohlberg, T. Schormann, and K. Zilles, "Brodmann's Areas 17 and 18 Brought into Stereotaxic Space—Where and How Variable?," *NeuroImage*, vol. 11, pp. 66–84, Jan. 2000. doi: 10.1006/nimg.1999.0516.

[390] R. A. Poldrack, J. A. Mumford, and T. E. Nichols, *Handbook of Functional MRI Data Analysis*. Cambridge University Press, 2011.

[391] J. V. Manjón, P. Coupé, L. Martí-Bonmatí, D. L. Collins, and M. Robles, "Adaptive non-local means denoising of MR images with spatially varying noise levels," *Journal of Magnetic Resonance Imaging*, vol. 31, no. 1, pp. 192–203, 2010. doi: 10.1002/jmri.22003.

[392] N. J. Tustison, B. B. Avants, P. A. Cook, Y. Zheng, A. Egan, P. A. Yushkevich, and J. C. Gee, "N4ITK: Improved N3 Bias Correction," *IEEE Transactions on Medical Imaging*, vol. 29, pp. 1310–1320, June 2010. doi: 10.1109/TMI.2010.2046908.

[393] Y. Zhang, M. Brady, and S. Smith, "Segmentation of brain MR images through a hidden Markov random field model and the expectation-maximization algorithm," *IEEE Transactions on Medical Imaging*, vol. 20, pp. 45–57, Jan. 2001. doi: 10.1109/42.906424.

8

[394] A. M. Dale, B. Fischl, and M. I. Sereno, "Cortical Surface-Based Analysis: I. Segmentation and Surface Reconstruction," *NeuroImage*, vol. 9, pp. 179–194, Feb. 1999. doi: 10.1006/nimg.1998.0395.

[395] S. D. Mayhew, S. C. Coleman, K. J. Mullinger, and C. Can, "Across the adult lifespan the ipsilateral sensorimotor cortex negative BOLD response exhibits decreases in magnitude and spatial extent suggesting declining inhibitory control," *NeuroImage*, vol. 253, p. 119081, June 2022. doi: 10.1016/j.neuroimage.2022.119081.

[396] H. J. Aizenstein, K. A. Clark, M. A. Butters, J. Cochran, V. A. Stenger, C. C. Meltzer, C. F. Reynolds, and C. S. Carter, "The BOLD Hemodynamic Response in Healthy Aging," *Journal of Cognitive Neuroscience*, vol. 16, pp. 786–793, June 2004. doi: 10.1162/089892904970681.

[397] J. Heij, L. Raimondo, J. C. W. Siero, W. van der Zwaag, S. O. Dumoulin, and T. Knapen, "Human population receptive field properties across cortical depth using ultrahigh spatiotemporal resolution fMRI," (San Diego, CA), 2022.

[398] M. Bianciardi, M. Fukunaga, P. van Gelderen, S. G. Horovitz, J. A. de Zwart, K. Shmueli, and J. H. Duyn, "Sources of functional magnetic resonance imaging signal fluctuations in the human brain at rest: a 7 T study," *Magnetic Resonance Imaging*, vol. 27, pp. 1019–1029, Oct. 2009. doi: 10.1016/j.mri.2009.02.004.

[399] R. A. Degraaf, Y. Luo, M. Terpstra, H. Merkle, and M. Garwood, "A New Localization Method Using an Adiabatic Pulse, BIR-4," *Journal of Magnetic Resonance, Series B*, vol. 106, pp. 245–252, Mar. 1995. doi: 10.1006/jmrb.1995.1040.

[400] Y. Behzadi, K. Restom, J. Liau, and T. T. Liu, "A component based noise correction method (CompCor) for BOLD and perfusion based fMRI," *NeuroImage*, vol. 37, pp. 90–101, Aug. 2007. doi: 10.1016/j.neuroimage.2007.04.042.

[401] S. Choi, H. Zeng, Y. Chen, F. Sobczak, C. Qian, and X. Yu, "Laminar-specific functional connectivity mapping with multi-slice line-scanning fMRI," *Cerebral Cortex*, vol. 32, pp. 4492–4501, Oct. 2022. doi: 10.1093/cercor/bhab497.

[402] S. Choi, Y. Chen, H. Zeng, B. Biswal, and X. Yu, "Identifying the distinct spectral dynamics of laminar-specific interhemispheric connectivity with bilateral line-scanning fMRI," *J Cereb Blood Flow Metab*, p. 0271678X2311584, Feb. 2023. doi: 10.1177/0271678X231158434.

List of Publications

Journal Publications

- **L. Raimondo***, J. Heij*, T. Knapen, J.C.W Siero, W. van der Zwaag, and S.O. Dumoulin, *Does the hemodynamic response function in visual cortex differ between age groups? A high spatio-temporal resolution fmri study with cortical depth dependency insights.* Submitted.

- J. Heij, **L. Raimondo**, J.C.W Siero, S.O. Dumoulin, W. van der Zwaag, and T. Knapen, *A selection and targeting framework of cortical locations for line-scanning fMRI.*
  Hum Brain Mapp (2023); DOI: 10.1002/hbm.26459.

- **L. Raimondo**, J. Heij, T. Knapen, S.O. Dumoulin, W. van der Zwaag, and J.C.W Siero, *Towards functional spin-echo bold line-scanning in humans at 7T.*
  Magn Reson Mater Phy (2023); DOI: 10.1007/s10334-022-01059-7.

- **L. Raimondo**, N. Priovoulos, C. Passarinho, J. Heij, T. Knapen, S.O. Dumoulin, J.C.W Siero, and W. van der Zwaag, *Robust high spatio-temporal line-scanning fmri in humans at 7T using multi-echo readouts, denoising and prospective motion correction.*
  Journal of Neuroscience Methods (2023); DOI: 10.1016/j.jneumeth.2022.109746.

- **L. Raimondo**, T. Knapen, I.A.F. de Oliveira, X. Yu, S.O. Dumoulin, W. van der Zwaag, and J.C.W. Siero, *A line through the brain: implementation of human line-scanning at 7T for ultra-high spatiotemporal resolution fmri.*
  J Cereb Blood Flow Metab (2021); DOI: 10.1177/0271678X211037266.

- **L. Raimondo**, I.A.F. de Oliveira , J. Heij, N. Priovoulos, P. Kundu, R. Ferranti Leoni, and W. van der Zwaag, *Advances in resting state fmri acquisitions for functional connectomics.*
  NeuroImage (2021); DOI: 10.1016/j.neuroimage.2021.118503.

- I.A.F. de Oliveira, W. van der Zwaag, **L. Raimondo**, S.O Dumoulin, and J.C.W. Siero, *Comparing hand movement rate dependence of cerebral blood volume and BOLD responses at 7T.*
  NeuroImage (2021); DOI: 10.1016/j.neuroimage.2020.117623.

- A.D. Hendriks, F. D'Agata, **L. Raimondo**, T. Schakel, L. Geerts, P.R. Luijten, D.W.J. Klomp, and N. Petridou, *Pushing functional MRI spatial and temporal resolution further: High-density receive arrays combined with shot-selective 2D CAIPIRINHA for 3D echo-planar imaging at 7 T.*
  NMR Biomed (2020); DOI: 10.1002/nbm.4281.

Conference Proceedings

- J. Heij, **L. Raimondo**, W. van der Zwaag, J.C.W Siero, S.O. Dumoulin, and T. Knapen, *Human population receptive field properties across cortical depth using ultrahigh spatiotemporal resolution fMRI.* ISMRM Benelux 2023, Brussels

- J. Heij, **L. Raimondo**, J.C.W. Siero, S.O. Dumoulin, W. van der Zwaag, T. Knapen, *Human population receptive fields across depth using ultrahigh spatiotemporal resolution line-scanning fMRI.* NVP 2022, Egmond

- **L. Raimondo**, N. Priovoulos, J. Heij, T. Knapen, S.O. Dumoulin, J.C.W Siero, and W. van der Zwaag, *Prospective motion correction in multi-echo line-scanning fMRI at 7T: sequence implementation and strategies for functional data analysis.* ISMRM 2022, London

- **L. Raimondo**, T. Knapen, S.O. Dumoulin, W. van der Zwaag, and J.C.W Siero, *Spin-echo line-scanning at 7T.* ISMRM 2022, London

- **L. Raimondo**, N. Priovoulos, J. Heij, T. Knapen, S.O. Dumoulin, J.C.W Siero, and W. van der Zwaag, *Prospective motion correction in multi-echo line-scanning fMRI at 7T: sequence implementation and strategies for functional data analysis.* UHF workshop 2022, Lisbon

- **L. Raimondo**, T. Knapen, S.O. Dumoulin, W. van der Zwaag, and J.C.W Siero, *Spin-echo line-scanning at 7T.* ISMRM Benelux 2022, Maasticht

- C. Passarinho, **L. Raimondo**, J. Heij, T. Knapen, S.O. Dumoulin, J.C.W Siero, and W. van der Zwaag, *Noise removal in Line-scanning fMRI.* ESMRMB 2021, Virtual

- J. Heij, **L. Raimondo**, J.C.W Siero, S.O. Dumoulin, W. van der Zwaag, and T. Knapen, *A framework for optimal planning during ultrahigh spatiotemporal resolution line-scanning* ESMRMB 2021, Virtual

- **L. Raimondo**, J. Heij, T. Knapen, S.O. Dumoulin, J.C.W Siero, and W. van der Zwaag, *Multi-echo line-scanning for ultra-high spatiotemporal resolution: optimal settings for BOLD sensitivity enhancement.* ISMRM 2021, Virtual

- J. Heij, **L. Raimondo**, J.C.W Siero, S.O. Dumoulin, W. van der Zwaag, and T. Knapen, *Combining functional and structural information for optimal planning during ultrahigh temporal resolution line-scanning.* ISMRM 2021, Virtual

- **L. Raimondo**, J. Heij, T. Knapen, S.O. Dumoulin, J.C.W Siero, and W. van der Zwaag, *Multi-echo line-scanning for ultra-high spatiotemporal resolution: optimal settings for BOLD sensitivity enhancement.* ISMRM Benelux 2021, Virtual

- **L. Raimondo**, T. Knapen, I.A.F. de Oliveira, X. Yu, S.O. Dumoulin, W. van der Zwaag, and J.C.W Siero, *Functional line-scanning in humans with ultra-high spatiotemporal resolution: reconstruction and BOLD sensitivity assessment.* ISMRM 2020, Virtual

- I.A.F. de Oliveira, W. van der Zwaag, **L. Raimondo**, S.O. Dumoulin, J.C.W. Siero, *Assessment of functional response nonlinearity in the motor cortex using 3D-EPI VASO at 7T.* ISMRM 2020, Virtual

- **L. Raimondo**, T. Knapen, I.A.F. de Oliveira, X. Yu, S.O. Dumoulin, W. van der Zwaag, and J.C.W Siero, *Functional line-scanning in humans with ultra-high spatiotemporal resolution: reconstruction and BOLD sensitivity assessment.* ISMRM Benelux 2020, Arnhem

- I.A.F. de Oliveira, W. van der Zwaag, **L. Raimondo**, S.O. Dumoulin, J.C.W. Siero, *Assessment of functional response nonlinearity in the motor cortex using 3D-EPI VASO at 7T.* ISMRM Benelux 2020, Arnhem

- **L. Raimondo**, T. Knapen, I.A.F. de Oliveira, X. Yu, W. van der Zwaag, and J.C.W Siero, *Preliminary results of functional line-scanning in humans: sub-millimetre, subsecond resolution evoked responses.* ESMRMB 2019, Rotterdam

- A.D. Hendriks, F. D'Agata, **L. Raimondo**, T. Schakel, L. Geerts, D.W.J. Klomp, and N. Petridou *Pushing fMRI spatial and temporal resolution further: high density receive arrays combined with shot-selective 2D CAIPIRINHA for 3D EPI scans at 7T.* ISMRM 2019, Montreal

ACKNOWLEDGEMENTS

Many people contributed, directly or indirectly, to this thesis, which simply represents the end of a very interesting and enriching journey.

First of all, I would like to express my deep gratitude towards my supervisors for making this PhD path possible. Having such a diverse supervision team has been, at the same time, challenging and rewarding.

Serge, thank you for welcoming me at Spinoza and for fulfilling the difficult role of having the last word in our MicroFunc meeting discussions.

Wietske, thank you for being an example to look at whenever I was feeling lost. Thank you for expressing my thoughts much better than I could do myself. And thank you for being present at every little step. I surely would have never get to this end without you.

Tomas, thank you for bringing the optimistic view I was always lacking for.

Jeroen, thank you for your instructive and highlighting inputs and feedbacks.

A very big acknowledgment goes to all my colleagues and Spinoza members. I honestly could have not wished for a better group to spend those four years! Even though I am probably not mentioning everyone, I am truly grateful to all of you.

Icaro, thank you for being my PhD student mentor. Your advices and help were the key for the happiness of my first year at Spinoza. Obrigada!

Shir, my favourite postdoc, thank you for all your hugs and support of those years.

Yuxuan and Akhil, my first friends-colleagues, thank for introducing me to the international Spinoza group.

Jurjen, thanks for sharing the line experience (and Monday meetings). You will always be the only one truly understanding our complicated relationship with line-scanning.

Nikos, thanks for all the random chats as much as for all your advices on how to arrive to the end of the PhD. I am missing a lot your "smooth-brain" moments at the fussball table.

Emma, even though it happened that I could not see you (dressed in white on a white bed), I clearly saw in you a lot of myself. Thank you for giving me the opportunity to analyse my past through your present.

Marco, grazie per essere tornato dai tuoi mesi (anni?!?!?) sabbatici in Italia, ricreando un ambiente sereno e leggero in ufficio.

Kathi and Sumiya, thank you for putting so much effort in making the PhD student group a real group. Hold on like that, girls! You're doing great!

Marcus, thank you for always sharing a fun fact to entertain us.

Esther, the sweetest of the group. Thank you for having always a nice word for everyone.

Bobby, thank you for your daily kindness and for your constant attention during presentations.

Thomas, thank you for fixing the 7T so quickly that I couldn't even realize it was broken.

Diederick, thank you for teaching me how to interact with Dutch people. Thank you for not judging my dumb questions and always finding a way to help me out.

Gianfranco, grazie per le migliori sessioni allo scanner ascoltando i Pinguini.

Wietske Z, Arjan, Maartje, Mayca, Anouk, Carlien, Ada, Jelle, Ines, Toni, Bram, Ineke, Minni, Elze, Dennis, Valeria, Jolien, Johan, Ron, Ningkai, thank you for being nice and polite colleagues. Was a pleasure to meet you all!

Thanks to all the students that spent some months at Spinoza. You all contributed to freshen the open space with your young and external opinions.

A special thank to Catarina, for giving me the energy I needed to finish one more project and for making me enjoying being part of it. I am very proud of you and I wish you all the best for the rest of you PhD!

To all the people I met during my years in the Netherlands: thanks for sharing moments and simply enjoying being together. From bouldering sessions to lazy dinners, I deeply appreciated all the time I spent with each of you.

Some of you will always have a special space in my mind and thoughts.

Alle mie paraninfe italiane, semplicemente grazie dal profondo del cuore.

Bea, grazie per essere stata un tornado che ha rispettato la mia quiete. Mi hai aperta verso il mondo senza che me ne rendessi conto. Grazie per la tua dolcezza costante, le tue attenzioni e la delicatezza di ogni tuo gesto.

Blondie, quanto è facile andare d'accordo quando si ha una testa in due? Grazie per essere stata una certezza in un mondo di sorprese. Anche se in ritardo rispetto a te, ho capito anch'io l'importanza di trovare qualcuno che resti fino alla fine. Grazie per essere stata quel qualcuno.

Jondrito, grazie per avermi insegnato l'arte del "take it chill". Thanks for all the time we spent chatting while pretending to do some sport. And thank you for balancing serious discussions with fully random moments. The "awkward facing dog" will always be in my heart.

Carletto, grazie per la tua innata spontaneità che sapeva trasformare anche le giornate più grigie. Sei stato un punto di riferimento imprescindibile di questi anni.

Elenaki mou, thanks for being such a generous heart. I couldn't appreciate more the passion and dedication you put in anything you do for other people.

Cyril, thanks for showing your (often well hidden) kind soul. I am very grateful to know that I can always count on you, wherever we will be.

Fred, grazie per avermi accolta nei Pollis+1. I giri in bici del sabato mattina insieme sono stati tra i momenti più felici dei weekend olandesi.

Nadi, you might not know it, but you are one of the people I admire most. Thanks for being such a great listener.

Flip, my Portoghesino. You were the best roommate I could have wished for! Thank you for all the coffee breaks and teas in our lovely houses.

Curriculum Vitae

Luisa Raimondo was born on the 27th February 1994 in Biella, Italy. She pursue her scientific high school studies at "Liceo Scientifico A. Avogadro" in Biella.

She moved to Torino to start her Bachelor's degree in Physics, obtained in 2016 at Università degli Studi di Torino.

She continued her Master in Nuclear, Sub-nuclear and Biomedical Physics at Università degli Studi di Torino. At the end of her Master's, she enrolled in an Erasmus Traineeship program at the University Medical Centre (UMC) in Utrecht, where she performed her Master's thesis on the CAIPIRINHA acceleration technique for high temporal resolution fMRI acquisitions at 7T.

After her graduation, she started her PhD in February 2019 at Spinoza Centre for Neuroimaging, Amsterdam. The research and findings of these four years resulted in this thesis.